An object-oriented model of the human lower extremity for inverse and forward dynamic simulation of human gait

Von der Fakultät für Ingenieurwissenschaften, Abteilung Maschinenbau der
Universität Duisburg-Essen
zur Erlangung des akademischen Grades

DOKTOR-INGENIEUR

genehmigte Dissertation

von
Daniel Strobach
aus
Geldern

Referent: Univ.-Prof. Dr.-Ing. Andrés Kecskeméthy
Korreferent: Univ.-Prof. Frans C. T. van der Helm

Tag der mündlichen Prüfung: 17.08.2009

Danksagung

Die vorliegende Arbeit entstand größtenteils während meiner Tätigkeit als wissenschaftlicher Assistent am Lehrstuhl Mechanik der Universität Duisburg-Essen. Mein besonderer Dank gilt Herrn Univ.-Prof. Dr.-Ing. Andrés Kecskeméthy für seine Unterstützung und die Möglichkeit zur Arbeit auf diesem außerordentlich interessanten Gebiet der Biomechanik sowie Herrn Univ.-Prof. Frans C. T. van der Helm für die Erstellung des Zweitgutachtens zu dieser Arbeit. Weiterhin möchte ich mich bei der Abteilung für Kinderchirurgie der Universitätsklinik Graz bedanken, die meine Arbeit stets mit Interesse verfolgt und die benötigte Datenbasis zur Verfügung gestellt hat.

Allen meinen ehemaligen Kollegen am Lehrstuhl für Mechanik und Robotik danke ich für die angenehme Zusammenarbeit. Zu besonderem Dank bin ich Herrn Dr.-Ing. Martin Tändl verpflichtet, der mich insbesondere bei der Lösung programmiertechnischer Fragestellungen ohne Berücksichtigung der Tageszeit unterstützt hat.

Keine Dissertation gelingt, wenn nicht das private Umfeld ebenfalls bereit ist, Opfer zu bringen. In diesem Zusammenhang kann ich weder meiner Frau noch meinen Eltern genug danken für ihre Geduld, ihre Unterstützung, die richtigen Worte zur richtigen Zeit und gelegentlich auch den berühmten Tritt in den Hintern.

Geldern, im Januar 2010 Daniel Strobach

Contents

List of Figures

List of Tables

Chapter 1

Introduction

1.1 Background and motivation of the presented work

Due to the growing number of surgical interventions and rising quality standards, the computer modeling of the human musculoskeletal system is playing an increasingly important role in medicine. In order to support traditional diagnosis and therapy planning, surgeons are seeking computer tools that allow for the prediction of therapy consequences prior to its application to the patient.

One specific field of application is the treatment of children suffering from cerebral palsy (described in the 19th century and termed "Little Disease" in honor of W.J. Little [http://www.about-cerebral palsy.org, 2009]). Generally, between 0.1% and 0.3% of all children born alive show the characteristic symptoms ([http://www.onmeda.de, 2008], [http://www.sonderpaed-online.de, 2008]); however in case of premature birth the risk increases by factors of 100-300. Causes can be prenatal (e.g. hypoxia, metabolism dysfunction; about 20% of all cases), perinatal (e.g. premature birth, umbilical chord complications; about 60% of all cases) and postnatal (e.g. meningitis, thrombosis, embolism; about 20% of all cases). In the most frequent clinical picture (75% of all cases) patients display increased tonicity leading to a hardening of muscles during motion causing spastic movement. The most important subdivision in this context are hemiplegia (32% of all cases) and diplegia (40% of all cases), where in the first case the symptoms concentrate on the extremities of the left or right half body and generally affect the arms stronger than the legs, and in the second case symptoms concentrate in

the lower extremity. Typical effects of the described symptoms are pathologic motion performances (e.g. talus equinus, see Fig. 1.1) due to range restrictions caused by muscle shortening and/or constant muscle contraction and/or joint acampsia.

Therapy approaches are chosen according to the degree of affection and cover conservative approaches such as medical treatment, physiotherapy, occupational therapy and orthopedics. A surgical intervention is chosen if classical therapies fail or are assumed to be insufficient. In this context, all surgical approaches aim at a correction of muscle contractions and deformations in order to establish muscular balance, such that "normal" motion performance is possible, or at least a progression of pathological motion performance is prevented. Typical examples here are (1) tendon transfer (modifying origin and/or insertion location [Delp et al., 1994], [Koh and Herzog, 1998], [Asakawa et al., 2002]), (2) tenotomy (also denoted tendotomy) (modification of tendon tissue) or myotomy (notching of muscle tissue, (fractional) apneurotic lengthening [Zwick et al., 2002]) in order to release a dynamical or fixed contraction of muscle tissue, (3) neurotomy (cutting specific nerves) to partially or even completely relax a spastic palsy irreversibly and (4) osteotomy (manual deformation of bones [Saraph et al., 2006]) if the grade of relaxation of muscle tissue achieved by tenotomy and/or myotomy is insufficient. In many cases an appropriate combination of the above mentioned methods is applied.

All surgical approaches have in common that the success of therapy is significantly dependent on the expertise of the specific surgeon. Furthermore most of the surgical approaches are irreversible, which creates the need for methods that help surgeons to assess a priori the consequences of changes in the biological system either leading to alternative therapy approaches avoiding a surgical intervention or, if intervention is unavoidable, at least reducing stress for the patient due to optimized operation planning. In the case of cerebral palsy, typical problems are the unknown optimal amount of tendon and/or muscle lengthening in the case tenotomy/myotomy/tendon transfer, the unknown optimal osteotomy quantities (angle, shortening/lengthening) applied to a specific bone, as well as the unknown effect of the total elimination of influence of a specific muscle. A computer program that allows the surgeons to perform patient specific operation planning must hence supply (1) the complete motion analysis of the biological system at hand, (2) a simple and flexible interface and (3) fast computational performance making it suitable for on-line applications. To this end, the complex interrelationships between bones, joints and ligaments are mapped to a limited set of characteristic quantities, and modeling of the musculoskeletal system is simplified to

a level in which all significant effects are reproduced while avoiding unnecessarily long computation times. For normal gait analysis, this can be accomplished by a multibody model containing only rigid bones and simplified joint models.

The CPU-time consumption in the dynamical simulation of human gait is mainly caused by the identification process of the time history of muscle activation profiles necessary to fulfill a prescribed motor task. To this end, several descriptions of muscle excitation/activation have been investigated (see e.g. [Davy and Audu, 1987], [Anderson and Pandy, 1999a], [Zajac, 1989] as well as [Lloyd and Besier, 2003], [Jonkers and Spaepen, 2003]). In this context, most approaches restrict themselves to simple motoric tasks, whereas complex motion tasks are still not treated in literature as they require a large number of parameters leading to extremely long computation times.

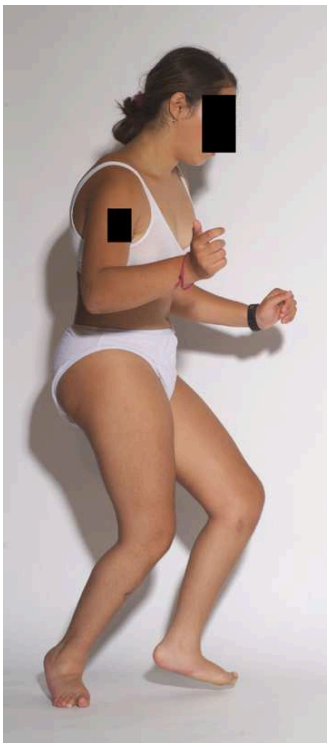

Figure 1.1: Typical clinical picture in pathological gait: talipes equinus

On the other hand, current diagnosis methods have such a large tolerance interval (approx. 30%-40%), that computer simulations would provide a major contribution if dynamics could be predicted with tolerances of 10%-20%. In this setting, methods for providing a first rough estimate of muscle activation time history that can be refined in further optimization stages would render a tool with which typical medical decisions could be already supported better than by conventional methods.

In this thesis, four problems in the quest for finding appropriate numerical tools for medical diagnosis of human gait are tackled. The first one is to set up an open-architecture, object-oriented library for forward dynamics simulation of human gait that allows one to include easily models of varying complexity and interdisciplinary nature. This is one of the main contributions of this thesis. The second one concerns algorithms for marker artefact reduction that can be used with standard motion tracking systems. In the third place, a numerical scoring technique is presented for supporting the medical diagnosis fixed/dynamic *talipes equinus* based on an analysis of muscle length rates. And finally, the identification of muscle activation profiles based on forward dynamics simulation is discussed. This is a major topic of research in current

gait biomechanics. Here, efficient methods for forward dynamics simulation are set up, including a new approach for muscle activation identification based on continuous base functions, and a systematic investigation of sensitivities in parameter variations is performed, showing that muscle activation identification needs additional measurements apart from pure kinematical tracking data in order to yield unique results.

1.2 Literature survey

The investigation of human motion in general and especially gait has been of interest throughout history. The origins of gait analysis in Europe are dated to the 17th century [Sutherland, 2001],[Paul, 1998], when G.A. Borelli (1608-1679, a student of B. Castelli who himself was a student of G. Galilei) investigated the physiological processes in living organisms on the basis of statics and hydraulics. The results of his consideration of the body as a simple machine were published in 1680 in his book *De motu animalium* [Borelli, 1680]. Principles of other famous scientists such as the classical mechanics of Sir I. Newton (1643-1727) and the Cartesian coordinate representation of R. Descartes (1596-1650) were applied in combination by W. Weber, E. Weber, W. Braune and O. Fisher between the middle of the 19th and the early 20th century, representing the first methodic investigation of human gait regarding to todays standards. ([Weber and Weber, 1836], [Braune and Fischer, 1889], [Fischer, 1904]).

A major contribution on the way to todays standards in gait analysis can be assumed to be the invention of automated motion capturing processes. Early (and completely unautomated) methods used photographs of reflective markers attached to specific anatomic landmarks and the subjects under investigation walking in the illumination of a strobe light. The resulting photographs were used to realize measurements of the individual segments. However, an obvious problem of this method was the need of manual measurements for all joint angles and its limitation mainly to investigations in the sagittal plane. Results of such investigations (which nevertheless are rather close to results obtained by recent technology) can be found in [Murray et al., 1964], [Murray et al., 1970]. In 1976, Jarret et. al ([Jarret et al., 1976]) proposed a system based on the work of Furnée ([Furnée, 1967]), who developed a single camera television system with an interface to a digital computer which allowed an automated recognition, digitalization and presentation of marker positions. This system and further developments on this method are the basis for the original VICON system developed by Oxford Metrics which represents a highly established system for gait analysis.

In parallel to the development of motion capturing techniques, electromyography measurements, i.e. the measurements of electrical activity of muscles (EMG) were invented. First major studies of the EMG during normal walking were performed by the group of Inman between 1940 and 1950. Although still poor in performance, labor intensive, invasive, computationally demanding and of only limited application of these methods in a clinical setting, these investigations represent a major step towards todays standards in gait analysis ([Inman et al., 1981]). Improvements in procedures, measurement techniques and equipment since then made EMG to become a standard ([Basmajian, 1974]). Today's techniques cover the use of surface electrodes and fine wire electrodes. The first method is non-invasive, painless and mainly appropriate to collect data of superficial muscles. However, measurement results can be severely influenced and contaminated by "crosstalk" of other muscles next to the location of the sensor and can therefore only give a basic tendency about muscle activity in a certain region. The latter method is invasive and occasionally painful for the person under investigation. However, the insertion of fine wire electrodes using hypodermic needles supplies detailed information about the activity of a few motor units within a particular muscle. The fact that this method is invasive and painful limits its applicability to gait analysis, however. In the context of gait analysis, EMG is mainly used to determine the timing of muscle activity, as a direct determination (measurement) of muscle force is impossible. More precisely, EMG measurements can only allow conclusions about muscle force generation if kinematic and dynamic data of synchronically performed motion capturing is considered.

The search for scientific methods of recording the magnitude of heel-ground contact also began in the 19th century. First publications concerning one-dimensional informations stem from Carlet ([Carlet, 1872]). The described method utilized air reservoirs to measure the force applied to heel and forefoot. Nevertheless, the achieved results reflect the measurements of a modern force plate fairly good ([Sutherland, 2005]). The first force platform that allowed its application in clinical use was invented by Cunningham and Brown, published in 1952 ([Cunningham and Brown, 1952]). This platform used strain gauge technology and divided the ground reaction forces into four components. Due to its sensitivity to temperature changes, a continuous calibration was necessary. The standard force plate applied today uses piezo-electric techniques and is commercially produced since 1969, supplying three-dimensional information about ground reaction force and moment.

A complete overview of the history and development of gait analysis can be found in

[Whittle, 1996], [Paul, 1998] and the publications of Sutherland ([Sutherland, 2001], [Sutherland, 2002] and [Sutherland, 2005]). Standard techniques and gait pattern in normal and pathological function are explicitly described and summarized by Perry ([Perry, 1992]).

The application of clinical gait analysis as it is known and applied today, consisting of the combined consideration of kinematic, kinetic and electromyography measurements and postprocessing of this data for assessment using inverse dynamics techniques, became standard in the late 1970's. Today, several companies supply hardware and software packages allowing for gait analysis and assessment based on characteristic kinematic and kinetic quantities in terms of charts and (animated) visualization of motion. Without being exhaustive, some established systems in this context are mentioned in the sequel. VICON's *BodyBuilder* supplies a plug-in for gait analysis ([http://www.vicon.com, 2008]), which combines motion capturing hardware using passive markers and high speed, high resolution CMOS cameras in combination with a rigid body model of the human lower extremity, allowing for inverse dynamics computations and patient-specific gait assessment in terms of charts. Information about muscle behavior, although assumed to be important for diagnosis of e.g. a dynamic of fixed *talipes equinus* is not available. Similarly, C-Motion Inc. ([http://www.c motion.com, 2006]) offers a software package termed *Visual3D*, allowing for classical gait analysis and data interpretation in terms of charts and 3d visualization, and using the standardized 'c3d' file format for the computation of kinematic quantities, enabling this system to be combinable with any standard motion capturing hardware that exports c3d data. The applied model of the human leg comprises 6 degrees of freedom. ZEBRIS ([http://www.zebris.de, 2006]) uses active markers with ultrasound technology to capture patient motion. The postprocessing of the captured data is performed by the software package *WinGait* to supply charts of the desired kinematic quantities. All these systems have in common that they only allow for evaluation of a "status quo", e.g. the quality of gait before and/or after therapy, a prediction of therapy results in general and of surgery results in particular is impossible.

Due to rising quality standards and significant improvement in computer technology and computational speed, recent research has focused on the development of computer tools supporting physicians and surgeons in diagnosis and therapy planning and therefore going beyond classical gait analysis. Combining mathematical muscle models with standard rigid body kinematics allows to compute forward dynamics simulations in addition to inverse dynamics results. An example for such a package

is *SIMM* (Software for Interactive Musculoskeletal Modeling, Musculographics Inc., [Delp and Loan, 1995], [Delp and Loan, 2000]) which provides generic building blocks for bones, joints, ligaments and muscles to generate arbitrary musculoskeletal systems. Forward dynamics computations are based on a Hill-type muscle model described in [Zajac, 1989]. The package additionally features the investigation of biomechanical consequences of surgery by simulation of bone deformations and reconstructions, joint replacements or tendon transfer ([Delp, 2000], [Delp et al., 1994], [Asakawa et al., 2002], [Arnold et al., 2000]). The system *AnyGait* ([Technology, 2003]), integrated in the *AnyBody* project of Aalborg University in Denmark provides a model of the lower extremity consisting of 7 rigid bodies for pelvis, thigh, shank and foot and includes 35 muscles for each leg. The program allows for inverse dynamics simulations of patient-specific gait motion using the gait cycle data (GCD) file format as kinematic input. *AnyGait* does not supply a very elaborate forward dynamics simulation functionality yet, which makes the package suitable only as a gait assessment tool to visualize characteristic quantities of gait. However, considering the primal simulation environment *AnyBody* as a software basis for the gait assessment plug-in, this simulation environment focuses on the modeling and the simulation of the complete human body, facilitating direct dynamics simulations. With respect to therapy and/or operation the functionalities are currently being extended. Most publications to be found using *AnyBody* consider ergonomic optimization questions of general motoric tasks ([Rasmussen et al., 2003], [Rasmussen et al., 2000]) or specified motion such as bicycling ([Rasmussen et al., 1999]) or cross country skiing ([Lund, 2005]). Other systems providing similar functionalities are not mentioned here in detail, however almost all established multibody simulation tools such as SIMPACK, ADAMS or MADYMO (for reference see [http://www.simpack.de, 2008], [http://www.adams.com, 2008] and [http://www.automotive.tno.nl, 2006], respectively) supply more or less detailed biomechanics applications within vehicle simulations (this list is not exhaustive).

In the context of the design of surgery planning software for specific pathologies such as cerebral palsy, certain methods of surgery — especially soft tissue intervention as neurotomy, tendotomy or myotomy — make the knowledge about the contribution of specific muscles to a resultant joint torque necessary. From the mechanical point of view, this problem is difficult to solve due to the high degree of redundancy resulting from a detailed model of the lower extremity. Exemplarily assuming hip joint, knee joint and ankle joint as simplified ball-and-socket joints with the total of nine degrees of freedom each, as well as a system of 35 muscles (as for *AnyGait*) or even more (as available in the presented software package) for actua-

tion, the number of actuators exceeds by far the number of degrees of freedom which are necessary to generate a prescribed motion. Approaches of direct force measurement using liquid metal strain gauge transducers, buckle transducers, implantable force transducers, pressure transducers, hall effect transducers or optic fiber transducers so far limit themselves mainly to animal experiments due to their possible severe invasive character ([An et al., 1990], [Platt et al., 1994], [Herzog et al., 1996], [Hall et al., 1999], [Meyer et al., 1990]). A good overview about strain and force transducers in human and veterinary tendon and ligament biomechanics can be found in [Ravary et al., 2004]. If the pathways of musclulotendon actuators and the levers of specific muscles with respect to the joints involved in the model for a loading condition is known, the resulting joint torque computed by inverse dynamics computations can be distributed to specific muscles solving a static optimization problem, implying a reasonable performance criterion that can be chosen on a problem-specific basis. While musclulotendon kinematics (e.g. length of musculotendon actuator and lengthening/shortening velocity, moment arms with respect to certain joints) can be determined using basic rigid body kinematics, and corresponding results can be used for diagnosis support and generalized therapy method investigations ([Delp et al., 1999b], [Schmidt et al., 1999], [Asakawa et al., 2004]), the results in muscle *force* computations are highly sensitive to the mathematical formulation of the underlying performance criterion. Commonly used criteria in literature are the minimization of metabolic energy (e. g. [Bhargava et al., 2004], [Anderson and Pandy, 1999a]) or the minimization of individual muscle stress ([Crowninshield and Brand, 1981]). Other authors use variations of the aforementioned formulations by normalization of the individual muscle forces by the maximum isometric force of the corresponding muscle or by the instantaneous maximum muscle moment. A more detailed survey on different performance criteria to resolve muscle redundancy can be found in [de Silva and Ambrósio, 2004]. The use of direct dynamics simulation of movement in general and gait especially has contributed to the general understanding of muscle-induced segmental energy redistribution, muscle co-functions and synergies. Furthermore, emulation of kinematic and kinetic prescription by dynamical simulation makes the extraction of unmeasurable quantities such as muscle force and energy consumption during a specific motor task possible. Very elaborate overviews of the general applicability of forward dynamics simulation can be found in [Zajac et al., 2002], [Zajac et al., 2003] and [Zajac, 2002]. Anderson and Pandy investigated that the results regarding muscle force computations achieved by static optimization formulations do not significantly differ from outcomes of dynamical simulations, putting the enormous computation times required

by forward dynamics simulations (about 1000 times more than for static optimization problems) into question. However, the application of forward dynamics simulation is unavoidable in several circumstances such as if (1) an accurate experimental data is not available, (2) activation time history plays an important role, (3) an appropriate time-independent performance criterion is not available or (4) novel movement is to be predicted ([Anderson and Pandy, 1999b]).

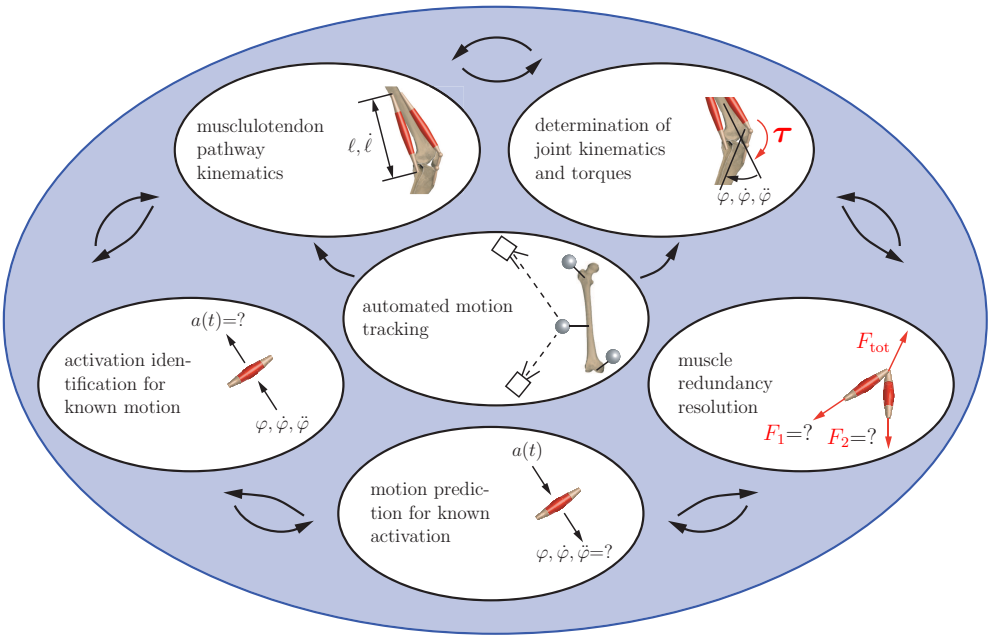

Figure 1.2: Selection of subproblems of gait biomechanics

With respect to certain surgery methods, e.g. in cerebral palsy therapy such as myotomy and tendotomy, the identification of muscle activation time histories *prior* to an operation can yield important information with respect to the grade of the clinical picture at hand and indicate the amount of surgery necessary to improve gait performance to a less pathological one. In the context of the aforementioned reasons for the application of dynamical simulations points (2) and (4) are especially fulfilled. Assuming muscle activation time histories to be known for a status quo, the modification of muscle model parameters can additionally predict motion performance after surgery, justifying the amount of required computational time. Two mainly used formulations in literature are the dismantling of tracking problems if kinematic data for a specific patient is available and it is necessary to follow a desired motion pattern, and dissolving problem formulations which only involve an initial and final state of

the model at hand if exact kinematic data is not available and/or the exact tracking of a prescribed trajectory is not important. While the first usually involves higher computational time than the latter, it is better applicable to clinical purposes due to the fact that it allows the resolution of muscle redundancy with respect to a patient specific measurement. However, several authors have reported computational times that still make the method useless for surgery planning. For example the investigation of a vertical jump in the sagittal plane including 9 muscle groups by [Spaegele, 1998] yielded computational times in the order of days, while a vertical jump optimization in three dimensions and including 54 musculotendon actuators described by Anderson and Pandy ([Anderson and Pandy, 1999a]) was solved in a time of the order of 2.5 month on a 180 MHz MIPS R5000 Silicon Graphics Indigo. The use of parallel computers (128 processors) enabled the parallel computation of the derivatives of the performance criterion involved in the optimization but still took almost a day (23.2 hours). Due to the fact that even for these restricted problem statements computational time is significantly high and parallel (super)computers are not yet standard equipment in hospitals, the only way to overcome these problems is a simplification of the involved models (segments, joints, musculotendon actuators, muscle activation). Additionally, all investigations using forward dynamics simulations to identify muscle activation time histories restrict themselves to clearly defined motoric tasks (e.g. [Davy and Audu, 1987], [Kuzelicki et al., 2005]) and are in no case appropriate to identify muscle activation time histories and/or forces for a complete gait cycle.

1.3 Thesis objectives and outline

Although clinical treatment methods are already very successful, physicians ask for support by computer tools in diagnosis as well as therapy planning. Since typically the solution of musculoskeletal biomechanics in general and gait biomechanics in particular involves subproblems of different complexity (Fig. 1.2) which are usually coupled in one way or the other, a flexible structure of the applied software is essential. Unfortunately, available software packages so far offer only a very limited applicability to research and for daily clinical life ([Erdemir et al., 2007]) and still leave two major open problems:

- since most software architectures are monolithic, improvements and extensions are difficult to implement
- the solution of musculoskeletal biomechanics requires interdisciplinary approaches.

As mentioned above, two existing frameworks for the simulation of musculoskeletal motion are *SIMM* and *AnyBody*. Table 1.1 compares some features of these software packages. It can be seen that both programs supply different philosophies in software architecture. While *SIMM* is implemented in a monolithic manner, *AnyBody* already features an object-oriented design. Hence, *AnyBody* accounts for the requirement to feature a flexible and open structure. However, in contrast to *SIMM*, many problems especially in a forward dynamics context cannot be addressed yet. Within the scope of

property/feature	***SIMM***	***AnyBody***
programming language	C	AnyScript
object-oriented structure	no	yes
generation of eq. of motion	KANE	NEWTON/EULER
representation of eq. of motion	minimal form	CARTESIAN
forward dynamics simulation	yes	no
dynamic optimization embedded	no	no
symbolic models	yes	no

Table 1.1: Comparison of a selection of features supplied by commercial software packages *SIMM* and *AnyBody* (not exhaustive)

the present thesis, a framework for the simulation of the inverse and forward dynamics of human gait is presented, which is intended to combine the beneficial properties of currently available software packages in order to improve applicability and flexibility for clinical applications. Its main features are:

- an object-oriented approach to realize an open structure,
- efficient and established code,
- an easy manageability.

For the implementation, the open and extensible, object-oriented software library MOBILE is used, which is well established in mechanical engineering applications. This software package supplies standard elements for multibody simulation and uses the kinetostatic transmission element concept for motion and force computations. Based on elementary objects such as elementary joints and rigid links as well as force elements,

special tailored classes were developed and summarized in a biomechanical library. After the presentation of the developed library, its usefulness will be illustrated at three examples:

(1) an automated improvement of motion tracking results,

(2) the analysis of musculotendon pathway kinematics,

(3) the identification of muscle activation time histories.

In this setting, the thesis is structured as follows: Chapter 2 briefly presents the basic notions in gait analysis and the anatomy of the human lower extremity. The latter part is concerned with essential notions and principles in the context of mathematical optimization theory.

In Chapter 3, the software basis for the developed library, MBSBILE, is briefly presented. Central notions such as the kinetostatic transmission element concept and its object-oriented implementation are introduced.

In Chapter 4 the model of the lower extremity used in this work is described. The initialization of the segment model by motion capturing data is explained. Different methods for scaling generic models to individual geometries are discussed. A brief overview of the central developed classes is given.

Chapter 5 describes the capabilities of the developed library for inverse dynamics simulations of human gait. In addition, two of the mentioned illustrative applications of the developed software are presented: (1) a method for the automated reduction of motion tracking errors and (2) a method for clinical diagnosis of *talipes equinus* by muscle length analysis.

Chapter 6 deals with the third illustrative application of the software package in terms of a dynamic analysis of muscle activation. A new simplified approach to muscle activation time history parameterization is described. Its performance is compared to a standard discretization in terms of (1) the feasibility of predicted muscle activation times, (2) the feasibility of the ensuing motion and (3) the consumption of computational time. Furthermore, a sensitivity analysis with respect to parameter perturbations is performed. All investigations are performed on simplified subsystems of the human leg.

Chapter 7 represents a summary and a short outlook to future developments and possibilities considering computational aspects and methodologies.

1.4 Remarks on mathematical notations

1.4.1 Vector notation, matrices

In this thesis, generally two types of vectors will appear. Those which have a *physical* meaning in spatial rigid-body kinematics and dynamics in Euklidian 3D Space, such as forces and velocities, are displayed in boldfaced font, e. g. $\mathbf{F}, \mathbf{v}$. General n-tuples, representing a collection of numbers not necessarily related to a physical meaning are displayed underlined, e.g. $\underline{q} \in \mathbb{R}^n$, i.e. $\underline{q} = (q_1, \dots q_n)^{\mathrm{T}}, q_1, \dots, q_n \in \mathbb{R}$. Such vectors appear for example in the representation of generalized coordinates of a multibody system or in the formulation of multivariate functions in the context of optimization problems.

Especially when considering physical vectors, a subscript right to the vector specifies the item or point to which the vector refers. Exemplarily, the vector $\mathbf{F}_{\mathrm{P}}$ denotes a force applied to a point P.

If not explicitly mentioned otherwise, a matrix is denoted by upper case letters, e.g. $A \in \mathbb{R}^{n \times m}$. In the context of linear mappings for the aforementioned matrix

$$\ker A = \left\{ \underline{x} \in \mathbb{R}^m \;\middle|\; A\underline{x} = 0 \right\} \tag{1.4.1}$$

denotes the *kernel* of A.

1.4.2 Coordinate systems and transformations

If the reference system in which the vector under consideration is decomposed is important to mention, this is indicated by an additional superscript left to the vector itself. In this context ${}^{\mathrm{I}}\mathbf{v}_{\mathrm{P}}$ therefore denotes a velocity, decomposed in a frame specified with name I, belonging to a point P. A change of decomposition of a vector is performed by multiplication of the vector with an appropriate transformation matrix $\mathbf{R}$. Considering two frames $\mathcal{K}_1$ and $\mathcal{K}_2$ of *different orientation* and a physical vector ${}^2\mathbf{b}$, the decomposition of the vector in frame $\mathcal{K}_1$ is given as

$${}^1\mathbf{b} = {}^1\mathbf{R}_2 \, {}^2\mathbf{b}\,, \tag{1.4.2}$$

where the right subscript of the transformation matrix in (1.4.2) is related to the frame in which the given vector is decomposed, and the left superscript indicates the frame

the vector is transformed to. Due to orthonormality $\mathbf{R}^{-1} = \mathbf{R}^{\mathrm{T}}$ of a transformation matrix, the inverse transformation is given by

$$\underbrace{{}^1\mathbf{R}_2^{\mathrm{T}}}_{={}^2\mathbf{R}_1} \, {}^1\mathbf{b} = {}^2\mathbf{b} \, . \tag{1.4.3}$$

Elementary rotations about single axes of coordinate frames are denoted as

$$\mathbf{R}_x(\varphi) = \mathbf{R}[\, x,\, \varphi \,] = \begin{bmatrix} 1 & 0 & 0 \\ 0 & \cos\varphi & -\sin\varphi \\ 0 & \sin\varphi & \cos\varphi \end{bmatrix} , \tag{1.4.4}$$

$$\mathbf{R}_y(\varphi) = \mathbf{R}[\, y,\, \varphi \,] = \begin{bmatrix} \cos\varphi & 0 & \sin\varphi \\ 0 & 1 & 0 \\ -\sin\varphi & 0 & \cos\varphi \end{bmatrix} , \tag{1.4.5}$$

$$\mathbf{R}_z(\varphi) = \mathbf{R}[\, z,\, \varphi \,] = \begin{bmatrix} \cos\varphi & -\sin\varphi & 0 \\ \sin\varphi & \cos\varphi & 0 \\ 0 & 0 & 1 \end{bmatrix} , \tag{1.4.6}$$

and are usually interpreted to be decomposed in the assumed fixed frame.

1.4.3 Functions and derivatives

Considering a scalar function $f(\underline{x}) \in \mathbb{R}$, $\underline{x} \in \mathbb{R}^n$, the gradient $\nabla f(\underline{x}) \in \mathbb{R}^n$ is defined as

$$\nabla f(\underline{x}) = \frac{\partial f(\underline{x})}{\partial \underline{x}} = \left[\frac{\partial f}{\partial x_1}, \, \ldots, \, \frac{\partial f}{\partial x_n} \right] . \tag{1.4.7}$$

The corresponding (square, symmetric) Hessian matrix $H_f(\underline{x}) \in \mathbb{R}^{n \times n}$, $\underline{x} \in \mathbb{R}^n$ is given as

$$H_f(\underline{x}) = \nabla^2 f(\underline{x}) = \begin{bmatrix} \dfrac{\partial^2 f}{\partial x_1^2} & \cdots & \dfrac{\partial^2 f}{\partial x_1 \partial x_n} \\ \vdots & \ddots & \vdots \\ \dfrac{\partial^2 f}{\partial x_1 \partial x_n} & \cdots & \dfrac{\partial^2 f}{\partial x_n^2} \end{bmatrix} . \tag{1.4.8}$$

For a vector function $\underline{f}(\underline{x}) = (f_1(\underline{x}), \ldots, f_m(\underline{x})) \in \mathbb{R}^m$, $\underline{x} \in \mathbb{R}^n$ the Jacobian $\mathbf{J}_f(\underline{x}) \in \mathbb{R}^{m \times n}$ is given as

$$\mathbf{J}_f(\underline{x}) = \frac{\partial \underline{f}(\underline{x})}{\partial \underline{x}} = \begin{bmatrix} \dfrac{\partial f_1(\underline{x})}{\partial x_1} & \cdots & \dfrac{\partial f_1(\underline{x})}{\partial x_n} \\ \vdots & \ddots & \vdots \\ \dfrac{\partial f_m(\underline{x})}{\partial x_1} & \cdots & \dfrac{\partial f_m(\underline{x})}{\partial x_n} \end{bmatrix}. \tag{1.4.9}$$

Chapter 2

Basic notions

2.1 Basic notions of gait motion and anatomy

Human walking is — although well known to any healthy person and one of the most common motoric tasks — a process of extreme complexity. The simple task of "walking from point A to point B" represents a sequence of procedures and interactions initiating a sequence of neural signals leading to appropriate time histories of muscle activation causing a desired limb motion. Although general control of motion is performed by the motor cortex, coordination and generation of patterns is provided by the cerebellum. Muscle forces are generated by spinal reflexes which in exchange react to sensory input of different proprioceptive sensors [Whittle, 1996]. Additionally, due to complex kinematic coupling of bones, joints and soft tissue as ligaments and muscles as well as the possible affection of the execution by several factors such as environment influences (e.g. sudden appearance of obstacles) and interaction with other individuals, the signal generation has to be flexible and can only in general be understood as the tracking of standard patterns. To identify these patterns and assess normal and pathological gait performances, the behavior of the human lower extremity is mapped to relatively few (characteristic) parameters. However, this limitation also reduces the field of application to normal walking, as parameters which gain importance in e.g. rapid movements (sports) such as bone elasticity and deformations, are usually neglected.

The important characteristics and terminologies in the context of normal gait analysis are briefly presented in the sequel.

2.1.1 Characteristic quantities and basic functionalities of gait

In clinical applications, gait motion is usually assessed by consideration of a complete *gait cycle* or *stride*, denoting the period between *heel strike* or *initial contact* of one foot until next heel strike/ground contact of the same foot. Gait is subdivided into periods of *single limb stance* and *double limb stance* where the first denotes periods where only one foot is in contact with the ground and the latter describes phases of stride where both feet are in contact with the ground. Stride begins with *initial double stance*, followed by a period of single limb stance. *Terminal double limb stance* denotes the second phase of double limb stance in the stride under consideration. Regarding each leg separately, phases of single support by one leg are referred to as *swing phase* of the opposite leg. The period of ground contact of each leg is termed *stance phase*. The terminologies *step* and *step length* refer to the period between the initial heel strike of one foot and the initial heel strike of the opposite foot. In a more detailed classification, leg motion during gait is subdivided into seven characteristic periods:

- *loading response* ranges from 0% to 10% of gait, starting with the initial contact (heel strike) of the foot under consideration and ends when the opposite foot is lifted
- *mid stance* runs from 10% to 30% and begins when the opposite foot leaves ground, ending at that point of time when body weight is completely borne by the leg under consideration (first period of single limb stance)
- *terminal stance* follows *mid stance* from 30% to 50% of gait cycle, its end defined by the initial contact of the opposite foot. Included in this period is the heel lift-off.
- *pre swing* starts at 50% with the initial contact of the opposite foot and is finished at 60% by "toe-off" of the leg regarded.
- *initial swing* lasts from 60% to 73% and represents the first swing phase of the considerer leg. Its end is defined at the instant in time when the leg is right in opposite to the leg supporting the body.
- *mid swing*, following initial swing lasts from 73% to 87% and ends when the shank of the supporting leg is in vertical position.
- *terminal swing* is the last swing phase from 87% to 100%, finished by the initial contact of the following gait cycle.

All notions are depicted in Fig. 2.1.

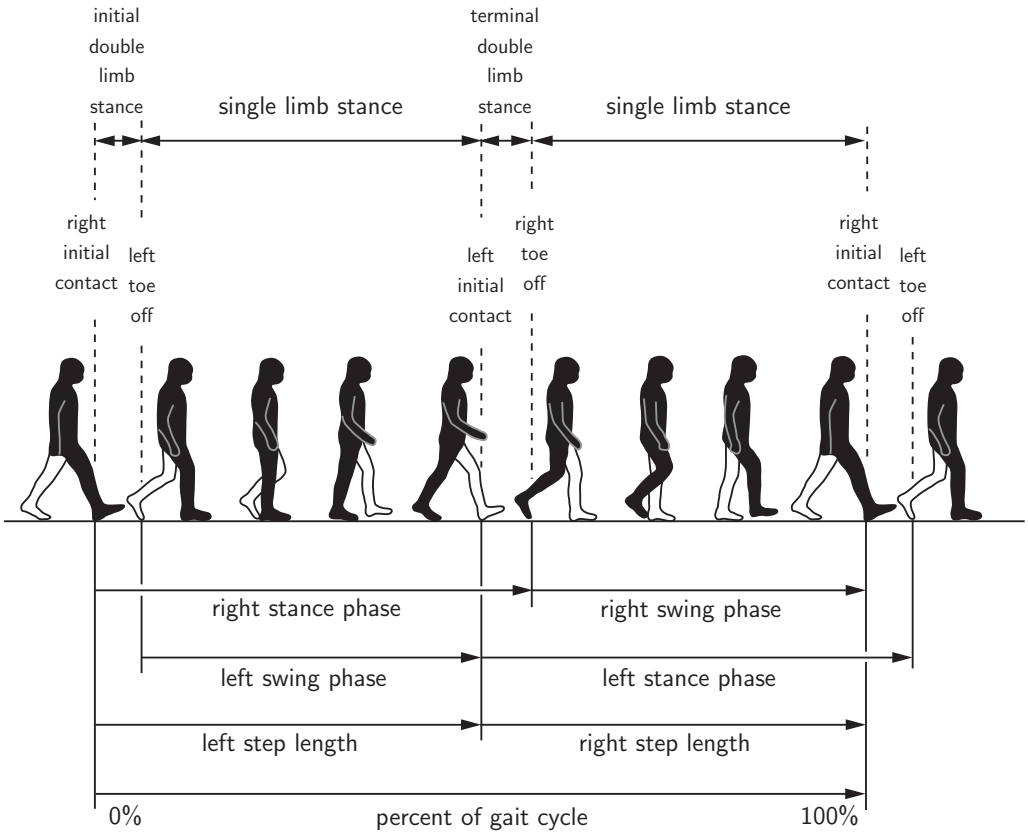

Figure 2.1: Different phases of human gait. The right leg is depicted in black, the left in white.

The average duration of characteristic periods in normal gait is displayed in a coarser graduation in Tab. 2.1 (table adapted from [Perry, 1992]). However, these numbers can only be understood as a general guide line, as significant changes can be caused by individual variations and pathological abnormalities.

Gait phase	duration [% of gait cycle]
initial double limb stance	10
single limb stance	40
terminal double limb stance	10
swing	40

Table 2.1: Typical duration of characteristic phases of gait

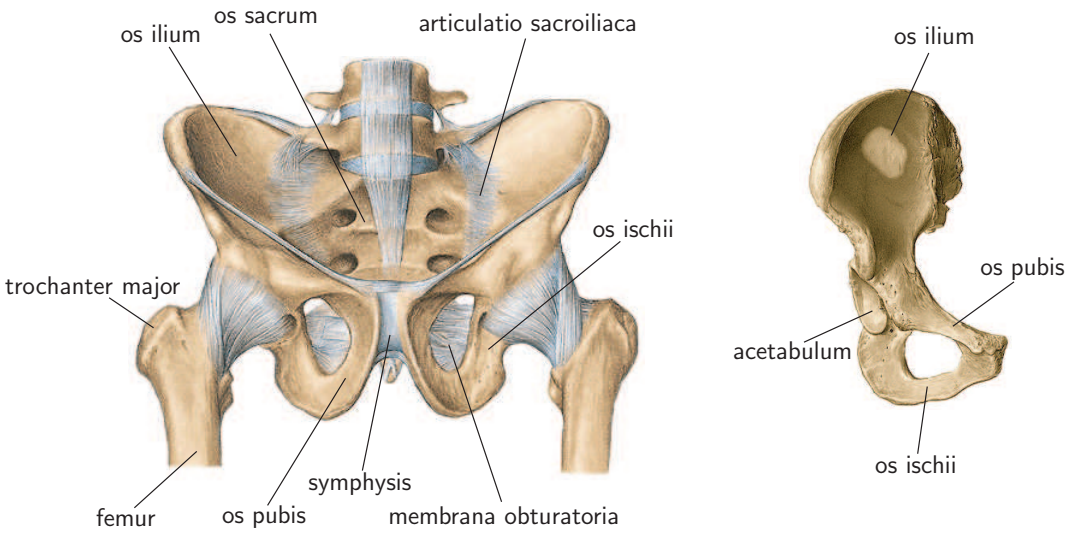

Figure 2.2: Left figure: ventral view of pelvis bone and ligament structure; Right figure: location of the acetabulum and subdivisions of pelvis bone (pictures adapted from [Sobotta, 2005])

Besides consideration of the mentioned quantities, *walking speed* and *cadence* are regarded, the latter denoting the number of steps per time unit (usually minutes), the first denoting the progression of the center of mass during gait. Observations show that healthy individuals choose a walking speed minimizing the consumed metabolic energy ([Ralston, 1976]) of about 80m/min, which has also been verified by other authors (see e.g. [Anderson and Pandy, 2001]).

2.1.2 General skeletal structure of the lower extremity

In the locomotion system of the human body, the interaction between *passive* and *active* elements is the basis for an efficient motion performance. Passive elements are bones, ligaments and joints, while muscles and supporting tissues are referred to as active elements. In the context of this thesis, only the lower part of the passive locomotor system – the lower extremities – and the related muscles are considered. A very elaborate overview of the complete human musculoskeletal system can be found in [Sobotta, 2005] and [Kapandji, 1999].

The human lower extremity can be considered as a chain of segments beginning at the pelvis with the hipbone (*os coxae*).

The hipbone itself consists of three parts, the iliac bone (*os ilium*), the ischium (*os ischii*) and the pubic bone (*os pubis*). The bodies of these bones together form the *acetabulum* (see Fig. 2.2, right figure). The interaction of the bones is represented by joints and additional structures consisting of cartilage as well as ligaments. The connection of the pelvis to the upper body between *os coxae* and the lower end of the spine at the sacrum (*os sacrum*), termed sacroiliac joint (*articulatio sacroiliaca*), consists of an amphiarthrosis and allows only very little relative motion between hipbone and sacrum. A synchondrosis between left and right *os pubis*, termed *symphysis*, serves as auxiliary stabilization of the hipbone. Additional ligaments (e.g. *membrana obturatoria*) serve as connections between *os ischii* and *os ilium* as well as *os ischii* and *os pubis*. Due to the participation of all three mentioned bone parts, loads in the hip joint are distributed uniformly in the hipbone. All important notions are displayed in Fig. 2.2.

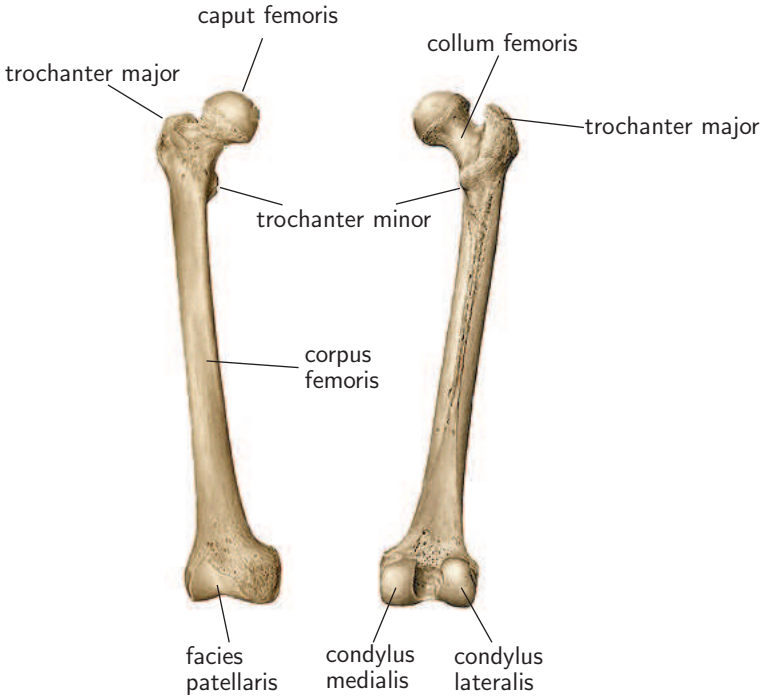

Figure 2.3: Left figure: ventral view of femur bone; Right figure: posterior view of femur bone (pictures adapted from [Sobotta, 2005])

The *femur* is the longest hollow bone in the human body and represents the osseous basis of the thigh segment. Its head at the proximal end articulates with the pelvis at the acetabulum forming the hip joint (*articulatio coxae*). The tilted femoral neck (*col-*

lum femoris) connects femoral head and the diaphysis of the *femur* (*corpus femoris*). At the distal end of the *femur* two condyles (*condylus medialis* and *condylus lateralis*) articulate with the *tibia*, forming the knee joint (*articulatio genus*). The articular surface of the two condyles at the anterior side shape the *facies patellaris*) which is in contact to the *facies articularis*, representing the posterior surface of the *patella* (see Fig. 2.3, Fig. 2.7).

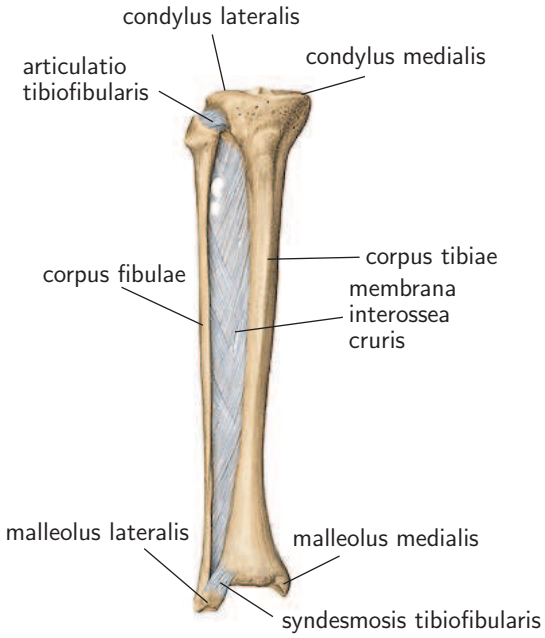

Figure 2.4: Anterior view of tibia and fibula, ligament structure (picture adapted from [Sobotta, 2005])

In contrast to the thigh segment, the osseous basis of the shank consists of two bones. Shinbone (*tibia*) and *fibula* are positioned in parallel, connecting the knee joint at their proximal end with the ankle joint (*articulatio talocruralis*, see Fig. 2.4). In combination with the homonymous parts of the *femur*, the articular surfaces *condylus medialis* and *condylus lateralis* form the knee joint (*articulatio genus*). At the distal end, the ankle joint represents the connection between the two bones of the shank and the foot. Concretely, *tibia* and *fibula* articulate with the foot at the *facies articularis malleoli* and the *facies articularis inferior* which are located at the underneath of the *malleolus medialis*. At the medial side of the *malleolus lateralis* of the *tibia*, the *facies articularis malleoli* (similarly named as the corresponding surface of the *tibia*) represents the connection to the foot. The most important connection of the shank

bones, the *membrana interossea cruris* mainly serves as an origin surface for muscles with deeper sub-dermal location. The *membrana interossea cruris* is supported at the distal end by the *syndesmosis tibiofibularis* and at the proximal end by the *articulatio tibiofibularis* which consists of an amphiarthrosis and allows only little relative motion between *tibia* and *fibula*.

The skeletal structure of the foot can be subdivided into three main sections *tarsus* (*ossa tarsi*), *metatarsus* (*ossa metatarsi*) and toes (*ossa digitorum pedis*). The area of transition between shank and foot (*tarsus*) consists of the seven tarsal bones: talus bone (*talus*), calcaneus bone (*calcaneus*), cuboid bone (*os cuboideum*), the three cuneiform bones (*os cuneiforme mediale*, *os cuneiforme intermedium*, *os cuneiforme laterale*) and navicular bone (*os naviculare*). All bones articulate via specific surfaces. Talus bone, calcaneus bone and navicular bone in particular form the ankle joint (*articulatio talicruralis*). The bones of the metatarsus (*os metatarsi I-V*) are hollow bones and directly associated with the toes. The toes themselves are sectioned into different phalanges (phalanx bones). While the great toe is composed of only two bones (*phalanx proximalis* and *phalanx media*), all other toes supply three phalanx bones (additionally to the two mentioned before, the *phalanx distalis* is added). The joints connecting the bones of the foot are compositely termed *articulationes pedis* and *articulationes digitorum pedis*.

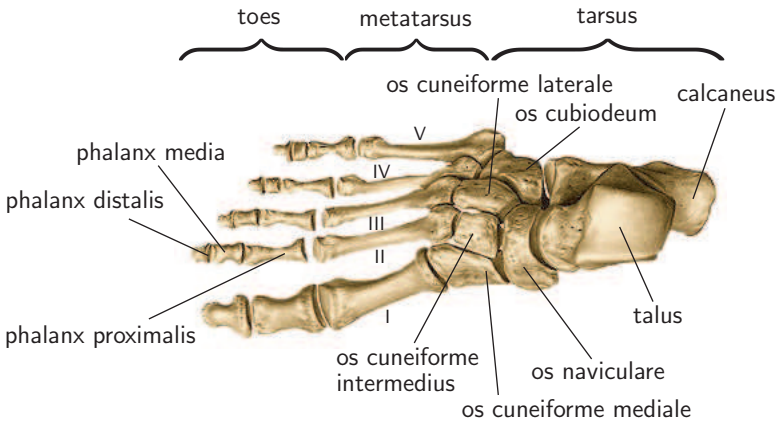

Figure 2.5: Dorsal view of the foot, bone structure of tarsus, metatarsus and toes (picture adapted from [Sobotta, 2005])

2.1.3 Joints of the human lower extremity

Joints can be classified according to structure and function. From the structural point of view, the human body supplies three kinds of joints:

- **Fibrous**, where bones are joined by tight and inflexible layers of dense connective tissue which mainly consist of collagen fibers. For adults these joints do not allow any movement, in case of children these structures can be flexible. Examples of such joints are cranial structures.
- **Cartilaginous**, where the connection entirely consists of cartilage, allowing only little relative movement between adjacent bones. An example of such joint structures is the pubic symphysis (see Chap. 2.1.2). These joints are also termed *synchondroses*.
- **Synovial**, where a space between the articulating bones exists. Synovial joints are usually grouped according to their shape which controls the movement they allow (e.g. ball-and-socket joint at the hip, bicondyloid joint at the knee).

Considering the functional perspective one obtains three characteristic attributes:

- **Synarthrosis**, permitting no movement (at least for adults, see above)
- **Amphiarthrosis**, allowing only for small movement; an example for an amphiarthrosis is the sacroiliac joint between pelvis bone and sacrum
- **Diarthrosis**, permitting a variety of movements (e.g. flexion, adduction, pronation); only synovial joints are diarthrodial

In the sequel only the three major joints of the human lower extremity are described, since for the simulation of movement described in this thesis only hip, knee and ankle joint are of particular interest.

Hip joint (*articulatio coxae*)

According to the introduced notions, the hip joint (*articulatio coxae*) represents a synovial joint. At the hip joint, *femur* and pelvis bone articulate in the form of a ball-and-socket joint. The ball of the joint is formed by the head of the *femur* (*caput*

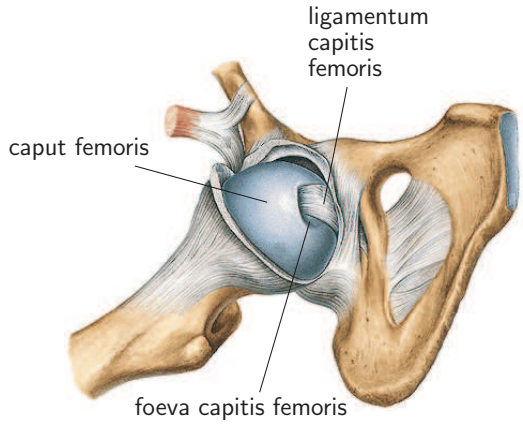

(a) joint ball in lateral, distal view; partially opened joint capsule and ex-articulated *caput femoris*

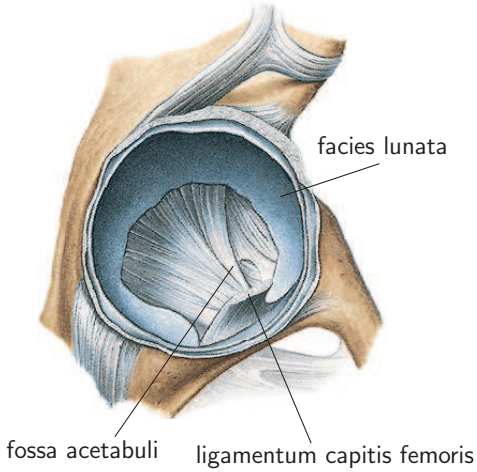

(b) joint socket in lateral, distal view; partially opened joint capsule and ex-articulated *caput femoris*

Figure 2.6: Hip joint (*articulatio coxae*): ball and socket, supporting ligament structure (pictures adapted from [Sobotta, 2005])

femoris), featuring a small dent at its superior medial side (*foeva capitis femoris*) at which the *ligamentum capitis femoris* is attached, being connected to the *fossa acetabuli* and besides other structures supports the stability of the joint (Fig. 2.6(a)).

The socket of the hip joint is formed of the *facies lunata* of the *acetabulum*. The *ligamentum capitis femoris*, which is connected to the head of the *femur*, has its origin in the *fossa acetabuli*, which is filled with a cushion of connective tissue stabilizing the hip joint (Fig. 2.6(b)). Of particular interest from the biomechanical point of view are the ranges of motion that are typically provided. As a ball-and-socket joint, it enables three independent moving directions: flexion-extension in the sagittal plane, adduction-abduction in the frontal plane and internal-external rotation about a longitudinal axis. The definition of the corresponding axes of rotation and motion ranges can be found in Tab. 2.2.

Knee joint (*articulatio genus*)

The knee joint (*articulatio genus*) represents a bicondyloid variety of a synovial joint comprising three articulating bodies and can be subsectioned into two separate joints. At the femoro-patellar joint *patella* and *femur* articulate via the *facies articularis*

motion	definition	max. range [deg]
flexion	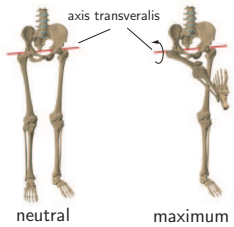	120°-130°
extension	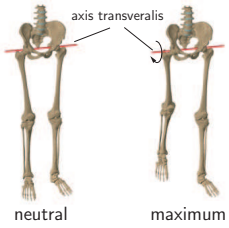	10°-15°
adduction	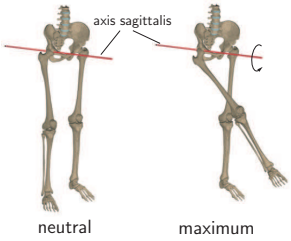	20°-30°
abduction	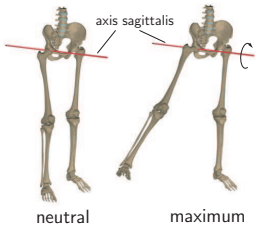	30°-45°
internal rotation	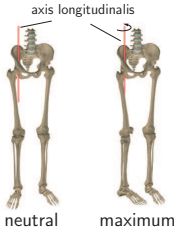	30°-45°
external rotation	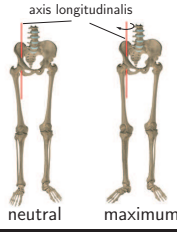	40°-50°

Table 2.2: Hip joint (*articulatio coxae*): notion definition and range of motion (data and pictures adapted from [Sobotta, 2005]).

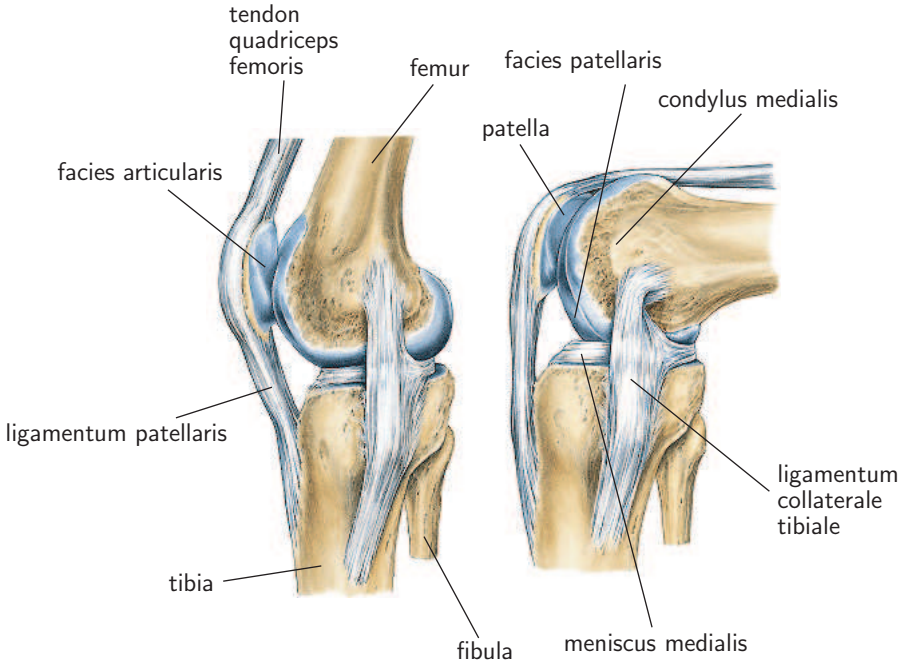

Figure 2.7: Knee joint (*articulatio genus*): bicondyloid variety of a synovial joint, general structure and specifications in extended and bended position, supporting ligament structure, right knee, medial view (picture adapted from [Sobotta, 2005])

(posterior surface of the *patella*) and the *facies patellaris* (anterior surface of *femur* located between the two femoral condyles). In extended position, the *patella* is in contact to the *femur* only with the distal part of the *facies articularis*, while increasing flexion leads to plane contact between the articulating surfaces. In vertical direction, the position of the *patella* with respect to the *tibia* is constant due to the fact that the *patella* is embedded in the *ligamentum patellae*. This nidation is also the reason for the *patella* serving as an hypomochlion for the muscle *quadriceps femoris* which is attached to the *ligamentum patellae* at its proximal side.

Additionally, with increasing knee flexion a relative motion of the *patella* with respect to the *tibia* in horizontal direction takes place, since the axis of rotation (*axis transversalis*) is moving due to the increasing curvature of the femoral condyles to the posterior side of the *femur*. As a result, the area of contact between *femur* and *tibia* relocates during the flexion process to the rear side of the articulating surface of the *tibia* while at the same time the changing curvature of the femoral condyles causes a displacement of the *axis transversalis* with respect to the *tibia* in vertical direction (Fig. 2.7, Tab. 2.3). The femoro-tibial joint links *femur* and *tibia*. A complex structure of ligaments (e.g. *ligamentum collaterale tibiale*) and menisci in combination with the muscles travers-

ing the joint provide stability and restrict motion to the intended range. All notions and an overview of the general joint structure are given in Fig.2.7. The definition of the corresponding axes of rotation and motion ranges can be found in Tab. 2.3. An internal/external rotation is only possible if the knee is already flexed.

motion	definition	max. range [deg]
flexion	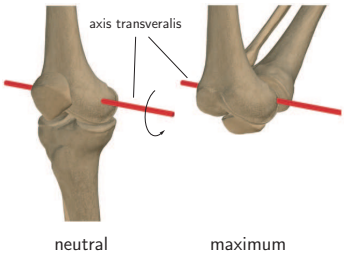	120° (passive 170°)
extension	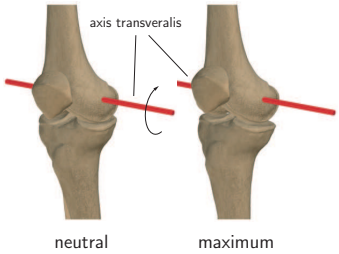	5°-10°
internal rotation	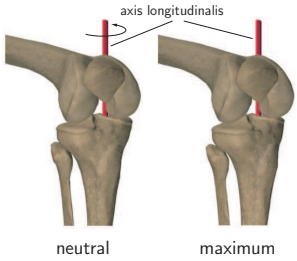	30°
external rotation	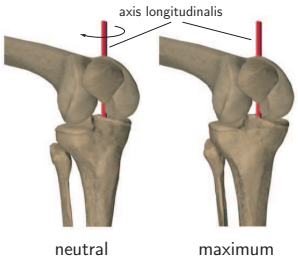	45°

Table 2.3: Knee joint (*articulatio genus*): notion definition and range of motion (data and pictures adapted from [Sobotta, 2005]). Internal and external rotation is only possible if the knee bended.

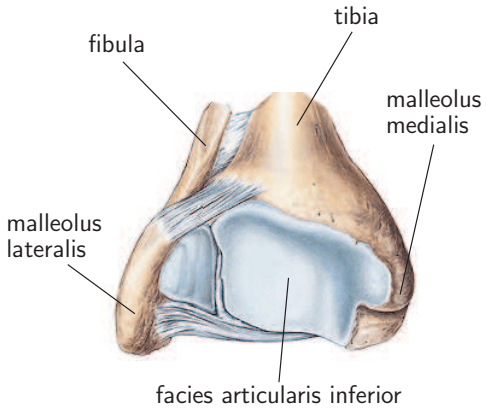

(a) socket of the upper ankle joint (*articulatio talicruralis*), view from superior

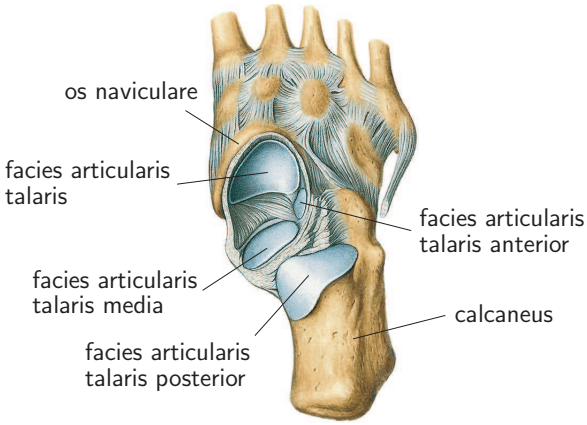

(b) socket of the anterior and posterior lower ankle joint (*articulatio talocalcaneonavicularis*, *articulatio subtalaris*), dorsal view

Figure 2.8: Ankle joint (*articulationes pedis*): subdivision in upper and lower part, general skeletal structure, joint sockets. The connection between both joints is represented by the *talus* (see Fig. 2.5) (pictures adapted from [Sobotta, 2005]).

Ankle joint (*articulationes pedis*)

Similar to the knee joint, the ankle joint(s) (*articulationes pedis*) is (are) strictly speaking a combination of several smaller joints. It is basically subsectioned into an upper part and a lower part, which serve different purposes (motion directions). At the upper ankle joint (*articulatio talocruralis*) the osseous basis of the shank, *tibia* and *fibula*, articulates with the proximal end of the *talus* via the *malleolus lateralis* of the *fibula*, the *malleolus medialis* of the *tibia* and the inferior surface of the distal *tibia*, *facies articularis inferior* (Fig. 2.4, Fig. 2.8(a)). From the structural point of view, this part of the ankle joint can be considered as a synovial hinge. It is responsible for dorsiflexion and plantarflexion about a transversal axis (*axis transversalis*).

The lower part of the ankle joint can be additionally subdivided into an anterior part, *articulatio talocalcaneonavicularis*, and a posterior part, *articulatio subtalaris*. In the posterior part, the distal end of the *talus* and the *calcaneus* articulate via three different surfaces of the *calcaneus* (*facies articularis talaris posterior*, *facies articularis talaris media* and *facies articularis talaris anterior*). Considering the anterior part of the joint, the *os naviculare* is additionally involved via its *facies articularis talaris*. From

the functional point of view, these two "sub-joints" work as a single unit, and are responsible for pronation (lifting the lateral side of the foot) and supination (lifting the medial side of the foot). If the upper part of the ankle joint is positioned in extreme flexion, a pronation movement causes an abduction (external rotation of the foot about an *axis longitudinalis* located along the shank). Similarly, supination leads to an adduction (internal rotation of the foot about an *axis longitudinalis* located along the shank). All notions and an overview of the general joint structure is given in Fig.2.8. The definition of the corresponding axes of rotation and motion ranges can be found in Tab. 2.4.

motion	definition	max. range [deg]
dorsiflexion	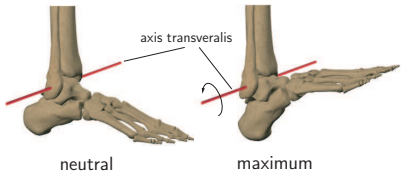	20°
plantarflexion	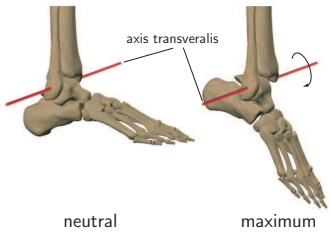	70°
pronation	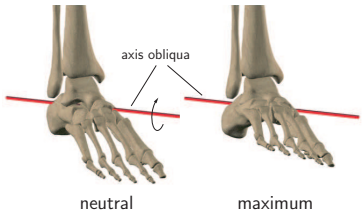	20°
supination	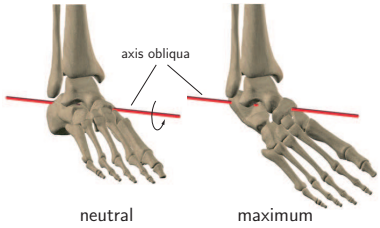	45°

Table 2.4: Ankle joint (*articulatio talicruralis*): notion definition and range of motion (data and pictures adapted from [Sobotta, 2005]).

2.1.4 Muscle structure

Muscles enable the human body to perform *active* movements. To this end, muscle tissue is stimulated by the central nervous system by an electrical pulse, starting a sequence of incidents which eventually develop a force. Generally, muscle tissue can be subdivided into three major groups, indicated by physiological and morphological properties ([Benninghoff, 1985], [Schiebler et al., 1997]):

- **smooth muscles** or **involuntary muscles**, being located in the walls of organs and not under conscious control,
- **cardiac muscles** also not under conscious control and showing regular contractions,
- **skeletal muscles**, which underly conscious control and are used to affect skeletal movement. Besides structural differences to the other types of muscle tissue, a significant characteristic of a skeletal muscle is the fact that it is attached to the skeleton, which is not valid for smooth or cardiac muscles.

To develop forces, muscles convert chemical energy (adenosine triphosphate) directly into mechanical energy and heat. Denoting the efficiency of muscle as the quotient of mechanical work output for a specific motor task and the chemical energy necessary for the same task (metabolic cost), a popular benchmark is an efficiency between 20–25%. Sophisticated investigations of action of skeletal muscles report a different efficiency for the concentric case (13.7%–16.3%) and the eccentric case (28.6%–40.8%) ([Ryschon et al., 1997]).

Since muscles are not able to elongate actively, each skeletal muscle requires the existence of one or more antagonistic muscles, which cause an elongation of the muscle mentioned first by own contraction. In contrast, synergistic muscles contract at the same time supporting each other to fulfill the required motoric task. A complex motoric task always results from a cooperation of synergistic and antagonistic muscles. Additionally, several muscles serve different functions. As an example, muscle *semimembranosus* is considered. Based on the configuration of the knee (for definition of knee flexion angle φ_k see Tab. 2.3), a contraction causes knee flexion ($0° < \varphi_k < 90°$) or internal rotation ($\varphi_k \approx 90°$) ([Sobotta, 2005]).

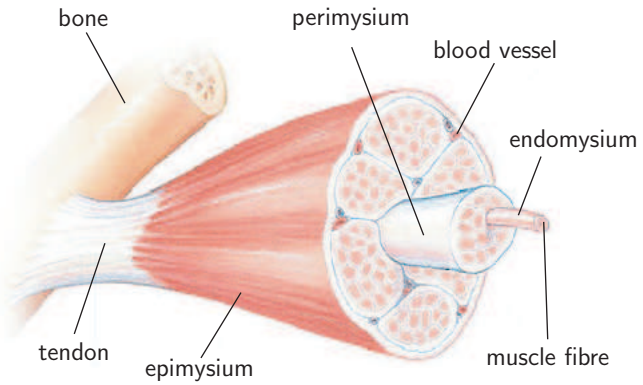

Figure 2.9: Macroscopic structure of skeletal muscles (picture published under GFDL)

Macroscopic and microscopic structure of the skeletal muscle

The elementary component of a skeletal muscle is a cylindric cell, termed the "striated" muscle fiber. Due to its typical length between 0.1mm and 150mm ([Benninghoff, 1985]) it is macroscopically identifiable. The striated appearance results from a regular assembly of each fiber, which is constructed of *fibrils*. Groups of muscle fibers are arranged in regular, parallel bundles which are enclosed by the *perimysium*. These bundles are grouped and enclosed by the *epimysium* (Fig. 2.9). In the outer regions, muscle fibers are adnated with the tendon which is responsible to transfer the developed force to the skeleton. The sliding filament theory developed by A.F. Huxley ([Huxley, 1957], [Huxley, 1974]) and H.E. Huxley ([Huxley, 1969]) describes the elementary processes taking place in a skeletal muscle during contraction. It is based in the principle of interaction of *actin* and *myosin* proteins forming *filaments* inside a *myofibril*, which itself is the characteristic building block of a muscle fiber.

As depicted in Fig. 2.10, a myofibril is subsectioned into *sarcomeres* of typically $\approx 2.5\mu m$ length. Inside a sarcomere, actin and myosin filaments are arranged in a parallel manner. In neural excitation, the myosin filament slides into the pocket formed by the actin filaments, resulting in a shortening of the sarcomere and therefore in a contraction of the corresponding muscle. The filaments themselves do not shorten during contraction. The potential of a muscle to develop force and to shorten is significantly influenced by the configuration of the sarcomeres. While the potential to produce *force* increases in correlation to the number of parallel sarcomeres in a muscle, the ability to *shorten* is increasing in case of a high number of serial sarcomeres ([Spaegele, 1998]).

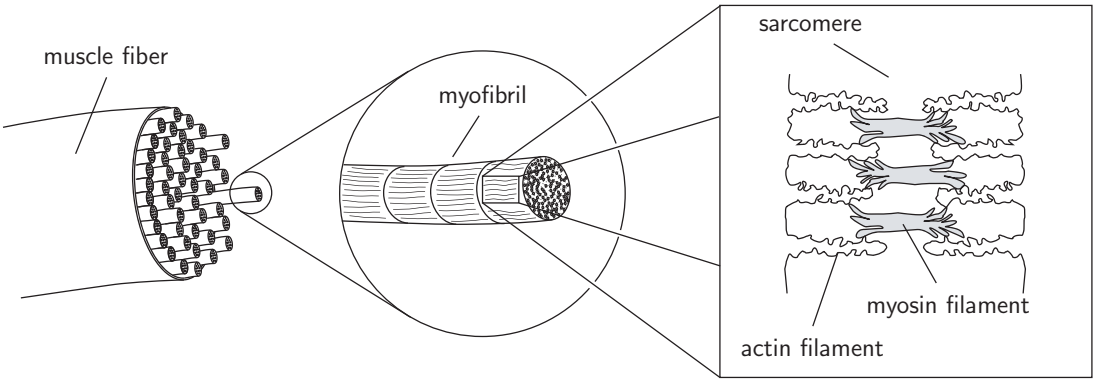

Figure 2.10: Microspcopic structure of skeletal muscles

2.2 Fundamentals of mathematical optimization

In applied mathematics, optimization problems appear in a wide range of topics such as economics, statistics and data-mining, climate research, the design of technical systems, data fitting or — more general — the identification of unknown parameters. In spite of the variety of application fields, the abstract formulation is similar for each problem: given a scalar *objective function* or *cost function* $f : A \longrightarrow \mathbb{R}$ from some set A into the set of real numbers, an element $\underline{x}^* \in A$ is sought such that $f(\underline{x}^*) \leq f(\underline{x})$ for all $\underline{x} \in A$ (*minimization problem*) or $f(\underline{x}^*) \geq f(\underline{x})$ for all $\underline{x} \in A$ (*maximization problem*). Both formulations are equivalent, since a minimization problem can be transferred to a maximization problem by regarding $\tilde{f} = -f$ and vice versa. A vector $\underline{x}^*$ solving the optimization problem is called a *global solution*. In most cases, A (the *search space*) represents a subset of the Euclidian space $\mathbb{R}^n$ which is specified by (linear and/or nonlinear) constraints. Typically, especially when the feasible region or the objective function does not present convexity, there can be several *local minima* or *local maxima* to which the solution algorithm may converge. In the given context, a local minimum is defined as a vector $\underline{x}^* \in A$ such that there exists a $\delta \in \mathbb{R}$ for which for all $\underline{x} \in A$ fulfilling $\|\underline{x} - \underline{x}^*\| \leq \delta$ the expression $f(\underline{x}^*) \leq f(\underline{x})$ is valid. The local maximum is similarly defined substituting "$\leq$" by "$\geq$" in the last relation. Since typically the algorithms are not capable of making a distinction between local and global solutions, the success of an optimization process is significantly influenced by several factors, in particular the *initial guess* that is assumed for the computations.

From the mathematical point of view, the procedure to determine a local minimum is simple. Considering a scalar, at least twice differentiable function $f(\underline{x}) : \mathbb{R}^n \to \mathbb{R}$, a

necessary condition to hold at a local minimizer $\underline{x}^*$ is

$$\nabla f(\underline{x}^*) = 0 \; . \tag{2.2.1}$$

If additionally the corresponding Hessian is positive semi-definite, i.e.

$$\underline{s}^{\mathrm{T}} H_f(\underline{x}^*)\underline{s} \geq 0 \qquad \text{for all} \quad \underline{s} \in \mathbb{R}^n \setminus \{0\} \; , \tag{2.2.2}$$

$\underline{x}^*$ represents a local minimum or a stationary point; (2.2.2) is termed a second order necessary condition. It becomes sufficient for a local minimum if (2.2.1) holds and the Hessian is positive definite (i.e. replacing "$\geq$" by "$>$" in (2.2.2)).

Each iteration step of most available algorithms reveals itself an iterative structure, displaying three major sub-steps. Assuming a function $f : \mathbb{R}^n \to \mathbb{R}$ to be minimized, each iteration step of the algorithm consists of

(a) in case that a given point $\underline{x}_k$ does not fulfill the sufficient conditions for being a local minimum of the objective function, determine a direction of search $\underline{s}_k \in \mathbb{R}^n$ in which the objective function decreases

(b) determine a scalar value α_k such that the objective function is minimized with respect to α, i.e. α_k represents the solution to the subproblem

$$\min_{\alpha} f\left(\underline{x}_k + \alpha \underline{s}_k\right) \tag{2.2.3}$$

(line search)

(c) set $\underline{x}_{k+1} = \underline{x}_k + \alpha_k \underline{s}_k$

Different methods correspond to different ways of choosing the search direction and solving the line search problem.

2.2.1 Major subfields and techniques

The classification of optimization problems is either related to the structure of the objective function under consideration and/or the appearance of additional constraints implied on the solution. Major subfields are

- **linear** programming, where the objective function is linear and any constraints specifying the set A are linear, too

- **quadratic** programming, which features a quadratic objective function but linear equalities and linear inequalities defining the set A

- **nonlinear** programming, studying the most general case of a nonlinear objective function and/or nonlinear constraints.

Due to the appearance of (linear and/or nonlinear) constraints, the principal procedure described above has to be modified and different optimality conditions have to be derived. For most problem specifications, certain algorithms have been developed, using *derivative-free*, *first-order* or *second-order* methods. A detailed description of the corresponding structures can be found in [Gill et al., 2004] and [Fletcher, 2003].

2.2.2 Optimality conditions for constrained optimization

Assuming $\underline{x}^* \in \mathbb{R}^n$ to be a candidate for a local minimum of the objective function under investigation, the following sufficient conditions for $\underline{x}^*$ being a (local) solution to the underlying optimization problem can be derived.

Linearly constrained optimization

Consider the *linearly constrained optimization problem*

$$\underset{\underline{x} \in \mathbb{R}^n}{\text{minimize}} \; f(\underline{x}) \qquad \text{subject to} \qquad A\underline{x} \geq \underline{b} \tag{2.2.4}$$

with $A \in \mathbb{R}^{m \times n}, \underline{b} \in \mathbb{R}^m$. Denoting $\underline{a}_i (1 \leq i \leq m)$ as the i-th row of A and provided that $\underline{x}^*$ is a feasible point, the examination of the *active* constraints in (2.2.4) is of special significance, i.e. the examination of constraints for which $\underline{a}_i^{\mathrm{T}} \underline{x}^* = b_i$. Constraints for which the equality condition is not valid are termed *inactive*. A feasible perturbation $\underline{p} \in \mathbb{R}^n$ in $\underline{x}^*$ is termed a *binding perturbation* when $\underline{a}_i^{\mathrm{T}} \underline{p} = 0$ (since a movement "along" such a perturbation leaves the corresponding constraint active and a sufficiently small change of $\underline{x}^*$ in direction of $\underline{p}$ does not violate any inactive constraint).

The following conditions represent *sufficient* conditions for optimality of $\underline{x}^*$ in (2.2.4):

$$A\underline{x}^* \geq \underline{b} \quad \text{with} \quad \hat{A}\underline{x}^* = \hat{\underline{b}}\,, \tag{2.2.5a}$$

$$Z^{\mathrm{T}}\nabla f(\underline{x}^*) = 0 \quad \Longleftrightarrow \quad \nabla f(\underline{x}^*) = \hat{A}^{\mathrm{T}}\underline{\lambda}^*\,, \tag{2.2.5b}$$

$$\lambda_i^* > 0 \quad \text{for} \quad i = 1, \ldots, t \text{ (active constraints)}\,, \tag{2.2.5c}$$

$$Z^{\mathrm{T}}H_f(\underline{x}^*)Z > 0\,, \tag{2.2.5d}$$

where $\hat{A} \in \mathbb{R}^{t\times n}, t \leq m$, holds the coefficients active constraints at $\underline{x}^*$, $Z \in \mathbb{R}^{n\times(t-r_{\hat{A}})}$, $r_{\hat{A}} = \dim\ker\hat{A}$ holds a basis of the kernel of $\hat{A}$, $\lambda_i^*, i = 1, \ldots, t$ represent *Lagrange multipliers* and $Z^{\mathrm{T}}H_f(\underline{x}^*)Z$ is termed the *projected Hessian*. In contrast to the unconstrained case, the Hessian $H_f(\underline{x}^*)$ does not have to be positive definite here.

Nonlinearly constrained optimization

Consider the *nonlinearly constrained optimization problem*

$$\underset{\underline{x}\,\in\,\mathbb{R}^n}{\text{minimize}}\ f(\underline{x}) \qquad \text{subject to} \qquad \underline{c}(\underline{x}) \geq 0 \tag{2.2.6}$$

for a nonlinear vector function $\underline{c} : \mathbb{R}^n \longrightarrow \mathbb{R}^m$. As for the linearly constrained problems, it is essential to determine "directions" of feasible perturbations of the potential optimal value $\underline{x}^*$. While in case of linear constraints these perturbations can be expressed in terms of a linear subspace, the situation for nonlinear constraints becomes more complicated. For an active constraint $\hat{c}_i,\ i \in \{\,1, \ldots, m\,\}$, i. e. $\hat{c}_i(\underline{x}^*) = 0$, in general there does not exist a feasible direction $\underline{p} \in \mathbb{R}^n$ such that $\hat{c}_i(\underline{x}^* + \varepsilon\underline{p}) = 0$ for sufficiently small $|\varepsilon|$. In case of nonlinear constraints, feasibility in case of perturbations can only be achieved by moving along a *feasible arc* $\underline{\alpha}(s)$, represented as a directed curve in $\mathbb{R}^n$, parameterized in a single variable, i.e. $\underline{\alpha} : \mathbb{R} \longrightarrow \mathbb{R}^n$. Assuming the arc is parameterized such that $\underline{\alpha}(0) = \underline{x}^*$, in order to remain feasible, the constraint function $\hat{c}_i$ must remain identically zero for all points on the arc, implying a vanishing derivative at $\underline{x}^*$ along the arc. The application of the chain rule yields

$$\frac{\mathrm{d}}{\mathrm{d}s}\hat{c}_i(\underline{\alpha}(s)) = \frac{\mathrm{d}\hat{c}_i}{\mathrm{d}\underline{\alpha}} \cdot \frac{\mathrm{d}\underline{\alpha}}{\mathrm{d}s} = \nabla\hat{c}_i(\alpha(s))^{\mathrm{T}} \cdot \frac{\mathrm{d}\underline{\alpha}}{\mathrm{d}s}\,. \tag{2.2.7}$$

and an evaluation of (2.2.7) for $s = 0$ leads to the constraint

$$\nabla\hat{c}_i(\underline{x}^*)^{\mathrm{T}}\underline{p} = 0, \tag{2.2.8}$$

where $\underline{p}$ denotes the tangent to the arc $\underline{\alpha}$ at $\underline{x}^*$. Assuming t ($0 \leq t \leq m$) constraints to be active, a similar consideration of all constraints implies that a tangent $\underline{p}$ to a feasible arc must fulfill

$$\hat{A}(\underline{x}^*)\underline{p} = 0 \tag{2.2.9}$$

where the rows of $\hat{A} \in \mathbb{R}^{t \times n}$ represent the gradients of the active constraints, i.e. $\hat{A}$ becomes the Jacobian matrix of the vector $\hat{c}(\underline{x}^*) \in \mathbb{R}^t$ of active constraints. Unfortunately, (2.2.9) is only a necessary, but not a sufficient condition unless $\hat{A}$ has full rank ([Gill et al., 2004], see also: constraint qualification). The following brief derivations are performed for the assumption that $\hat{A}$ has full rank.

Consideration of a direction $\underline{p}$ fulfilling (2.2.9) and the necessity of f in (2.2.6) to be stationary for $\underline{x}^*$ to be optimal, again the application of the chain rule yields

$$\left.\frac{\mathrm{d}f(\underline{\alpha}(s))}{\mathrm{d}s}\right|_{s=0} = \nabla f(\underline{x}^*)^{\mathrm{T}}\underline{p} = 0 \; . \tag{2.2.10}$$

As a consequence (similar to the case of linear constraints), since (2.2.10) is to be valid for all $\underline{p}$ fulfilling (2.2.9), the consideration of all involved active constraints results in the requirement that the *projected gradient* of f at $\underline{x}^*$, $Z(\underline{x}^*)^{\mathrm{T}}\nabla f(\underline{x}^*)$ vanishes, i.e.

$$Z(\underline{x}^*)^{\mathrm{T}}\nabla f(\underline{x}^*) = 0 \tag{2.2.11}$$

using the same definitions as above.

It is important to mention that in contrast to unconstrained and linearly constrained optimization problems also the second derivative of the feasible arc is required. A necessary condition for $\underline{x}^*$ to be optimal is given in terms of a positive definite *projected Hessian of the Lagrangian function*

$$Z^{\mathrm{T}}(\underline{x}^*)H_L(\underline{x}^*, \underline{\lambda}^*)Z(\underline{x}^*) \tag{2.2.12}$$

with the matrix Z defined above and the Hessian of the Lagrangian function

$$H_L(\underline{x}^*, \underline{\lambda}^*) = H_f(\underline{x}^*, \underline{\lambda}^*) - \sum_{i=1}^{t} \lambda_i^* \hat{H}_{c_i}(\underline{x}^*) \tag{2.2.13}$$

which is represented as a linear combination of the objective Hessian and the Hessians $\hat{H}_{c_i}$ of the active constraints ([Gill et al., 2004]).

In summary, the following conditions represent *sufficient* conditions for optimality of $\underline{x}^*$ in (2.2.6):

$$\underline{c}(\underline{x}^*) \geq 0 \quad \text{with} \quad \hat{\underline{c}}(\underline{x}^*) = 0 \,, \tag{2.2.14a}$$

$$Z^{\mathrm{T}}(\underline{x}^*)\nabla f(\underline{x}^*) = 0 \quad \Longleftrightarrow \quad \nabla f(\underline{x}^*) = \hat{A}^{\mathrm{T}}(\underline{x}^*)\underline{\lambda}^* \,, \tag{2.2.14b}$$

$$\lambda_i^* > 0 \quad \text{for} \quad i = 1, \ldots, t \text{ (active constraints)} \,, \tag{2.2.14c}$$

$$Z^{\mathrm{T}}(\underline{x}^*)H_L(\underline{x}^*, \underline{\lambda}^*)Z(\underline{x}^*) > 0 \,. \tag{2.2.14d}$$

2.2.3 Quadratic programming with constraints

The conditions presented in Sec. 2.2.2 are based on an analytical investigation of the functions involved in the optimization problem at hand. In most applications, these functions are only available in terms of a numerical approximation. The method applied to the optimization problems described in this thesis is supplied by the Numerical Algorithms Group (NAG) via the NAG C library ([Numerical Algorithms Group, 2004]).

Let $\underline{x} \in \mathbb{R}^n, n \in \mathbb{N}$ denote the input parameters of a given computer simulation model and $\hat{q}(t), q(\underline{x}, t) \in \mathbb{R}, t \in [0, T]$ the measured time history and the computed time history of a certain model quantity (e.g. a joint coordinate or muscle activation), respectively. For a given $m \in \mathbb{N}$, the definition of the time increment $\Delta t = T/m$ yields a limited number of *output sampling times* $t_i = i\Delta t$ and corresponding *output sampling values*

$$\hat{q}_i = \hat{q}(t_i) = \hat{q}(i\Delta t) \qquad \text{for} \qquad i \in \{0, \ldots, m\} \,. \tag{2.2.15}$$

The objective is now to identify the design parameters $\underline{x}$ for a given initial guess $\underline{x}_0$ such that the computed time history of the variable under investigation best fits the prescribed values for this variable. Mathematically, this can be formulated in terms of a least-squares programming problem stated in the following form:

$$\underset{\underline{x} \in \mathbb{R}^n}{\text{minimize}} \quad f(\underline{x}) = \frac{1}{2}\sum_{i=0}^{m}(\hat{q}_i - q_i)^2 \quad \text{subject to} \quad \underline{\ell} \leq \begin{bmatrix} \underline{x} \\ A_L\underline{x} \\ \underline{c}(\underline{x}) \end{bmatrix} \leq \underline{u} \,. \tag{2.2.16}$$

In (2.2.16) $q_i = q(\underline{x}, i\Delta t)$ represents the computed value of the considered variable for a design parameter set $\underline{x}$ at time t_i ($i \in \{0, \ldots, m\}$). The objective function $f : \mathbb{R}^n \longrightarrow \mathbb{R}$ represents the (smooth nonlinear) sum of squares of the sub-functions

$f_i = \hat{q}_i - q_i$. Constraints are optional and can be imposed on the design parameters $\underline{x}$ in terms of lower and upper bounds such that $\underline{\ell}_B \leq \underline{x} \leq \underline{u}_B,\ \underline{\ell}_B, \underline{u}_B \in \mathbb{R}^n$, and linear constraints $\underline{\ell}_L \leq A_L \underline{x} \leq \underline{u}_L,\ A_L \in \mathbb{R}^{n_L \times n}, \underline{\ell}_L, \underline{u}_L \in \mathbb{R}^{n_L}$, where $n_L \in \mathbb{N}$ denotes the number of linear constraints. Nonlinear constraints are regarded in terms of a vector function $\underline{c} : \mathbb{R}^n \longrightarrow \mathbb{R}^{n_N}$ such that $\underline{\ell}_N \leq \underline{c}(\underline{x}) \leq \underline{u}_N,\ \underline{\ell}_N, \underline{u}_N \in \mathbb{R}^{n_N}$, where n_N denotes the number of nonlinear constraints. Definition of

$$\underline{\ell} = \begin{bmatrix} \ell_B \\ \ell_L \\ \ell_N \end{bmatrix} \in \mathbb{R}^{n+n_L+n_N} , \quad \underline{u} = \begin{bmatrix} \underline{u}_B \\ \underline{u}_L \\ \underline{u}_N \end{bmatrix} \in \mathbb{R}^{n+n_L+n_N} \tag{2.2.17}$$

yields the compact formulation of (2.2.16). The optimization problem (2.2.16) is solved using a sequential programming method (SQP) which is briefly described in the following chapter. A general overview of optimization methods is given in [Gill et al., 2004] and [Fletcher, 2003].

2.2.4 The applied optimization routine

For the optimization computations performed within the scope of this thesis, the NAG e04unc routine, supplied by the NAG C library was used. Its iterative structure is displayed in Fig. 2.11 in a simplified overview. The method of operation is clarified by means of the two-dimensional function

$$\hat{f}(x_1, x_2) = x_1^2 + \exp(x_2)\cos^2(x_2) \tag{2.2.18}$$

in the sequel, which is to be minimized for $(x_1, x_2) \in [\,-2,\ 2\,] \times [\,-0.5,\ 3\,]$ and two arbitrary initial guesses $\underline{x}_0^1 = (-1.5, 0.466)$ and $\underline{x}_0^2 = (-1.5, 0.467)$ (see Fig. 2.12(a) and Fig. 2.12(b)). For purposes of clarity, nonlinear constraints have been dropped off.

Since

$$\nabla \hat{f}(x_1, x_2) = [\,2x_1 \quad \exp(x_2)\cos(x_2)\,(\cos(x_2) - 2\sin(x_2))\,] , \tag{2.2.19}$$

a (global) minimum is computed for $\underline{x}_1^* = (\,0,\ \pi/2\,)$ with $f(0, \pi/2) = 0$. In addition, due to the bounded domain, a second (local) minimum is located in $\underline{x}_2^* = (\,0,\ -0.5\,)$ with $f(0, -0.5) = 0.46712$.

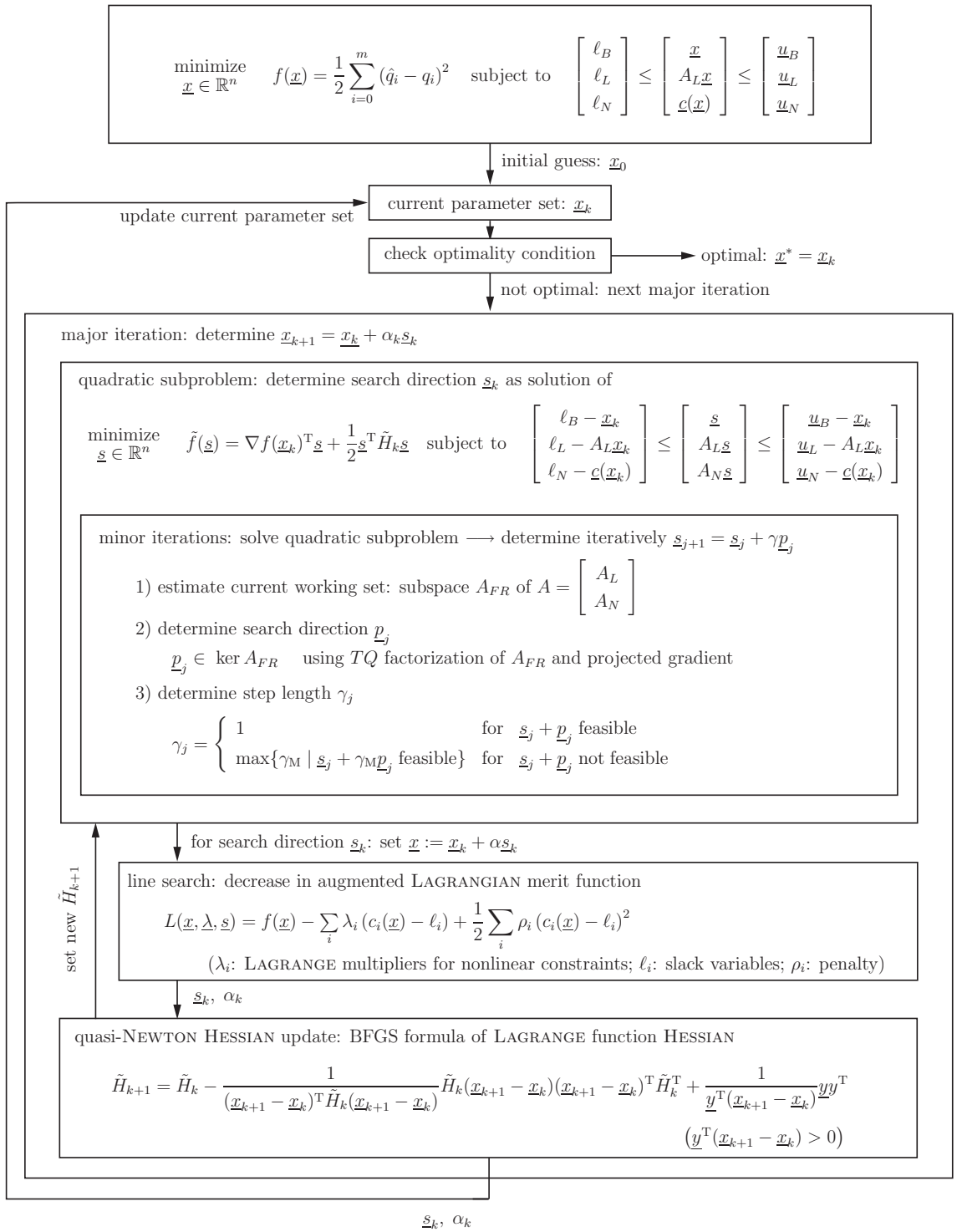

Figure 2.11: Iterative structure of applied optimization tool. Details can be found in [Numerical Algorithms Group, 2004]

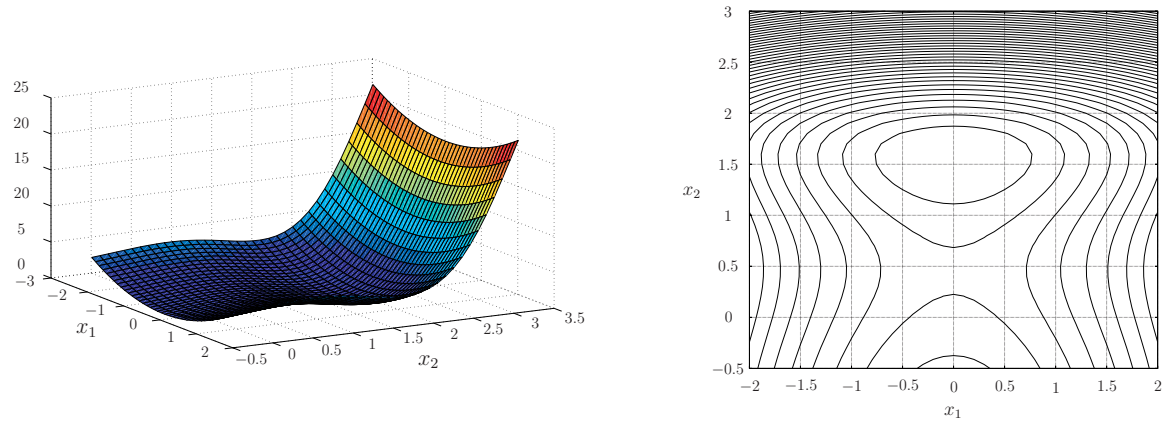

(a) Surface plot of example function (2.2.18)

(b) Contour plot of example function (2.2.18)

Figure 2.12: Example function for visualization of the method of operation of the applied optimization routine

A reformulation of the objective function to a least square representation yields

$$\begin{aligned} \hat{f}(x_1, x_2) &= x_1^2 + \exp(x_2)\cos^2(x_2) && (2.2.20)\\ &= (0 - x_1)^2 + \left(0 - \sqrt{\exp(x_2)}\cos(x_2)\right)^2 && (2.2.21)\\ &:= f_1(x_1, x_2)^2 + f_2(x_1, x_2)^2, && (2.2.22) \end{aligned}$$

leading to the following problem statement according to (2.2.16):

$$\underset{\underline{x} \in \mathbb{R}^2}{\text{minimize}} \quad f(\underline{x}) := \frac{1}{2}\sum_{i=1}^{2} f_i(x_1, x_2)^2 \tag{2.2.23}$$

subject to

$$\begin{bmatrix} -2 \\ -0.5 \end{bmatrix} \leq \begin{bmatrix} x_1 \\ x_2 \end{bmatrix} \leq \begin{bmatrix} 2 \\ 3 \end{bmatrix}. \tag{2.2.24}$$

Denoting $\underline{\tilde{f}}(\underline{x}) = (f_1(x_1), f_2(x_2))$ the corresponding Jacobian of $\underline{\tilde{f}}(\underline{x})$ becomes

$$\mathbf{J}_{\underline{\tilde{f}}}(\underline{x}) = \begin{bmatrix} -1 & 0 \\ 0 & -\dfrac{\exp(x_2)\cos(x_2)}{2\sqrt{\exp(x_2)}} + \sqrt{\exp(x_2)}\sin(x_2) \end{bmatrix}. \tag{2.2.25}$$

It can be shown that the Hessian of the underlying objective function in (2.2.23) is

represented by

$$H_f(\underline{x}) = \mathbf{J}_{\underline{\tilde{f}}}^{\mathrm{T}} \mathbf{J}_{\underline{\tilde{f}}} + \sum_{i=1}^{2} f_i(\underline{x}) H_{f_i}(\underline{x}) \tag{2.2.26}$$

yielding here

$$H_f(\underline{x}) = \begin{bmatrix} 1 & 0 \\ 0 & \exp(x_2) \end{bmatrix} . \tag{2.2.27}$$

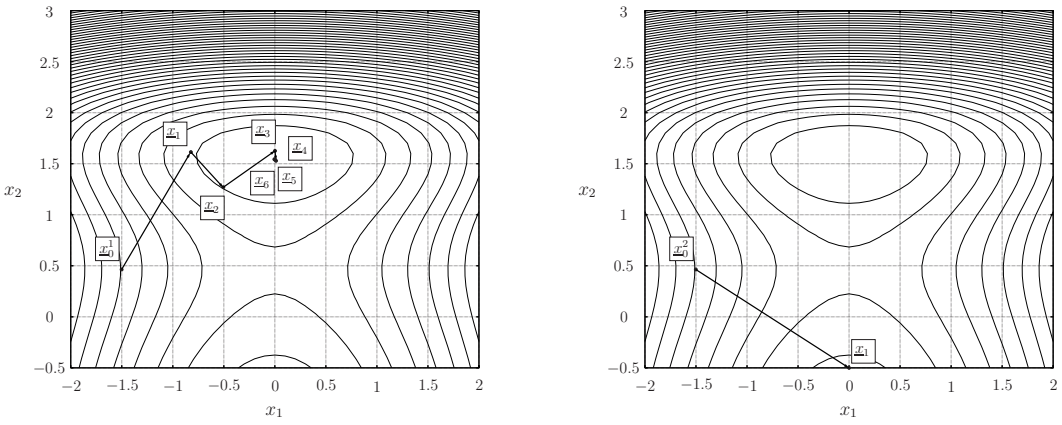

(a) Iterative approximation to optimal solution for function (2.2.18) with initial guess $\underline{x}_0^1$

(b) Iterative approximation to optimal solution for function (2.2.18) with initial guess $\underline{x}_0^2$

Figure 2.13: Iterative approximation to optimal solution for function (2.2.18)

Since only in exceptional cases the derivatives of the objective function can be analytically determined, in the usual case the algorithm uses central and forward finite differences to approximate the corresponding partial derivatives to determine the Jacobian. The algorithm uses the Hessian of the related Lagrange function to regard nonlinear constraints (if any), in the present example the Lagrange function degenerates to the objective function itself. Only in the first (major) iteration the Hessian is approximated by neglecting the sum term in (2.2.26), all subsequent iterations are performed with an appropriately updated Hessian computed applying a BFGS formula (Broyden-Fletcher-Goldfarb-Shanno). In case that the Hessian update is not positive definite, additional modifications are performed. Details of the implementation can be found in [Numerical Algorithms Group, 2004]. Table 2.5 displays the intermediate results and the final solution of the algorithm for the two different initial guesses $\underline{x}_0^1$

and $\underline{x}_0^2$ applied to example function (2.2.18). For details of the nomenclature consider Fig. 2.11.

While the result for initial guess $\underline{x}_0^1$ represents the global minimum mentioned above, a marginal variation in the initial position yields an unsatisfactory solution (Fig. 2.13). Additionally, in the first case the final iterate fulfills all criteria corresponding a local minimum (clean exit of optimization routine) whereas in the latter case the routine exits with a convergence error message.

The example illustrates characteristic obstacles in multi-dimensional optimization, which are mostly not under the users control. In particular, the choice of an appropriate initial guess appears essential to achieve a correct solution. Consequences of these problems especially in the context of dynamic optimization of specific motor tasks are described in Chapter 6.

Table 2.5: Characteristic quantities during minimization of example function

	initial guess: $\underline{x}_0^1$				initial guess: $\underline{x}_0^2$			
iteration counter k	$H_f(\underline{x}_k)$	$\tilde{H}_f(\underline{x}_k)$	$\underline{s}_k$	α_k	$H_f(\underline{x}_k)$	$\tilde{H}_f(\underline{x}_k)$	$\underline{s}_k$	α_k
1	$\begin{bmatrix} 1 & 0 \\ 0 & 1.594 \end{bmatrix}$	$\begin{bmatrix} 1 & 0 \\ 0 & 0.00006 \end{bmatrix}$	$(1.5, 2.533)$	0.45	$\begin{bmatrix} 1 & 0 \\ 0 & 1.593 \end{bmatrix}$	$\begin{bmatrix} 1.26 & 0.41 \\ 0.41 & 0.13 \end{bmatrix}$	$(1.5, -0.966)$	1
2	$\begin{bmatrix} 1 & 0 \\ 0 & 3.62 \end{bmatrix}$	$\begin{bmatrix} 0.632 & 0.22 \\ 0.22 & 0.075 \end{bmatrix}$	$(2.023, -2.1165)$	0.16	—	—	—	—
3	$\begin{bmatrix} 1 & 0 \\ 0 & 5.12 \end{bmatrix}$	$\begin{bmatrix} 1 & 0 \\ 0 & 2.38 \end{bmatrix}$	$(0.50318, 0.34685)$	1	—	—	—	—
4	$\begin{bmatrix} 1 & 0 \\ 0 & 4.61 \end{bmatrix}$	$\begin{bmatrix} 0.92 & 0.12 \\ 0.12 & 3.14 \end{bmatrix}$	$(0.01318, -0.1034)$	1	—	—	—	—
5	$\begin{bmatrix} 1 & 0 \\ 0 & 4.82 \end{bmatrix}$	$\begin{bmatrix} 1 & 0 \\ 0 & 4.34 \end{bmatrix}$	$(-0.01318, 0.04282)$	1	—	—	—	—
6	$\begin{bmatrix} 1 & 0 \\ 0 & 4.81 \end{bmatrix}$	$\begin{bmatrix} 0.99 & -0.0002 \\ -0.0002 & 4.48 \end{bmatrix}$	$(0, -0.00135)$	1	—	—	—	—

Chapter 3

Multibody dynamics using kinetostatic transmission elements

The dynamics of multibody systems and its computer simulation have been topic of research ever since computer technology turned out to be key to the solution of any kind of problems involving exceptional computational effort. Nowadays, all steps in the development of new engineering products are significantly supported by the application of appropriate software packages in one way or the other. Especially the possibility to simulate almost arbitrarily constructed multibody systems contributed to the two most important factors in successful engineering: modern software packages (1) allow for a flexible construction without having to bear costs of prototype development and (2) reduce time and therefore cost of development in comparison to traditional engineering by significant factors. An elaborate background on multibody simulation is given in [Wittenburg, 2007].

Since due to rising computer standards software quality and ability is still increasing, different principles and features are merged to complex simulation tools that are not only applicable to pure engineering but find fields of application in other areas of research such as biomechanics.

The present chapter gives an introduction into the formulation of multibody dynamics using the kinetostatic transmission element concept ([Kecskeméthy, 1993]), which is the environment of implementation for the presented framework.

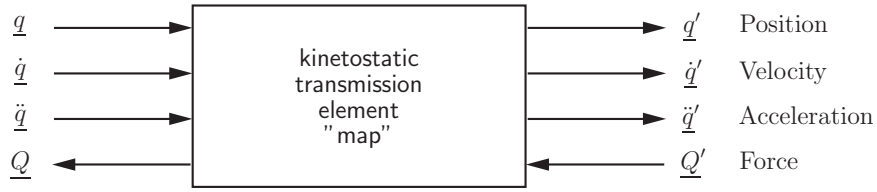

Figure 3.1: Principle of the kinetostatic transmission element

3.1 The notion of the kinetostatic transmission element

Basically, multibody systems are constructed of components between which motion and force is transmitted. The idea of the *kinetostatic transmission element* provides a systematic description of these two fundamental properties. Two different types of objects have to be discerned in the present context, namely *state objects* and *transmission objects*. While state objects are capable of information about position, velocity, acceleration and load at an arbitrary position, transmission objects take care of the transmission of the different types of information from one set of state objects to another. Mechanical components can be regarded as such transmission elements.

3.1.1 Transmission elements

As mentioned above, transmission elements map kinematic (motion) information from an "input" set of state objects to an "output" set of state objects. This principle is discussed in the sequel for an input vector $\underline{q} \in \mathbb{R}^n$ and an output vector $\underline{q}' \in \mathbb{R}^m$.

The operation of motion transmission consists of three sub-operations. Position transmission is given by

$$\underline{\text{position:}} \qquad \underline{q}' = \underline{\phi}(\underline{q})\,. \tag{3.1.1}$$

Differentiation with respect to time defines velocity transmission by virtue of

$$\underline{\text{velocity:}} \qquad \dot{\underline{q}}' = \mathbf{J}_\phi \dot{\underline{q}} \tag{3.1.2}$$

where $\mathbf{J}_\phi = \partial\underline{\phi}/\partial\underline{q} \in \mathbb{R}^{m\times n}$ denotes the Jacobian of the transmission element at hand. An additional time derivative yields the acceleration transmission rule

$$\underline{\text{acceleration:}} \qquad \ddot{\underline{q}}' = \mathbf{J}_\phi \ddot{\underline{q}} + \dot{\mathbf{J}}_\phi \dot{\underline{q}}\,. \tag{3.1.3}$$

Force transmission can be defined assuming *ideal* transmission elements, i.e. assuming that transmission elements neither consume nor generate power. Equating virtual work at input and output yields

$$\delta \underline{q}^{\mathrm{T}} \underline{Q} = \delta \underline{q}'^{\mathrm{T}} \underline{Q}' \,, \tag{3.1.4}$$

and, after substituting $\delta \underline{q}' = \mathbf{J}_\phi \delta \underline{q}$ and noting that this condition has to hold for arbitrary virtual displacements $\delta \underline{q} \in \mathbb{R}^n$, one obtains the *force transmission* function

$$\underline{\text{force:}} \qquad \underline{Q} = \mathbf{J}_\phi^{\mathrm{T}} \underline{Q}' \,. \tag{3.1.5}$$

In general, the Jacobian $\mathbf{J}_\phi$ is not necessarily square. Thus, for most transmission elements the relationship (3.1.5) cannot be reversed and the natural direction of force transmission ("output" to "input") is *opposite* to the direction of motion transmission ("input" to "output", see Fig. 3.1).

The case of non-ideal transmission elements can be taken into account by adding terms $\underline{\widehat{Q}}$ to the right hand side of (3.1.5) that represent the internally generated applied forces of the transmission element. The force transmission is then performed by virtue of

$$\underline{Q} = \mathbf{J}_\phi^{\mathrm{T}} \underline{Q}' + \underline{\widehat{Q}} \,. \tag{3.1.6}$$

3.1.2 State objects

State objects can be of two types, scalar or spatial. Spatial state objects (Fig. 3.2(a)) contain information referring to the motion of a spatial frame $\mathcal{K}$ with respect to an implicitly defined inertial reference frame $\mathcal{K}_0$ as well as the load being applied to the origin of $\mathcal{K}$. Scalar state objects (Fig. 3.2(b)) bear resemblance to the spatial ones such that position, velocity and acceleration correspond to the value of the variable β and its time derivatives. The load is assumed to represent the generalized force being exerted along the direction of the variable β. As a convention a positive virtual displacement $\delta\beta$ is to result in a positive load Q_β and supplies energy to the system.

In case of the spatial state objects, the location of the frame $\mathcal{K}$ is given in terms of the radius vector $\mathbf{r}$ which connects the origin of the (implicitly defined) inertial frame $\mathcal{K}_0$ and that of $\mathcal{K}$. As a convention, all vectors are assumed to be decomposed in the moving frame $\mathcal{K}$. The orientation of $\mathcal{K}$ is parameterized as the rotation matrix $\mathbf{R}$ which transforms the vector components related to $\mathcal{K}$ to components related to the inertial frame (see also Sec. 1.4.2).

$$\{\mathcal{K}\} = \left\{ \begin{array}{l} \mathbf{R} \\ \mathbf{r} \\ \boldsymbol{\omega} \\ \mathbf{v} \\ \dot{\boldsymbol{\omega}} \\ \mathbf{a} \\ \boldsymbol{\tau} \\ \mathbf{f} \end{array} \right\} \begin{array}{l} \text{rotation} \\ \text{translation} \\ \text{angular velocity} \\ \text{linear velocity} \\ \text{angular acceleration} \\ \text{linear acceleration} \\ \text{torque} \\ \text{force} \end{array} \qquad \{\beta\} = \left\{ \begin{array}{c} \beta \\ \dot{\beta} \\ \ddot{\beta} \\ Q_\beta \end{array} \right\} \begin{array}{l} \text{position} \\ \text{velocity} \\ \text{acceleration} \\ \text{generalized force} \end{array}$$

(a) Spatial state object (b) Scalar state object

Figure 3.2: Basic structure of state objects: spatial and scalar

Angular and translational velocity vectors $\boldsymbol{\omega}$ and $\mathbf{v}$ as well a force and moment vectors $\mathbf{f}$ and $\boldsymbol{\tau}$ can be grouped to corresponding twist and wrench vectors $\underline{t}$ and $\underline{w}$, respectively, being defined as

$$\underline{t} = \begin{bmatrix} \boldsymbol{\omega} \\ \mathbf{v} \end{bmatrix}, \qquad \underline{w} = \begin{bmatrix} \boldsymbol{\tau} \\ \mathbf{f} \end{bmatrix}. \tag{3.1.7}$$

Position entries of scalar state objects can be of translational or rotational type. Translational entries are unbounded and correspond to the real numbers $\mathbb{R}$ whereas rotational entries are cyclic and topologically correspond to the 1-Torus T^1. Since in case of angular variables it is not the variable value itself but its sine or cosine that is of interest for computations, angular state variables additionally feature these values directly.

3.1.3 Assembly of mechanical systems

The assembly process consists of attaching instances of specific state objects to the input and output of the transmission elements in use (Fig. 3.3). The spatial objects (reference frames) serve as the interconnection between the applied transmission elements, while the scalar variables are used as actuator inputs on the one hand or hold the values of sensors performing scalar measurements on the other hand.

The transmission of motion and force for the concatenated system is then performed by evaluating the transmission functions of the individual transmission functions sequentially. To this end, the order of concatenation is essential, meaning that it has to

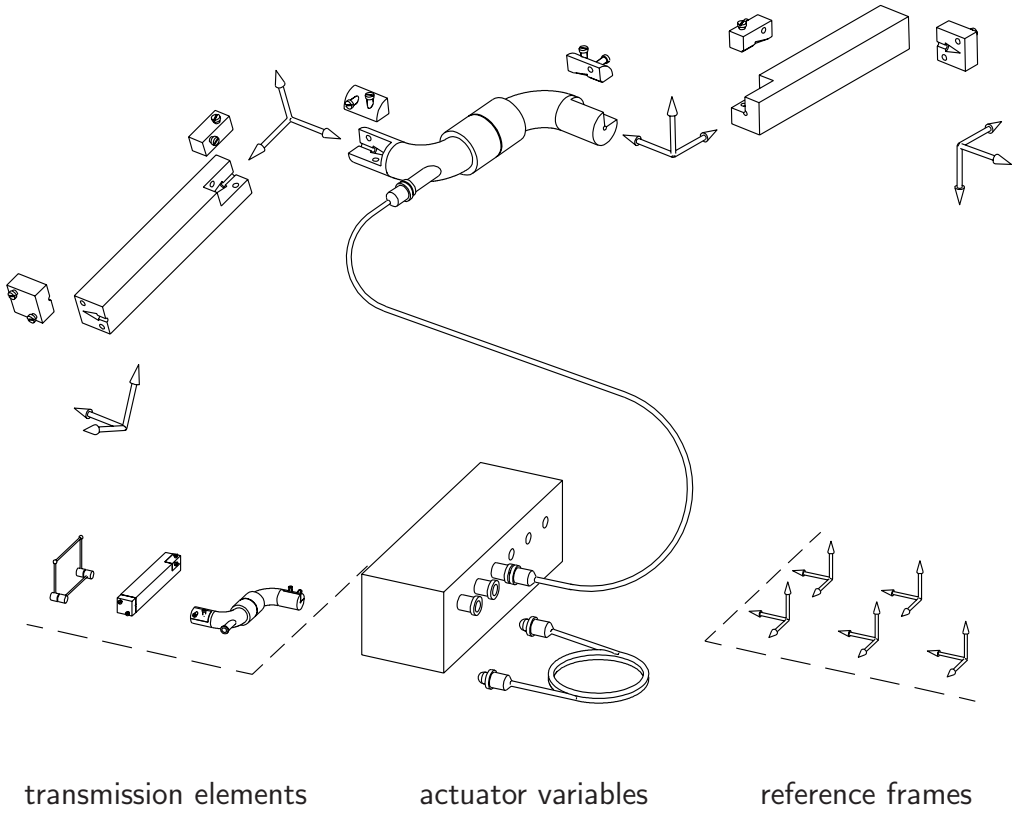

Figure 3.3: Elementary objects in multibody systems [Kecskeméthy, 1993]

be performed from basis to end. The example of a serial robot visualizes this nicely: the motion at the first axis influences position and velocity of the following parts while a force applied to the end effector is propagated to the base of the robot in opposite direction.

3.1.4 Computation of Jacobians

The Jacobian of a kinetostatic transmission element appearing in equations (3.1.2) and (3.1.3) refers to a single transmission element only. However, in some applications it is necessary to compute the Jacobian $\mathbf{J}_G$ describing the global mapping of all generalized velocities $\dot{\underline{q}}$ of the system at hand to a specific physical velocity $\mathbf{v}$. A simple method to achieve the desired Jacobian is given in [Kecskeméthy, 1993] and described briefly in the sequel.

Assuming a system with f degrees of freedom, $\underline{q} \in \mathbb{R}^f$, choosing $j \in \{1, \ldots, f\}$ and

setting

$$\dot{q}_k = 0 \qquad \forall \;\; k \in \{1, \ldots, f\},\; k \neq j \tag{3.1.8}$$

and

$$\dot{q}_j = 1 \;, \tag{3.1.9}$$

the principle displayed in (3.1.2) yields a velocity vector for a given system configuration which corresponds to the jth column of the sought Jacobian $\mathbf{J}_G$, i. e.

$$[\mathbf{J}_G]_j = \underline{\dot{q}'}\Big|_{\dot{q}_i = \begin{cases} 1 & \text{for} \quad \text{i = j} \\ 0 & \text{otherwise} \end{cases}} \;. \tag{3.1.10}$$

By sequential evaluation of (3.1.10) for all $j \in \{1, \ldots, f\}$ the complete Jacobian can be determined columnwise.

3.1.5 Object oriented implementation

Object-oriented programming, particularly the C++ programming language, is especially suitable for the implementation of systems containing quantities that have many common properties ([Stroustrup, 2000]). In the given context, all possible types of kinetostatic transmission elements have the common feature of motion and force transmission. This property can be regarded as the basis for defining "services" required for a responsibility-driven design. The C++ multibody library MOBILE ([Kecskeméthy, 1993]) applies the object-oriented programming paradigm to realize this concept. Basic and characteristic services of the available objects are motion and force transmission implemented as virtual functions "`doMotion`" and "`doForce`". To this end, all elements are derived from a base class "`MoMap`" which introduces both mentioned functions. The leaves of the inheritance tree then correspond to the concrete implementation of transmission elements as described in Sec. 3.1.1, namely joints, rigid connections and more complex mechanisms which are generated by concatenation of other elements and contain an own implementation of the virtual functions "`doMotion`" and "`doForce`". The concept of *polymorphism* furthermore allows for access of a specific object as an object of the base class "`MoMap`" without knowledge of the concrete implementation details actuating behind the (abstract) access. As a typical illustrative example, consider the brake of a car. Such a component is operated (in most cases) by

the driver without particular knowledge of the specific type of brakes that is installed in his/her car. This is similar to the invocation of motion and/or force transmission for a transmission element. The abstract invoking mechanism furthermore enables an easy construction of complex mechanical systems by simple concatenation of transmission elements without regarding their specific type. Thus, the transmission of motion and force of a concatenated chain is performed by sequentially invoking the functions "`doMotion`" and "`doForce`" as described in Sec. 3.1.1.

All kinetostatic transmission elements are connected by reference frames which belong to the group of state objects described in Section 3.1.2. Their main functionality consists of storing the dynamic state of a certain point of the system under investigation. Motion and force transmission refers to these characteristic points by passing the corresponding information to the adjacent element and finally through the complete system. In the context of force transmission, the transmission process can be subdivided into two parts. External forces are transmitted in case of an internal switch being set to `DO_EXTERNAL`. If the switch is set to `DO_INTERNAL`, also internal forces which emerge from the corresponding element (e.g. inertia forces, spring forces) are transmitted by adding them to the external forces transmitted from the preceding transmission element.

In [Kecskeméthy, 1993] the specifications of the MOBILE library as well as the theoretical background are presented in detail. Here, the usage shall be briefly introduced using the code fragment given in Figure 3.4, representing the model of a massless simple pendulum.

```
MoFrame K0, K1, K2 ;  // frames to interconnect transmission elements
MoAngularVariable phi ;  // generalized variable for revolute joint R
MoElementaryJoint R ( K0, K1, phi ) ;  // revolute joint R
MoVector l ;  // vector defining the shape of the rigid link L
MoRigidLink L ( K1, K2, l ) ;  // rigid link L
MoMapChain chain ;
chain << R << L ;  // concatenation of all transmission elements
chain.doMotion () ;  // motion transmission of whole chain
chain.doForce  () ;  // force transmission of whole chain
```

Figure 3.4: Example fragment of a MOBILE program

The objects `MoElementaryJoint R` and `MoRigidLink L` are kinetostatic transmission elements which act on the involved reference frames `K0`, `K1`, and `K2`. The variable `MoAngularVariable phi` represents a state object holding information about the involved angle and the vector `MoVector l` is aligned with the pendulum. Concrete values for the vector components are assigned later in the program. By concatenating joint and link to the kinetostatic transmission chain `MoMapChain chain` the invocation of motion and force transmission in the last two lines performs the transmission process itself.

3.2 Dynamics by virtue of kinetostatics

The generation of the equations of motion using MOBILE can be accomplished by repeatedly solving the inverse dynamics of a system consisting of kinetostatic transmission elements ([Kecskeméthy, 1993]). To describe the procedure briefly, objects representing *force sources* such as inertia elements or applied forces are described, since they represent the essential dynamic properties of a multibody system. Finally a short description of the available tools to perform numerical integration of the achieved equations is given.

3.2.1 Force and inertia objects

The objects being considered in the sequel differ from the ideal kinetostatic transmission elements described in Section 3.1.1, since they do not transmit kinetostatic quantities but purely generate force or moment information as a function of given kinematic quantities. The corresponding principle is displayed in Figure 3.5.

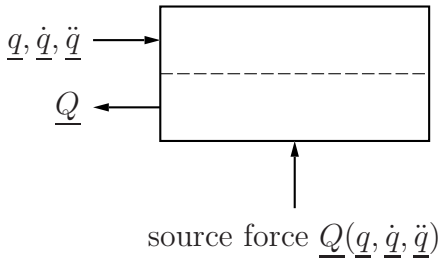

Figure 3.5: Principle of a source force element

Force elements generate applied forces according to kinematic information. A typical example is the spring-damper element. Generally, this kind of elements apply some externally generated wrench $\underline{\mathrm{w}}^{(e)}$.

Mass elements represent the inertial properties of the rigid bodies involved in the system. They comprise body mass m, a tensor of inertia $\boldsymbol{\Theta}_C$ (defined w.r.t. to the center of mass C) and an offset vector Δs, representing the offset between center of mass C and the origin of the frame $\mathcal{K}$ the mass element is attached to. Similar to the decomposition of vectors described in Sec. 3.1.2, as a convention all tensorial entries are decomposed with respect to frame $\mathcal{K}$. Assuming now that the motion of $\mathcal{K}$ is known in terms of translational acceleration, angular velocity and acceleration $\mathbf{a}$, $\boldsymbol{\omega}$ and $\dot{\boldsymbol{\omega}}$, respectively, the d'Alembert forces applied by the body to the origin of the frame $\mathcal{K}$ result in

$$\mathbf{f} = -m\left[\mathbf{a} + \dot{\boldsymbol{\omega}} \times \Delta s + \boldsymbol{\omega} \times (\boldsymbol{\omega} \times \Delta s)\right] \quad , \tag{3.2.1}$$

$$\boldsymbol{\tau} = -\left[\,\boldsymbol{\Theta}_S\,\dot{\boldsymbol{\omega}} + \boldsymbol{\omega} \times \boldsymbol{\Theta}_S\,\boldsymbol{\omega}\,\right] + \Delta s \times \mathbf{f} \quad . \tag{3.2.2}$$

3.2.2 Generation of dynamic equations

Assuming a mechanical system of $f \in \mathbb{N}$ degrees of freedom, the procedure of generating the corresponding equations of motion are described in the following. To this end, $\underline{q} = [q_1, \ldots, q_f]^{\mathrm{T}}$ denotes the independent generalized coordinates.

After the completion of the concatenation process of all kinetostatic transmission elements representing the mechanical elements and characteristic properties of the system, one obtains a kinetostatic transmission element mapping the motion of the generalized coordinates to the motion of the involved frames. In opposite direction, force information stored in the frame objects can be passed to the generalized coordinates, representing the generalized forces. In addition, the composed kinetostatic transmission element, the "kinematic subsystem", can be extended by an arbitrary number of mass and force objects. This yields the overall kinetostatic transmission element representation of the complete mechanical system, denoted "global kinematics" φ_S and displayed in Fig. 3.6.

Execution of motion and force transmission for the complete system φ_S yields a function $\varphi_S^{D^{-1}}$ that maps the generalized coordinates $\underline{q}$ and the corresponding time derivatives

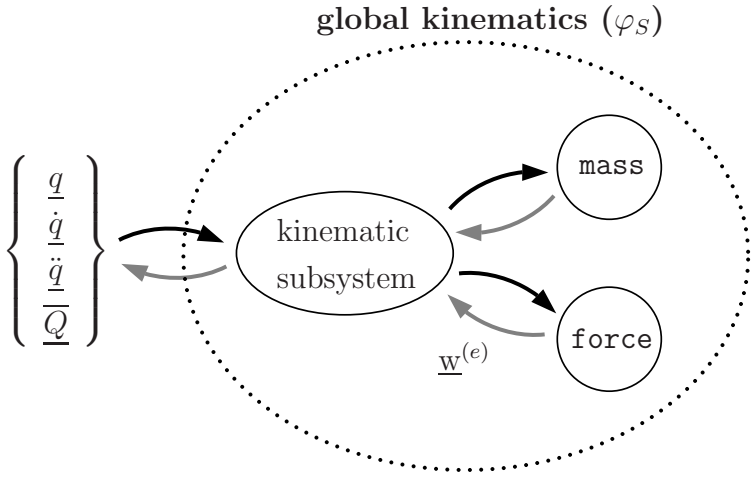

Figure 3.6: Model of the inverse dynamics of a multibody system

$\underline{\dot{q}}, \underline{\ddot{q}}$ to a set of *residual* generalized forces $\underline{\overline{Q}}$ at the input of the global kinematics. Since the contribution of the involved mass elements is linearly depended on the accelerations of the corresponding reference frames this function represents the inverse dynamics of the system and has the structure

$$\underline{\overline{Q}} = \varphi_S^{D^{-1}}(\underline{q},\, \underline{\dot{q}},\, \underline{\ddot{q}}\,;\, \underline{\mathrm{w}}^{(e)}\,;\, t) = -M(\underline{q}\,;\, t)\underline{\ddot{q}} - \underline{\widehat{Q}}(\underline{q},\, \underline{\dot{q}}\,;\underline{\mathrm{w}}^{(e)}\,;\, t)\,, \tag{3.2.3}$$

where the wrench $\underline{\mathrm{w}}^{(e)}$ collects all externally applied forces and M and $\underline{\widehat{Q}}$ represent the generalized mass matrix and the generalized forces, respectively. These quantities are usually unknown. The residual forces $\underline{\overline{Q}}$ can be regarded as the generalized forces necessary to achieve dynamic equilibrium for a given system state. However, the residual forces can be used to determine the generalized mass matrix M as well as the generalized forces $\underline{\widehat{Q}}$ by virtue of the procedure described in the following:

$\underline{\widehat{Q}}$: To determine $\underline{\widehat{Q}}$, setting $\underline{\ddot{q}} = 0$, equation (3.2.3) yields a vector of generalized $\underline{\widehat{Q}}$ that directly corresponds to the vector of residuals, since the term $-M(\underline{q}\,;\, t)\underline{\ddot{q}}$ vanishes.

M: The generalized mass matrix M is computed by firstly eliminating $\underline{\widehat{Q}}$ in equation (3.2.3). This can be done by switching-off of all influences arising from applied, generalized Coriolis and centrifugal forces. Additionally setting $\ddot{q}_i = 1$ for one $i \in \{1 \ldots f\}$ while $\ddot{q}_k = 0$ for all $k \in \{1, \ldots, f\},\ k \neq i$ makes the left hand side of equation (3.2.3) identical to the ith column of the generalized mass matrix $\mathbf{M}$. Repeating this procedure for all $i \in \{1, \ldots, f\}$ consecutively yields the complete

mass matrix. As shown in equation (3.2.3), the generalized mass matrix M is only influenced by the values of the generalized coordinates $\underline{q}$

The application of the described procedure requires $f + 1$ evaluations of the inverse dynamics for one set of equations. Since in f of these evaluations the velocities are set to zero, only linear terms in the acceleration transmission have to be evaluated, omitting the computationally expensive (quadratic) velocity terms. Thus, the computational overload of the described simplified method is within reasonable limits ([Kecskeméthy and Hiller, 1994]).

3.2.3 Numerical integration in MOBILE

The numerical integration of the dynamic equations determined for simulation can be performed in MOBILE using the integrated interfaces to common integration routines. For the solution to specific problems different integration schemes are implemented such as explicit Euler, Adams-Moulton-Bashfort or LSODAR (Livermore solver for ordinary differential equations, with automatic method switching for stiff and non-stiff problems and with root-finding). The latter can be efficiently used for systems showing a partially stiff behavior, for example systems that involve impact simulations. The general usage of the integration objects provided by MOBILE is depicted in the code fragment listed in Fig. 3.7 instancing the `MoAdamsIntegrator`.

```
MoEqmBuilder eom ( vars , chain , k0 ) ;
MoMechanicalSystem mechsys ( eom ) ;
MoAdamsIntegrator integrator ( mechsys ) ;
integrator.doMotion ( dt ) ;
```

Figure 3.7: Code fragment illustrating the use of integrator objects

The first line generates an object of type `MoEqmBuilder` which is responsible for the determination of the dynamic equations. The initializing values `vars`, `chain` and `k0` represent the generalized coordinates, the chain of kinetostatic transmission elements and the specification of the inertial frame of the system at hand, respectively. In the second line, an object of type `MoMechanicalSystem` is initialized with the preceeding object, transforming the equations of motion to a state space form required for

most standard numerical integration schemes. Finally, this set of equations is then passed to the integrator object of type `MoAdamsIntegrator` itself, finally performing an integration step with output step-size `dt` by execution of the last line in the code fragment.

In the given context, it is important to mention that the integration interfaces supplied by the software package can handle additional dynamic systems besides the pure integration of the equations of motion of a mechanical system. Thus, the governing equations of the muscle model described in Sec. 6.1.1 which represent a first order differential equation can be solved comfortably in parallel to the integration of the mechanical system. Furthermore, rheonomic constraints can be handled by declaring the corresponding variables to be neglected in the integration process. The necessary variations in the initialization process are shown in Fig. 3.8.

```
MoEqmBuilder eom ( vars, rheonvars, chain , k0 ) ;
MoMechanicalSystem mechsys ( eom ) ;
MoHillMuscleActuator muscle;
MoDynamicSystemList dynlist;
dynlist << mechsys << muscle;
MoAdamsIntegrator integrator ( dynlist ) ;
integrator.doMotion ( dt ) ;
```

Figure 3.8: Code fragment illustrating the handling of dynamic systems in combination with integrator objects

In contrast to Fig. 3.7, the object of type `MoEqmBuilder` is initialized with an additional list `rheonvars`, which gathers the rheonomic variables. In addition to the code fragment in Fig. 3.7 the muscle object `MoHillMuscleActuator` represents an additional dynamic system which has to be handled synchronously to the mechanical part. The `MoDynamicSystemList` groups all dynamic systems that are to be integrated and is used to initialize the integrator object. As before, the execution of the last line performs an integration time-step with output step-size `dt`.

Chapter 4

Kinetostatic model of the human lower extremity

Modeling of the human lower extremity essentially depends on an accurate individual anthropometric data set. Segment geometries can today be estimated with comparatively little effort by automated motion capturing. The most characteristic example here is given by the distance between the center of two adjacent joints. Other important quantities such as segment masses or inertia properties are still difficult to obtain on a patient-specific basis. To this end, mostly estimations based on clinical surveys are applied, representing averaged values for the desired quantities. Winter ([Winter, 1990]) supplies an elaborate data set based on a work of Drillis and Contini ([Drillis and Contini, 1966]), where segment dimensions and inertia properties are given as functions of total body weight and height. However, due to the multitude of influencing factors such as sex, age, grade of adiposity (or slenderness), the reliability of the results obtained when applying such values is limited.

In the present Chapter, all methods to obtain individual data sets for segment modeling are described in a generic manner without focusing on algorithmic details. A more elaborate description is given in the cited reports.

4.1 Patient-specific kinematics

The quality of results of considerations of gait kinematics is obviously sensitive to errors in the determination of segmental geometries, which in particular can be specified to

the determination of bone geometries. Especially early investigations were heavily dependent on data records such as mentioned above ([Winter, 1990]) due to the operating expense (for scientists and patients) to achieve individual data by own measurements and/or because of lack of technical equipment. The development of automated motion capturing devices was the key step to achieve patient-specific data with comparatively little effort. In the sequel, the principle of motion capturing using passive markers is described. For information about different techniques (e.g. active markers) the reader is referred to the appropriate literature.

4.1.1 Gait laboratory

Motion capturing was performed in a gait laboratory using a VICON motion capturing system, consisting of 6 infrared cameras operating at 50 Hz. The cameras map the motion of reflective markers (diameter $d_{\mathrm{M}} = 0.9\,\mathrm{mm} - 2.5\,\mathrm{mm}$) which are attached to the person under investigation at defined landmarks of the lower extremity (see Fig. 4.1 and Tab. 4.1), yielding marker trajectories for the respective trial ([Hartley and Zisserman, 2004]). The raw marker trajectories used in this work are filtered by a quintic spline filter before they are used for the determination of segment geometries. In addition to the pure kinematic measurement, a force plate (see Sec. 4.2.1) synchronically measures ground reaction forces and moments, which are used in the inverse dynamics simulations (see Chap. 5).

4.1.2 Marker placement

The present work is based on the Helen-Hayes marker configuration. The basic set consists of 15 markers attached to the lower extremity at anatomical significant locations which allow for the determination of principal axes of the segments under consideration.The location of the markers in depicted in Fig. 4.1. The explicit description of the anatomical position is summarized in Tab. 4.1 (marker name abbreviations are defined in Fig. 4.1).

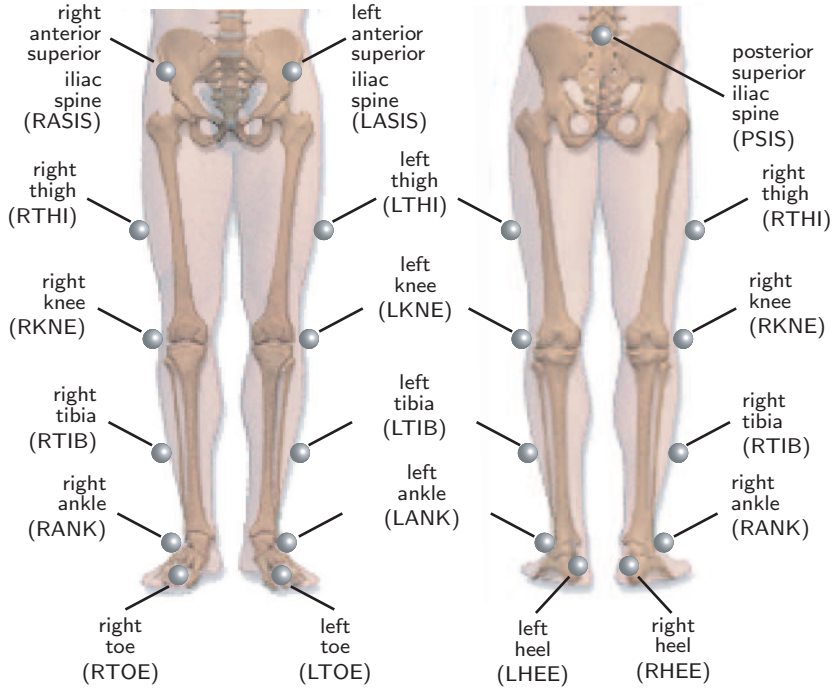

Figure 4.1: Marker placement for lower extremity (ventral and dorsal view) according to VICON Clinical Manager, Helen-Hayes-configuration, [Oxford Metrics, 2004]

4.1.3 Simplified mathematical description of segmental kinematics

In the following, the procedure to obtain kinematic data from the recorded marker trajectories based on [Davis et al., 1991] and [Oxford Metrics, 2004] is described by the kinematic structure elements of MOBILE for further reference.

The determination of the specific segment/bone geometries is based on assumptions that underly partially significant simplifications, e.g. the consideration of the skeletal structure as a concatenation of rigid bodies. Nevertheless, the described procedures represent a successful compromise between model simplifications, patient stress in the data collection process, computational efficiency and results. For each limb, the procedure consists of two steps, for which, depending on the available information at each time, the order of execution may change for the segment under consideration:

- definition of an embedded (segment fixed) local coordinate system
- estimation of the joint center of the corresponding distal joint center with respect to the previously defined embedded frame

marker name	anatomical position	function
RASIS / LASIS	right/left *spina iliaca anterior superior*	determination of pelvis orientation and hip joint center location (both for left and right)
PSIS	superior aspect at the L5-sacral interface	determination of pelvis orientation
RTHI / LTHI	on lower right/left thigh laterally aligned with the long axis of the thigh in line with the flexion/extension axis of the knee	determination of orientation of right/left thigh segment
RKNE / LKNE	along flexion/extention axis of rotation at lateral femoral condyle of right/left femur	determination of knee joint center
RTIB / LTIB	on lower right/left shank laterally aligned with the long axis of the thigh in line with the flexion/extension axis of the knee	determination of orientation of right/left shank segment
RANK / LANK	along flexion/extension axis of rotation at lateral malleolus of right/left fibula	determination of ankle joint center
RTOE / LTOE	center of the foot between metatarsus II and III	determination of orientation of right/left foot (together with RHEE / LHEE)
RHEE / LHEE	posterior calcaneus at same height as respective toe marker	determination of orientation of right/left foot (together with RTOE / LTOE)

Table 4.1: Location and function of markers for lower extremity according to Helen-Hayes configuration, [Oxford Metrics, 2004]

To this end, besides pure marker kinematics, additional patient specific data is necessary which is typically measured prior to the motion capturing process. Quantities influencing the results of the modeling process are the marker diameter d_{M}, the specific leg length ℓ_{leg}, the specific knee width w_{K}, the specific ankle width w_{A} as well as the anterior/posterior component of the LASIS/RASIS/hip center distance x_{dis} in the sagittal plane of the pelvis. Distances are considered in meters and are typically determined individually for right and left leg. The following descriptions require the trajectories of the above mentioned markers and the trial-specific quantities to be known. Specific

limitations and necessary improvements are discussed in Sec. 5.2.

Pelvis kinematic model

The determination of the pelvis geometry is based on a procedure developed at the Newington Children's Hospital, Newington, USA ([Davis et al., 1991]). It resulted from a radiographic examination of 25 hip studies. Although the size of the control group was relatively small, the procedure and the determined values have become standard in modern gait analysis. The significant quantities are depicted in Fig. 4.2.

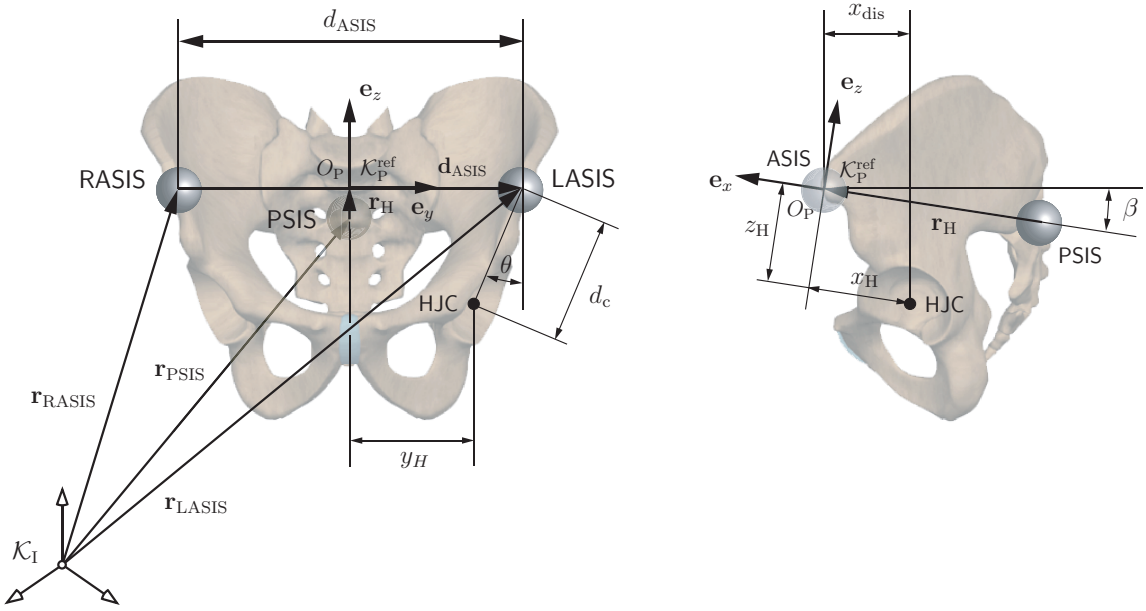

Figure 4.2: Pelvis kinematic model (coronal and sagittal plane view) according to VICON Clinical Manager ([Oxford Metrics, 2004], [Davis et al., 1991]), picture adapted from [Sobotta, 2005]

The pelvis-fixed coordinate frame $\mathcal{K}_{\mathrm{P}}^{\mathrm{ref}}$ is constructed from the measured radius vectors ${}^{\mathrm{I}}\mathbf{r}_{\mathrm{RASIS}}$, ${}^{\mathrm{I}}\mathbf{r}_{\mathrm{LASIS}}$ and ${}^{\mathrm{I}}\mathbf{r}_{\mathrm{PSIS}}$. Its origin O_{P} (given in absolute coordinates defined by the inertial frame $\mathcal{K}_I$) is positioned at

$$ {}^{\mathrm{I}}\mathbf{r}_{O_{\mathrm{P}}} = {}^{\mathrm{I}}\mathbf{r}_{\mathrm{RASIS}} + \frac{1}{2}\,{}^{\mathrm{I}}\mathbf{d}_{\mathrm{ASIS}} \tag{4.1.1} $$

where ${}^{\mathrm{I}}\mathbf{d}_{\mathrm{ASIS}} = 1/2\left({}^{\mathrm{I}}\mathbf{r}_{\mathrm{LASIS}} - {}^{\mathrm{I}}\mathbf{r}_{\mathrm{RASIS}}\right)$. The y-axis is defined along the connection

between right and left *spina iliaca superior anterior*, using the unit vector

$$ {}^{\mathrm{I}}\mathbf{e}_{y_{\mathrm{P}}} = \frac{{}^{\mathrm{I}}\mathbf{d}_{\mathrm{ASIS}}}{\| {}^{\mathrm{I}}\mathbf{d}_{\mathrm{ASIS}} \|} \,. \tag{4.1.2} $$

The x-axis is aligned along the normal to ${}^{\mathrm{I}}\mathbf{d}_{\mathrm{ASIS}}$ through the marker located at the superior aspect at the L5-sacral interface (*spina iliaca posterior superior*) . The corresponding unit vector is defined as

$$ {}^{\mathrm{I}}\mathbf{e}_{x_{\mathrm{P}}} = \frac{{}^{\mathrm{I}}\mathbf{r}_{\mathrm{H}}}{\| {}^{\mathrm{I}}\mathbf{r}_{\mathrm{H}} \|} \tag{4.1.3} $$

where ${}^{\mathrm{I}}\mathbf{r}_{\mathrm{H}} = {}^{\mathrm{I}}\mathbf{r}_{\mathrm{O_P}} - {}^{\mathrm{I}}\mathbf{r}_{\mathrm{PSIS}}$ with ${}^{\mathrm{I}}\mathbf{r}_{\mathrm{O_P}}$ given in (4.1.1).

The z-axis is defined according to the unit vector

$$ {}^{\mathrm{I}}\mathbf{e}_{z_{\mathrm{P}}} = {}^{\mathrm{I}}\mathbf{e}_{x_{\mathrm{P}}} \times {}^{\mathrm{I}}\mathbf{e}_{y_{\mathrm{P}}} \,. \tag{4.1.4} $$

Implicitly, by definition of the embedded coordinate frame $\mathcal{K}_{\mathrm{P}}^{\mathrm{ref}}$, the orientation of the pelvis segment with respect to the inertial frame $\mathcal{K}_{\mathrm{I}}$ is described by virtue of the transformation matrix ${}^{\mathrm{I}}\mathbf{R}_{\mathrm{P}}$, given as

$$ {}^{\mathrm{I}}\mathbf{R}_{\mathrm{P}} = \left[{}^{\mathrm{I}}\mathbf{e}_{x_{\mathrm{P}}} \; {}^{\mathrm{I}}\mathbf{e}_{y_{\mathrm{P}}} \; {}^{\mathrm{I}}\mathbf{e}_{z_{\mathrm{P}}} \right] \,. \tag{4.1.5} $$

To locate the right and left hip joint center (HJC), respectively, additional quantities are involved, which are taken from the hip joint study mentioned above. The distance d_{c} between RASIS/LASIS and corresponding HJC was found by linear regression (R-square coefficient 0.9) as a function of leg length ℓ_{leg} to

$$ d_{\mathrm{c}} = 0.115\, \ell_{\mathrm{leg}} - 0.0153 \,. \tag{4.1.6} $$

It represents the length of the projection of the connecting line between RASIS/LASIS and corresponding HJC into the coronal plane. The angles defined in Fig. 4.2 were chosen as $\theta = 28.4°$ and $\beta = 18.0°$. Both values represent the median of the radiographic study. Hence, the location of the HJC is expressed with respect to the local frame $\mathcal{K}_{\mathrm{P}}^{\mathrm{ref}}$ as

$$ x_{\mathrm{H}} = (-x_{\mathrm{dis}} - d_{\mathrm{m}}) \cos\beta + d_{\mathrm{c}} \cos\theta \sin\beta \,, \tag{4.1.7} $$

$$ y_{\mathrm{H}} = \pm \left(d_{\mathrm{c}} \sin\theta - \frac{d_{\mathrm{ASIS}}}{2} \right) \,, \tag{4.1.8} $$

$$ z_{\mathrm{H}} = (-x_{\mathrm{dis}} - d_{\mathrm{M}}) \sin\beta - d_{\mathrm{c}} \cos\theta \cos\beta \,, \tag{4.1.9} $$

where the sign in (4.1.8) depends on the side for which the HJC is sought ("$-$" for left HJC, "$+$" for right HJC).

Thigh kinematic model

Orientation and position of a thigh segment is derived from the known position of the corresponding HJC in combination with the locations of the markers RTHI/LTHI and RKNE/LKNE. The principle is depicted on the example of a right thigh in Fig. 4.3 and derived for the same situation in the following. The process is based on the assumption that the thigh segment lies in the plane $\mathcal{P}_\mathrm{T}$ defined by the corresponding hip joint center, thigh marker and knee joint marker.

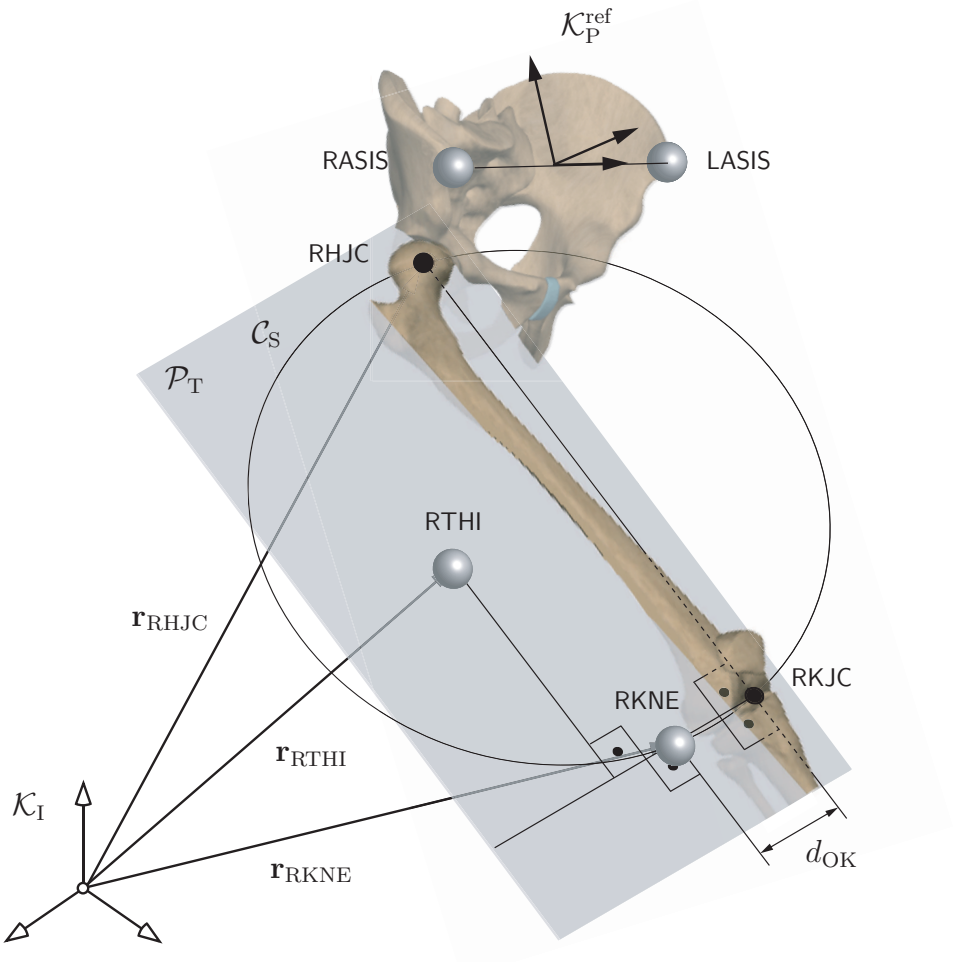

Figure 4.3: Thigh kinematic model according to VICON Clinical Manager ([Oxford Metrics, 2004], [Davis et al., 1991]), example for right thigh, picture adapted from [Sobotta, 2005]

In addition, the known position of the RHJC, the corresponding knee joint marker and the sought position of the corresponding knee joint center are assumed to be located on a circle $\mathcal{C}_\mathrm{T}$ in the plane $\mathcal{P}_\mathrm{T}$. In the displayed example, the use of ${}^\mathrm{I}\mathbf{r}_\mathrm{RHJC}$, ${}^\mathrm{I}\mathbf{r}_\mathrm{RTHI}$ and ${}^\mathrm{I}\mathbf{r}_\mathrm{RKNE}$ in combination with the known knee offset $d_\mathrm{OK} = 1/2\,(w_\mathrm{K} + d_\mathrm{M})$ yields the position of the knee right joint embedded in the plane $\mathcal{P}_\mathrm{T}$. Implicitly, the described method also embeds the *axis transversalis* of the knee joint in this plane since the connections between RKJC and RHJC as well as RKJC and RKNE are considered as coplanar and perpendicular.

The specification of the thigh-fixed reference frame $\mathcal{K}_\mathrm{T}^\mathrm{ref}$ is shown in Fig. 4.4. Its origin is located at the hip joint center determined by the offset vector

$$ {}^\mathrm{P}\mathbf{r}_\mathrm{RHJC} = [\, x_\mathrm{H}\; y_\mathrm{H}\; z_\mathrm{H}\,]^\mathrm{T} \tag{4.1.10} $$

defined with respect to the pelvis reference frame $\mathcal{K}_\mathrm{P}^\mathrm{ref}$ according to (4.1.7) – (4.1.9), yielding the absolute position in space by virtue of

$$ {}^\mathrm{I}\mathbf{r}_\mathrm{RHJC} = {}^\mathrm{I}\mathbf{R}_\mathrm{P}\, {}^\mathrm{P}\mathbf{r}_\mathrm{RHJC}\,, \tag{4.1.11} $$

using the transformation matrix (4.1.5). The unit vector in z-direction can be decomposed in the inertially-fixed frame and thus results as

$$ {}^\mathrm{I}\mathbf{e}_{z_\mathrm{T}} = \frac{{}^\mathrm{I}\mathbf{r}_\mathrm{RHJC} - {}^\mathrm{I}\mathbf{r}_\mathrm{RKJC}}{\| {}^\mathrm{I}\mathbf{r}_\mathrm{RHJC} - {}^\mathrm{I}\mathbf{r}_\mathrm{RKJC}\|}\,. \tag{4.1.12} $$

The y-direction ${}^\mathrm{I}\mathbf{e}_{y_\mathrm{T}}$ is assumed to be normal to ${}^\mathrm{I}\mathbf{e}_{z_\mathrm{T}}$ and embedded in the plane $\mathcal{P}_\mathrm{T}$ and (in case of the exemplarily treated right leg) oriented in medial direction. Obviously,

$$ {}^\mathrm{I}\mathbf{e}_{y_\mathrm{T}} = \frac{{}^\mathrm{I}\mathbf{r}_\mathrm{RKNE} - {}^\mathrm{I}\mathbf{r}_\mathrm{RKJC}}{\|{}^\mathrm{I}\mathbf{r}_\mathrm{RKNE} - {}^\mathrm{I}\mathbf{r}_\mathrm{RKJC}\|}\,. \tag{4.1.13} $$

Finally, the unit vector in x-direction is found as

$$ {}^\mathrm{I}\mathbf{e}_{x_\mathrm{T}} = {}^\mathrm{I}\mathbf{e}_{y_\mathrm{T}} \times {}^\mathrm{I}\mathbf{e}_{z_\mathrm{T}}\;\;. \tag{4.1.14} $$

The transformation matrix describing the orientation of the thigh segment with respect to the inertial frame is defined by

$$ {}^\mathrm{I}\mathbf{R}_\mathrm{T} = \left[\, {}^\mathrm{I}\mathbf{e}_{x_\mathrm{T}}\; {}^\mathrm{I}\mathbf{e}_{y_\mathrm{T}}\; {}^\mathrm{I}\mathbf{e}_{z_\mathrm{T}}\,\right]\;. \tag{4.1.15} $$

More sophisticated methods take care of dislocations of the thigh marker with respect to the plane defined by the connecting lines RHJC — RKJC and RKJC — RKNE ([Davis et al., 1991]).

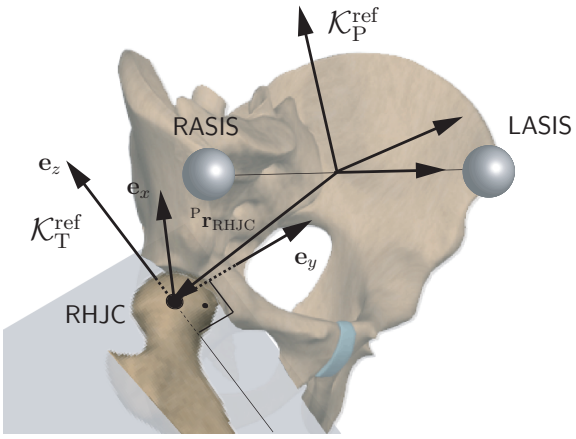

Figure 4.4: Definition of thigh-fixed reference frame

Shank kinematic model

Position and orientation information for the shank segment can be determined similarly to the extraction of the thigh kinematics from the measured marker trajectories. The involved corresponding quantities $\mathcal{C}_{\mathrm{S}}$, $\mathcal{P}_{\mathrm{S}}$, ${}^{\mathrm{I}}\mathbf{r}_{\mathrm{RKJC}}$, ${}^{\mathrm{I}}\mathbf{r}_{\mathrm{RTIB}}$, ${}^{\mathrm{I}}\mathbf{r}_{\mathrm{RANK}}$ and and $d_{\mathrm{OA}} = 1/2\,(w_{\mathrm{A}} + d_{\mathrm{M}})$ are shown in Fig. 4.5 for the example of a right shank.

The origin of the shank-fixed frame $\mathcal{K}_{\mathrm{S}}^{\mathrm{ref}}$ is located in the RKJC. Its defining axes are determined by unit vector

$$ {}^{\mathrm{I}}\mathbf{e}_{z_{\mathrm{S}}} = \frac{{}^{\mathrm{I}}\mathbf{r}_{\mathrm{RKJC}} - {}^{\mathrm{I}}\mathbf{r}_{\mathrm{RAJC}}}{\| {}^{\mathrm{I}}\mathbf{r}_{\mathrm{RKJC}} - {}^{\mathrm{I}}\mathbf{r}_{\mathrm{RAJC}}\|}\,, \tag{4.1.16} $$

the connection between RANK and RAJC,

$$ {}^{\mathrm{I}}\mathbf{e}_{y_{\mathrm{S}}} = \frac{{}^{\mathrm{I}}\mathbf{r}_{\mathrm{RANK}} - {}^{\mathrm{I}}\mathbf{r}_{\mathrm{RAJC}}}{\|{}^{\mathrm{I}}\mathbf{r}_{\mathrm{RANK}} - {}^{\mathrm{I}}\mathbf{r}_{\mathrm{RAJC}}\|}\,, \tag{4.1.17} $$

and

$$ {}^{\mathrm{I}}\mathbf{e}_{x_{\mathrm{S}}} = {}^{\mathrm{I}}\mathbf{e}_{y_{\mathrm{S}}} \times {}^{\mathrm{I}}\mathbf{e}_{z_{\mathrm{S}}}\,. \tag{4.1.18} $$

As in the case of the pelvis and thigh segment, the corresponding transformation matrix ${}^{\mathrm{I}}\mathbf{R}_{\mathrm{S}}$ from shank to inertial frame is given by

$$ {}^{\mathrm{I}}\mathbf{R}_{\mathrm{S}} = \left[\, {}^{\mathrm{I}}\mathbf{e}_{x_{\mathrm{S}}}\ {}^{\mathrm{I}}\mathbf{e}_{y_{\mathrm{S}}}\ {}^{\mathrm{I}}\mathbf{e}_{z_{\mathrm{S}}} \,\right]\,. \tag{4.1.19} $$

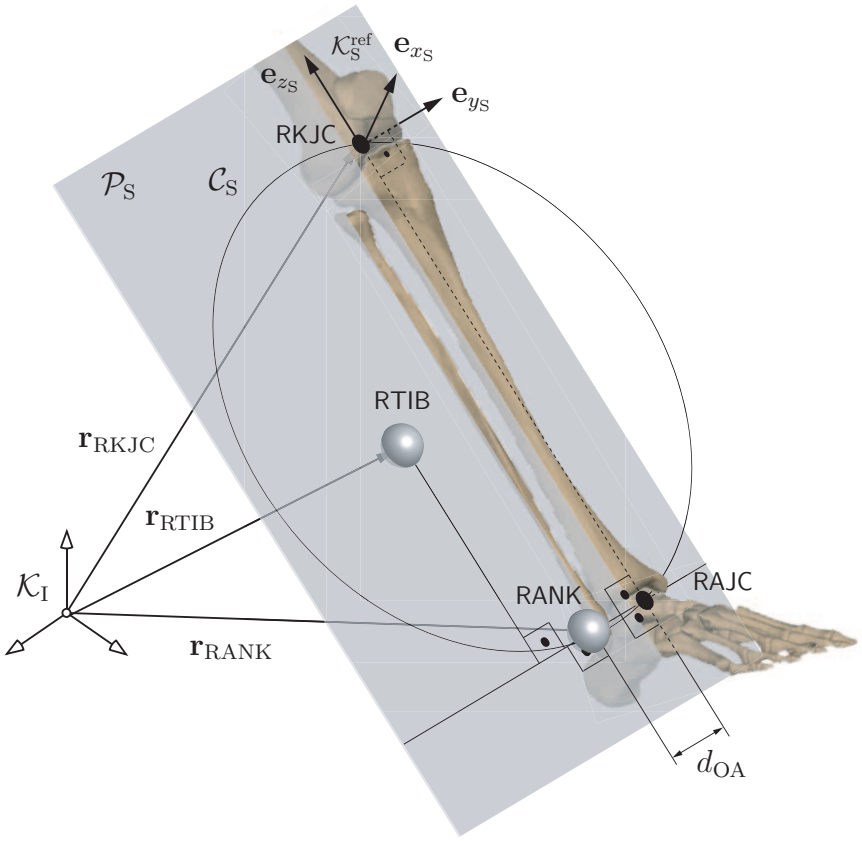

Figure 4.5: Shank kinematic model according to VICON Clinical Manager ([Oxford Metrics, 2004], [Davis et al., 1991]), example for right shank, picture adapted from [Sobotta, 2005]

Foot kinematic model

In contrast to the aforementioned segments, modeling the kinematic properties of the foot does not involve the determination of a distal joint center, facilitating the corresponding process of defining the significant segment model quantities. Fig. 4.6 explains the kinematic model of the (right) foot in detail. It is mainly based on the trajectories of the markers RHEE and RTOE. The previously determined RAJC represents the point of reference for the foot segment.

The orientation of the corresponding coordinate axes of the segment-fixed coordinate frame $\mathcal{K}_{\mathrm{F}}^{\mathrm{ref}}$ is given as follows. The vector

$$ {}^{\mathrm{I}}\mathbf{d}_{\mathrm{F}} = {}^{\mathrm{I}}\mathbf{r}_{\mathrm{RTOE}} - {}^{\mathrm{I}}\mathbf{r}_{\mathrm{RHEE}} \tag{4.1.20} $$

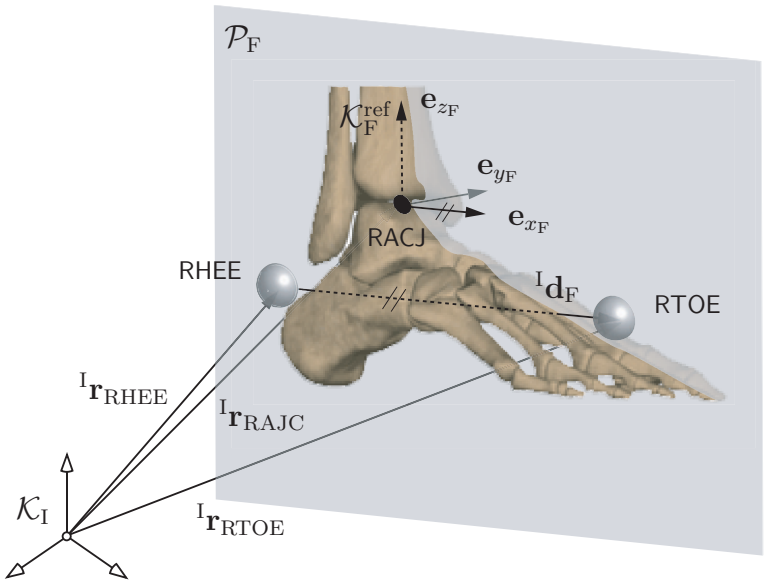

Figure 4.6: Foot kinematic model according to VICON Clinical Manager ([Oxford Metrics, 2004], [Davis et al., 1991]), example for right foot, picture adapted from [Sobotta, 2005]

is used to define the x-direction in terms of

$$ {}^\mathrm{I}\mathbf{e}_{x_\mathrm{F}} = \frac{{}^\mathrm{I}\mathbf{d}_\mathrm{F}}{\|{}^\mathrm{I}\mathbf{d}_\mathrm{F}\|} \,. \tag{4.1.21} $$

It is embedded in the plane $\mathcal{P}_\mathrm{F}$ defined by the locations of the markers RHEE, RTOE and the previously determined RAJC. ${}^\mathrm{I}\mathbf{e}_{y_\mathrm{F}}$ is defined perpendicular to this plane and oriented in medial direction. It can be constructed as

$$ {}^\mathrm{I}\mathbf{e}_{y_\mathrm{F}} = \frac{\left({}^\mathrm{I}\mathbf{r}_\mathrm{RAJC} - {}^\mathrm{I}\mathbf{r}_\mathrm{RHEE}\right) \times \left({}^\mathrm{I}\mathbf{r}_\mathrm{RTOE} - {}^\mathrm{I}\mathbf{r}_\mathrm{RAJC}\right)}{\|({}^\mathrm{I}\mathbf{r}_\mathrm{RAJC} - {}^\mathrm{I}\mathbf{r}_\mathrm{RHEE}) \times ({}^\mathrm{I}\mathbf{r}_\mathrm{RTOE} - {}^\mathrm{I}\mathbf{r}_\mathrm{RAJC})\|} \,. \tag{4.1.22} $$

Finally, the z-direction is defined by

$$ {}^\mathrm{I}\mathbf{e}_{z_\mathrm{F}} = {}^\mathrm{I}\mathbf{e}_{x_\mathrm{F}} \times {}^\mathrm{I}\mathbf{e}_{x_\mathrm{F}} \,, \tag{4.1.23} $$

leading to the transformation matrix

$$ {}^\mathrm{I}\mathbf{R}_\mathrm{F} = \left[{}^\mathrm{I}\mathbf{e}_{x_\mathrm{F}} \; {}^\mathrm{I}\mathbf{e}_{y_\mathrm{F}} \; {}^\mathrm{I}\mathbf{e}_{z_\mathrm{F}} \right] \,. \tag{4.1.24} $$

4.1.4 Relative kinematics

In total, for each patient a typical data set contains the orientation of pelvis, right and left thigh, right and left shank as well as right and left foot in terms of the

transformation matrices

$$ {}^{\mathrm{I}}\mathbf{R}_{\mathrm{P}},\ {}^{\mathrm{I}}\mathbf{R}_{\mathrm{T}}^{\mathrm{right}},\ {}^{\mathrm{I}}\mathbf{R}_{\mathrm{T}}^{\mathrm{left}},\ {}^{\mathrm{I}}\mathbf{R}_{\mathrm{S}}^{\mathrm{right}},\ {}^{\mathrm{I}}\mathbf{R}_{\mathrm{S}}^{\mathrm{left}},\ {}^{\mathrm{I}}\mathbf{R}_{\mathrm{F}}^{\mathrm{right}},\ {}^{\mathrm{I}}\mathbf{R}_{\mathrm{F}}^{\mathrm{left}} \tag{4.1.25} $$

and the location of the origin of each segment-fixed coordinate frame

$$ {}^{\mathrm{I}}\mathbf{r}_{\mathrm{O_P}},\ {}^{\mathrm{I}}\mathbf{r}_{\mathrm{RHJC}},\ {}^{\mathrm{I}}\mathbf{r}_{\mathrm{LHJC}},\ {}^{\mathrm{I}}\mathbf{r}_{\mathrm{RKJC}},\ {}^{\mathrm{I}}\mathbf{r}_{\mathrm{LKJC}},\ {}^{\mathrm{I}}\mathbf{r}_{\mathrm{RAJC}},\ {}^{\mathrm{I}}\mathbf{r}_{\mathrm{LAJC}}\ . \tag{4.1.26} $$

All other kinematic data is derived hereof. Of particular interest is the determination of the segment vectors connecting adjacent joints as well as the relative orientation of two consecutive segments. Typically, the definition of the segment vectors appears simple, since they represent the difference of the radius vectors describing the position of the corresponding joint centers. By multiplication with the appropriate transformation matrix, the segment vector is decomposed in the corresponding segment-fixed frame. Exemplarily, the right thigh segment vector $\mathbf{s}_{\mathrm{T}}^{\mathrm{right}}$ can be decomposed in the thigh-fixed frame $\mathcal{K}_{\mathrm{T}}^{\mathrm{ref}}$ as

$$ {}^{\mathrm{T}}\mathbf{s}_{\mathrm{T}}^{\mathrm{right}} = \underbrace{{}^{\mathrm{T}}\mathbf{R}_{\mathrm{I}}}_{({}^{\mathrm{I}}\mathbf{R}_{\mathrm{T}})^{\mathrm{T}}} \left({}^{\mathrm{I}}\mathbf{r}_{\mathrm{RKJC}} - {}^{\mathrm{I}}\mathbf{r}_{\mathrm{RHJC}} \right)\ . \tag{4.1.27} $$

Joint angles are extracted from the transformation matrices representing the relative change in orientation between neighbored segments. As an example, the relative rotation of the right thigh segment with respect to the pelvis segment can be expressed as

$$ {}^{\mathrm{P}}\mathbf{R}_{\mathrm{T}}^{\mathrm{right}} = {}^{\mathrm{P}}\mathbf{R}_{\mathrm{I}}\, {}^{\mathrm{I}}\mathbf{R}_{\mathrm{T}}^{\mathrm{right}} = \left({}^{\mathrm{I}}\mathbf{R}_{\mathrm{P}} \right)^{\mathrm{T}}\, {}^{\mathrm{I}}\mathbf{R}_{\mathrm{T}}^{\mathrm{right}} \tag{4.1.28} $$

With respect to an assumed parameterization of the rotation and regarding possible singularities, the corresponding hip joint angles can be extracted from the matrix (4.1.28). The principle is applied in the object-oriented modeling approach and described in Sec. 4.4.3.

4.1.5 Resultant data sets and limitations, postprocessing

The kinematic data extracted from gait laboratory measurement was postprocessed using the VICON Clinical Manager software package ([Oxford Metrics, 2004]). As a result, for each patient under investigation a single step for right and left leg was extracted, yielding kinematic data for a complete gait cycle, stored in GCD format. In addition, specific instants during gait such as begin and end of foot-ground contact are

determined. In each data set, gait cycle is normalized to 51 bundles of transformation matrices and segment vectors computed according to (4.1.27) and (4.1.28) for each involved segment and joint.

Since the motion capturing process is highly dependent on the expertise of the physician, the accuracy of marker placement and significantly sensitive to measurement noise and inaccuracies the resultant data sets contain unavoidable errors. A typical example in that context is the relative motion between the attachment point of a marker at skin surface and the sub-dermal bone location, which is not intercepted by the described model and leads to so-called “artefacts”. The assumption of a constant offset between joint marker position and joint center can therefore pretend varying bone lengths during gait. A method to reduce the influence of this phenomenon is described in Sec. 5.2.

In order to determine the joint angle rates and accelerations, numerical differentiation schemes were used involving typical numerical problems known in this context. Filtering techniques were applied to reduce the influence of such errors. Moreover, the consideration of the transformation matrices contained in a postprocessed data set revealed non-orthonormal matrices which were corrected to fulfill the defined requirement. Both procedures are briefly described in Sec. 5

4.2 Additional measurements

In order to be able to compute the inverse dynamics of gait, besides pure kinematic information the knowledge about ground reaction forces and moments as well as internal joint loads is also necessary. The main information in this context is collected by ground reaction force and moment measurement using a force plate. In addition, electromyography (EMG) measurements are executed to achieve information about muscle (group) activity. While force recording is typically performed synchronously to the motion capturing process, EMG measurements usually result from separate trials to avoid an interference of gait performance. Because of the EMG hardware, persons typically do not perform in a ”normal” manner and the motion capturing results would appear adulterated.

The use of both devices is described in Sec. 4.2.1 and Sec. 4.2.2. The data sets applied in this work supply both, ground reaction force and moment as well as EMG information. While the first is essential to the computation of the inverse dynamics of gait presented in Chap. 5, the latter is used only for plausibility check purposes (Chap. 6).

4.2.1 Force plate

Ground reaction force and moment is measured synchronously to the motion capturing process and normalized similarly to the kinematic data in the GCD-file. The devices used for the present work are Kistler® force plates. In principle, the resulting forces at the corners of the squared plate are measured. Regarding dimensions and other system parameters, the time history of the resultant force and moment applied to the center of the force plate are computed thereof.

For classical gait analysis purposes, in general there is no quantification of pressure distribution in the sole of the foot in contact to the plate. The definition of the *center of pressure* is used to find the location at which only a moment about the vertical axis and a force is applied. The geometric interrelations are shown in Fig. 4.7.

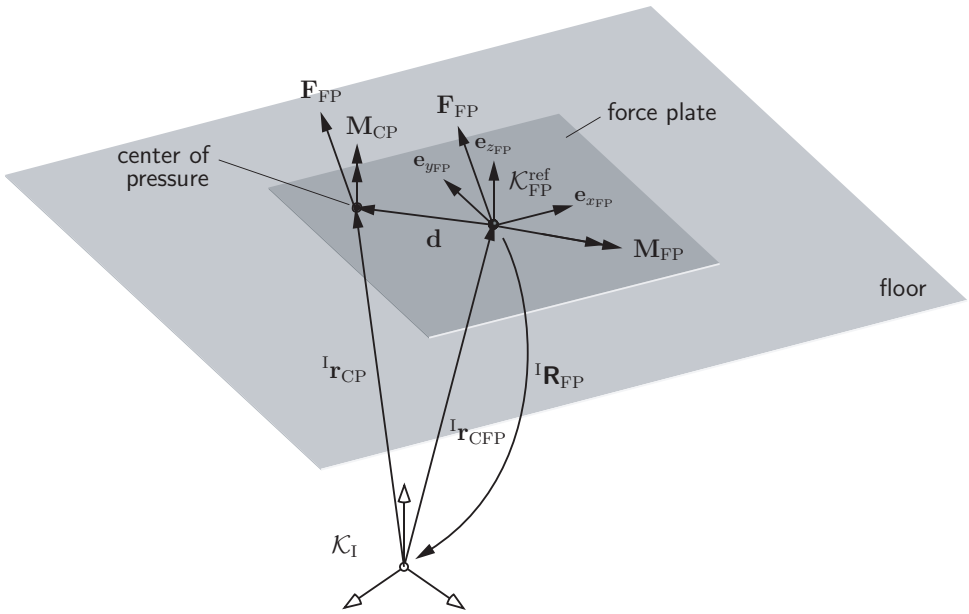

Figure 4.7: Principle of center of pressure at the force plate

Assuming the location ${}^{\mathrm{I}}\mathbf{r}_{\mathrm{CFP}}$ and orientation ${}^{\mathrm{I}}\mathbf{R}_{\mathrm{FP}}$ of the force plate reference frame $\mathcal{K}_{\mathrm{FP}}^{\mathrm{ref}}$ as well as the moment ${}^{\mathrm{I}}\mathbf{M}_{\mathrm{FP}}$ and force ${}^{\mathrm{I}}\mathbf{F}_{\mathrm{FP}}$ applied to the force plate center with respect to the inertial frame $\mathcal{K}_{\mathrm{I}}$ to be known, the position ${}^{\mathrm{I}}\mathbf{r}_{\mathrm{CP}}$ is determined by evaluation of moment equilibrium at the force plate with respect to the origin of frame

$\mathcal{K}_{\mathrm{FP}}^{\mathrm{ref}}$. Since

$$
\begin{aligned}
{}^{\mathrm{I}}\mathbf{M}_{\mathrm{FP}} &= {}^{\mathrm{I}}\mathbf{d} \times {}^{\mathrm{I}}\mathbf{F} + {}^{\mathrm{I}}\mathbf{M}_{\mathrm{CP}} && (4.2.1)\\
&= \left({}^{\mathrm{I}}\mathbf{r}_{\mathrm{CP}} - {}^{\mathrm{I}}\mathbf{r}_{\mathrm{CFP}}\right) \times {}^{\mathrm{I}}\mathbf{F} + {}^{\mathrm{I}}\mathbf{M}_{\mathrm{CP}} && (4.2.2)
\end{aligned}
$$

and typically assuming the x-y-plane of frames $\mathcal{K}_{\mathrm{I}}$ and $\mathcal{K}_{\mathrm{FP}}^{\mathrm{ref}}$ to be equal and the corresponding z-axes to be parallel, an explicit formulation of (4.2.2) becomes

$$
{}^{\mathrm{I}}\begin{bmatrix} M_x \\ M_y \\ M_z \end{bmatrix} = {}^{\mathrm{I}}\begin{bmatrix} x_{\mathrm{CFP}} - x_{\mathrm{CP}} \\ y_{\mathrm{CFP}} - y_{\mathrm{CP}} \\ 0 \end{bmatrix} \times {}^{\mathrm{I}}\begin{bmatrix} F_x \\ F_y \\ F_z \end{bmatrix} + {}^{\mathrm{I}}\begin{bmatrix} 0 \\ 0 \\ M_{\mathrm{CP}} \end{bmatrix} \tag{4.2.3}
$$

$$
= {}^{\mathrm{I}}\begin{bmatrix} F_z\,(y_{\mathrm{CP}} - y_{\mathrm{CFP}}) \\ -F_z\,(x_{\mathrm{CP}} - x_{\mathrm{CPF}}) \\ F_y\,(x_{\mathrm{CP}} - x_{\mathrm{CFP}}) - F_x\,(y_{\mathrm{CP}} - y_{\mathrm{CFP}}) \end{bmatrix} + {}^{\mathrm{I}}\begin{bmatrix} 0 \\ 0 \\ M_{\mathrm{CP}} \end{bmatrix}. \tag{4.2.4}
$$

Thus, resolution of (4.2.4) yields ${}^{\mathrm{I}}\mathbf{r}_{\mathrm{CP}} = [\,x_{\mathrm{CP}}\ y_{\mathrm{CP}}\ 0\,]^{\mathrm{T}}$ and ${}^{\mathrm{I}}\mathbf{M}_{\mathrm{CP}} = [\,0\ 0\ M_{\mathrm{CP}}\,]^{\mathrm{T}}$ with

$$
\begin{aligned}
x_{\mathrm{CP}} &= x_{\mathrm{CFP}} - \frac{M_y}{F_z}, && (4.2.5)\\
y_{\mathrm{CP}} &= \frac{M_x}{F_z} + y_{\mathrm{CFP}}, && (4.2.6)\\
M_{\mathrm{CP}} &= M_z + \frac{F_y M_y}{F_z} + \frac{F_x M_x}{F_z}\,. && (4.2.7)
\end{aligned}
$$

For a reasonable measurement it holds $F_z > 0$ (the foot can only "push" the force plate).

4.2.2 Electromyography

Electromyography (EMG) detects the electrical potential generated by muscle cells when these cells contract. The contraction itself is the result of the activation of motor units of the muscle under investigation. A motor unit is defined as one motor neuron (the "end" of a nerve connected to the muscle) and all of the muscle fibers it innervates. When a motor unit fires, an impulse also termed the action potential is carried down the motor neuron to the muscle. The area where the nerve contacts the muscle is called the neuromuscular junction, or the motor end plate. After the action potential is transmitted across the neuromuscular junction, an action potential is elicited in all

of the innervated muscle fibers of that particular motor unit. The sum of all this electrical activity is known as a motor unit action potential which can be measured as voltage between the electrodes of the EMG sensor in case of a repeated "firing" of motor neurons (typically with a frequency of $7 - 20\,\mathrm{Hz}$). The characteristic range of measured voltages is between $50\,\mu\mathrm{V}$ and $20 - 30\,\mathrm{mV}$.

Two basic techniques are commercially used, surface EMG and needle (or fine-wire) EMG. While the latter is suitable for a high resolution investigation of particular muscle areas, the first is capable to monitor the general behavior of complete muscles or muscle groups. In the context of gait analysis, surface EMG is almost solely used. However, since several factors such as sub-dermal muscle depth, cleanness of skin (= electric conductivity), accurate electrode placement and technical circumstances (e.g. a pre-amplification of the signal is usually not possible, leading to an amplification of also the measurement noise) to get a usable signal, significant postprocessing (rectification, filtering etc.) is necessary. All these factors qualify the results of surface EMG measurements only for principal statements about regions and time of muscle activation. The EMG signals used in the scope of this thesis originated from surface EMG measurements and are used for plausibility checks only in Chap. 6.

4.3 Segmental inertia properties

Knowledge about individual segment inertia parameters is essential to achieve realistic results in the simulation of human motion. However, an individual determination of these parameters is still difficult. Recent techniques such as magnetic resonance imaging (MRI) are only suitable for scientific studies with a reasonably small number of individuals since (1) the physical stress coming along with the investigation procedure is in most cases improper for clinical purposes and (2) such investigations come along with significant costs. In addition, modern techniques do not necessarily yield essentially better results than comparatively old studies (e.g. [Cheng et al., 2000] compared to [Dempster, 1955]). A detailed historical overview of different investigation techniques and results can be found in [Bjørnstrup, 1995] and [Bjørnstrup, 1996].

4.3.1 Estimation strategies

Since in most cases a detailed data set of the specific subject under investigation is not available, several approaches have been made to find reasonable assumptions about segment mass, density, volume and the resulting inertia. Generally, these approaches can be structured into three major subgroups.

Despite of the mentioned limitations, clinical studies and cadaver studies represent the basis of *regression models*. Here, inertia properties are estimated by means of a statistical analysis of control group data. Typically, the result is a number of equations that allows conclusion on unknown segmental parameters as a function of other characteristics of the body examined. The applicability of this method is limited, since mostly the extend of the survey is poor and adjustments of the governing equations are impossible. An example for this method can be found in [Hinrichs, 1985].

Scaling models are either based on the exact knowledge of the parameters of a specific segment or use statistical averages. Scaling is typically done as a function of representative measurements such as body weight, body height or segment length, see e.g. [Forwood et al., 1985]. In contrast to the regression models, here for the resultant scaling factors a physical correlation is available.

The *approximation of body segments as defined geometric volumes* represents the most flexible model, but, depending on the complexity of the underlying volumes also the most complex one. Several authors have reported different solutions, a very elaborate one is given by Hatze ([Hatze, 1977], [Hatze, 1980]) who approximates the complete human body by 17 separate segments. However, since the average duration of the accomplishment of the 242 measurements necessary to feed the model equations is specified as 80 minutes, the applicability of the method is limited and becomes unsuitable for clinical examinations of pathological gait patterns.

In general, all methods have in common that the simplifications coming along with the modeling process can lead to infeasible results. The typical assumption of rigid segments neglects the dynamical influence of soft tissue relative motion with respect to the bones during the investigated motor task. However, several authors have reported rather little influence of this phenomenon to the computational results (e.g. maximally 6 % in [Hatze, 1980]).

In the thesis at hand, three different models were implemented and compared in terms of the resulting computational differences (see Chap. 5). The influence of wobbling

masses which intuitively is assumed to increase especially for pre-obese or obese individuals is neglected in the model. Recent publications show that the neglect of this influence is permitted at least when considering normal gait motion ([Alonso et al., 2007]).

4.3.2 Scaling model according to Winter

Inertia properties proposed in [Winter, 1990] are based on an investigation of Dempster ([Dempster, 1955]) who estimated segment lengths and joint center locations relative to anatomical landmarks and a survey of Drillis and Contini, which resulted in an average set of segment lengths as a percentage of body height ([Drillis and Contini, 1966]). The principle is depicted for the lower extremity in Fig. 4.8 .

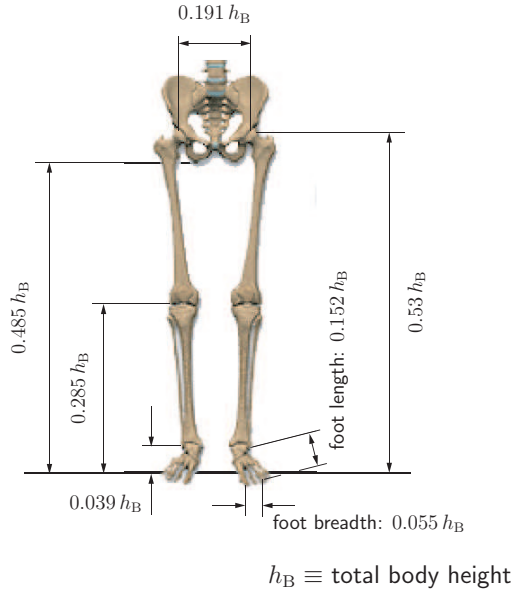

Figure 4.8: Lower extremity segment lengths as a function of body height according to Drillis and Contini (data adapted from [Winter, 1990], picture adapted from [Sobotta, 2005])

Derived thereof, segmental mass is expressed as a percentage of the total body weight. Density quantities are also based on the studies of Drillis and Contini, involving the *ponderal index* p that allows for the estimation of average body density as a function of total body weight w_B and total body height h_B. As a consequence, the average body density

$$\rho_{av} = 0.69\frac{kg}{m^3} + 0.9\frac{kg\sqrt[3]{kg}}{m\sqrt[3]{m}}p \quad \text{with} \quad p = \sqrt[3]{\frac{h_B}{w_B}} \tag{4.3.1}$$

in kg/m^3 is used as a scaling factor to approximate segmental densities. Basis for the scaling procedure is the higher proportion of bone in the distal segments which causes a higher density than determined for the proximal segments. Obviously, a short, adipose person has a smaller ponderal index than a tall, slim person. As a consequence, the interpretation of (4.3.1) yields that a tall, slim person has a lower average body density than a short, adipose person.

A limitation of the considerations in [Winter, 1990] is the fact that the moment of inertia about the longitudinal axes of the segments is assumed negligible while the

other two principal moments of inertia are regarded equal. However, since the focus of this thesis is the investigation of typical gait motion, these simplifications are justifiable. Denoting the total body mass by m_{body}, the segment mass by m_{segment}, the distance

segment	definition	$k^{\text{m}}_{\text{segment}} = \frac{m_{\text{segment}}}{m_{\text{Body}}}$	$k^{\ell}_{\text{segment}} = \frac{\ell^{\text{COM}}_{\text{segment}}}{\ell_{\text{segment}}}$	$k^{\text{I}}_{\text{segment}} = \frac{r^{\text{I}}_{\text{segment}}}{\ell_{\text{segment}}}$	$\rho \left[\frac{\text{kg}}{[\text{dm}^3]}\right]$
HAT	from articulation of vertebrae L4-L5 upwards	0.536	0.626)*	0.496)*	—
pelvis	from articulation of vertebrae L4-L5 to greater trochanter	0.142	0.105	—	—
thigh	from greater trochanter to femoral condyles	0.100	0.433	0.323	1.05
shank	from femoral condyles to medial malleolus	0.0465	0.433	0.302	1.09
foot	from lateral malleolus to head of metatarsus II	0.0145	0.500	0.475	1.10

)* Data via Dempster, Miller and Nelson, *Biomechanics of Sport*, Lea and Felbinger, 1973, with a slightly different segment definition including the pelvis segment

Table 4.2: Lower extremity segment definition and mass distribution adapted from Winter ([Winter, 1990]). Distances are to be considered with respect to the proximal segment limit.

between proximal segment limit and the segment center of mass by $\ell^{\mathrm{COM}}_{\mathrm{segment}}$, the total segment length by ℓ_{segment}, the radius of gyration by $r^{\mathrm{I}}_{\mathrm{segment}}$, the segment density by ρ_{segment} and the corresponding ratios by $k^{\mathrm{m}}_{\mathrm{segment}}$, $k^{\ell}_{\mathrm{segment}}$, $k^{\mathrm{I}}_{\mathrm{segment}}$ and $k^{\rho}_{\mathrm{segment}}$ defined in Tab. 4.2, segmental inertia properties can be computed as

$$m_{\mathrm{segment}} = k^{\mathrm{m}}_{\mathrm{segment}} m_{\mathrm{body}} \tag{4.3.2}$$

$$\ell_{\mathrm{COM}} = k^{\ell}_{\mathrm{segment}} \ell_{\mathrm{segment}} \tag{4.3.3}$$

$$I_x = I_y = m_{\mathrm{segment}} \left(k^{\mathrm{I}}_{\mathrm{segment}} \ell_{\mathrm{segment}} \right)^2 \tag{4.3.4}$$

$$\rho_{\mathrm{segment}} = k^{\rho}_{\mathrm{segment}} \rho_{\mathrm{av}} \tag{4.3.5}$$

using (4.3.1) and referring to the principal moments of inertia as I_x and I_y.

4.3.3 Point model

In case of the point mass model, mass is assumed to be concentrated in the segment center of mass given according to the data reported in Tab. 4.2. The total segment length ℓ_{segment} necessary to compute the location of the center of mass according to (4.3.3) is computed from the GCD data set described in Sec. 4.1.5 as the length of differences of the appropriate vectors given in (4.1.26). Difficulties arising in this context are discussed in Chap. 5.

4.3.4 Cylinder model

In case of the approximation of the segments as circular cylinders, density ρ_{segment} and mass m_{segment} were taken from Tab. 4.2 while the segment lengths ℓ_{segment} are computed from the GCD data set described in Sec. 4.1.5. The assumption of homogenous mass distribution then allows for the computation of the radius of the cylinder from

$$r^2_{\mathrm{cylinder}} = \frac{m_{\mathrm{segment}}}{10^3 \rho_{\mathrm{segment}} \pi \ell_{\mathrm{segment}}} \tag{4.3.6}$$

where the scaling factor results from the conversion of the segment density from Tab. 4.2 to SI-units. The principal moments of inertia can then be expressed as functions of the

squared cylinder radius r^2_{cylinder}, yielding

$$I_x = I_y = \frac{1}{4} m_{\text{segment}} r^2_{\text{cylinder}} + \frac{1}{12} m_{\text{segment}} \ell^2_{\text{segment}} , \tag{4.3.7}$$

$$I_z = \frac{1}{2} m_{\text{segment}} r^2_{\text{cylinder}} \quad . \tag{4.3.8}$$

The center of mass of each segment is located in the geometrical center of the respective cylinder.

4.4 Object-oriented modeling of the passive locomotor system

In general, the passive locomotor system includes bones, joints and ligaments as well as the surrounding masses. Its main purpose, the support of the upper part of the body as well the efficient force transmission between the individual segments indicates the consideration of each segment and each inter-segmental joint as an expedient structuring. The lower extremity in the whole is then represented as a concatenation of the involved joints and segments in a tree-like structure, having its root at the pelvis segment and its tip at the feet.

To model the system according to the kinetostatic transmission element concept and to apply the ideas of Chap. 3, the kinematic and kinetic models explained in Sec. 4.1 and Sec. 4.3 were implemented on the basis of the multibody library MOBILE.

4.4.1 Segmental inertia model

Instances of objects of type `MassProperty` represent the inertia properties of a body segment based on the considerations in Sec. 4.3. The class allows for the application of the different inertia models, i.e. all introduced models (Winter, point mass and cylinder) are available and their usage is controlled via appropriate switches. The implementation makes use of the MOBILE-class `MoMassElement`, basically initializing the necessary quantities such as inertia tensor, segment mass and location of application with respect to the particular model.

4.4.2 Segment modeling

The necessary dissection of the human leg into discrete units was performed according to the intuitive demarcation given by the skeletal structure. Hence, in terms of an object-oriented approach, the essential properties of the locomotor system are condensed in two elementary object types: segments and joints. While the latter exclusively approximate the kinematic behavior of the biological system, the first are also holding information about the respective kinetics.

The class BodySegment

Each segment is instantiated as an object of class `BodySegment` which itself is derived from the class `MoMap` as described in Chap. 3. As illustrated in Fig. 4.9(c) on the example of a right thigh, it is characterized by three spatial state objects $\mathcal{K}_{\text{prox}}^{(\cdots)}$, $\mathcal{K}_{\text{dist}}^{(\cdots)}$ and $\mathcal{K}_{\text{COM}}^{(\cdots)}$, which represent the state of the proximal segment end, the distal segment end, and the spatial state of the segments center of mass, respectively. These frames are instantiated as objects of type `MoFrame` supplied by the MOBILE library. The superscript $''(\cdots)''$ represents the segment affiliation (Pelvis, Thigh, Shank or Foot). Proximal and distal frame act as input and output frame for a rigid link representing the osseous segment part. In addition, the segmental inertia properties are represented by an object of type `MassProperty` which is described in Sec. 4.4.1.

To initialize the segment object, according to Sec. 3.1.2 the involved frames require knowledge of the corresponding translation $\mathbf{r}$ and orientation $\mathbf{R}$ (see Fig. 3.2). Since objects of class `BodySegment` facilitate both inverse and direct dynamics simulation, the initialization steps are different. While in case of forward dynamics computations, only an initial state needs to be supplied (see Chap. 6), in case of inverse dynamics, also information about segment kinematics during a complete gait cycle needs to be known. In the current context, this information is extracted from the kinematic data held by the GCD file and based on the kinematic models described in Sec. 4.1.3. The kinematic data extraction procedure is described in Sec. 5.1.1.

For all segments, proximal and distal frame are assumed to be located in the respective joint center, leading to a simplified kinematical representation of the involved joints (see Sec. 4.4.3). The segment length $\ell_{(\cdots)}$ corresponds to the length of the vector from proximal to distal joint center according to (4.1.26). Here, the pelvis segment represents a special case since for left and right side two separate objects are instantiated.

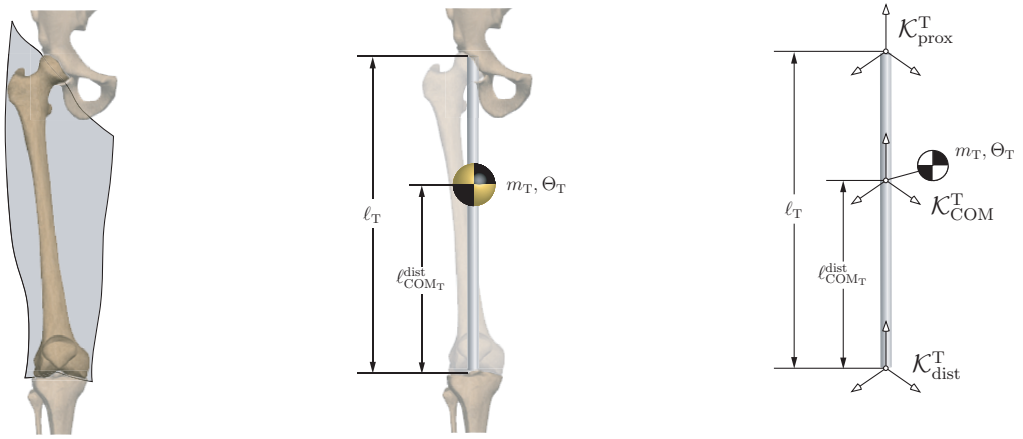

(a) Biological composition of subsystem "thigh"

(b) Idealization of subsystem "thigh"

(c) Iconic model of subsystem "thigh"

Figure 4.9: Illustration of abstraction for modeling body segments on the example of a right thigh

The orientation of the proximal segment frames is set equal to the transformation matrices identified for the segment fixed frames given in (4.1.25). The rigidity assumption excludes a relative orientation between proximal and distal segment frame, redounding to

$$\mathbf{R}^{(\cdots)}_{\text{prox}} \equiv \mathbf{R}^{(\cdots)}_{\text{dist}} \ . \tag{4.4.1}$$

In inverse dynamics applications, all other kinematic quantities representing the spatial state are supplied by the postprocessed kinematic GCD-file contents (see Sec. 5.1.1). In contrast, for forward dynamics computations, these quantities are computed during the numerical integration using the motion transmission functions principally described in Sec. 3.1.1.

Hence, objects of type `BodySegment` serve as containers for ″sub-objects″ featuring the intuitive segment properties such as proximal and distal segment end, osseous part, mass properties and time history of location and orientation in case of inverse dynamics simulations.

4.4.3 Joint modeling

As explained in Sec. 2.1, the kinematic functionality of especially knee and ankle joint is complex. In the scope of this thesis, simplified joint structures were chosen which

are briefly described in the following Sections. However, the object oriented implementation and the clearly defined interface between segments and joints allows for a quick replacement of particular objects without code modifications in the remaining parts.

Prescription of pelvis position and orientation: free-body joint

The location and orientation of the pelvis with respect to the inertially fixed frame is described by a 6-DOF kinetostatic transmission element of class `FreeBodyJoint`. It combines three prismatic and three revolute joints of type `MoElementaryJoint` prescribing the location of the pelvis reference frame origin and orientation with respect to the inertial frame using a Bryant-angle representation. The arrangement of the revolute joints is chosen such that their axes intersect in a single point, yielding a ball-and-socket joint.

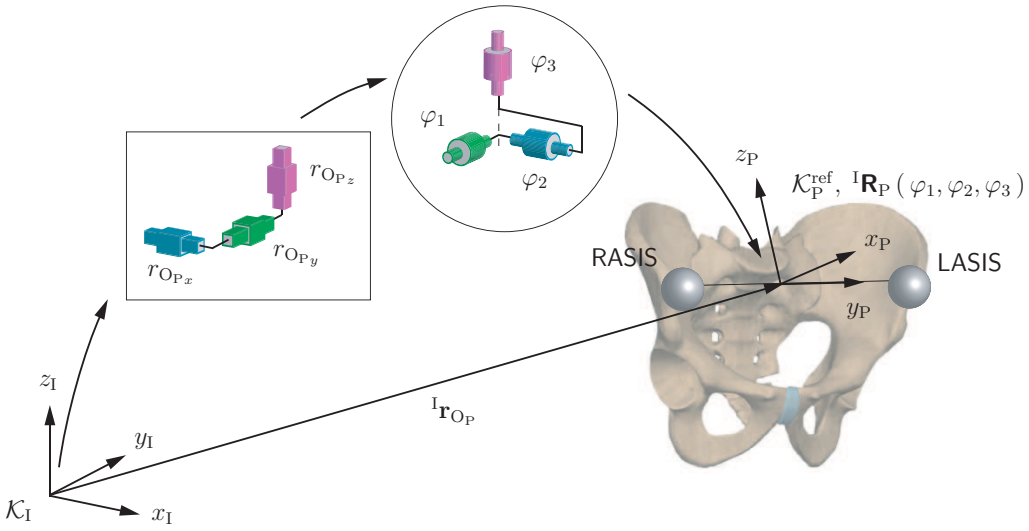

Figure 4.10: Free-body joint model for pelvis motion simulation

The principle is depicted in Fig. 4.10. The translational coordinates $r_{\mathrm{O_P}x}, r_{\mathrm{O_P}y}$ and $r_{\mathrm{O_P}z}$ are directly extracted from the origin vector ${}^{\mathrm{I}}\mathbf{r}_{\mathrm{O_P}}$ (for definition, see Sec. 4.1.3), the angles φ_1, φ_2 and φ_3 representing the orientation are computed according to the details in Sec. 5.1.2.

Inter-segmental joints: Hip joint, knee joint, ankle joint

Hip joint, knee joint and ankle joint are all idealized as ball-and-socket joints. While this appears reasonable in case of the hip, for knee and ankle severe simplifications have to be accepted, e.g. particular kinematic characteristics (pronation/supination at the foot or a moving *axis transversalis* at the knee during flexion/extension) are neglected. Although in both cases sophisticated modeling approaches exist (for knee joint models see [Wismans et al., 1980], [Yamaguchi and Zajac, 1989], [Blankevoort et al., 1991] and [Shelburne and Pandy, 1997]; examples for ankle joint modeling can be found in [Leardini et al., 1999a], [Leardini et al., 1999b] and [Dettwyler et al., 2004]), their applicability is limited, since all models either dependent on the knowledge of subject-specific bone geometries or are based on geometric assumptions from (small) control group measurements. While the first are usually not accessible in detail by a standard gait laboratory measurement, for the latter results after scaling to subject-specific dimensions are to be assessed carefully.

In terms of an object oriented implementation, the ball-and-socket joint corresponds to the revolute joints part in the free-body joint described above.

While for inverse dynamics applications a purely kinematic joint model is sufficient, forward dynamics simulations require the definition of additional force transmission terms to be added to the model to realize the joint angle restrictions defined in Tab. 2.2, Tab. 2.3 and Tab. 2.4.

Hence, as proposed for example in publications of Anderson and Pandy, virtual torsional springs serve as auxiliary arresters, generating a resisting torque t_{res} about a joint axis as a function of the corresponding joint angle according to

$$t_{\mathrm{res}} = k_1 \exp\left[-w_\ell \left(\varphi - \underline{\varphi}\right)\right] - k_2 \exp\left[-w_u \left(\overline{\varphi} - \varphi\right)\right] \tag{4.4.2}$$

([Anderson and Pandy, 1999a], [Anderson and Pandy, 2001]). Here, w_ℓ, w_u and φ denote appropriate dimensionless weighting factors and the current joint angle in radians, respectively. The coefficients $k_1, k_2 > 0$ possess the unit Nm and serve as shaping parameters. Furthermore,

$$\underline{\varphi} = \varphi^- + \Delta\varphi, \qquad \overline{\varphi} = \varphi^+ - \Delta\varphi \tag{4.4.3}$$

represent the biological joint range limits φ^+, φ^- in positive and negative direction in radians, linearly combined with an angle offset $\Delta\varphi$ which serves as a shaping parameter for the resulting torque curve. While the biological joint limits can be read off from

Tab. 2.2, Tab. 2.3 and Tab. 2.4, the offset $\Delta\varphi$ is to be supplied arbitrarily by the user. In the current context, $\Delta\varphi = 0.0873$ rad ($\equiv 5°$) was chosen.

4.5 Kinetostatic transmission chain of the lower extremity

The main characteristic of the developed library is that it is implemented as a construction kit for the setup of a complete leg model. This construction kit consists of the concatenation of instances of the available classes, leading to an alternating sequence of segment and joint objects. Its basic structure is depicted in Fig. 4.11.

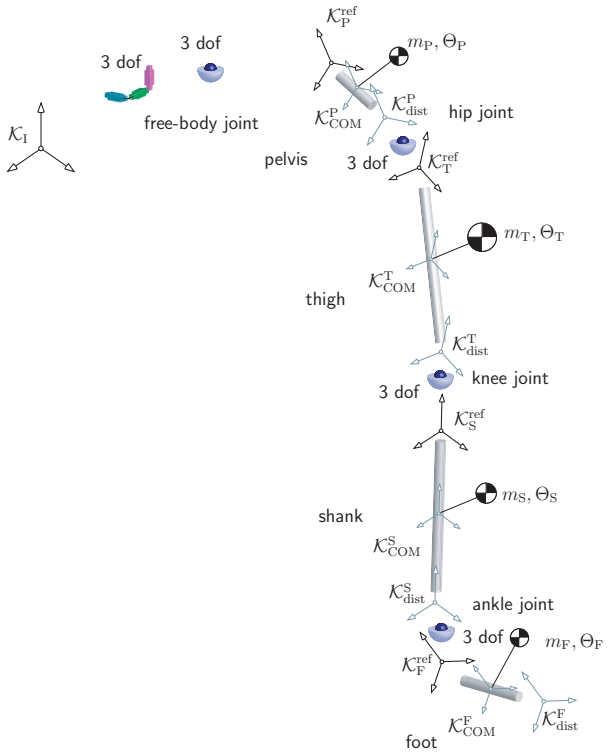

Figure 4.11: Dissection and model illustration for human lower extremity

There, the inertial frame and all proximal segmental frames (displayed in black) are measured in position and orientation. In contrast, orientation and location of the distal segment frames as well as the locations of the centers of mass for each segment

property/feature	***SIMM***	***AnyBody***	**M□BILE**
programming language	C	AnyScript	C++
object-oriented structure	no	yes	yes
generation of eq. of motion	KANE	NEWTON/EULER	kinetostatics
repres. of eq. of motion	minimal form	CARTESIAN	minimal form
forward dynamics simulation	yes	no	yes
dynamic opt. embedded	no	no	yes
symbolic models	yes	no	yes

Table 4.3: Comparison of a selection of features supplied by commercial software packages *SIMM* and *AnyBody* to features supplied by the presented framework (not exhaustive)

(displayed in grey) are computed from the measured data and by model assumptions, respectively. Proximal and distal segment frames represent the interfaces to the intersegmental joints, i.e. except for the foot segment the distal segment frame serves as input frame for the following joint while the proximal segment frame corresponds to the output frame of the preceeding joint. In total, the model consists of four segment objects and four joint objects featuring 15 degrees of freedom.

The open architecture benefits are (1) model manageability, (2) an easily improvable model depth and (3) the extensibility of model broadness. If desired, any functional unit (e.g. a certain joint model) can be replaced by a model of arbitrary complexity without the necessity to modify other model parts or code. It would be even possible to replace complete substructures of the leg chain such as the shank by appropriate mechatronic prosthesis including the necessary controls without influencing existing model sections. In comparison to the commercial frameworks already presented in Sec. 1.3, the proposed library combines the advantage of an open-architecture design with those of improved numerical methodologies such as the representation of the equations of motion in minimal form (Tab. 4.3). In addition, the present approach features features full applicability in inverse and forward dynamics contexts and therefore represents a basis to target any of the typical gait dynamics problems illustrated in Fig. 1.2. As mentioned in the introduction, in the sequel three of these subproblems will be investigated by application of the developed library to illustrate its usefulness.

Chapter 5

Reproduction of the inverse dynamics of human of gait

The inverse dynamics of human gait can be expressed by the equations of motion of a mechanical system with $f \in \mathbb{N}$ degrees of freedom in minimal form

$$M\left(\underline{q};\, t\right)\, \underline{\ddot{q}} + \underline{b}\left(\underline{q},\, \underline{\dot{q}};\, t\right) = \underline{Q}\left(\underline{q},\, \underline{\dot{q}};\, t\right)\ , \tag{5.0.1}$$

where $\underline{q} \in \mathbb{R}^{f\times 1}$ denote the generalized coordinates and with

$$\begin{array}{lcl} M\left(\underline{q};\, t\right) \in \mathbb{R}^{f\times f} & \hat{=} & \text{generalized mass matrix,} \\ \underline{b}\left(\underline{q},\, \underline{\dot{q}};\, t\right) \in \mathbb{R}^{f\times 1} & \hat{=} & \text{generalized Coriolis, centrifugal} \\ & & \text{and gyroscopic forces,} \\ \underline{Q}\left(\underline{q},\, \underline{\dot{q}};\, t\right) \in \mathbb{R}^{f\times 1} & \hat{=} & \text{generalized applied forces .} \end{array} \tag{5.0.2}$$

Hereby, the generalized applied forces in (5.0.2) can be expressed as

$$\underline{Q}\left(\underline{q},\, \underline{\dot{q}};\, t\right) = \underline{Q}_{\mathrm{c}}\left(\underline{q},\, \underline{\dot{q}};\, t\right) + \underline{Q}_{\mathrm{g}}\left(\underline{q},\, \underline{\dot{q}};\, t\right) + \underline{Q}_{\mathrm{j}}\left(\underline{q},\, \underline{\dot{q}};\, t\right)\ , \tag{5.0.3}$$

where the indices c, g and j on the right hand side of (5.0.3) denote the forces resulting frome contacts, gravity and internal joint moments, respectively.

The goal of inverse dynamics simulations is to determine the generalized forces applied to the involved joints that cause the system under investigation to behave as observed in terms of the (known) generalized coordinate time history. In mathematical terms, using (5.0.3) this corresponds to a resolution of (5.0.1) for $\underline{Q}_{\mathrm{j}}\left(\underline{q},\, \underline{\dot{q}};\, t\right)$, i. e.

$$\underline{Q}_{\mathrm{j}}\left(\underline{q},\, \underline{\dot{q}};\, t\right) = M\left(\underline{q};\, t\right)\, \underline{\ddot{q}} + \underline{b}\left(\underline{q},\, \underline{\dot{q}};\, t\right) - \underline{Q}_{\mathrm{c}}\left(\underline{q},\, \underline{\dot{q}};\, t\right) - \underline{Q}_{\mathrm{g}}\left(\underline{q},\, \underline{\dot{q}};\, t\right)\ . \tag{5.0.4}$$

To this end, the following quantities are needed:

(a) the time history of the generalized coordinates $\underline{q}$ and their corresponding time derivatives $\underline{\dot{q}}$ and $\underline{\ddot{q}}$,

(b) physical properties of the involved bodies and joints (e.g. dimensions),

(c) inertia properties of all involved substructures (i.e. appropriate mass models),

(d) the contributions of generalized gravitational $\underline{Q}_{\mathrm{g}}\left(\underline{q},\, \underline{\dot{q}};\, t\right)$ and generalized contact forces $\underline{Q}_{\mathrm{c}}\left(\underline{q},\, \underline{\dot{q}};\, t\right)$ to the generalized applied forces $\underline{Q}\left(\underline{q},\, \underline{\dot{q}};\, t\right)$.

Note, that in the given context, $\underline{Q}_{\mathrm{c}}\left(\underline{q},\, \underline{\dot{q}};\, t\right)$ corresponds to the measured time history of ground reaction forces (see Sec. 4.2.1). Unmeasurable contributions such as the influence of aerodynamic friction are neglected.

5.1 Inverse dynamics input data

5.1.1 Kinematic input

According to the mentioned requirements, time histories of the involved generalized coordinates have to be determined from the measured data supplied by the GCD file. Resulting from the multibody model described in Chap. 4, for each leg the 15 generalized coordinates are

(1) position and orientation of the pelvis reference frame $\mathcal{K}_{\mathrm{P}}^{\mathrm{ref}}$ (variables of free-body joint, see Sec. 4.4.3) ,

(2) inter-segmental angles (variables of hip, knee and ankle joint model, see Sec. 4.4.3) .

The determination process is subdivided into two basic steps:

(1) the computation of the time histories of the generalized coordinates from the rotation matrices stored in the GCD data set

(2) the numerical derivation of the variable histories to compute the angle rates and the angular accelerations.

While the first appears relatively straightforward, in the latter case measurement noise (which corresponds to a high frequency data contingent) can lead to useless results in the differentiation process. To reduce this effect, the raw data computed in step (1) is filtered prior to the differentiation.

5.1.2 Generalized coordinates time history

To describe position and orientation of each segment of a lower extremity, as described in Sec. 4.1.4, the GCD data set supplies transformation matrices (4.1.25) and radius vectors (4.1.26). While the translational variables of the free-body joint are directly given in terms of the radius vector ${}^{\mathrm{I}}\mathbf{r}_{\mathrm{O_P}}$ of the pelvis reference frame, the joint variables describing pelvis orientation, hip, knee and ankle angles have to be computed indirectly. According to (4.1.28), the relative orientation of two neighbored segments can be computed. In the resulting transformation matrix describes the relative orientation of the distal segment (*input*) frame of the proximal segment with respect to the proximal (*output*) frame of the distal segment. It can be interpreted as the result of a sequence of elementary rotations about the axes of the input frame of the corresponding joint. In the given context, the rotations are parameterized in Bryant angles in the commonly used order of rotations in biomechanics (flexion/extension — adduction/abduction — internal/external rotation), i.e.

$$\mathcal{K}_{\mathrm{in}} \xrightarrow[\text{of } \mathcal{K}_{\mathrm{in}} \text{ about } \varphi_1]{\text{rotation about } y\text{−axis}} \mathcal{K}' \xrightarrow[\text{of } \mathcal{K}' \text{ about } \varphi_2]{\text{rotation about } x\text{−axis}} \mathcal{K}'' \xrightarrow[\text{of } \mathcal{K}'' \text{ about } \varphi_3]{\text{rotation about } z\text{−axis}} \mathcal{K}_{\mathrm{out}} \tag{5.1.1}$$

Using (1.4.4)–(1.4.6), the relative transformation matrix ${}^{\mathrm{out}}\mathbf{R}_{\mathrm{in}}$ is considered as

$$\begin{aligned}
{}^{\mathrm{out}}\mathbf{R}_{\mathrm{in}} &= \mathbf{R}_{y_{\mathrm{in}}}(\varphi_1)\,\mathbf{R}_{x'}(\varphi_2)\,\mathbf{R}_{z''}(\varphi_3) && (5.1.2)\\
&= \begin{bmatrix} \cos\varphi_1 & 0 & \sin\varphi_1 \\ 0 & 1 & 0 \\ -\sin\varphi_1 & 0 & \cos\varphi_1 \end{bmatrix} \cdot \begin{bmatrix} 1 & 0 & 0 \\ 0 & \cos\varphi_2 & -\sin\varphi_2 \\ 0 & \sin\varphi_2 & \cos\varphi_2 \end{bmatrix} \cdot && (5.1.3)\\
&\quad \cdot \begin{bmatrix} \cos\varphi_3 & -\sin\varphi_3 & 0 \\ \sin\varphi_3 & \cos\varphi_3 & 0 \\ 0 & 0 & 1 \end{bmatrix} && (5.1.4)\\
&= \begin{bmatrix} \varrho_{11} & \varrho_{12} & \varrho_{13} \\ \varrho_{21} & \varrho_{22} & \varrho_{23} \\ \varrho_{31} & \varrho_{32} & \varrho_{33} \end{bmatrix} && (5.1.5)
\end{aligned}$$

with

$$\begin{aligned}
\varrho_{11} &= \cos\varphi_1\cos\varphi_3 + \sin\varphi_1\sin\varphi_2\sin\varphi_3 \ , \\
\varrho_{12} &= \cos\varphi_3\sin\varphi_1\sin\varphi_2 - \cos\varphi_1\sin\varphi_3 \ , \\
\varrho_{13} &= \cos\varphi_2\sin\varphi_1 \ , \\
\varrho_{21} &= \cos\varphi_2\sin\varphi_3 \ , \\
\varrho_{22} &= \cos\varphi_2\cos\varphi_3 \ , \\
\varrho_{23} &= -\sin\varphi_2 \ , \\
\varrho_{31} &= \cos\varphi_1\sin\varphi_2\sin\varphi_3 - \cos\varphi_3\sin\varphi_1 \ , \\
\varrho_{32} &= \cos\varphi_1\cos\varphi_3\sin\varphi_2 + \sin\varphi_1\sin\varphi_3 \ , \\
\varrho_{33} &= \cos\varphi_1\cos\varphi_2 \ .
\end{aligned} \tag{5.1.6}$$

Using

$$\operatorname{atan2}(x,y) = \begin{cases}
\arctan\left(\dfrac{y}{x}\right) & \text{for} \quad x > 0 \\
\arctan\left(\dfrac{y}{x}\right) + \pi & \text{for} \quad x < 0 \text{ and } y \geq 0 \\
\arctan\left(\dfrac{y}{x}\right) - \pi & \text{for} \quad x < 0 \text{ and } y < 0 \\
+\dfrac{\pi}{2} & \text{for} \quad x = 0 \text{ and } y > 0 \\
-\dfrac{\pi}{2} & \text{for} \quad x = 0 \text{ and } y < 0 \\
0 & \text{for} \quad x = 0 \text{ and } y = 0
\end{cases} \ , \tag{5.1.7}$$

yields for the unknown angles φ_1, φ_2 and φ_3

$$\begin{aligned}
\varphi_1 &= \operatorname{atan2}\left(\frac{\varrho_{13}}{\cos\varphi_2}, \ \frac{\varrho_{33}}{\cos\varphi_2}\right) \ , \\
\varphi_2 &= \arcsin\left(-\varrho_{23}\right) \ , \\
\varphi_3 &= \operatorname{atan2}\left(\frac{\varrho_{21}}{\cos\varphi_2}, \ \frac{\varrho_{22}}{\cos\varphi_2}\right) \ .
\end{aligned} \tag{5.1.8}$$

The alternative possible solution $\varphi_2 = \pi - \arcsin\left(-\varrho_{23}\right)$ corresponds to unnaturally large abduction/adduction angles and is neglected. Furthermore, in practice, abduction/adduction angles of $\pm 90°$ cannot appear (see Tab. 2.2, Tab. 2.3 and Tab. 2.4) such that no numerical problems have to be expected due to the evaluation of (5.1.7). Here, φ_1, φ_2 and φ_3 in (5.1.8) correspond to the flexion/extension, adduction/abduction and internal/external rotation, respectively. As described in Sec. 5.1.2, these values are used correspondingly in the joint models introduced in Sec. 4.4.3.

As a result, values for all generalized coordinates are available for the normed time scale prescribed by the GCD data file, i.e. there exist 51 values for each joint coordinate holding the time history of each variable for a complete gait cycle.

5.1.3 Interpolation of generalized coordinates

The previously described quantities are extracted directly from the standard data of a normed gait cycle. Thus, in order to realize different time scales in motion reproduction and enable investigation of events outside the standard scheme, the angles determined by the methods described in Sec. 5.1.2 are interpolated linearly at arbitrary positions between two measured time instants.

To that end, a relative rotation matrix (decomposed in an inertially fixed frame $\mathcal{K}_\mathrm{I}$)

$$\Delta\mathbf{R}_i = \left({}^{\mathrm{I}}\mathbf{R}_{i-1}\right)^{\mathrm{T}}\ {}^{\mathrm{I}}\mathbf{R}_i = \begin{bmatrix} \varrho_{11} & \varrho_{12} & \varrho_{13} \\ \varrho_{21} & \varrho_{22} & \varrho_{23} \\ \varrho_{31} & \varrho_{32} & \varrho_{33} \end{bmatrix} \tag{5.1.9}$$

representing the change in orientation of a frame between time instants $i-1$ and i, $i \in \{1, \ldots, 51\}$ is interpreted in terms of rotation vector parameterization.

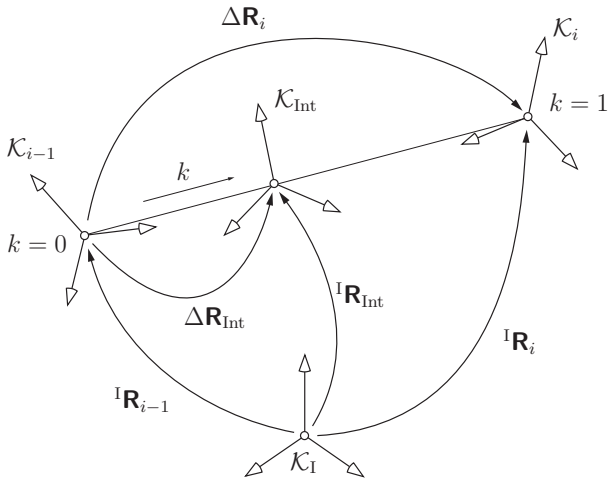

Figure 5.1: Interpolation of rotation matrices

Hence, the resulting rotation angle φ and the corresponding rotation axis $\underline{u}$ ($\|\underline{u}\| = 1$) can be computed as

$$\varphi = \arccos\left(\frac{\varrho_{11} + \varrho_{22} + \varrho_{33} - 1}{2}\right), \tag{5.1.10}$$

and

$$\underline{u} = \begin{cases} \varphi = 0 & : \text{ arbitrary with } \|\underline{u}\| = 1 \\ \varphi = \pi & : \begin{cases} \varrho_{11} > \varrho_{22}, \varrho_{33} & \begin{cases} u_x = \sqrt{\dfrac{\varrho_{11}+1}{2}} \\ u_y = \dfrac{\varrho_{12}+\varrho_{21}}{4u_x} \\ u_z = \dfrac{\varrho_{13}+\varrho_{31}}{4u_x} \end{cases} \\ \varrho_{22} > \varrho_{11}, \varrho_{33} & \begin{cases} u_x = \dfrac{\varrho_{12}+\varrho_{21}}{4u_y} \\ u_y = \sqrt{\dfrac{\varrho_{22}+1}{2}} \\ u_z = \dfrac{\varrho_{23}+\varrho_{32}}{4u_y} \end{cases} \\ \varrho_{33} > \varrho_{11}, \varrho_{22} & \begin{cases} u_x = \dfrac{\varrho_{13}+\varrho_{31}}{4u_z} \\ u_y = \dfrac{\varrho_{23}+\varrho_{32}}{4u_z} \\ u_z = \sqrt{\dfrac{\varrho_{33}+1}{2}} \end{cases} \end{cases} \\ \varphi \in \mathbb{R} \setminus \{0, \pi\} & : \dfrac{1}{\sin\varphi} \begin{bmatrix} \varrho_{32} - \varrho_{23} \\ \varrho_{13} - \varrho_{31} \\ \varrho_{21} - \varrho_{12} \end{bmatrix} \end{cases} \tag{5.1.11}$$

Considering the situation depicted in Fig. 5.1, the rotation axis according to (5.1.11) remains constant for the transition from $\mathcal{K}_{i-1}$ to $\mathcal{K}_i$. To compute an intermediate orientation, i.e. to determine the rotation matrix $\Delta\mathbf{R}_{\text{Int}}$, the corresponding intermediate angle $\Delta\varphi$ is interpolated linearly between 0 and 1, i.e.

$$\Delta\varphi = k\varphi, \qquad k \in [\,0, 1\,]\ . \tag{5.1.12}$$

Thus, the sought rotation matrix appears as a function of the interpolation angle

(5.1.12) (or the interpolation parameter k, respectively) and results to

$$\begin{aligned}\Delta\mathbf{R}_{\mathrm{Int}}(\Delta\varphi) &= \Delta\mathbf{R}_{\mathrm{Int}}(k\varphi)\\ &= \begin{bmatrix}1&0&0\\0&1&0\\0&0&1\end{bmatrix}\cos(\Delta\varphi)+\begin{bmatrix}0&-u_z&u_y\\u_z&0&-u_x\\-u_y&u_x&0\end{bmatrix}\sin(\Delta\varphi)+\\ &\quad+\begin{bmatrix}u_xu_x&u_xu_y&u_xu_z\\u_yu_x&u_yu_y&u_yu_z\\u_zu_x&u_zu_y&u_zu_z\end{bmatrix}(1-\cos(\Delta\varphi))\ .\end{aligned}\tag{5.1.13}$$

Since $\Delta\mathbf{R}_{\mathrm{Int}} = \left({}^{\mathrm{I}}\mathbf{R}_{i-1}\right)^{\mathrm{T}}\,{}^{\mathrm{I}}\mathbf{R}_{\mathrm{Int}}$, to describe the orientation of the interpolated frame $\mathcal{K}_{\mathrm{Int}}$ with respect to the inertial frame one obtains

$${}^{\mathrm{I}}\mathbf{R}_{\mathrm{int}} = {}^{\mathrm{I}}\mathbf{R}_{i-1}\Delta\mathbf{R}_{\mathrm{Int}}\ .\tag{5.1.14}$$

The transformation to the joint coordinates of the involved joints is then performed according to (5.1.2)–(5.1.8).

The location of the corresponding frame origin is interpolated similarly by using the same interpolation parameter k and setting

$${}^{(\cdots)}\mathbf{r}_{\mathrm{Int}} = {}^{(\cdots)}\mathbf{r}_{i-1} + k\left({}^{(\cdots)}\mathbf{r}_i - {}^{(\cdots)}\mathbf{r}_{i-1}\right)\tag{5.1.15}$$

where the superscript "$(\cdots)$" denotes the decomposition frame.

5.1.4 Derivatives of generalized coordinates

To be able to evaluate (5.0.4), first and second time derivatives have to be computed from the data obtained according to Sec. 5.1.2 and/or Sec. 5.1.3 for each involved generalized coordinate. These quantities are generally not included in a standard gait laboratory measurement output file and are determined numerically. To minimize the influence of measurement noise especially in the second time derivatives, the generalized coordinate values resulting from the computations described above are filtered.

Digital filtering of joint coordinate time histories

Since at the time of filtering all data is available, one can perform offline filtering. Thus, the application of digital filters suitable for the filtering of series of time-discrete signals was chosen.

The filtering process for linear and time invariant filters itself basically consists of mapping an input data set $\{ u \} = \{ u_1, u_2, u_3, \dots u_n \}$ to an output data set $\{ y \} = \{ y_1, y_2, y_3, \dots y_n \}$ via evaluation of suitable recurrence relations. Hereby the output signals in time domain are computed as a weighted sum of the available values,

$$y_k = b_n u_k + b_{n-1} u_{k-1} + \cdots + b_0 u_{k-n} - a_{n-1} y_{k-1} - \cdots - a_0 y_{k-n} \tag{5.1.16}$$

where $a_0, \dots, a_{n-1}$ and $b_0, \dots, b_n$ represent weights chosen according to the problem-specific demand for input and output series elements, respectively. Furthermore, $u_k = u(t_k) = u(kT)$ is assumed to be a measured signal for a time interval T.

The design of a filter is performed in the frequency domain after transformation via Z-transform $\mathcal{Z}\{ \cdot \}$. The corresponding Z-transfer function in the frequency domain

$$H(z) := \frac{\mathcal{Z}\{ y \}}{\mathcal{Z}\{ u \}} \tag{5.1.17}$$

$$= \frac{b_n z^n + b_{n-1} z^{n-1} + \cdots + b_1 z + b_0}{a_n z^n + a_{n-1} z^{n-1} + \cdots + a_1 z + a_0} \tag{5.1.18}$$

reflects the coefficients from (5.1.16) in the representation given in (5.1.18).

For this thesis, several digital filters have been implemented which are not all described in detail. The chosen design is exemplarily given for a low-pass Butterworth filter of order two. Hence, the difference equation (5.1.16) simplifies to

$$y_k = b_2 u_k + b_1 u_{k-1} + b_0 u_{k-2} - a_1 y_{k-1} - a_0 y_{k-2} \tag{5.1.19}$$

and the coefficients are chosen as

$$\begin{aligned}
b_0 &= \frac{\omega_c^2}{1 + \sqrt{2}\omega_c + \omega_c^2} , \\
b_1 &= \frac{2\omega_c^2}{1 + \sqrt{2}\omega_c + \omega_c^2} , \\
b_2 &= \frac{\omega_c^2}{1 + \sqrt{2}\omega_c + \omega_c^2} , \\
a_0 &= \frac{2\omega_c^2}{1 + \sqrt{2}\omega_c + \omega_c^2} \left(1 - \frac{1}{\omega_c^2} \right) , \\
a_1 &= \frac{2\omega_c^2}{1 + \sqrt{2}\omega_c + \omega_c^2} \left(1 + \frac{1}{\omega_c^2} \right) - 1 ,
\end{aligned} \tag{5.1.20}$$

where

$$\omega_c = \tan\left(\frac{\pi f_c}{f_s}\right) \tag{5.1.21}$$

with the *cut-off frequency* f_c and the sampling frequency f_s.

To avoid difficulties for $k \leq 2$ according to the representation (5.1.19), and to compensate a phase shift in the output signal and in the implementation, two actions are taken:

(1) The sequence input data is repeated sequentially three times. Hence, for the target data

$$\{\ q_0, q_1, \ldots, q_{50}\ \},$$

the data passed to the filter is

$$\{\ q_0, q_1, \ldots, q_{50}, q_0, q_1, \ldots, q_{50}, q_0, q_1, \ldots, q_{50}\ \}.$$

Thus, the data of interest is located in the middle of the sequence to filter, assuming a cyclic transition between start and end values of the measurement. A benefit of the applied method is that the overshoot in the beginning is compensated when reaching the "relevant" pieces of data. The sampling frequency f_c was chosen as 8 Hz in the implementation.

(2) The output resulting from the filtering process is then filtered a second time in reverse order, canceling the phase shift from the first run and representing a filtering result corresponding to a filter of order four. Hence, a stronger elimination of high frequency signals is achieved above cut-off frequency f_c in combination with a lesser damping below. Fig. 5.2 illustrates the difference between a one-pass and a two-pass filtering process.

Details for the design of digital Butterworth filters can be found in [Schweiger, 1983].

Numerical time derivatives

Based on the knowledge of a (filtered) joint-coordinate sequence

$$\{\ q\ \} = \{\ q_0, q_1, \ldots, q_{50}\ \} \tag{5.1.22}$$

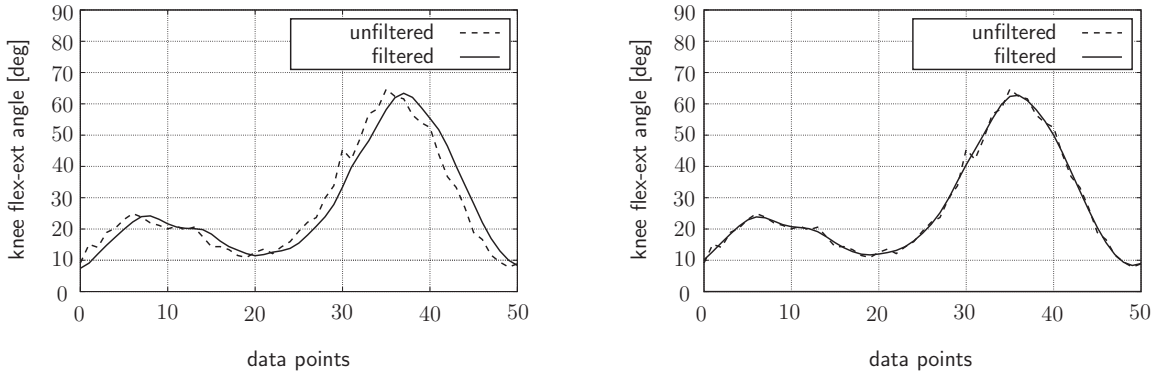

(a) One-pass Butterworth filter

(b) Two-pass Butterworth filter

Figure 5.2: Butterworth filter: phase shift elimination by two-pass filter on the example of knee flexion-extension angle data

and the associated intermediate time step T, the corresponding time derivatives are computed numerically using the following difference formulas:

$$\dot{q}_i = \begin{cases} \dfrac{-3q_0 + 4q_1 - q_2}{2T} & \text{for} \quad i = 0 \ , \\ \dfrac{-q_{i-1} + q_{i+1}}{2T} & \text{for} \quad 0 < i < 50 \ , \\ \dfrac{q_{50} - 4q_{49} + 3q_{48}}{2T} & \text{for} \quad i = 50 \ . \end{cases} \tag{5.1.23}$$

Each second time derivate is computed similarly by repeated application of (5.1.23).

5.2 Motion tracking error treatment

5.2.1 Problem description

The motion-capturing process described above is based on generic assumptions to estimate joint center positions from the record of marker motion. Typically, several factors can handicap this estimation process and lead to systematic errors. The errors result from

- wrong generic assumptions,
- marker placement inaccuracy,

- relative motion between skin and bones (skin artefacts),
- measurement noise.

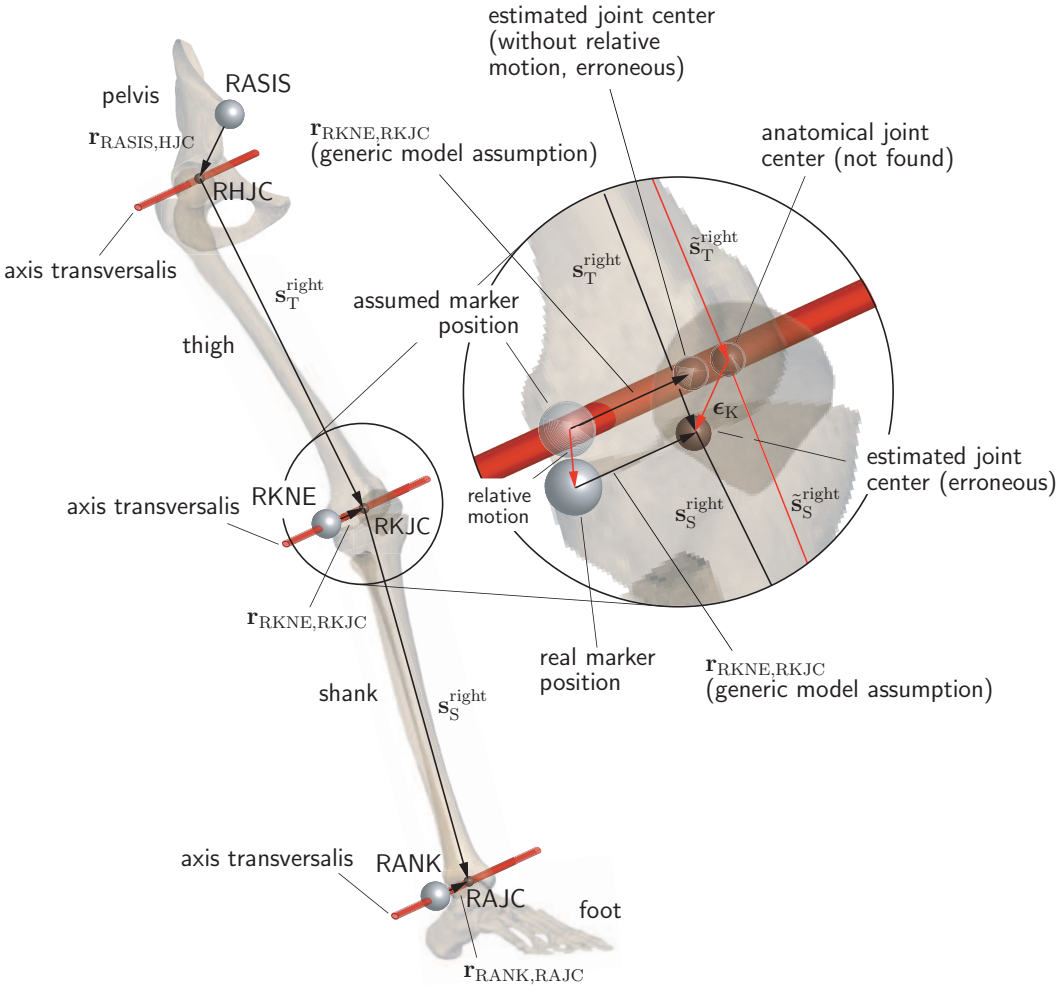

Figure 5.3: Principal illustration of segment vector errors generic model assumptions. Essential involved symbols are explained in Tab. 5.1, picture adapted from [Sobotta, 2005]

In Fig. 5.3, the problem is visualized for the example of a right knee. From a macroscopic point of view, based on a known position of the involved markers (exemplarily visualized is RKNE) the location of the corresponding right knee joint center (RKJC) is computed based on generic model assumptions and specimen-specific measurements. Hereby, a deviation between the real location of the RKJC and the assumed position occurs.

symbol	explanation
$\mathbf{r}_{\mathrm{RASIS,RHJC}}$	vector describing the location of RHJC with respect to RASIS
$\mathbf{r}_{\mathrm{RKNE,RKJC}}$	vector describing the location of RKJC with respect to RKNE
$\mathbf{r}_{\mathrm{RANK,RAJC}}$	vector describing the location of RAJC with respect to RANK
$\mathbf{s}_{\mathrm{T}}^{\mathrm{right}}$	(erroneous) thigh segment vector according to model (difference vector between estimated RHJC and estimated RKJC)
$\mathbf{s}_{\mathrm{S}}^{\mathrm{right}}$	(erroneous) shank segment vector according to model (difference vector between estimated RKJC and estimated RAJC)
$\tilde{\mathbf{s}}_{\mathrm{T}}^{\mathrm{right}}$	correct thigh segment vector according to anatomy (difference vector between real RHJC and real RKJC)
$\tilde{\mathbf{s}}_{\mathrm{S}}^{\mathrm{right}}$	correct shank segment vector according to anatomy (difference vector between real RKJC and real RAJC)
$\boldsymbol{\epsilon}_{\mathrm{K}}$	unidentified difference vector from the assumed position of the RHJC to the real location of the RHJC

Table 5.1: Nomenclature in Fig. 5.3

This is illustrated for the example of motion tracking records for a male person of 1.35 m body height (data supplied by Department of Paediatric Surgery, Medical University Graz, Austria). Denoting the average segment vector for the segment "segm" given by the GCD set for 51 measurements as

$$\underline{\bar{\ell}}^{\,\mathrm{segm}} = \frac{1}{51}\sum_{i=0}^{50} \underline{\ell}_i^{\,\mathrm{segm}}, \tag{5.2.1}$$

the Euclidian norm of a segment vector reveals variations between $\pm 4\%$ in case of the thigh (right side thigh segment vector, Fig. 5.4(d)) and between $+2\%$ and -6% in case of the shank (left side shank segment vector, Fig. 5.4(e)).

For the pelvis segment, comparatively small variations in all components contribute to the behavior displayed in Fig. 5.4(a) and Fig. 5.4(b).

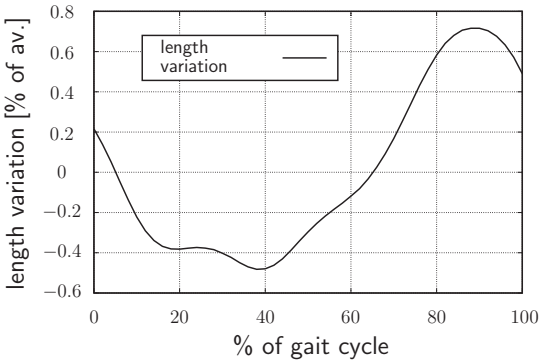

(a) Left pelvis bone length vector

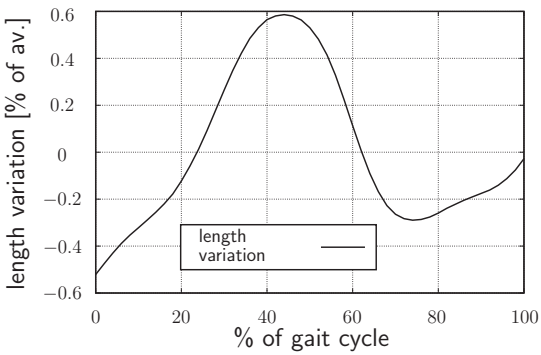

(b) Right pelvis bone length vector

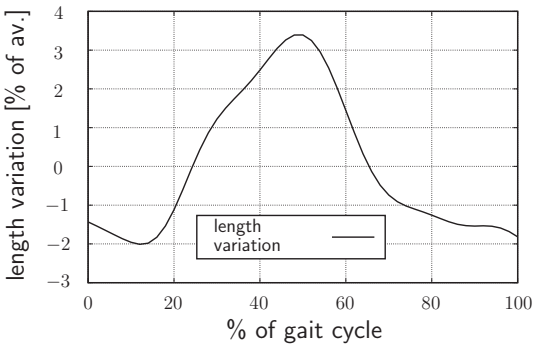

(c) Left thigh bone length vector

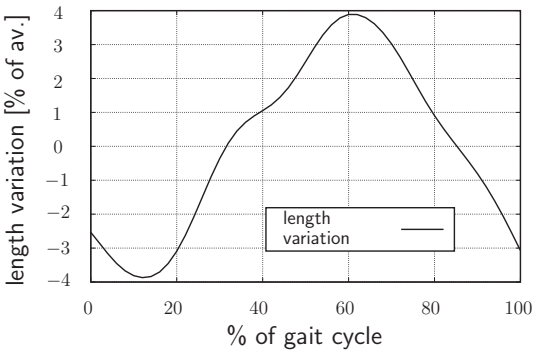

(d) Right thigh bone length vector

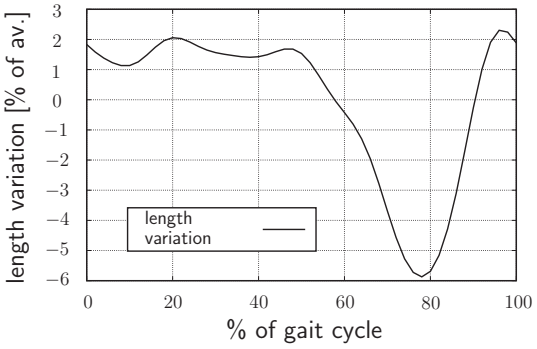

(e) Left shank bone length vector

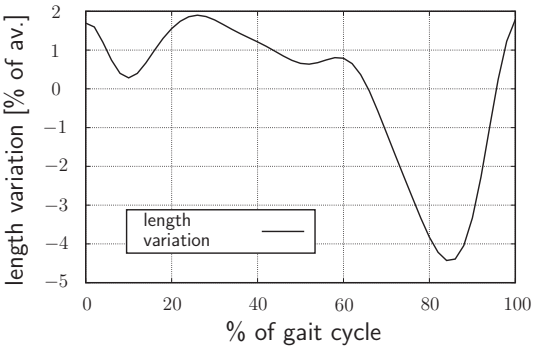

(f) Right shank bone length vector

Figure 5.4: Bone length variations in raw GCD data set with respect to average value (Euklidian norm)

5.2.2 Method: Biofidelic measurement data fitting approach

In order to reduce the influence of tracking errors, the offsets at hip, knee and ankle are determined more precisely by optimization. The offsets are denoted as vectors $\boldsymbol{\epsilon}_{\mathrm{H}}$, $\boldsymbol{\epsilon}_{\mathrm{K}}$ and $\boldsymbol{\epsilon}_{\mathrm{A}}$ in the following. The basic idea of the proposed procedure is illustrated in

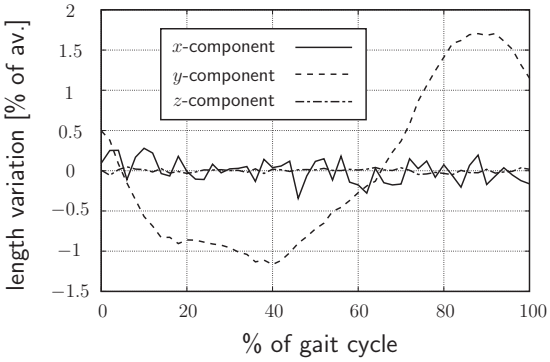

(a) Left pelvis bone vector components

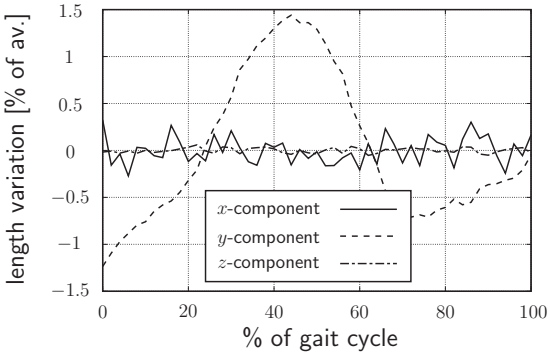

(b) Right pelvis bone vector components

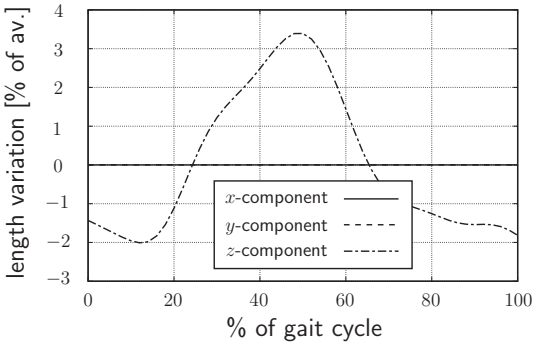

(c) Left thigh bone vector components

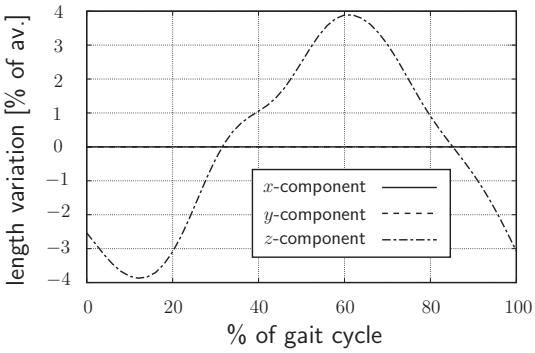

(d) Right thigh bone vector components

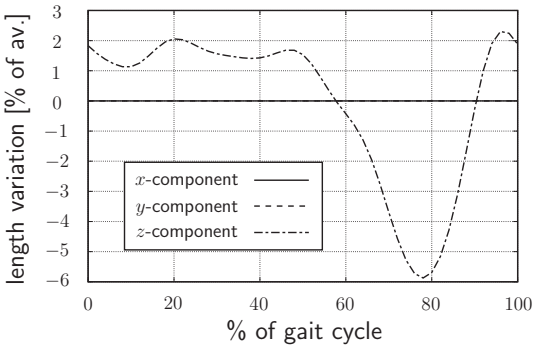

(e) Left shank bone vector components

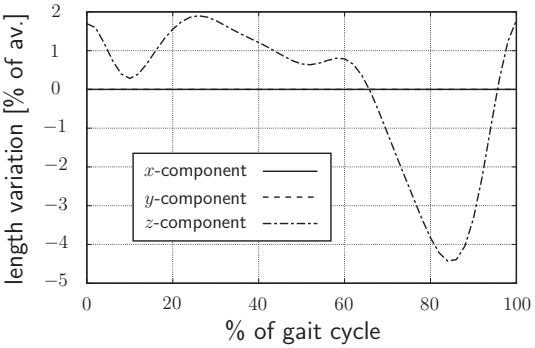

(f) Right shank bone vector components

Figure 5.5: Bone vector component variations in raw GCD data set with respect to average value, vector decomposition in segment fixed reference frame

Fig. 5.6 for the example of a right thigh segment.

Goal of the method is to determine the unknown segment vector $\underline{\tilde{s}}_{\mathrm{T}}$, the bone-fixed offset vector $\boldsymbol{\epsilon}_{\mathrm{K}}$ and the rotating vector ${}^{\mathrm{H}}\mathbf{R}_{\mathrm{T,i}}\boldsymbol{\epsilon}_{\mathrm{H}}$ such that these vectors and the measured segment vectors $\underline{s}_{\mathrm{T,i}}$ form a closed circle for each time instant.

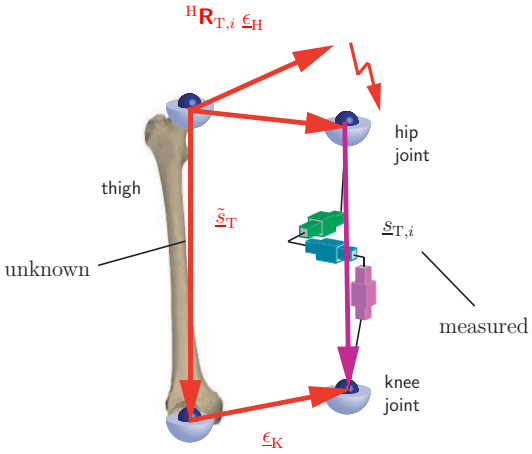

Figure 5.6: Basic principle of tracking error reduction

For the complete lower extremity, this principle is formulated in terms of a self-configuring model, termed the *prediction skeleton* ([Kecskeméthy et al., 2003]). The prediction skeleton is a virtual device intended to reproduce the motion "seen" by the cameras (Fig. 5.7, right box). It comprises three additional prismatic joints between the ends of each limb such as to allow for virtual bone length variations, denoted by vectors $\mathbf{s}_{\mathrm{P}}^{(\cdots)}$, $\mathbf{s}_{\mathrm{T}}^{(\cdots)}$ and $\mathbf{s}_{\mathrm{S}}^{(\cdots)}$ for pelvis, thigh and shank, respectively. The superscript "$(\cdots)$" functions as wild card for the side identifier "left" and "right". The anatomic skeleton (Fig. 5.7, left box) is rigidly connected via the unidentified offset vectors $\boldsymbol{\epsilon}_{\mathrm{H}}$, $\boldsymbol{\epsilon}_{\mathrm{K}}$ and $\boldsymbol{\epsilon}_{\mathrm{A}}$ at hip, knee, and ankle.

As illustrated above, the task is to determine vectors $\boldsymbol{\epsilon}_{\mathrm{H}}$, $\boldsymbol{\epsilon}_{\mathrm{K}}$ and $\boldsymbol{\epsilon}_{\mathrm{A}}$ as well as the bone length vectors $\tilde{\mathbf{s}}_{\mathrm{P}}^{(\cdots)}$, $\tilde{\mathbf{s}}_{\mathrm{T}}^{(\cdots)}$ and $\tilde{\mathbf{s}}_{\mathrm{S}}^{(\cdots)}$ of the actual pelvis, thigh and shank, respectively, such that the twin skeleton mechanism produces the same bone length variations as those measured for the prediction skeleton for given measured time histories of the rotation matrices ${}^{\mathrm{I}}\mathbf{R}_{\mathrm{P}}$, ${}^{\mathrm{I}}\mathbf{R}_{\mathrm{T}}^{(\cdots)}$ and ${}^{\mathrm{I}}\mathbf{R}_{\mathrm{S}}^{(\cdots)}$ at pelvis, hip and knee, respectively.

This task is solved by means of mathematical optimization. Here, the optimization method described in Sec. 2.2.4 is applied. The fitting of the predicted leg model to the anatomic leg parameters consists of two steps.

(1) In a first step, the prediction skeleton is fitted with unlocked prismatic joints to the output of the motion capturing system, using assumptions for the location of the predicted joint centers. As described above, the predicted model will display varying bone lengths if there is a mismatch of predicted and anatomic geometric parameters (see Fig. 5.4).

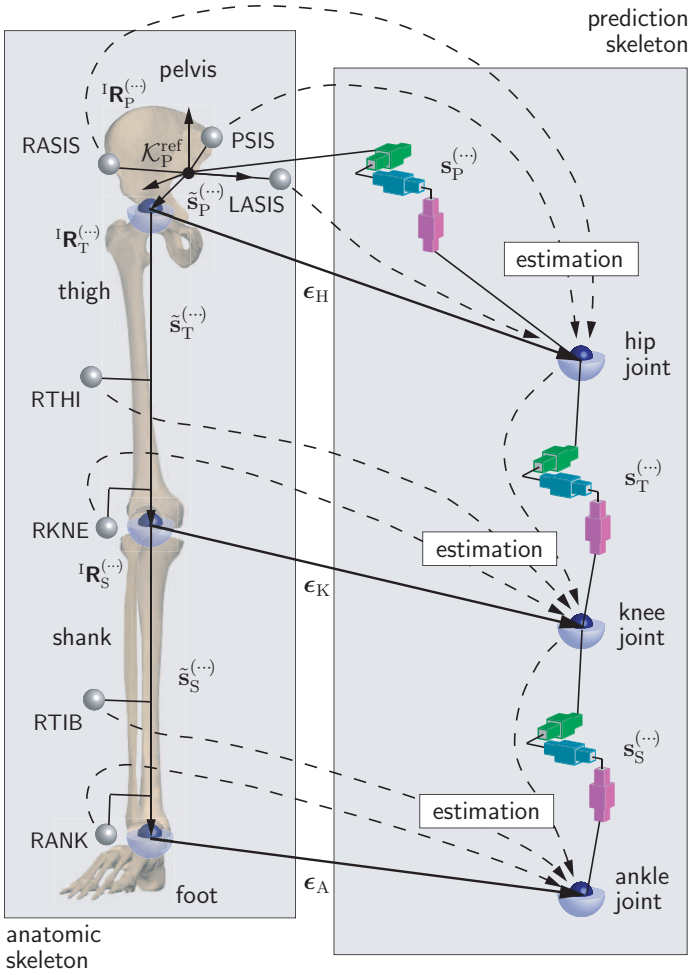

Figure 5.7: Prediction skeleton for biofidelic adaption of measurement, basic sketch

(2) In a second step, the bone length variations of the prediction skeleton are evaluated through a complete gait cycle. In order to fit the prediction skeleton to the anatomic skeleton, the kinematics of the twin kinematic skeleton model are evaluated at discrete instants in time t_i, $i = 1, \ldots, 51$ of the time history of the measured joint rotations at pelvis, hip and the knee over a gait cycle (for the definition of the involved quantities see Sec. 4.1.5). Let ${}^{\mathrm{H}}\mathbf{R}^{(\cdots)}_{\mathrm{T},i}$ and ${}^{\mathrm{T}}\mathbf{R}^{(\cdots)}_{\mathrm{S},i}$ denote the measured relative rotation matrices for the hip and the knee joint as well as $\mathbf{s}^{(\cdots)}_{\mathrm{P}_i}$, $\mathbf{s}^{(\cdots)}_{\mathrm{T}_i}$ and $\mathbf{s}^{(\cdots)}_{\mathrm{S}_i}$ the corresponding varying bone lengths of the prediction model at those points, respectively. Furthermore,

$$\bar{\mathbf{s}}^{(\cdots)}_{\mathrm{P}} = \frac{1}{51}\sum_{i=1}^{51}\mathbf{s}^{(\cdots)}_{\mathrm{P}_i}\,, \quad \bar{\mathbf{s}}^{(\cdots)}_{\mathrm{T}} = \frac{1}{51}\sum_{i=1}^{51}\mathbf{s}^{(\cdots)}_{\mathrm{T}_i}\,, \quad \bar{\mathbf{s}}^{(\cdots)}_{\mathrm{S}} = \frac{1}{51}\sum_{i=1}^{51}\mathbf{s}^{(\cdots)}_{\mathrm{S}_i} \tag{5.2.2}$$

denote the averaged predicted limb vectors. Assuming the vectors $\tilde{\mathbf{s}}^{(\cdots)}_{\mathrm{P}}, \mathbf{s}^{(\cdots)}_{\mathrm{P}_i}$ and

$\boldsymbol{\epsilon}_{\mathrm{H}}$ to be decomposed in the pelvis reference frame $\mathcal{K}_{\mathrm{P}}^{\mathrm{ref}}$, the vectors $\tilde{\mathbf{s}}_{\mathrm{T}}^{(\cdots)}, \mathbf{s}_{\mathrm{T}_i}^{(\cdots)}$ and $\boldsymbol{\epsilon}_{\mathrm{K}}$ to be decomposed in the thigh reference frame $\mathcal{K}_{\mathrm{T}}^{\mathrm{ref}}$ (for definition see Sec. 4.1.3) and with the shank-fixed vectors $\tilde{\mathbf{s}}_{\mathrm{S}}^{(\cdots)}, \mathbf{s}_{\mathrm{S}_i}^{(\cdots)}$ and $\boldsymbol{\epsilon}_{\mathrm{A}}$ (decomposition in the shank reference frame $\mathcal{K}_{\mathrm{S}}^{\mathrm{ref}}$, for definition see Sec. 4.1.3), the goal is to find design variables

$$\underline{x} = \left[\underline{\tilde{s}}_{\mathrm{P}}^{(\cdots)},\ \underline{\epsilon}_{\mathrm{H}},\ \underline{\tilde{s}}_{\mathrm{T}}^{(\cdots)},\ \underline{\epsilon}_{\mathrm{K}},\ \underline{\tilde{s}}_{\mathrm{S}}^{(\cdots)},\ \underline{\epsilon}_{\mathrm{A}} \right] \tag{5.2.3}$$

such that the objective function

$$\begin{aligned} f(\underline{x}) = \frac{1}{2} \sum_{i=1}^{51} \left[\mathbf{s}_{\mathrm{P}_i}^{(\cdots)} - \underline{\epsilon}_{\mathrm{H}} - \underline{\tilde{s}}_{\mathrm{P}}^{(\cdots)} \right]^2 + \\ + \frac{\alpha}{2} \sum_{i=1}^{51} \left[\left({}^{\mathrm{H}}\mathbf{R}_{\mathrm{T},i}^{(\cdots)} \right)^{\mathrm{T}} \underline{\epsilon}_{\mathrm{H}} + \mathbf{s}_{\mathrm{T}_i}^{(\cdots)} - \underline{\epsilon}_{\mathrm{K}} - \underline{\tilde{s}}_{\mathrm{T}}^{(\cdots)} \right]^2 + \\ + \frac{\alpha}{2} \sum_{i=1}^{51} \left[\left({}^{\mathrm{T}}\mathbf{R}_{\mathrm{S},i}^{(\cdots)} \right)^{\mathrm{T}} \underline{\epsilon}_{\mathrm{K}} + \mathbf{s}_{\mathrm{S}_i}^{(\cdots)} - \underline{\epsilon}_{\mathrm{A}} - \underline{\tilde{s}}_{\mathrm{S}}^{(\cdots)} \right]^2 \end{aligned} \tag{5.2.4}$$

subject to

$$\begin{array}{rcccl} \bar{\mathbf{s}}_{\mathrm{P}}^{(\cdots)} - \underline{\delta}_1 & \leq & \underline{\tilde{s}}_{\mathrm{P}}^{(\cdots)} & \leq & \bar{\mathbf{s}}_{\mathrm{P}}^{(\cdots)} + \underline{\delta}_1\ , \\ \bar{\mathbf{s}}_{\mathrm{T}}^{(\cdots)} - \underline{\delta}_1 & \leq & \underline{\tilde{s}}_{\mathrm{T}}^{(\cdots)} & \leq & \bar{\mathbf{s}}_{\mathrm{T}}^{(\cdots)} + \underline{\delta}_1\ , \\ \bar{\mathbf{s}}_{\mathrm{S}}^{(\cdots)} - \underline{\delta}_1 & \leq & \underline{\tilde{s}}_{\mathrm{S}}^{(\cdots)} & \leq & \bar{\mathbf{s}}_{\mathrm{S}}^{(\cdots)} + \underline{\delta}_1\ , \\ -\underline{\delta}_2 & \leq & \underline{\epsilon}_{\mathrm{H}} & \leq & \underline{\delta}_2\ , \\ -\underline{\delta}_2 & \leq & \underline{\epsilon}_{\mathrm{T}} & \leq & \underline{\delta}_2\ , \\ -\underline{\delta}_2 & \leq & \underline{\epsilon}_{\mathrm{S}} & \leq & \underline{\delta}_2\ , \end{array} \tag{5.2.5}$$

with

$$\underline{\delta}_1 = [\ 0.01,\ 0.01,\ 0.05\ ], \qquad \underline{\delta}_2 = [\ 0.03,\ 0.03,\ 0.08\ ], \tag{5.2.6}$$

is minimized (values given in m). The optimization constraints according to (5.2.5)/(5.2.6) result from the assumption that the correct joint center locations can be expected in the vicinity of the locations estimated on basis of the marker motion. For the same reason, the initial guess was chosen as

$$\underline{\tilde{s}}_{\mathrm{P}_0}^{(\cdots)} = \bar{\mathbf{s}}_{\mathrm{P}}^{(\cdots)}\ , \qquad \underline{\tilde{s}}_{\mathrm{T}_0}^{(\cdots)} = \bar{\mathbf{s}}_{\mathrm{T}}^{(\cdots)}\ , \qquad \underline{\tilde{s}}_{\mathrm{S}_0}^{(\cdots)} = \bar{\mathbf{s}}_{\mathrm{S}}^{(\cdots)}\ , \tag{5.2.7}$$

and

$$\underline{\epsilon}_{\mathrm{H}_0} = \underline{\epsilon}_{\mathrm{K}_0} = \underline{\epsilon}_{\mathrm{A}_0} = [\ 0,\ 0,\ 0\ ]\ . \tag{5.2.8}$$

The fact that the design variables all allow for larger variations in each z-component than in $x-$direction and $y-$direction is owed to the observation that the variations in limb vector length are most significantly influenced by variations in the longitudinal limb axis coordinate (see Fig. 5.5). This observation is supported by the fact that (except in cases of extreme adiposity) significant relative marker displacement can be expected to appear in parallel to the bone surface (i.e. in proximal-distal limb direction).

The weighting factor $\alpha > 1$ in (5.2.4) accommodates the observation that thigh and shank vectors display more significant length variations than the corresponding pelvis vector. This indicates a better estimation of the hip joint center based on pure marker location consideration and advises a concentration on the correction of knee and ankle joint location. In the presented example $\alpha = 2$ was applied, all computations using $\alpha \geq 2$ yielded similar results.

5.2.3 Data-fitting results

The method was applied to measured gait kinematics of 28 persons (=56 legs). The results will be presented in two steps. At first, the results for the example data given in Fig. 5.4/Fig. 5.5 is presented. After that, a summary of the results for all applied cases is given.

Results for example data set

The results for the example data given in Fig. 5.4/Fig. 5.5 are shown in Tab. 5.2. The corresponding limb vector length variations are displayed in Fig. 5.8 and Fig. 5.9.

It can be seen that by the optimized values the method yields almost equal segment lengths for opposite limbs and that the pelvis segment vector is corrected by 0.02 m.

By the automatic correction, knee and ankle joint centers are relocated only marginally in terms of anterior-posterior (x) and lateral-medial (y) direction but more significantly in proximal-distal (z) direction. In case of the knee joint, the new joint center is located posterior, more lateral and more cranial than the original one. The relocated ankle joint is located slightly posterior and more cranial than the original location. The presented data reveals a relocation of the hip joint in anterior, lateral and cranial direction. Compared to the raw motion capturing data given in Fig. 5.4, Fig. 5.8 and

side	vector	x	y	z
left	$\boldsymbol{\epsilon}_{\mathrm{H}}$	0.000735	0.003653	0.018244
	$\boldsymbol{\epsilon}_{\mathrm{K}}$	-0.005244	0.000570	0.025450
	$\boldsymbol{\epsilon}_{\mathrm{A}}$	-0.010627	-0.001586	0.006080
right	$\boldsymbol{\epsilon}_{\mathrm{H}}$	0.027860	-0.002527	0.023716
	$\boldsymbol{\epsilon}_{\mathrm{K}}$	-0.000744	-0.008834	0.023022
	$\boldsymbol{\epsilon}_{\mathrm{A}}$	-0.002859	-0.010915	0.003291

Table 5.2: Joint center relocation vectors after optimization (in m, decomposition as stipulated in Sec. 5.2.2)

Fig. 5.9 show a reduction of the original length variations of all segment vectors from 12.727 % (left thigh) up to 35 % (right thigh). The average reduction of segment vector length variation for the presented application is 25.731 %.

side	joint	posterior	anterior	medial	lateral	proximal	distal
left	hip	37.5%	62.5%	75%	25%	100%	0%
	knee	100%	0%	87.5%	12.5%	100%	0%
	ankle	100%	0%	100%	0%	31.25%	68.75%
right	hip	41.66%	58.33%	33.33%	66.66%	100%	0%
	knee	91.66%	8.33%	8.33%	91.66%	100%	0%
	ankle	100%	0%	0%	100%	50%	50%

Table 5.3: Results of joint center relocation: suggested direction of relocation in percent of investigated data sets

Discussion of results

The direction of relocation can indicate necessary improvements in model assumptions. Since the group of patients shows large variations in body height (between 1.08 m and 1.76 m, average 1.28 m), only the *direction* of joint center relocation was considered. Tab 5.3 shows for each joint the proposed direction of relocation in percent of investigated data set.

It can be seen that for hip and knee joint there exists a systematic error drift towards

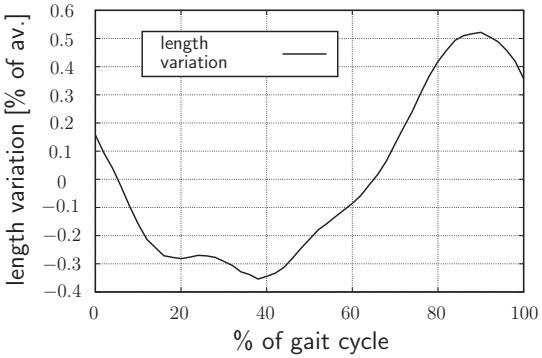

(a) Left pelvis bone length vector

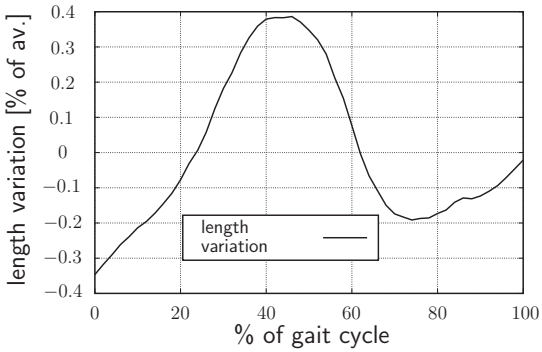

(b) Right pelvis bone length vector

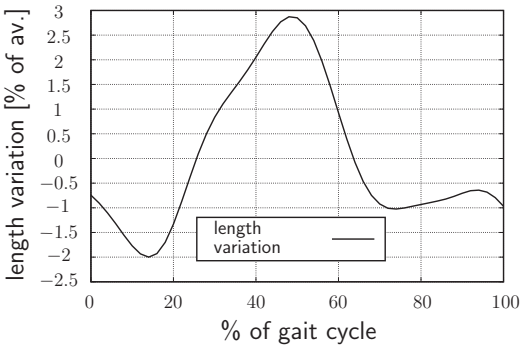

(c) Left thigh bone length vector

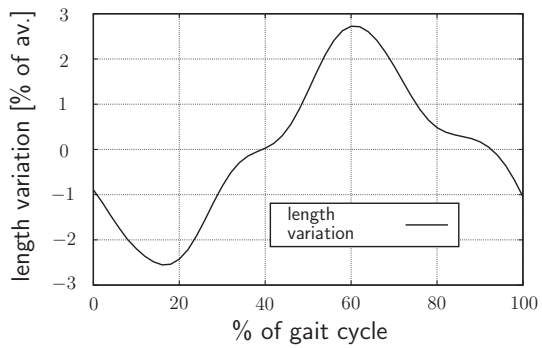

(d) Right thigh bone length vector

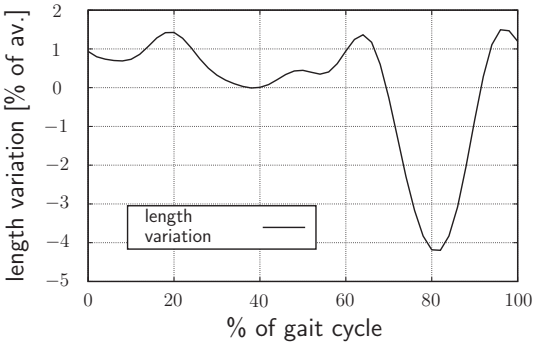

(e) Left shank bone length vector

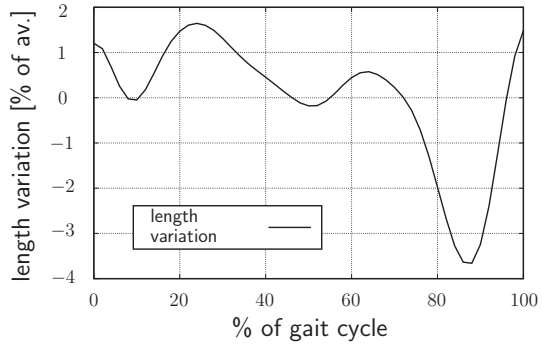

(f) Right shank bone length vector

Figure 5.8: Bone length variations for relocated joint centers with respect to average value (Euclidian norm)

proximal direction with respect to the originally assumed location. Furthermore ankle and knee joint are mostly arranged posterior to the raw data position. A summary of the results in terms of the reduction of vector length variation is given in Tab. 5.4. There, for each segment the average variation of all data sets with respect to the corresponding average length is given before the application of the proposed method

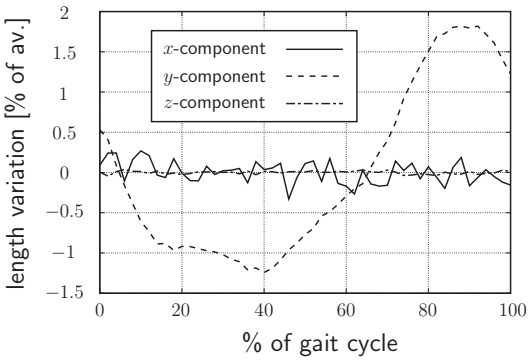

(a) Left pelvis bone vector components

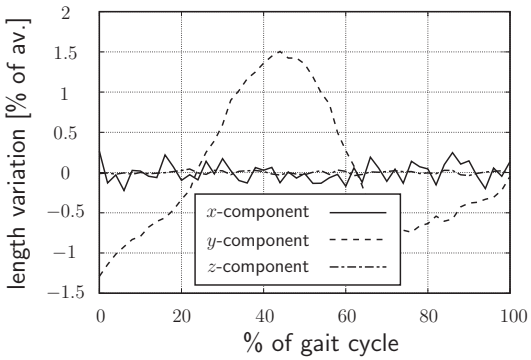

(b) Right pelvis bone vector components

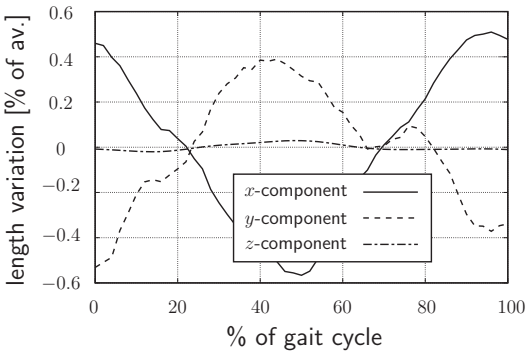

(c) Left thigh bone vector components

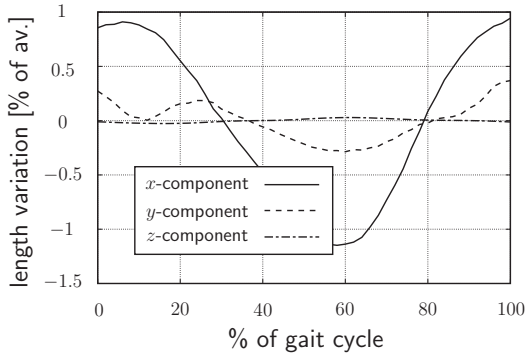

(d) Right thigh bone vector components

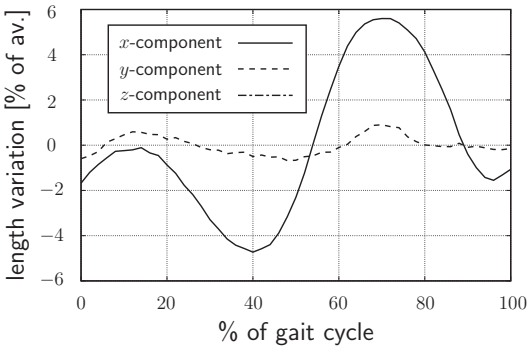

(e) Left shank bone vector components

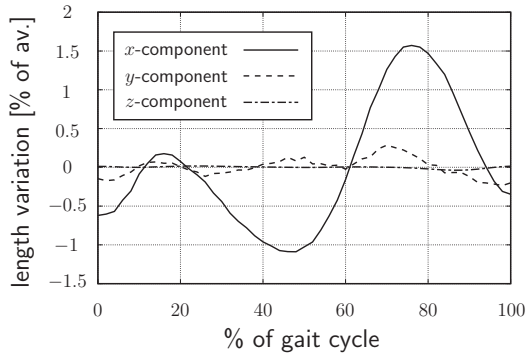

(f) Right shank bone vector components

Figure 5.9: Bone vector component variations for relocated joint centers with respect to averaged component value, vector decomposition in segment fixed reference frame

(3rd column) and after the application of the method (4th column). The last column displays the achieved improvement (=reduction of vector length variation). It can be seen that an average reduction of between 19% (left thigh) and at most 32% (right shank) could be achieved.

side	segment	variation before appl.	variation after appl.	improvement
left	pelvis	1.2%	0.9%	25%
	thigh	4.2%	3.4%	19%
	shank	4.4%	3.2%	27%
right	pelvis	1.3%	0.9%	31%
	thigh	4.0%	3.1%	23%
	shank	4.1%	2.8%	32%

Table 5.4: Bone length variation reduction after joint center relocation in percent with respect to initial variation over all investigated data sets

Discussion

The proximal relocation of the hip joint in all investigated cases (Tab. 5.3) indicates a systematic error in the generic model. Since the number of hip studies is relatively small (Sec. 4.1.3), a larger control group is needed in order to improve the generic model.

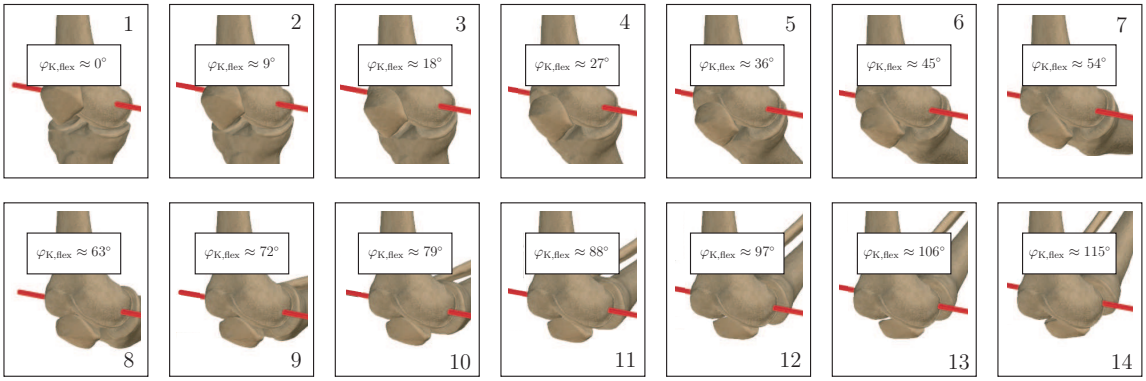

Figure 5.10: Illustration of moving axis transversalis during knee flexion (pictures adapted from [Sobotta, 2005])

A more accurate bone length determination can be achieved by taking into account the following effects:

(1) Since the knee axis transversalis (see Sec. 2.1.3) moves with respect to the femur as the knee flexion angle increases (Fig. 5.10, sequence 1–14), the generic assumption of a fixed axis — although correct for a ball-and-socket joint — yields

variations in bone lengths. As the axis moves in posterior direction, the offset vectors computed by the proposed method yield a better average approximation of the individual anatomy than the generic model.

(2) The complex structure of the ankle joint causes the axes of rotation not to intersect (the axis transversalis belongs to the upper ankle joint, the axis obliqua belongs to the lower ankle joint, Sec. 2.1.3). In addition, the decomposition of joint motion to flexion-extension, abduction-adduction and internal/external rotation is not realistic since the anatomical joint couples abduction-adduction and internal/external rotation by pronation and supination. Variations of shank segment length therefore strongly depend on individual anatomy.

The variations remaining after optimization can be further reduced by more complex joint models.

5.3 Results of inverse dynamics simulation

5.3.1 Functionality of kinetostatic transmission objects

After application of the data correction process presented in Sec. 5.2.2, the chain of kinetostatic transmission elements resulting from the modeling (Fig. 4.11) uses the corresponding motion and force transmission functions of the particular objects to compute the overall inverse dynamics. Motion transmission takes its beginning at the inertially fixed frame and is performed throughout the leg chain towards its distal end. There, ground reaction force and moment information is regarded and the chain is transversed in opposite direction to transmit the corresponding forces, taking also into account the segmental inertia properties. In the principal depiction of this flow of information given in Fig. 5.11, the musculotendon actuator lengths and velocities are presented in braces, since strictly speaking these quantities do not represent inverse dynamics results but are achieved using extended kinematics computations. The models applied in this context are described in Sec. 5.4.2 and are displayed in Fig. 5.13.

5.3.2 Time control

Time control in the inverse dynamics simulation is exercised by means of a supplementary object of type `CommonModelSimulationData` supplying all involved kinetostatic

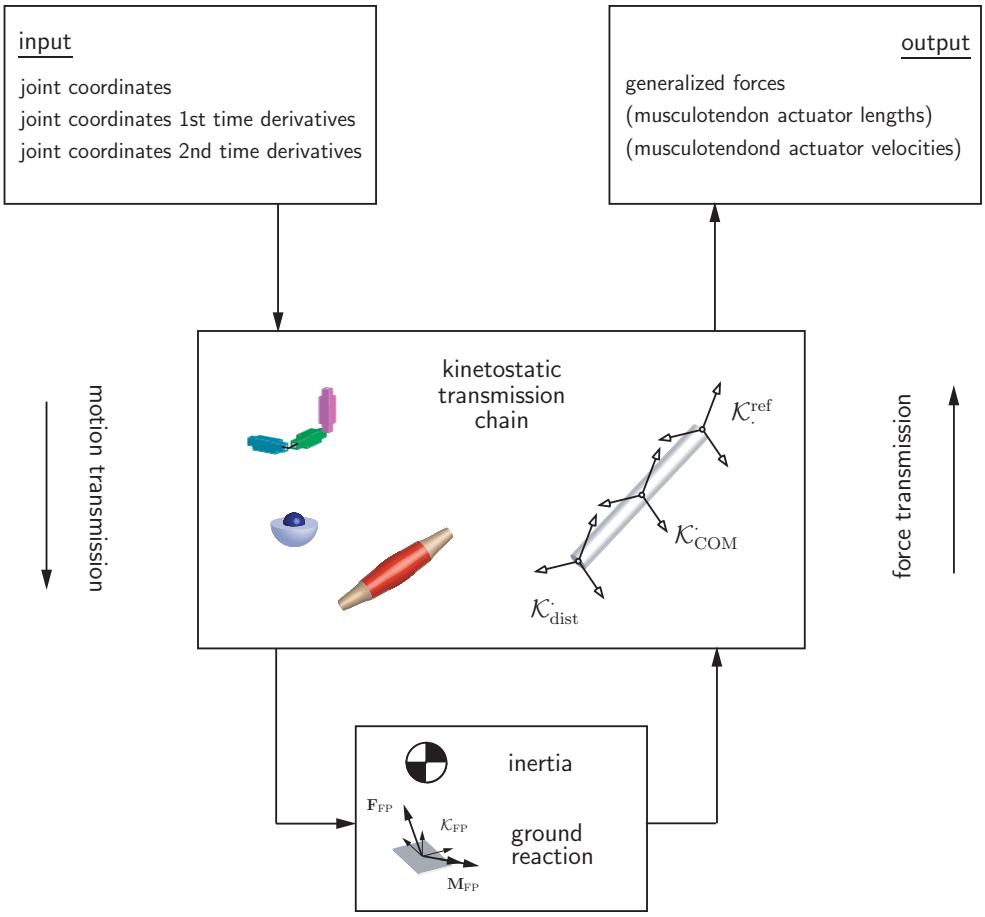

Figure 5.11: Motion and force transmission in inverse dynamics

transmission elements with a common time scale as well as gait cycle specific values such as the time increment T between two recorded positions used in the computation of the joint coordinate derivatives.

5.3.3 Mass model influence

The presented models and procedures allow for the computation of all quantities typically assessed during classical gait analysis. Aside from the generalized forces (i.e. the joint moments), also the muscular power contribution at a joint $\mathcal{G}_i$,

$$P_i = \underline{Q}_i \cdot \underline{q}_i \ , \tag{5.3.1}$$

can be regarded. Fig. 5.12 discusses moment and power normalized with respect to body weight at the right hip joint for flexion/extension motion of a male adult and the

mass models presented in Sec. 4.3.

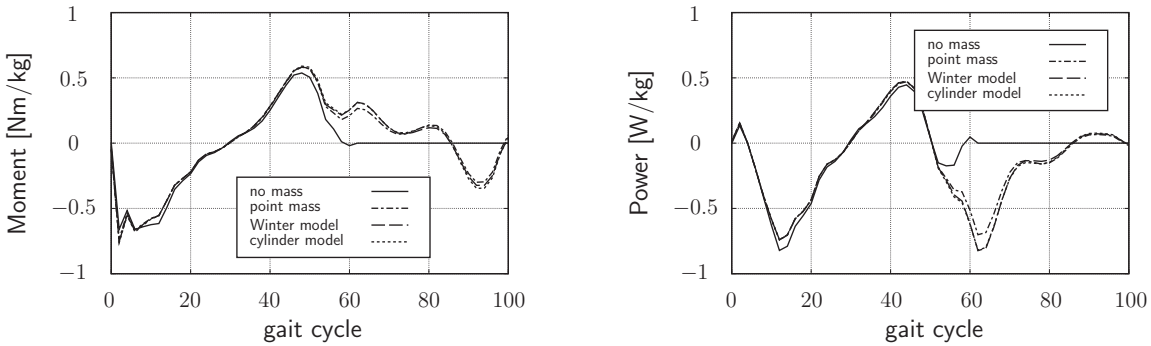

(a) Hip flexion/extension moment

(b) Hip flexion/extension power

Figure 5.12: Moment and power for hip flexion/extension motion: influence of different mass models

As it can be seen, even the crude model of point masses yields acceptable results, while during the stance phase also complete neglecting of mass is allowable. Hence, the rough modeling approaches and simplifications are justified and represent a flexible and extensible library for further applications and improvements ([Kecskeméthy et al., 2003]).

5.4 Musculotendon-pathway consideration in inverse dynamics

In addition to standard gait motion analysis systems, the developed framework features the computation of musculotendon-pathway lengths. As briefly presented in Sec. 5.5, these information may provide support in the diagnosis of special pathologies in gait motion. The modeling of the musculotendon pathway is explained in the sequel. The applicability of the computed data for diagnosis purposes is clarified by the example presented in Sec. 5.5

5.4.1 Musculotendon pathway

The musculotendon pathway is modeled according to the concept described in Section 3.1 as a ribbon that is spanned between a bone fixed muscle origin point and a

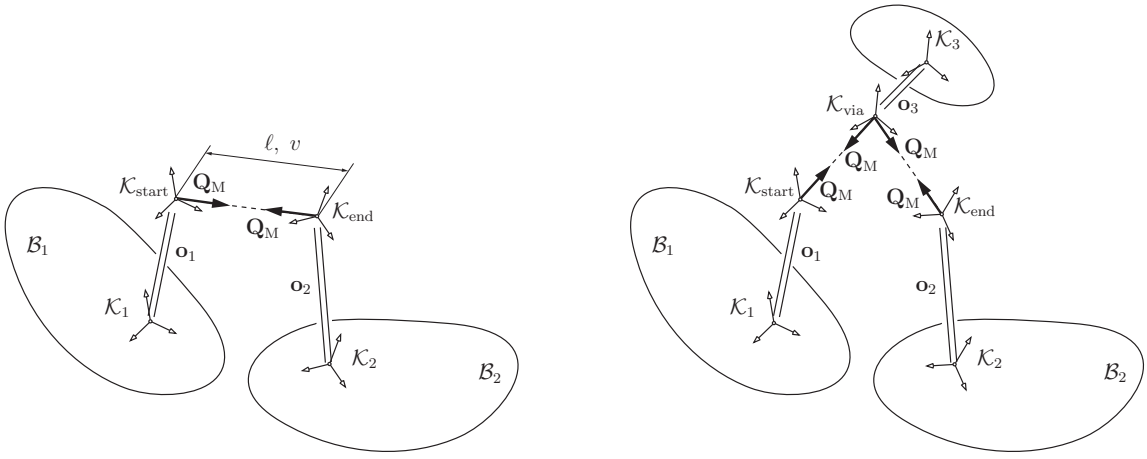

(a) Basic muscle object

(b) Muscle object with via point

Figure 5.13: Modeling principle of musculotendon actuator kinematics

corresponding muscle insertion point ([Stolz, 2002], [Strobach et al., 2005]). As shown in Fig. 5.13, these points are represented as spatial reference frame objects $\mathcal{K}_{\text{start}}$ and $\mathcal{K}_{\text{end}}$. Optionally, the position of these frames can be defined with respect to bone-fixed reference frames, denoted by $\mathcal{K}_1, \mathcal{K}_2$ in Fig. 5.13(a) by declaration of constant offset vectors $\mathbf{o}_1$ and $\mathbf{o}_2$. Usually, the bone fixed frames agree with the proximal segment reference frames. If necessary, for example to "wrap" the actuator around bones, "via points" as displayed in Fig. 5.13(b) can be introduced similarly to origin and insertion points.

The location of the appearing muscles reference and via points is given in Appendix A. The presented coordinates are to be interpreted with respect to the reference frame of the denoted segment. Usually, the given landmarks have to be relocated by isometric scaling to adapt the model to the particular geometries of the person under investigation. The force $\mathbf{Q}_{\text{M}}$ displayed in Fig. 5.13 which is applied to the skeletal chain at muscle origin and insertion points is computed according to the procedure explained in Sec. 6.1.1.

5.4.2 Musculotendon lengthening

The total length ℓ and the lengthening/shortening velocity v of the musculotendon pathway is computed as the sum of partial lengths defined by the straight connections of origin point, via point(s) and muscle insertion during motion transmission. For the

multibody modeling of the musculotendon system, the complete structure is considered as a single kinetostatic transmission element computing its length from the state of the involved frames. The mathematical background is described in Sec. 5.4.3. This simple model already yields useful information supporting in the diagnosis of specific pathological gait patterns.

5.4.3 Elementary measurements in MBILE

The determination of musculotendon pathway kinematics is done by application of a so-called "chord" object supplied as member of a group of *elementary measurements* within MBILE ([Kecskeméthy, 1993]). The implementation of the applied measurement (distance between two points) as kinetostatic transmission element is illustrated in the following.

Distance between two points

To determine the distance between two points, the situation depicted in Fig. 5.14 is considered. Motion transmission for the elementary measurements consists of the computation of the corresponding measurement parameter g as well as its time derivatives $\dot{g}$ and $\ddot{g}$. Basis for these calculations is the (known) motion of two reference frames $\mathcal{K}_\ell, \mathcal{K}_r$. The grey frame in the lower part of the picture represents the inertial frame, $\mathbf{d}$ is the radius vector between the origins of both involved frames.

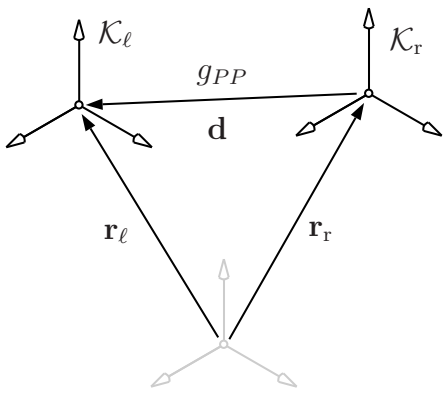

Figure 5.14: Elementary measurement: distance between two points

In the position transmission the scalar value g_{PP} is computed by virtue of

$$g_{PP} = \sqrt{\mathbf{d} \cdot \mathbf{d}} = \|\mathbf{r}_\ell - \mathbf{r}_r\| \ . \tag{5.4.1}$$

The corresponding velocity $\dot{g}_{PP}$ is gained by taking the time derivative of equation 5.4.1, yielding

$$\begin{aligned} \dot{g}_{PP} &= \frac{1}{2\sqrt{\mathbf{d} \cdot \mathbf{d}}} \cdot 2\mathbf{d} \cdot \dot{\mathbf{d}} = \frac{\mathbf{d} \cdot \dot{\mathbf{d}}}{\sqrt{\mathbf{d} \cdot \mathbf{d}}} = \frac{\mathbf{d} \cdot (\mathbf{v}_\ell - \mathbf{v}_r)}{\|\mathbf{r}_\ell - \mathbf{r}_r\|} \\ &= \frac{1}{g_{PP}} \left[\ 0 \ , \ \mathbf{d}^{\mathrm{T}} \ , \ 0 \ , \ -\mathbf{d}^{\mathrm{T}} \ \right] \begin{bmatrix} \boldsymbol{\omega}_\ell \\ \mathbf{v}_\ell \\ \boldsymbol{\omega}_r \\ \mathbf{v}_r \end{bmatrix} \ . \end{aligned} \tag{5.4.2}$$

Finally, acceleration transmission is performed by evaluation of

$$\begin{aligned} \ddot{g}_{PP} &= \frac{\left(\ddot{\mathbf{d}} \cdot \mathbf{d} + \dot{\mathbf{d}} \cdot \dot{\mathbf{d}}\right) \sqrt{\mathbf{d} \cdot \mathbf{d}} - \left(\dot{\mathbf{d}} \cdot \mathbf{d}\right) \frac{\dot{\mathbf{d}} \cdot \mathbf{d} + \mathbf{d} \cdot \dot{\mathbf{d}}}{2\sqrt{\mathbf{d} \cdot \mathbf{d}}}}{\mathbf{d} \cdot \mathbf{d}} \\ &= \frac{\ddot{\mathbf{d}} \cdot \mathbf{d}}{g_{PP}} + \frac{\dot{\mathbf{d}} \cdot \dot{\mathbf{d}}}{g_{PP}} - \frac{\left(\dot{\mathbf{d}} \cdot \mathbf{d}\right)^2}{g_{PP}^3} \\ &= \frac{1}{g_{PP}} \left[\ 0 \ , \ \mathbf{d}^{\mathrm{T}} \ , \ 0 \ , \ -\mathbf{d}^{\mathrm{T}} \ \right] \begin{bmatrix} \dot{\boldsymbol{\omega}}_\ell \\ \mathbf{a}_\ell \\ \dot{\boldsymbol{\omega}}_r \\ \mathbf{a}_r \end{bmatrix} + \frac{1}{g_{PP}} \left[\ 0 \ , \ 1 \ , \ 0 \ , \ -1 \ \right] \begin{bmatrix} \boldsymbol{\omega}_\ell \\ \mathbf{v}_\ell \\ \boldsymbol{\omega}_r \\ \mathbf{v}_r \end{bmatrix} - \\ &\qquad -\frac{1}{g_{PP}^3} \left(\left[0 \ , \ \mathbf{d}^{\mathrm{T}} \ , \ 0 \ , \ -\mathbf{d}^{\mathrm{T}} \ \right] \begin{bmatrix} \boldsymbol{\omega}_\ell \\ \mathbf{v}_\ell \\ \boldsymbol{\omega}_r \\ \mathbf{v}_r \end{bmatrix} \right)^2 \ . \end{aligned} \tag{5.4.3}$$

A detailed description of all available objects is given in [Kecskeméthy, 2003].

5.5 Application: Diagnosis of talipes equinus

Application of the described lower extremity model allows for the computation of musculotendon pathway kinematics for 43 lower extremity muscles on basis of a patient-

specific motion capturing result. This data represent the basis of the diagnosis procedure described in the sequel. The investigations were performed in cooperation with the Department for Paediatric Surgery at the Medical University of Graz, Austria, who supplied the gait data.

5.5.1 Problem statement

A special clinical problem is the so-called *talipes equinus*. Here, patients typically suffer from a constant plantar-flexion of the ankle joint which is caused by a contraction of muscle *gastrocnemius*. Patients are classified in two groups:

- for patients showing a "dynamic" clinical picture, physiotherapy can yield essential improvement in mobility and is usually sufficient,
- for patients diagnosed as a "fixed" muscle *gastrocnemius*, a surgical intervention is required as a therapy.

Typically, a "dynamic" patient turns into a "fixed" patient if the necessary therapy is applied too late or is insufficient.

Currently, the classification of a patient is only possible by a physical test to be performed under anesthesia. To avoid the risks for the patient coming along with this method, an automated diagnosis procedure based on muscle length analysis was developed in order to allow for a diagnosis purely based on processed motion capturing data. To this end, the kinematics of all 43 lower extremity muscles supplied by the model were investigated for patients with a known medical diagnosis to detect distinctive features.

5.5.2 Working hypothesis for diagnosis

The observation of musculotendon pathway kinematics unveiled a characteristic behavior of the *gluteus* muscle group during the swing phase of gait. This muscle group is mainly responsible for hip joint motion and was found to play an important role for hip rotation in the context of cerebral palsy ([Delp et al., 1999a]). The consideration of the normalized, absolute muscle length gradient of these muscles during swing phase showed a different representative number of extrema for patients medically diagnosed

a "dynamic" *gastrocnemius* (2 major maxima, see e.g. Fig. 5.18 for muscle *gluteus medius anterior*) and a "fixed" *gastrocnemius* (1 major maximum, see e.g. Fig. 5.16, Fig. 5.17 for muscle muscle *gluteus medius anterior*). Although all muscles of the mentioned muscle group displayed this behavior more or less distinctively, muscle *gluteus medius anterior* showed the most pronounced behavior.

The observations yielded the following results:

(1) In case of a ***fixed*** muscle *gastrocnemius*, the normalized, absolute gradient of muscle *gluteus medius anterior* length features a ***single*** significant maximum during swing phase.

(2) If muscle *gastrocnemius* appears ***dynamic***, ***two*** significant maxima appear in the normalized, absolute gradient of muscle *gluteus medius anterior* length during swing phase.

The effects are illustrated in Fig. 5.15.

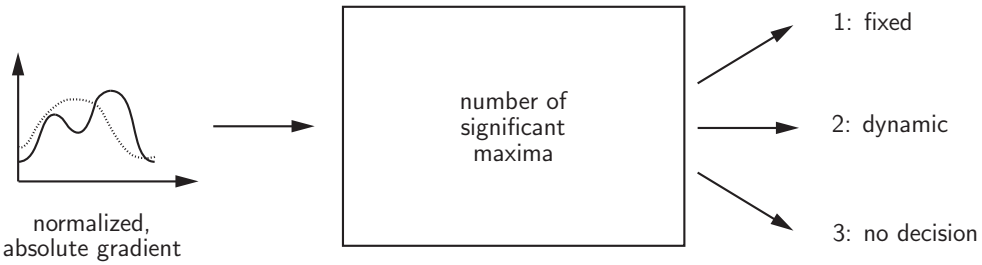

Figure 5.15: Simplified illustration of working hypothesis for diagnosis of dynamic or fixed muscle *gastrocnemius*

This hypothesis was applied to a group of 22 patients with a medical diagnosis of either fixed (14 persons) or dynamic (8 persons) *gastrocnemius* and its output was checked for consistency with respect to the medical diagnosis. The method can be subdivided into three major steps which will be described in the following sections:

(1) the computation of the absolute, normalized gradient of muscle *gluteus medius anterior* for the swing phase of gait for all available data sets of the patient under investigation (Sec. 5.5.3),

(2) an automated detection of the number of major peaks in these gradients by frequency analysis (Sec. 5.5.4),

(3) the accomplishment of an averaging process for the results achieved in step (2) leading to the final diagnosis (Sec. 5.5.5).

5.5.3 Gradient contour evaluation

The kinematical processing of GCD data (see Sec. 4.1.5) by the kinematic model described in Chap. 4 yields the length of 43 muscles for a complete gait cycle in the form of 51 equidistant data points for each muscle. Further postprocessing can be performed using the standard engineering toolbox Matlab®. For each patient, between 7 and 13 GCD files were processed.

For each GCD file, the absolute gradient of was determined as follows:

(1) Let $\nu \in \{\,1,\ldots,22\,\}$ denote the patient, ${}_m\ell_i$, $i \in \{\,0,\ldots,50\,\}$, the muscle length at time step t_i and $m \in \{\,1,\ldots,43\,\}$ the involved muscle. Moreover, let $\kappa(\nu) \in \{\,1,\ldots,\kappa_{\max}(\nu)\,\}$ denote the κ-th GCD file for patient ν, where $\kappa_{\max}(\nu) \in \{\,7,\ldots,13\,\}$. The average muscle length for patient ν, muscle m, trial $\kappa(\nu)$ is then

$$ {}^{\nu}_{m}\bar{\ell}^{\kappa(\nu)} = \frac{1}{51}\sum_{i=0}^{50} {}^{\nu}_{m}\ell_i^{\kappa(\nu)} \; . \tag{5.5.1} $$

(2) Next, one introduces the normalized muscle lengths for that patient ν, muscle m, trial $\kappa(\nu)$ as

$$ {}^{\nu}_{m}\hat{\ell}_i^{\kappa(\nu)} = \frac{{}^{\nu}_{m}\ell_i^{\kappa(\nu)}}{{}^{\nu}_{m}\bar{\ell}^{\kappa(\nu)}} \; , \qquad i = 0,\ldots,50 \; . \tag{5.5.2} $$

(3) The absolute gradient sequence ${}^{\nu}_{m}G^{\kappa(\nu)}$ for patient ν, muscle m, trial $\kappa(\nu)$ is then

defined as

$$
{}^{\nu}_{m}G_i^{\kappa(\nu)} = \begin{cases} \left\| \dfrac{{}^{\nu}_{m}\hat{\ell}_1^{\kappa(\nu)} - {}^{\nu}_{m}\hat{\ell}_0^{\kappa(\nu)}}{h} \right\| & \text{for} \quad i = 0 \\ \left\| \dfrac{{}^{\nu}_{m}\hat{\ell}_{i+1}^{\kappa(\nu)} - {}^{\nu}_{m}\hat{\ell}_{i-1}^{\kappa(\nu)}}{2h} \right\| & \text{for} \quad i = 1 \\ \left\| \dfrac{{}^{\nu}_{m}\hat{\ell}_{i-2}^{\kappa(\nu)} - 8\,{}^{\nu}_{m}\hat{\ell}_{i-1}^{\kappa(\nu)} + 8\,{}^{\nu}_{m}\hat{\ell}_{i+1}^{\kappa(\nu)} - {}^{\nu}_{m}\hat{\ell}_{i+2}^{\kappa(\nu)}}{12h} \right\| & \text{for} \quad i = 2, \ldots, 48 \\ \left\| \dfrac{{}^{\nu}_{m}\hat{\ell}_{i+1}^{\kappa(\nu)} - {}^{\nu}_{m}\hat{\ell}_{i-1}^{\kappa(\nu)}}{2h} \right\| & \text{for} \quad i = 49 \\ \left\| \dfrac{{}^{\nu}_{m}\hat{\ell}_{50}^{\kappa(\nu)} - {}^{\nu}_{m}\hat{\ell}_{49}^{\kappa(\nu)}}{h} \right\| & \text{for} \quad i = 50 \end{cases} \tag{5.5.3}
$$

Since patient specific cadence was not available in all cases, the step size h in (5.5.3) was set to $h = 0.02$s, representing a typical average value.

Fig. 5.16, Fig. 5.17 and Fig. 5.18 show all available normalized, absolute gradients of muscle *gluteus medius anterior* during the second half of gait cycle for all investigated patients.

As described in Sec. 2.1.1, swing phase of gait begins at $\approx 60\%$ of gait cycle. Fig. 5.16–5.17 show that, for a majority of patients with diagnosis "fixed", the curves feature one major peak within this range. In case of patients with diagnosis "dynamic" (Fig. 5.18), however, most of the patients show a two-peak-behavior.

5.5.4 Automated detection of peaks

The number of peaks in the gradient sequence can be determined by the Discrete Fast Fourier Transform (DFT).

Let ${}^{\nu}_{m}\tilde{G}_{\ell}^{\kappa(\nu)}$, $\ell = 1, \ldots 21$, denote the last 21 data points obtained according to (5.5.3) for patient ν, trial $\kappa(\nu)$ and muscle m. This data corresponds to the swing phase of the patient under investigation (Fig. 5.19).

Application of DFT to these data sets for $k = 1, \ldots, 21$ and $\kappa(\nu) = 1, \ldots, \kappa_{\max}(\nu)$ leads to

$$
{}^{\kappa(\nu)}_{m}\|X(k)\|^2 = \left\| \sum_{\ell=1}^{21} {}^{\nu}_{m}\tilde{G}_{\ell}^{\kappa(\nu)} e^{-j\alpha} \right\|^2, \qquad \alpha = \frac{2\pi(k-1)(\ell-1)}{21}\,. \tag{5.5.4}
$$

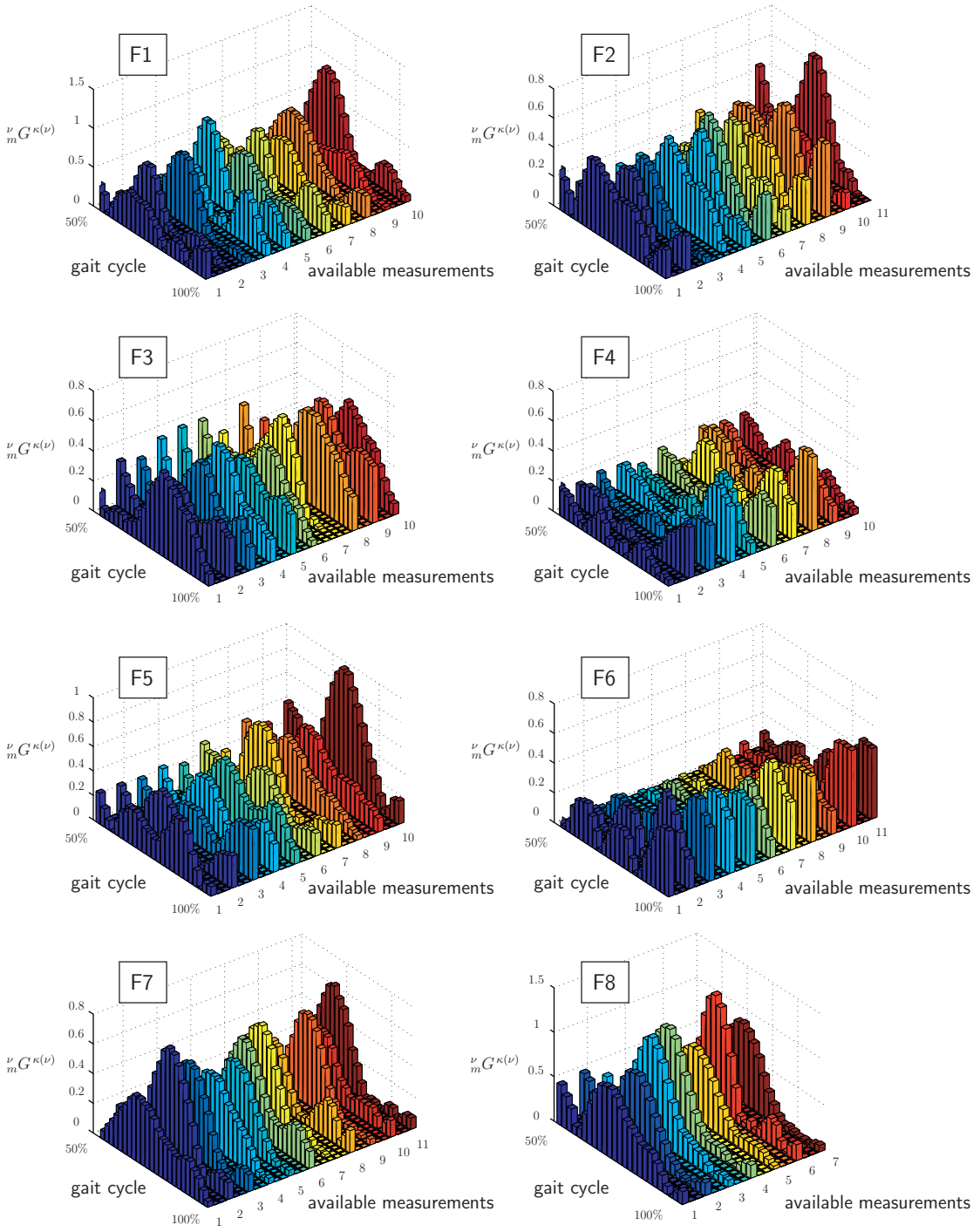

Figure 5.16: Absolute, normalized gradient ${}^{\nu}_{m}G^{\kappa(\nu)}$ for all available measurements of muscle *gluteus medius anterior* for second half of gait cycle (patients with medical diagnosis "fixed", patients F1–F8, Fig. 1/2)

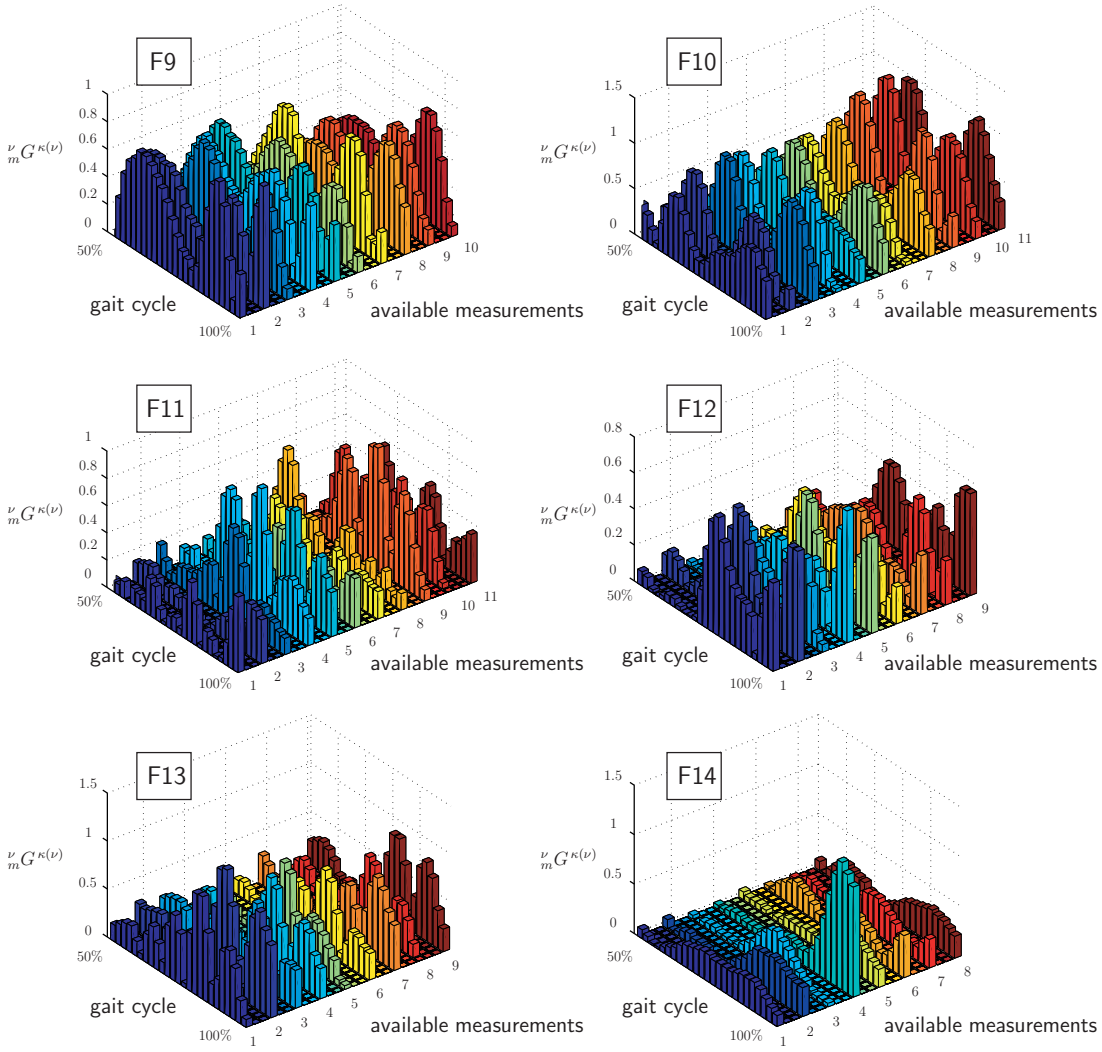

Figure 5.17: Absolute, normalized gradient ${}^{\nu}_{m}G^{\kappa(\nu)}$ for all available measurements of muscle *gluteus medius anterior* for second half of gait cycle (patients with medical diagnosis "fixed", patients F9–F14, Fig. 2/2)

Fig 5.20 and Fig. 5.21 show qualitative illustrations of typical results of the application of DFT to the above defined data sets. The following characteristics were observed after processing all available data:

1) For trials with a single peak behavior, the maximum value of ${}^{\kappa(\nu)}_{m}\|X(k)\|^2$ was always found for $k = 1$.

2) For trials with double peak behavior, the maximum value of ${}^{\kappa(\nu)}_{m}\|X(k)\|^2$ was always found for $k > 1$.

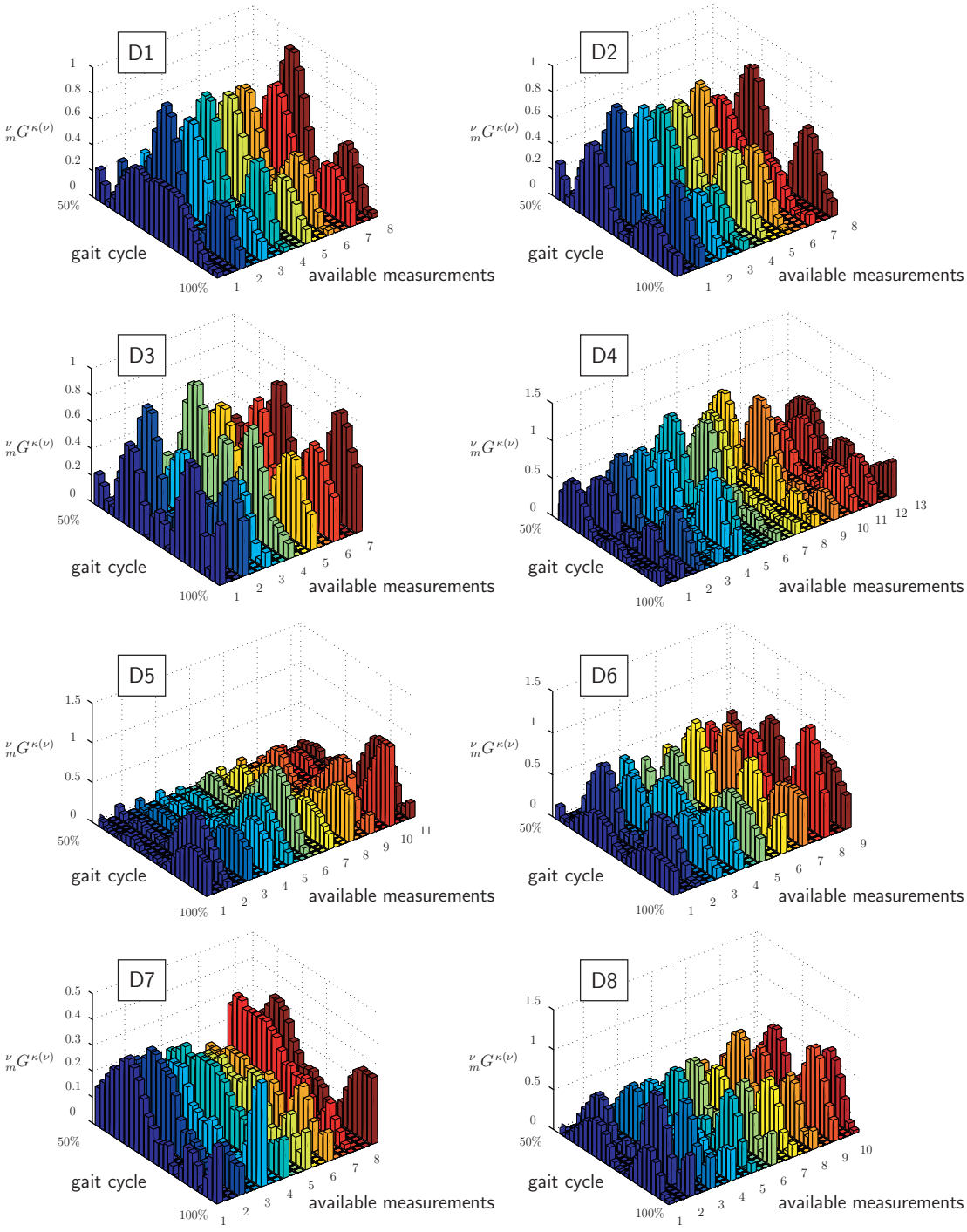

Figure 5.18: Absolute, normalized gradient ${}^{\nu}_{m}G^{\kappa(\nu)}$ for all available measurements of muscle *gluteus medius anterior* for second half of gait cycle (patients D1–D8 with medical diagnosis "dynamic")

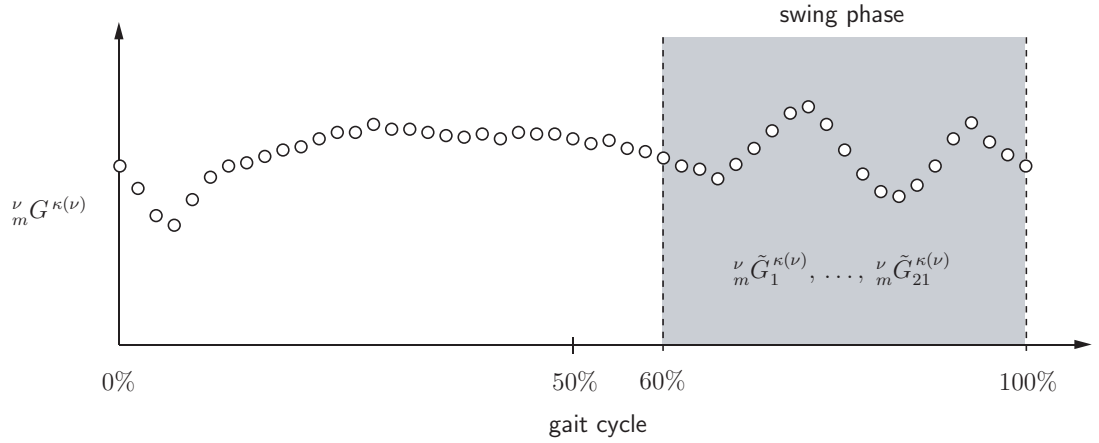

Figure 5.19: Principal illustration: input data determination for DFT

3) Independently from the medical diagnosis, for index $k > 10$ no significant variation in ${}^{\kappa(\nu)}_{m}\|X(k)\|^2$ could be observed. Hence, only the first 10 values were assumed relevant and are considered in the sequel.

5.5.5 Rules for diagnosis

Denoting the location of the maximal value resulting from (5.5.4) as

$$ {}^{\nu}_{m}\bar{k}^{\kappa(\nu)} = \left\{ k \;\middle|\; \max_{1\le k\le 10} {}^{\kappa(\nu)}_{m}\|X(k)\|^2 \right\} , \tag{5.5.5} $$

the average location of the maxima of the DFT result with respect to all available data sets for each patient becomes

$$ {}^{\nu}_{m}\bar{F} = \frac{1}{\kappa_{\max}(\nu)} \sum_{\kappa=1}^{\kappa_{\max}(\nu)} {}^{\nu}_{m}\bar{k}^{\kappa(\nu)} . \tag{5.5.6} $$

Taking the standard deviation

$$ {}^{\nu}_{m}\sigma = \sqrt{\frac{1}{\kappa_{\max}-1} \sum_{\kappa=1}^{\kappa_{\max}} \left({}^{\nu}_{m}\bar{k}^{\kappa} - {}^{\nu}_{m}\bar{F} \right)^2} \tag{5.5.7} $$

into account, the value computed according to (5.5.6) was analyzed using the decision rules described in Tab. 5.5. These were defined according to the following requirements:

1) The limit values f_1, f_2, f_3 and s yield a maximum agreement to the medical diagnosis.

2) The number of wrong diagnoses is minimized.

3) For data sets showing a large standard deviation no prediction is given.

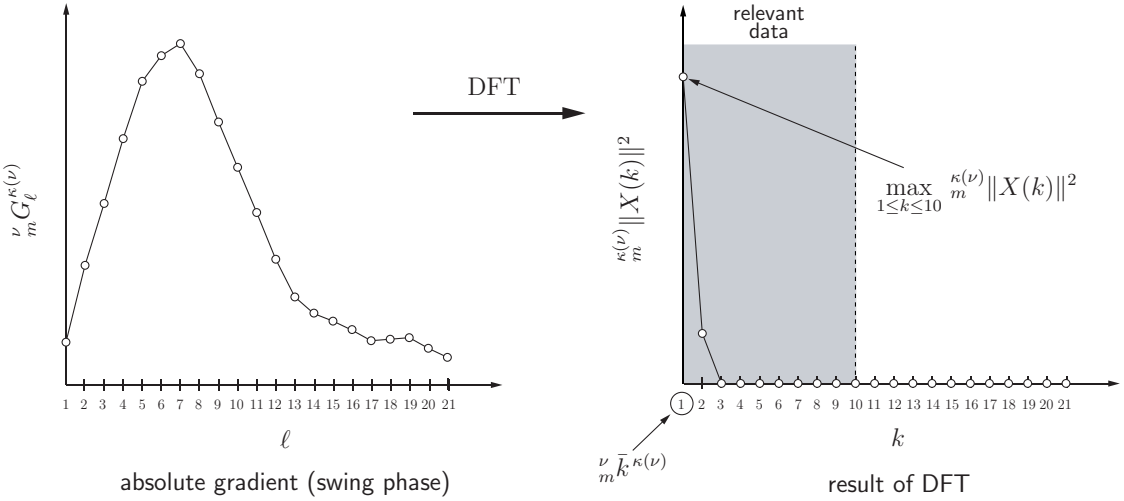

Figure 5.20: Qualitative illustration for medical diagnosis "fixed": result of DFT application (patient ν, trial $\kappa(\nu)$, muscle m)

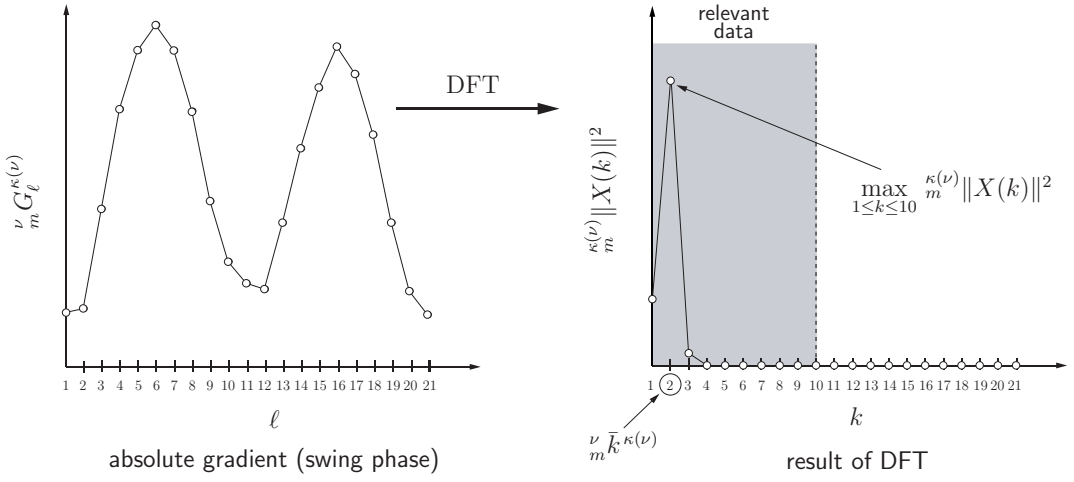

Figure 5.21: Qualitative illustration for medical diagnosis "dynamic": result of DFT application (patient ν, trial $\kappa(\nu)$, muscle m)

numerical result ($f_1 = 1.45, f_2 = 1.7, f_3 = 1.5, s = 0.7$)		prediction
$\bar{F} < f_1$ and $\sigma < s$		fixed
$\bar{F} > f_2$ and $\sigma < s$		dynamic
$f_1 \leq \bar{F} \leq f_2$	$f_1 \leq \bar{F} \leq f_3$ and $\bar{F} + \sigma < f_2$	fixed
	$f_3 < \bar{F} \leq f_2$ and $\bar{F} - \sigma > f_1$	dynamic
else		no
or $\sigma > s$		prediction

Table 5.5: Decision rules for dynamic and fixed *gastrocnemius* diagnosis

5.5.6 Results and discussion

The evaluation of the available data sets lead to the results given in Tab. 5.6. Considering those patients for which a diagnosis is proposed, in case of the medical diagnosis "fixed", 90% of all patients are diagnosed in accordance to the clinical statement. For patients showing a dynamic muscle *gastrocnemius* diagnosed by the traditional procedure, results achieved an agreement of 71% with respect to the medical diagnosis. This indicates that the predictions for the "fixed" case (critical=operation) appear very good, while the results for the "dynamic" case (less critical=physiotherapy) are not so good.

This may be due to several reasons:

(1) The total number of investigated patients is still small.

(2) Within the broad threshold between dynamic and fixed muscles, the medical diagnosis tends to drift towards "dynamic" (e.g. in order to avoid operation) while the numeric diagnosis opts for the more severe diagnosis "fixed".

(3) Kinematic data for each leg should be correlated.

The observations made in this chapter show that muscle length analysis can be used for supporting clinical scoring. Based on this approach, future research could include larger groups of patients and additional numerical methods such as neuronal networks.

patient	medical diagnosis	numerical results				
		$\kappa_{\max}$	$\bar{F}$	σ	prediction	consistency to medical diagnosis
D1	dynamic	8	1.875	0.35355	dynamic	yes
D2	dynamic	8	2	0	dynamic	yes
D3	dynamic	7	1.7143	0.48795	dynamic	yes
D4	dynamic	13	1.3846	0.50637	fixed	no
D5	dynamic	11	1	0	fixed	no
D6	dynamic	9	2	0	dynamic	yes
D7	dynamic	8	1.25	0.7071	—	—
D8	dynamic	10	1.9	0.31623	dynamic	yes
F1	fixed	11	1.2727	0.4671	fixed	yes
F2	fixed	11	1.0909	0.30151	fixed	yes
F3	fixed	10	1.1	0.31623	fixed	yes
F4	fixed	10	1.1	0.31623	fixed	yes
F5	fixed	10	1.4	0.5164	fixed	yes
F6	fixed	11	1.1818	0.40452	fixed	yes
F7	fixed	11	1.0909	0.30151	fixed	yes
F8	fixed	7	1	0	fixed	yes
F9	fixed	10	1.7	0.48305	—	—
F10	fixed	11	1.8182	0.40452	dynamic	no
F11	fixed	11	2.7273	1.3484	—	—
F12	fixed	9	2.2222	0.97183	—	—
F13	fixed	9	1.3333	1	—	—
F14	fixed	8	1.125	0.35355	fixed	yes

Table 5.6: Results of computer-assisted numerical diagnosis for all investigated patients

Chapter 6

Forward dynamics

In the context of dynamics of musculoskeletal motion, two general questions can appear:

(1) What motion results from a given input signal for a dynamic muscle model (e.g. neuronal excitation)?

(2) Which input signal for a dynamic muscle model is required to reproduce a tracked motion?

While the first question is quite easy to answer if appropriate models of skeleton and muscle are available (Fig. 6.1), solving the direct problem (2) is more difficult.

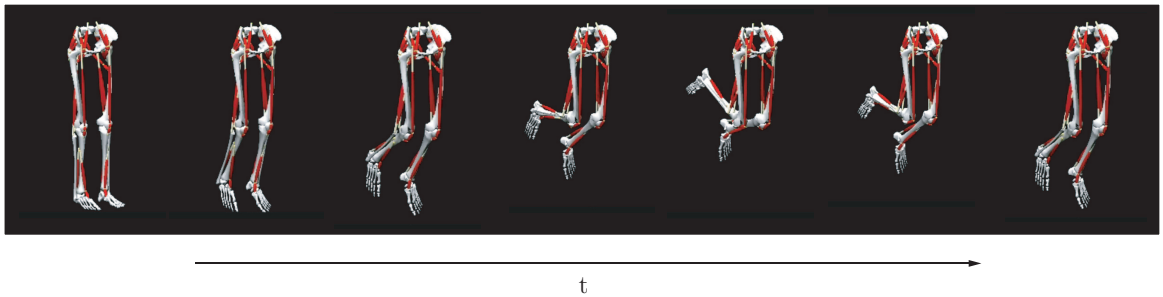

Figure 6.1: Example illustration of forwards dynamics simulation

The objective of this chapter is to realize a method to identify muscle activations such that a tracked motion is reproduced by direct dynamics. Main topics in this context are:

- the description of a HILL-type muscle model which represents the dynamic properties of muscle,
- a simplified model of muscle activation for fast, rough muscle activation identification and
- the choice of kinematically consistent objective functions for motion tracking.

The applicability of the proposed method is illustrated at simplified subsystems of the human leg.

6.1 Strategies for muscle modeling

A skeletal muscle consists of macro- and microscopic structures which react on stimuli by the central nervous system. For the mathematical modeling, basically two strategies are possible:

- *Molecular muscle models* are directly based on the sliding filament theory. These models describe the total muscle force as the superposition of molecular contributions of each filament and use partial differential equations to describe the interactions between the filaments of each muscle and to display the distribution of neuronal signals along the muscle. A compact description of this kind of model is given e.g. in [Spaegele, 1998].
- *Phenomenological muscle models* neglect the concrete microscopic structure of muscle tissue, mapping the observed macroscopic muscle behavior on "black box" function blocks. The black-box model is characterized by a *contractile element* dependent on activation and a *passive element* which displays the elastic properties of muscle tissue. The parameters of the models are determined by measurements that have been performed on primed muscles for maximal stimulation by several authors (e.g. [Hill, 1938]).

In the context of multibody dynamics, the phenomenological model type offers two main advantages:

1) A first-order property of differential equations allows for an easy and efficient numeric solution.

2) A small number of required parameters makes experimental validation easy.

6.1.1 The Hill-type muscle model

For the modeling of the dynamic behavior of muscle several approaches can be found (e.g. [Zajac, 1989]). The muscle model applied in the present thesis was developed by Hill in 1938 ([Hill, 1938], [Hill, 1953]). Its conceptual structure is displayed in Fig. 6.2 The model comprises three basic elements. The *contractile element* computes the

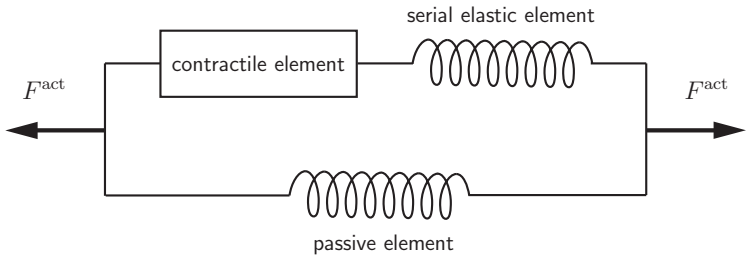

Figure 6.2: Conceptual structure of a Hill type muscle model

force a muscle can generate actively and uses the current state of muscle (length and lengthening/shortening velocity) as input parameters additionally to the activation. In series to the active element of muscle, a *serial elastic element* represents the elastic properties of tendon. The tendon force F^{act} is given as a function of tendon length and applied to the skeleton. It equilibrates the force produced by the contractile element. The model is completed by a *passive element* which represents the passive properties of muscle tissue.

Muscle kinematics

While in inverse dynamics applications actuator kinematics represent *output* values and can serve as a diagnostic indicator, actual total length of musculotendon pathway and corresponding lengthening/shortening velocity represent essential *input* values for the application of muscle driven musculoskeletal models in forward dynamics simulations. The corresponding values used in the scope of this thesis are based on the musculotendon pathway model described in Sec. 5.4.2, and are independent of the dynamic actuator model. Here also, the object-oriented approach allows for selected model improvements without modifications in other parts.

Muscle dynamics

The force generated by the muscle is computed as a superposition of the contributions yielded by the particular actuator substructures displayed in Fig. 6.2 and becomes

$$F = \underbrace{F^{\mathrm{M}} F_{\mathrm{P}}(\tilde{\ell})}_{\text{passive part}} + \underbrace{F^{\mathrm{M}} a(t) F_{\mathrm{L}}(\tilde{\ell}) F_{\mathrm{H}}(\tilde{v})}_{\text{active part}} \tag{6.1.1}$$

where $a(t)$ denotes the level of activation as a function of time, F^{M} the maximum isometric muscle force, $\tilde{\ell} = \ell / \left(\ell^{\mathrm{M}} + \ell^{\mathrm{S}}\right)$ the normalized musculotendon actuator length and $\tilde{v} = v/v_{\max}$ the normalized muscle velocity. The quantities $F^{\mathrm{M}}, \ell^{\mathrm{M}}$ and ℓ^{S} were adapted from biometric data supplied by [Yamaguchi, 2001] and are summarized in Appendix A. For the maximal shortening velocity $v_{\max}$, different values are known (between two and eight muscle lengths per second). Commonly accepted is the fact that the nominal muscle length represents an indicator of the ability of "slow" or "fast" shortening characteristics. In this thesis, the maximal shortening velocity of muscles is assumed as $v_{\max} = 5\ell^{\mathrm{M}}$. Recent literature studies reveal dependency of $v_{\max}$ of the activation level ([Camilleri and Hull, 2005]). However, such dependencies are neglected in the present context.

The influence of the current muscle state is characterized by the dimensionless functions $F_{\mathrm{P}}(\tilde{\ell}), F_{\mathrm{L}}(\tilde{\ell})$ and $F_{\mathrm{H}}(\tilde{v})$, which render appropriate weighting factors to the terms in (6.1.1). The *passive curve*

$$F_{\mathrm{P}}(\tilde{\ell}) = \begin{cases} \dfrac{1}{\exp\left(\mathrm{PEsh}\right) - 1}\left[\exp\left(\dfrac{\mathrm{PEsh}}{\mathrm{PExm}}\left(\tilde{\ell} - 1\right)\right) - 1\right] & \tilde{\ell} > 1 \\ 0 & \tilde{\ell} < 1 \end{cases} \tag{6.1.2}$$

represents a nonlinear reversible spring behavior that comes into effect when the muscle-tendon complex is stretched beyond its specific reference length. The parameter PExm describes the relative elongation $\left(\ell - \left(\ell^{\mathrm{M}} + \ell^{\mathrm{S}}\right)\right) / \left(\ell^{\mathrm{M}} + \ell^{\mathrm{S}}\right)$ caused by a passive muscle force of magnitude F^{M}, PEsh modifies the slope of the curve. These constants are typically determined empirically and were taken from ([Automotive, 2003]), applying PEsh = 5.0 and PExm = 0.8. The characteristics of the passive curve are displayed in Fig. 6.3 for a variety of parameters.

The ability of a muscle to generate forces due to an activation is described in terms of the *force-length curve*

$$F_{\mathrm{L}}(\tilde{\ell}) = \exp\left[-\left(\frac{\tilde{\ell} - 1}{\mathrm{Sk}}\right)^2\right], \qquad \tilde{\ell} \text{ arbitrary} \tag{6.1.3}$$

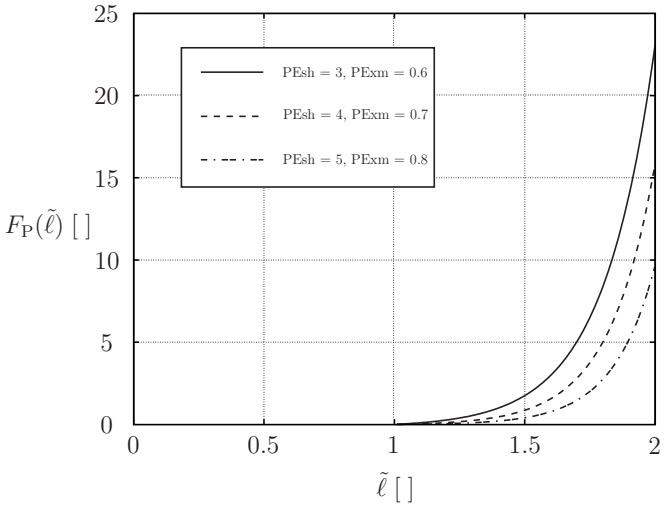

Figure 6.3: Passive force contribution in Hill-type muscle model

and the *force-velocity* relationship or *Hill-curve*

$$F_{\mathrm{H}}(\tilde{v}) = \begin{cases} 0 & \text{for} \quad \tilde{v} \leq -1 \\ \dfrac{1+\tilde{v}}{1-\dfrac{\tilde{v}}{\mathrm{CEsh}}} & \text{for} \quad \tilde{v} \in (-1, 0] \\ \dfrac{1+\tilde{v}\dfrac{\mathrm{CEml}}{\mathrm{CEshl}}}{1+\dfrac{\tilde{v}}{\mathrm{CEshl}}} & \text{for} \quad \tilde{v} > 0 \end{cases} \tag{6.1.4}$$

The parameters Sk in (6.1.3) and CEsh, CEshl and CEml in (6.1.4) are determined empirically and taken from ([Automotive, 2003]) as $\mathrm{Sk} = 0.4, \mathrm{CEsh} = 0.25, \mathrm{CEshl} = 0.075$ and $\mathrm{CEml} = 1.8$. The typical shapes of both relations are depicted in Fig. 6.4.

The total muscle force according to (6.1.1) is displayed in Fig.6.5 and was determined for a constant activation level $a(t) \equiv 1$ and a maximum muscle force $F = 1\,\mathrm{N}$.

In addition to the abovementioned formulas, according to [Zajac, 1989] the muscular contraction dynamics is considered, describing the force generated by the muscle due to an activation $a(t)$ as the solution of the first order differential equation

$$\frac{\mathrm{d}\tilde{F}^T}{\mathrm{d}\tau} = f\left(\tilde{\ell}^{\mathrm{MT}}, \tilde{F}^{\mathrm{T}}, a(\tau)\right) \ . \tag{6.1.5}$$

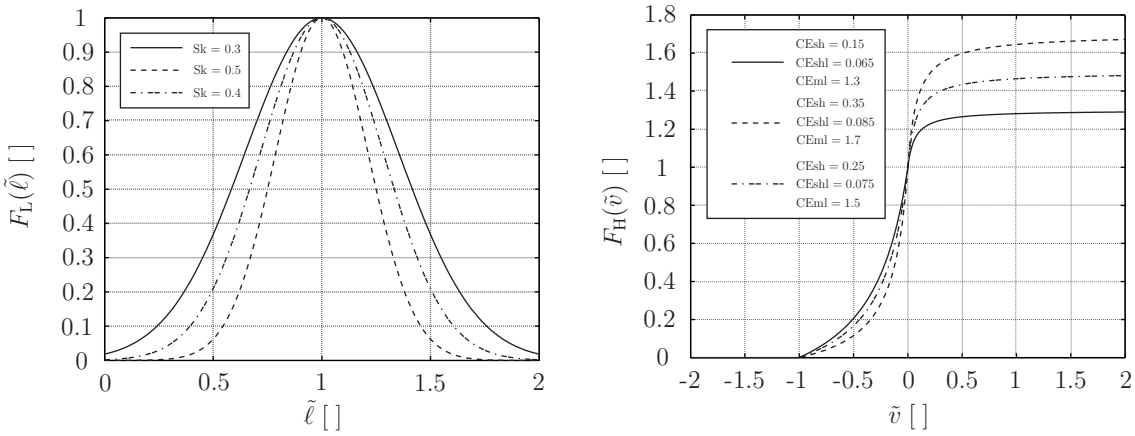

(a) Force-length relation (b) Force-velocity relation

Figure 6.4: Force-length relation and force-velocity relation for Hill-type muscle model for a variety of parameters

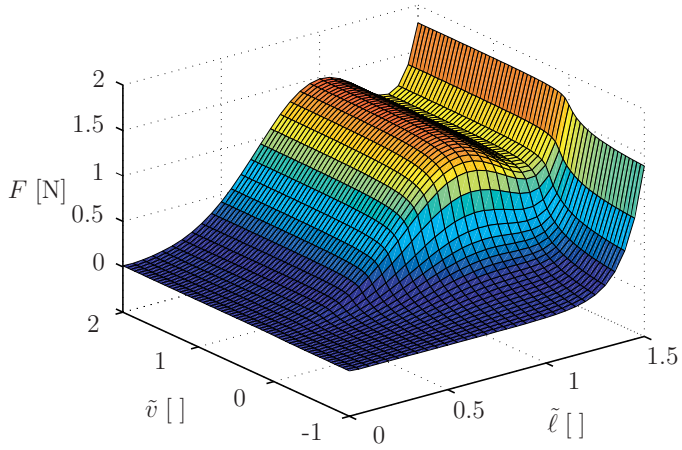

Figure 6.5: Total muscle force characteristics for simplified Hill-type muscle model

where

$$\begin{aligned} & f\left(\tilde{\ell}^{\mathrm{MT}}, \tilde{F}^{\mathrm{T}}, a(\tau)\right) \\ = \; & \tilde{k}^{\mathrm{T}}\left[\tilde{v}^{\mathrm{MT}} - F_{\mathrm{H}}^{-1}\left(\left\{\tilde{\ell}^{\mathrm{MT}} - \left(\tilde{\ell}_{\mathrm{S}}^{\mathrm{T}} + \frac{\tilde{F}^{\mathrm{T}}}{\tilde{k}^{\mathrm{T}}}\right)\right\}, \tilde{F}^{\mathrm{T}}, a(\tau)\right)\right] . \end{aligned} \tag{6.1.6}$$

In (6.1.5), $\tilde{F}^{\mathrm{T}}$ denotes the force applied to the skeleton via the tendon part of the musculotendon complex, normed with respect to the maximum force F^{M} the specific muscle can generate, i. e. $\tilde{F}^{\mathrm{T}} = F^{\mathrm{T}}/F^{\mathrm{M}}$. Moreover, $\tilde{\ell}^{\mathrm{MT}} = \ell^{\mathrm{MT}}/\ell^{\mathrm{M}}$ represents the actuator length normalized by the muscle part of the actuator, $a(\tau)$ is the activation

as a function of the dimensionless time $\tau = t/\tau_c$ where τ_c is a muscle-specific time-scaling factor. In the presented work, $\tau_c = 0.2$s has been chosen, corresponding to the maximal shortening velocity $v_{\max}$ of muscle. Moreover, in (6.1.6) $\tilde{k}^{\mathrm{T}}$ represents the tendon stiffness that can be read off from the force-strain relation of tendon displayed in Fig. 6.6.

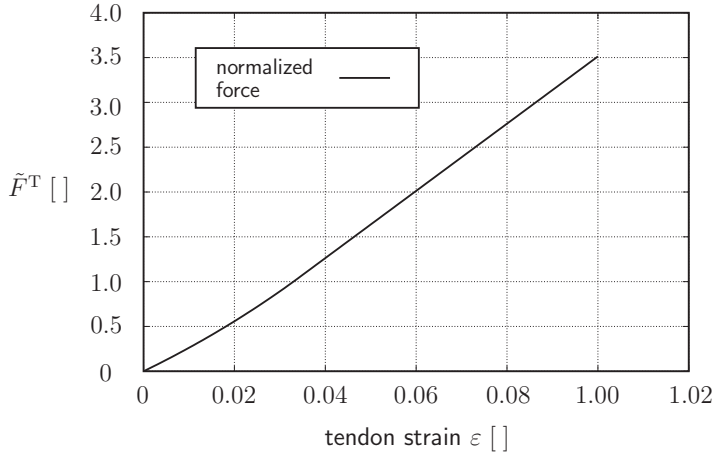

Figure 6.6: Normalized tendon force $\tilde{F}^{\mathrm{T}}$ as a function of tendon strain ε

The tendon is modeled as a nonlinear spring featuring only tension forces. In Fig. 6.6, a strain $\varepsilon = 0$ corresponds to a length of tendon equal to its slack length ℓ^{S} according to literature. As described by [Zajac, 1989], the force-strain relation is assumed to be linear above an elongation of $\varepsilon = 0.033$, displaying a constant tendon stiffness $\tilde{k}^{\mathrm{T}} = 37.5$. The force generated via this model can exceed the maximum muscle force that can be *actively* generated. A strain of $\varepsilon = 0.1$ is assumed unrealistic, leading to simulation termination. In addition, for an elongation of $\varepsilon = 0.033$, the tendon force corresponds to the maximal muscle force F_0^{M}. The description of the curve shape below this value differs in literature. In the scope of this thesis, this part of the force-strain relation of the tendon was approximated according to [Zajac, 1989] by

$$\tilde{F}^{\mathrm{T}}(\varepsilon) = \frac{1}{\exp(0.4) - 1}\left[\exp\left(\frac{0.4\varepsilon}{0.033}\right) - 1\right], \qquad \varepsilon \in (0, 0.033]\ . \tag{6.1.7}$$

During integration of (6.1.5), for a given value of the state variable $\tilde{F}^{\mathrm{T}}$, tendon strain is determined by evaluation of the inverse function of (6.1.7), taking the equilibrium of muscle and tendon force into account.

Further considerations of (6.1.6) show that the expression inside the squared brackets represents the actual tendon velocity which is computed from the superposition of the normalized actuator velocity $\tilde{v}^{\mathrm{MT}}$ and the normalized velocity of the muscular part of the actuator $\tilde{v}^{\mathrm{M}} = F_{\mathrm{H}}^{-1}(\tilde{\ell}^{\mathrm{MT}}, \tilde{F}^{\mathrm{T}}, a(\tau))$, with F_{H} defined according to (6.1.4). The dependency of the function F_{H}^{-1} on the arguments $\tilde{\ell}^{\mathrm{MT}}, \tilde{F}^{\mathrm{T}}$ and $a(\tau)$ results from the resolution of (6.1.1) with respect to $\tilde{v}^{\mathrm{M}}$. Considering the inverse force-velocity relation

$$F_{\mathrm{H}}^{-1}(x) = \begin{cases} -1 & \text{for} \quad x < 0 \\ \dfrac{x-1}{1+\dfrac{x}{\mathrm{CEsh}}} & \text{for} \quad x \in [0,1] \\ \dfrac{(x-1)\mathrm{CEshl}}{\mathrm{CEml}-x} & \text{for} \quad x > 1 \end{cases} \tag{6.1.8}$$

with parameters CEsh = 0.25 and CEshl = 0.075 ([Automotive, 2003], see Fig. 6.7), its function argument x

$$x = \frac{F^{\mathrm{M}} - F^{\mathrm{M}} F_{\mathrm{P}}(\tilde{\ell}^{\mathrm{M}})}{F^{\mathrm{M}} a(t) F_{\mathrm{L}}(\tilde{\ell}^{\mathrm{M}})} \,. \tag{6.1.9}$$

results from the resolution of (6.1.1) with respect to $\tilde{v}^{\mathrm{M}}$.

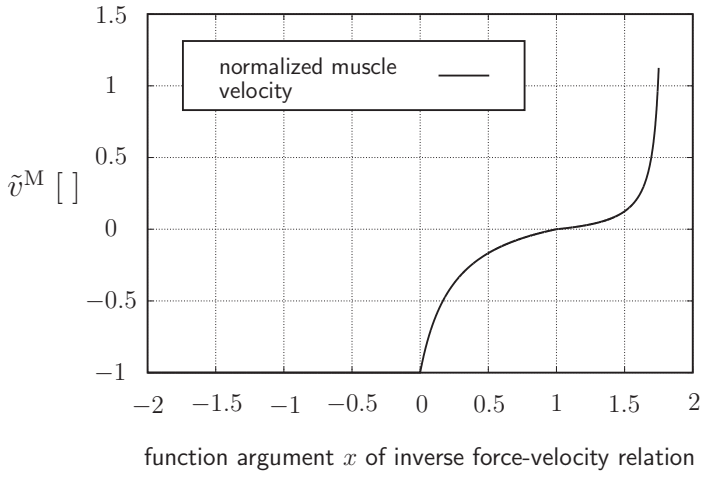

Figure 6.7: Inverse force-velocity relation of the Hill-type model

During the evaluation of (6.1.9), numerical problems appear when an activation $a(t) = 0$ is applied. This problem is circumvented as suggested by Zajac ([Zajac, 1989]) by applying a lower limit $a_{\min} = 10^{-6}$ such that $a(t) > a_{\min}$ for all t.

Input to the muscle model are the activation and the state of the muscle (length and lengthening/shortening velocity). While the latter is easily computed by virtue of the method described in Section 6.1.1, activation is modeled in a simplified manner and used as a design parameter for the dynamic optimization model, as described next.

6.2 Modeling of muscle activation time histories

A common method in literature to describe the complete neuro-muscular effects is to combine a HILL-type muscle model with a model describing the dynamics of muscle activation (see. Fig. 6.8). For the activation sub-model, the neuronal signal, termed *excitation* in the following, serves as the only input. The generated output is then considered as muscle *activation* and is (among other input data) passed to the model representing the dynamic properties of a muscle. A detailed discussion of such model types can be found in [Zajac, 1989].

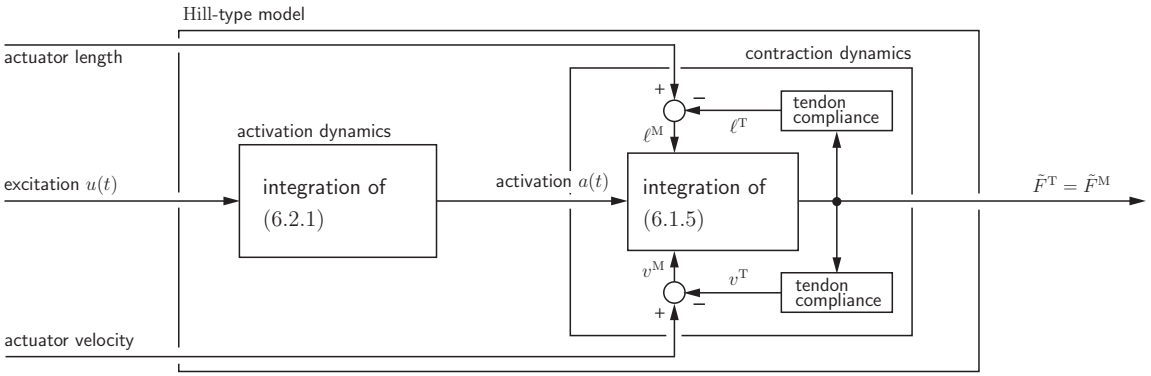

Figure 6.8: Block diagram displaying sub-model interaction in a Hill-type muscle model

To be able to perform forward dynamics simulations, two options are possible:

(1) Discretization of the input signals on *excitation level*. In this case, the modeling is exact, but time consuming.

(2) Discretization of the input signals on *activation level*, neglecting activation dynamics. As shown in more detail in Sec. 6.2.2, this yields an improvement in computational time. At the same time, such simplifications can lead to infeasibility problems in muscle activation prediction. For example, the neglect of the

PT_1-behavior of activation dynamics can yield an unnatural abrupt increase or decrease of muscle activation.

In this section, a brief description of an activation dynamics model is given (Sec. 6.2.1). After that, the computational benefit achieved by neglect of activation dynamics in the modeling is illustrated (Sec. 6.2.2). The section finishes with the proposal of two simplified discretizations of muscle *activation* (Sec 6.2.3).

6.2.1 Literature model description: activation dynamics

To get insight into muscle activation time histories, typically, EMG measurements are performed synchronously to a motion capturing process. However, the achieved results can mostly only serve for verification purposes due to their sensitivity to several factors such as sub-dermal muscle depth, skin preparation and interference of crossing muscles. In addition, the measurement results do not yield muscle *activation* $a(t)$, but instead represent neuronal *excitation* $u(t)$. The relationship between the two is given by the differential equation

$$\frac{\mathrm{d}a(t)}{\mathrm{d}t} + \left[\frac{1}{\tau_{\mathrm{act}}}\left(\beta + [1-\beta]\,u(t)\right)\right] a(t) = \left(\frac{1}{\tau_{\mathrm{act}}}\right) u(t) \tag{6.2.1}$$

with $0 < \beta = \text{const.} < 1$. The constant parameters β and τ_{act} influence activation and deactivation rates. While the activation rate is directly given in terms of τ_{act}, the deactivation rate is represented in terms of $\tau_{\mathrm{act}}/\beta := \tau_{\mathrm{deact}}$, i.e. β represents the ratio of activation and deactivation rates. Typically, τ_{deact} is larger than τ_{act}. The values for all parameters currently underly discussion and vary in literature.

The parameterization of muscle excitation $u(t)$ is part of the modeling assumptions. Mostly, piecewise constant (Fig. 6.9) or piecewise linear parameterizations are applied. Exemplary results of the integration of (6.2.1) are displayed in Fig. 6.9 for $\tau_{\mathrm{act}} = 0.015\mathrm{s}, \tau_{\mathrm{deact}} = 0.05\mathrm{s}$ ([Thelen, 2003]). Differences in amplitude and a delay of the activation time history with respect to the excitation can be observed. Nevertheless, the location of peaks in both curves are comparable which represents the basis of the simplifications described in Sec. 6.2.2.

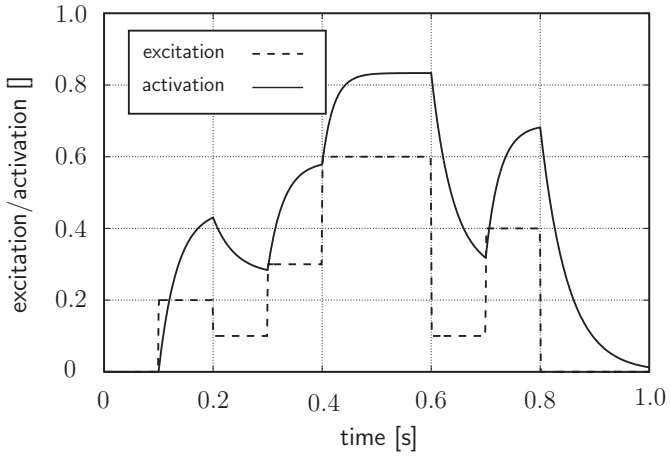

Figure 6.9: Muscle excitation/activation mapping

6.2.2 Computational effort

Computational time represents an important issue in forward dynamics simulation of human gait (see e.g. [Spaegele, 1998], [Anderson and Pandy, 1999a]). In this respect, it appears reasonable to find a compromise between model accuracy and computational speed. This is even more so as already the input data is quite inaccurate due to (1) imprecise measurements, (2) simplifying assumptions and/or (3) scaling.

In the thesis at hand, a first simplification is the neglect of activation dynamics. The corresponding computational speeds are illustrated for the swing phase of a single leg with two options:

(1) A 1-DOF model driving the knee joint only. The knee joint is modeled as a simple hinge, driven by an antagonistic muscle pair (*biceps femoris caput brevis* and *vastus intermedius*). The number of muscles was increased by adding *vastus lateralis* and *vastus medialis* subsequently to investigate CPU time sensitivity to that influence.

(2) A 2-DOF model driving knee and ankle joint. Both joints are modeled as simple hinges driven by antagonistic muscle pairs (*biceps femoris caput brevis* and *vastus intermedius* at the knee, *tibialis anterior* and *tibialis posterior* at the ankle). The number of muscles was increased by adding *vastus lateralis* and *vastus medialis* subsequently to investigate CPU time sensitivity to that influence.

All other involved joints are driven by rheonomic constraints prescribing measured kinematics. Segmental dimensions and inertias stem from literature biometric data (Appendix A), joint kinematics are provided by gait laboratory measurements for an individual with segment properties comparable to literature data. For each model option, two simulation setups were tested and compared in terms of CPU time consumption during integration:

(a) Prescription of *muscle activation* using a simplified model, neglecting activation dynamics.

(b) Prescription of *muscle excitation* using the literature model including activation dynamics.

The model of muscle activation in the simplified approach is described in Sec. 6.2.3.

To achieve comparable results for the simulation setups (a) and (b), the corresponding input data was prescribed such that the resulting motion at the respective dynamically driven joints appear in the range of at most ± 2 degrees of a measured target curve. Numerical integration was performed using an Adams-Moulton-Bashforth integrator with equal setup.

		no activation dynamics (simulation setup (a))			activation dynamics (simulation setup (b))		
		# of integrations			# of integrations		
# of DOF	# of muscles	1000	5000	10000	1000	5000	10000
1	2	1	1	1	1,98	1,99	1,97
1	3	1	1	1	2,0	2,0	2,01
1	4	1	1	1	2,1	2,1	2,1
2	4	1	1	1	2,02	2,02	2,02
2	5	1	1	1	2,01	2,0	2,01
2	6	1	1	1	2,1	2,1	2,1

Table 6.1: CPU time consumption comparison during integration: activation dynamics vs. neglect of activation dynamics

The data presented in Tab. 6.1 relates CPU-time consumption to the number of integrations. Data reported for the model including activation dynamics (simulation setup

(b)) is always set in relation to the simulation run for the simplified model (simulation setup (a)) using the same model option, i.e. the same number of DOF and involved muscles. As can be seen, the average CPU time consumption using the simplified approach is reduced by factor two, considering the pure number of integrations. This factor does not appear sensitive to increasing the number of involved muscles.

6.2.3 Actuator profile simplifications

Considering full gait cycle, literature data suggests that a specific muscle typically shows a limited number of periods with strong activation (typically, 1–2 "bumps", see, e.g., [Crowninshield and Brand, 1981], [Perry, 1992]). This observation is used to reduce the complexity of the function search space within a possible dynamic optimization process as described below.

Based on the investigation results discussed in Sec. 6.2.2, a simplified model of muscle activation profile is proposed that employs linear combinations of a limited number of exponential basis functions rendering smooth "bump" behavior. The fact that the basis functions are chosen in terms of exponential $\mathcal{C}^\infty$-functions accommodates the typical literature approach which assumes muscle activation to be differentiable (since it represents a solution of the differential equation (6.2.1)).

For a "two-bump" activation profile, the corresponding dimensionless activation function becomes

$$a(t) = A_1 e^{-C_1(t-T_1)^2} + A_2 e^{-C_2(t-T_1)^2}, \tag{6.2.2}$$

where the dimensionless amplitudes $A_1, A_2 \in [\,0,\ 1\,]$, the time parameters $T_1 < T_2 \in [\,t_0,\ t_1\,], [T_1] = [T_2] = \mathrm{s}$, and the width influence parameters $C_1, C_2 \in [\,0,\ 2000\,], [C_1] = [C_2] = 1/\mathrm{s}^2$, represent the shaping parameters of the approach (see Fig. 6.10(a)). Here, t_0 and t_1 represent start and end of an investigated time interval and are chosen in a problem specific manner. Independently of the choice of the involved parameters, the activation function is bounded above by 1. In the sequel, the parameterization according to (6.2.2) will be termed the "exponential approximation".

The approach supplies a limited number of six parameters for each considered muscle in the illustrated case. In case that additional basis functions are required, this extension increases the number of design parameter by three for each function. The horizontal tangent at the beginning and the end of an activation period prevents an

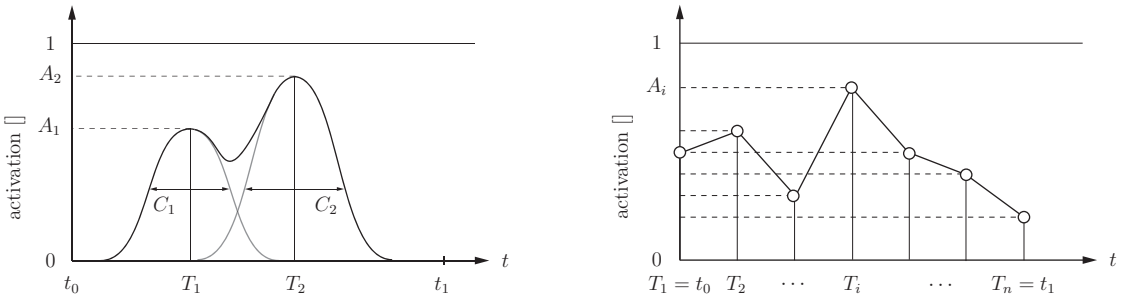

(a) exponential activation approximation

(b) polygonal activation approximation

Figure 6.10: Simplified muscle activation model: exponential and polygonal approximation

abrupt increase and decrease of muscle activation and therefore limits infeasibilities resulting from the neglect of an activation dynamics model.

Another approach for activation function modeling typically applied on *excitation level* is to use the piecewise linear approximation

$$a(t) = A_i + (t - T_i)\frac{A_{i+1} - A_i}{T_{i+1} - T_i}, \qquad i = 0, \ldots, n\,; \quad t \in [T_i, T_{i+1})\,, \tag{6.2.3}$$

where $T_0 < \ldots < T_i < \ldots < T_n \in [\,t_0,\ t_1\,]\,, [T_i] = \mathrm{s}$, represent (preselected and fixed) sampling times and the dimensionless amplitudes $A_i \in [\,0,\ 1\,]$ denote the corresponding (variable) sampling values (see Fig. 6.10(b)). The parameter n denotes the number of design parameters to be passed to the optimizing routine. The parameterization according to (6.2.3) will be termed "polygonal approximation" in the sequel. For a sufficiently small number of sampling points, this model also features a non-abrupt behavior at the beginning and the end of an activation period and therefore also limits infeasibilities resulting from the neglect of an activation dynamics model.

Approach (6.2.3) was assumed to perform quicker than (6.2.2) in forward dynamics simulations due to the extremely simple mathematical description and to supply larger "local" flexibility because of an arbitrary number of design variables A_i. However, the same large number n of design parameters can make optimum finding difficult, or even prevent the optimizer of converging, coming typically along with significantly longer computation times.

The proposed discretizations were applied to simplified subsystems of the human leg to predict muscle activation by dynamic optimization. A description of the biomechanical models and the discussion of the simulation results is given in Sec. 6.3.

6.3 Dynamic optimization

In this section, after the presentation of the applied objective functions as well as the simplified biomechanical models used in the model experiments, the results of the application of the proposed method are evaluated in target motion approximation quality, feasibility of the predicted muscle activation time histories in comparison to measurements reported in literature, performance in terms of computational time as well as the sensitivity with respect to parameter perturbations.

6.3.1 Objective functions for dynamic optimization

The choice of an appropriate objective function in dynamic optimization is a topic of continuing research. The commonly applied assumption of a minimized consumption of metabolic energy ([Anderson and Pandy, 2001]) is suitable for generic studies, but for patient-specific identification especially for pathological gait motion a more kinematically-oriented approach is needed. In this setting, four basic objective functions were tested:

$$F_1(\underline{x}) = \frac{1}{2m}\sum_{i=1}^{m}\left(\varphi^t(t_i) - \varphi^c(t_i,\underline{x})\right)^2 , \tag{6.3.1}$$

$$F_2(\underline{x}) = \frac{1}{2m}\sum_{i=1}^{m}\left(\varphi^t(t_i) - \varphi^c(t_i,\underline{x})\right)^2 + \frac{\alpha_{2,1}}{2}\sum_{i=1}^{m}\left(\dot{\varphi}^t(t_i) - \dot{\varphi}^c(t_i,\underline{x})\right)^2 \tag{6.3.2}$$

$$\begin{aligned} F_3(\underline{x}) \;=\; & \frac{1}{2m}\sum_{i=1}^{m}\left(\varphi^t(t_i) - \varphi^c(t_i,\underline{x})\right)^2 + \frac{\alpha_{3,1}}{2m}\sum_{i=1}^{m}\left(\dot{\varphi}^t(t_i) - \dot{\varphi}^c(t_i,\underline{x})\right)^2 + \\ & + \frac{\alpha_{3,2}}{2m}\sum_{i=1}^{m}\left(\ddot{\varphi}^t(t_i) - \ddot{\varphi}^c(t_i,\underline{x})\right)^2 , \end{aligned} \tag{6.3.3}$$

$$\begin{aligned} F_4(\underline{x}) \;=\; & \frac{1}{2m}\sum_{i=1}^{m}\left(\varphi^t(t_i) - \varphi^c(t_i,\underline{x})\right)^2 + \frac{\alpha_{4,1}}{2m}\sum_{i=1}^{m}\left(\dot{\varphi}^t(t_i) - \dot{\varphi}^c(t_i,\underline{x})\right)^2 + \\ & + \frac{\alpha_{4,2}}{2m}\sum_{i=1}^{m}\left(\ddot{\varphi}^t(t_i) - \ddot{\varphi}^c(t_i,\underline{x})\right)^2 + \frac{\alpha_{4,3}}{2m}\sum_{i=1}^{m}\sum_{j=1}^{p}\frac{F_j(t_i)^2}{\mathrm{PCSA}_j^2} , \end{aligned} \tag{6.3.4}$$

where $\underline{x}$ is the vector of muscle activation parameters. The target angle $\varphi^t(t_i)$ is obtained by sampling the measured angle $\varphi(t)$ at m discrete instants in time. The

parameter m denotes the number of output sampling points. Likewise, the computed angle $\varphi^c(t_i, \underline{x})$ is obtained by performing a forward dynamics simulation of the complete model and sampling this function at the prescribed output points in time t_i. Target angular velocities and accelerations were not directly measured, but computed by numerical differentiation of the angle time histories. Target angular velocity $\dot{\varphi}^t(t_i)$ and target angular acceleration $\ddot{\varphi}^t(t_i)$ as well as computed angular velocity $\dot{\varphi}^c(t_i, \underline{x})$ and computed angular acceleration $\ddot{\varphi}^c(t_i, \underline{x})$ are then obtained by sampling the results of the numerical differentiations. The fourth term in (6.3.4) represents a criterion to maximize the endurance of function according to [Crowninshield and Brand, 1981], which here only serves to resolve muscle redundancy. Here p denotes the number of muscles considered and PCSA_j represents the physiological cross section area of the muscles involved. These numbers are adopted from [Yamaguchi, 2001]. Finally, $F_j(t_i)$ are the computed forces of each muscle at sampling time t_i.

The weighting factors $\alpha_{2,1}, \alpha_{3,1}, \alpha_{3,2}, \alpha_{4,1}, \alpha_{4,2}$ and $\alpha_{4,3}$ in (6.3.2)–(6.3.4) were chosen in terms of total simulation time T such that no differences in physical dimensions of the individual terms appear. Typical numerical values are given in Table 6.3.1. The performed model experiments showed that the results of the optimization procedures are highly sensitive to the choice of values of these scaling parameters.

weight	$\alpha_{2,1}$	$\alpha_{3,1}$	$\alpha_{3,2}$	$\alpha_{4,1}$	$\alpha_{4,2}$	$\alpha_{4,3}$
value	T	T	$T^2 \cdot 10^{-3}$	T	$T^2 \cdot 10^{-3}$	10^{-5}

Table 6.2: Weights applied in the cost functions (6.3.2)–(6.3.4)

6.3.2 Model experiments and results

Several simple and/or reduced model experiments were performed and the resulting activation time histories compared to literature results. The results of two of them are discussed in detail in the following.

Model experiment 1

Fig. 6.11 shows the first example. It consists of a subsystem of the right leg comprising a fixed hip, thigh, shank and foot segment. The model is driven by two pairs of

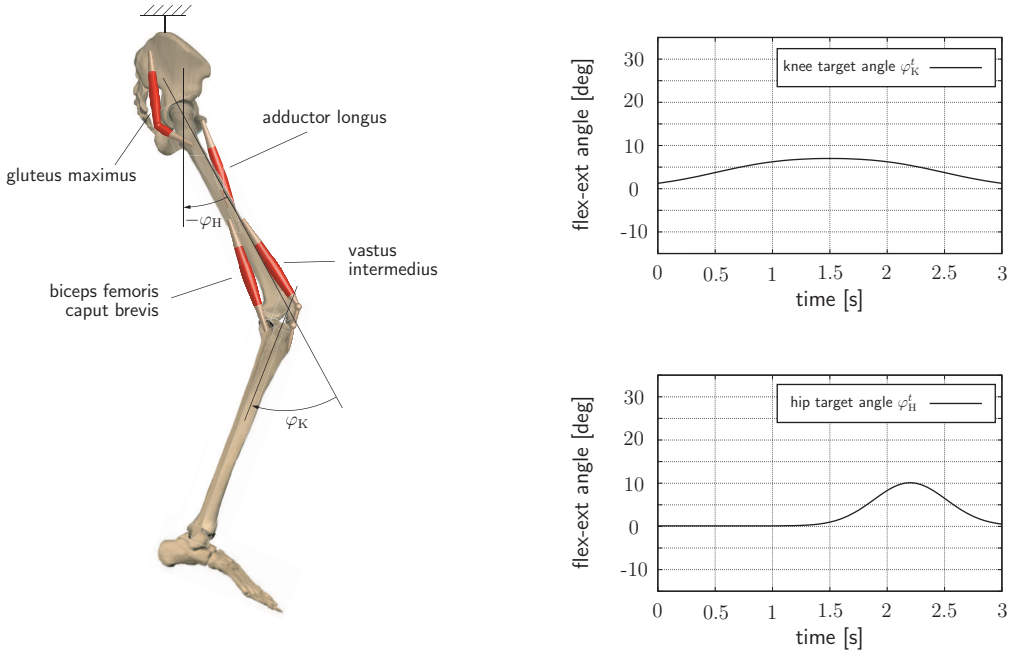

Figure 6.11: Model experiment 1: two-joint subsystem of right leg and exemplary hip and knee target motion prescription (bone geometries taken from [Sobotta, 2005])

antagonistic muscles (*adductor longus, gluteus maximus, biceps femoris caput brevis, vastus intermedius*), serving as representatives of all muscles responsible for the corresponding joint flexion-extension motion. Hip and knee joint are assumed to supply only one degree of freedom for flexion-extension each and are modeled as simple hinges. All other joints are arrested in neutral position. The total simulation time was set to $T = 3$s. Biometric data was chosen according to [Yamaguchi, 2001] and is summarized in Appendix A. The objective function for the optimization problem was chosen according to (6.3.1) for hip and knee flexion-extension angle. The output sampling step size $\Delta t = t_{i+1} - t_i$ was varied between 0.001 s and 0.5 s leading to $m = T/(\Delta t + 1)$ between 6 and 3000. The number of muscles included in the system lead to $n = 24$ design parameters in case of the smooth function approach (6.2.2) and was changed in case of the input sampling approach (6.2.3) between $n = 24$ and $n = 40$.

Performance of each approach was assessed in terms of CPU time and approximation quality at the final iterate $\underline{x}^*$. Activation time history was not in the focus here since the motion prescription was purely academic. Typical results of the optimization procedure are displayed in Fig. 6.12 for $\Delta t = 0.1$ s ([Strobach et al., 2005], [Strobach and Kecskeméthy, 2005]).

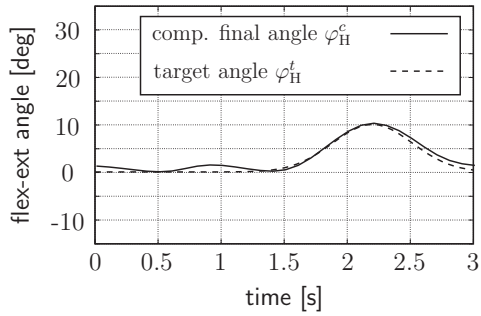

(a) hip flexion angle (polygonal approximation)

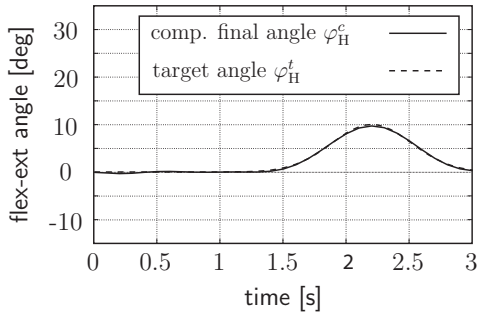

(b) hip flexion angle (exponential approximation)

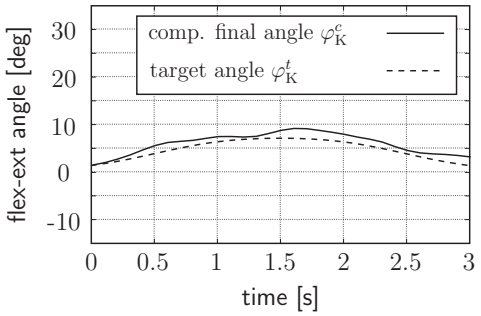

(c) knee flexion angle (polygonal approximation)

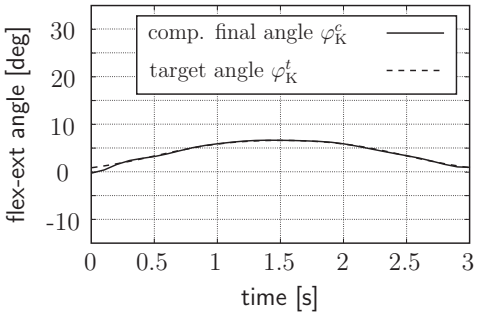

(d) knee flexion angle (exponential approximation)

Figure 6.12: Optimization results for the biomechanical system shown in Fig. 6.11

In the polygonal approximation (Fig. 6.12(a) and Fig. 6.12(c)) the total number of sampling times T_i was set to 10, i.e. $n = 9$ in (6.2.3). As can be seen, the exponential approximation renders a better fitting to the target curves in comparison to the polygonal approach. Evaluation of the objective function for the experiment settings related to Fig. 6.12 showed a 5 times lower function value at the final iterate. At the same time, the exponential approximation performed in 35% less computational time than the polygonal approximation.

This result appeared independently of variations in the number of output sampling step sizes Δt. Even a significant increase in the number of design parameters in the polygonal approximation does not yield a comparatively acceptable target approximation. In addition, much longer computational times were observed, making the polygonal approximation unsuitable for rough estimations of muscle activation.

Model experiment 2

The second example system represents a variation where pelvis motion in the sagittal plane, hip flexion-extension motion as well as ankle dorsi-plantarflexion motion is prescribed by rheonomic constraints. Hence, muscles *gluteus maximus* and *adductor longus* can be omitted. The prescribed motion is given in terms of measured kinematics of a male adult's right leg swing-phase motion.

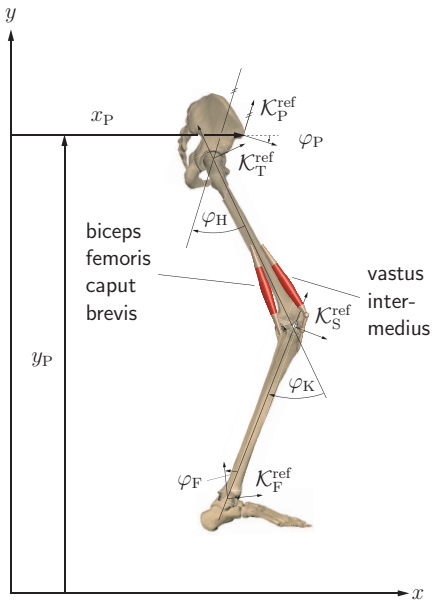

Figure 6.13: Model experiment 2: planar subsystem of right leg with guided pelvis, hip and ankle joint motion (bone geometries taken from [Sobotta, 2005])

The biometric data of the measured specimen is comparable to the biometric data reported in [Yamaguchi, 2001], therefore the kinematic data could be directly applied to the literature specimen without scaling. Measured hip and knee joint angles, angle rates and angular accelerations are displayed in Fig. 6.14 for the swing phase period of 0.456s. The objective function used in this example was chosen according to (6.3.4). Here, the last term can be expressed as

$$\frac{\alpha_{4,3}}{2}\sum_{i=1}^{m}\left(\frac{F_b(t_i)}{\mathrm{PCSA}_b}+\frac{F_v(t_i)}{\mathrm{PCSA}_v}\right)^2, \tag{6.3.5}$$

where, $F_b(t_i), F_v(t_i), \mathrm{PCSA}_b$ and PCSA_v denote the forces in muscle *biceps femoris caput brevis* and *vastus intermedius* at time t_i and the corresponding physiological cross section areas, respectively.

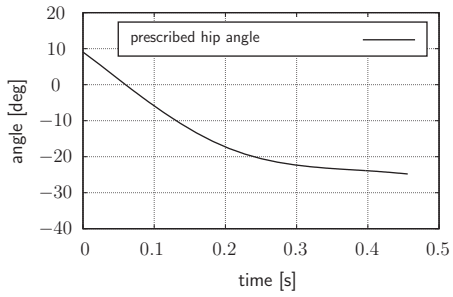

(a) hip flex-ext angle prescription

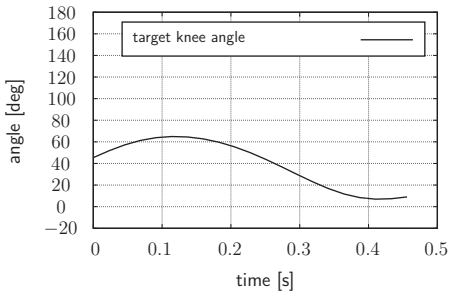

(b) knee flex-ext angle target

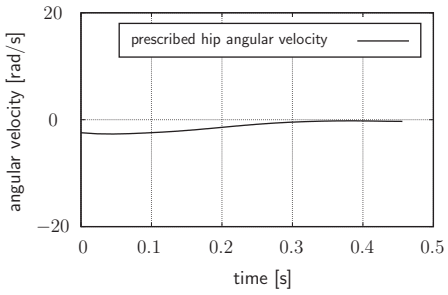

(c) hip flex-ext angular velocity prescription

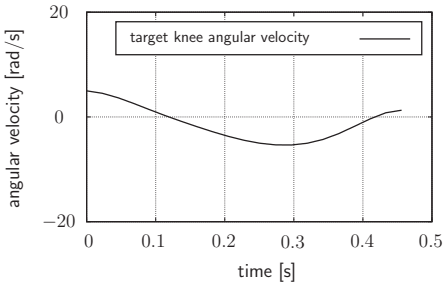

(d) knee flex-ext angular velocity target

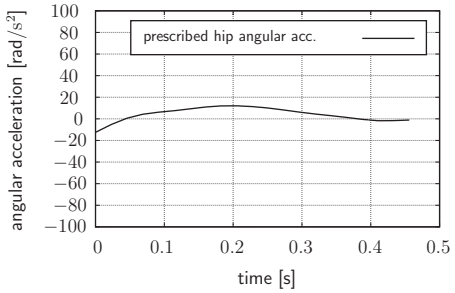

(e) hip flex-ext angular acceleration prescription

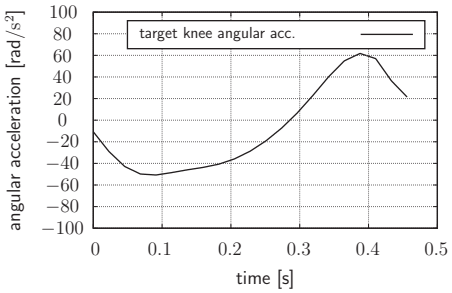

(f) knee flex-ext angular acceleration target

Figure 6.14: Model experiment 2: swing phase flexion-extension prescribed hip and target knee motion for two-joint system

The following termination criteria were introduced:

$$K_1 \geq \frac{1}{\Delta\varphi^2_{\mathrm{K,max}}} \sum_{i=1}^{m} \left(\varphi_{\mathrm{K}}(t_i) - \varphi^c_{\mathrm{K}}(t_i, \underline{\tilde{x}})\right)^2 , \tag{6.3.6}$$

$$K_2 \geq \frac{1}{\Delta\dot{\varphi}^2_{\mathrm{K,max}}} \sum_{i=1}^{m} \left(\dot{\varphi}_{\mathrm{K}}(t_i) - \varphi^c_{\mathrm{K}}(t_i, \underline{\tilde{x}})\right)^2 , \tag{6.3.7}$$

$$K_3 \geq \frac{1}{\Delta\ddot{\varphi}^2_{\mathrm{K,max}}} \sum_{i=1}^{m} \left(\ddot{\varphi}_{\mathrm{K}}(t_i) - \varphi^c_{\mathrm{K}}(t_i, \underline{\tilde{x}})\right)^2 . \tag{6.3.8}$$

Physically, these requirements correspond to an averaged approximation of the target curve within a given threshold.

The number of output sampling points was set to $m = 46$ (corresponding to a sampling rate of 0.01s), weights in the objective function were chosen according to Tab. 6.3.1. For the termination criteria, $K_1 = 0.6, K_2 = 0.2,\ K_3 = 0.4$ and $\Delta\varphi_{\mathrm{K,max}} = 2°, \Delta\dot{\varphi}_{\mathrm{K,max}} = 2\mathrm{rad/s}$ and $\Delta\ddot{\varphi}_{\mathrm{K,max}} = 2\mathrm{rad/s}^2$ were applied. The optimization run using the polygonal approximation was performed for 15 sampling points amplitudes. Initial amplitudes were determined by sampling the corresponding initial guess assumed for the exponential approximation ([Strobach and Kecskeméthy, 2006]).

The resulting activation time histories are shown in Fig. 6.15. There, the solid line represents the predicted activation time history for the exponential discretization, the dashed line corresponds to the prediction achieved by application of the polygonal approximation and the shaded regions cover measured periods of activation reported in literature for knee flexor/extensor muscle groups (e.g. [Perry, 1992], [Bechtol, 1975]). It can be seen that the exponential approach yields activation time predictions that match to literature reports for both muscles. In contrast, the polygonal discretization shows deviations from literature data especially for muscle *biceps femoris caput brevis* in the first half of swing phase (Fig. 6.15(a)).

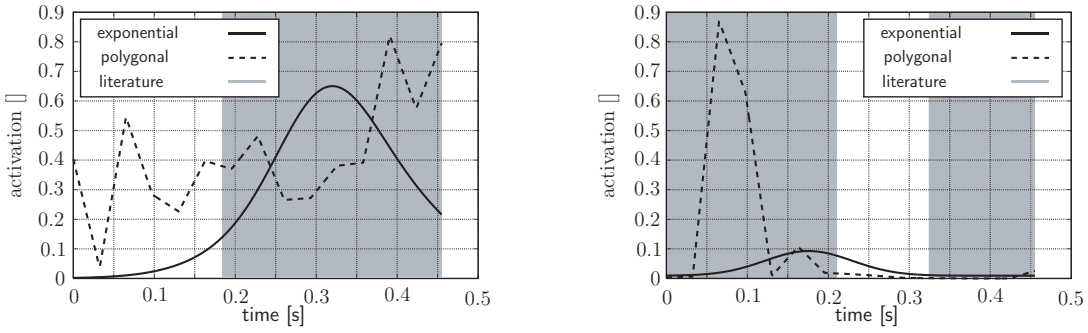

(a) *biceps femoris caput brevis* activation

(b) *vastus intermedius* activation

Figure 6.15: Model experiment 2: Optimization results for swing phase target motion (predicted muscle activation profiles)

Results in terms of target motion approximation are displayed in Fig. 6.16. The predicted knee joint position, velocity and acceleration matches to *pm* 4% the prescribed target. However, a detailed consideration of the results for the angular acceleration

shows a unnatural jerky motion for the polygonal approximation (Fig. 6.16(f)), while the exponential parameterization (Fig. 6.16(e)) leads to a naturally smooth performance. This jerky behavior is a direct consequence of the alternating muscle activation predicted by the polygonal parameterization (Fig. 6.15(a)).

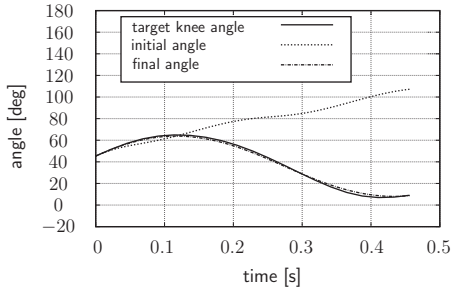

(a) knee flexion-extension angle (exponential approximation)

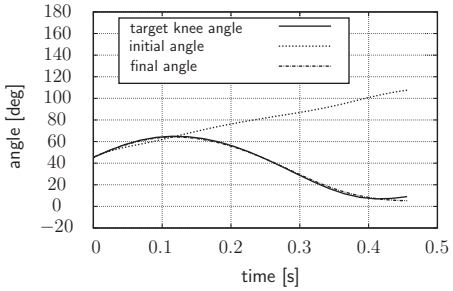

(b) knee flexion-extension angle (polygonal approximation)

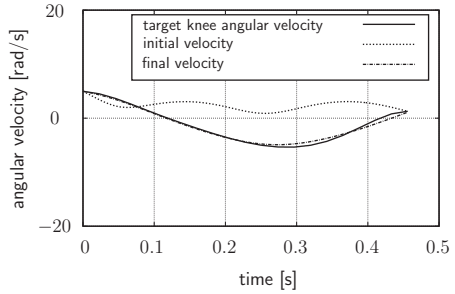

(c) knee flexion-extension angular velocity (exponential approximation)

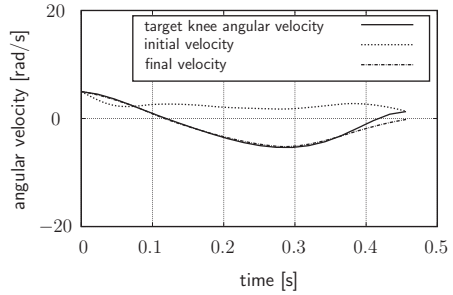

(d) knee flexion-extension angular velocity (polygonal approximation)

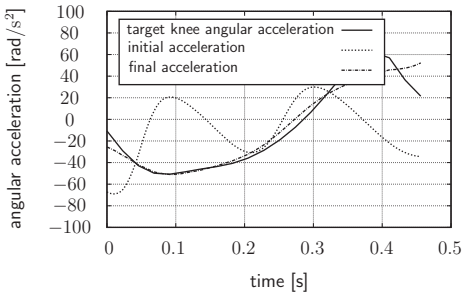

(e) hip flexion-extension angular acceleration (exponential approximation)

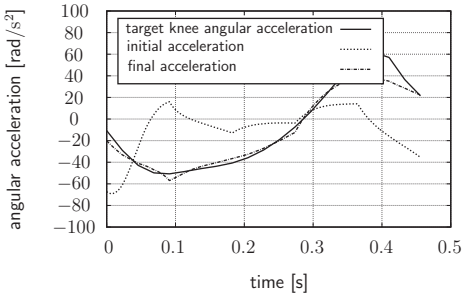

(f) knee flexion-extension angular acceleration (polygonal approximation)

Figure 6.16: Model experiment 2: Optimization results for swing phase target motion (angle, angular velocity and angular acceleration)

To compare both approaches in terms of computational efficiency, the number of output sampling times and the number of sampling points in case of the polygonal parameterization were varied and the results were assessed in terms of approximation quality (= final value of the applied objective function) and required computational time. As a representative example, Tab. 6.3 displays the results for 15 sampling values in the polygonal discretization and an objective function restricted to pure position approximation as defined in (6.3.1). Similar results were achieved for other combinations.

parameterization	# output sampling points	CPU-time	initial cost	final cost
polygonal	25	1686	166.8	3.612
polygonal	75	7621	156.2	0.37
exponential	25	451	164.0	0.3
exponential	75	2795	119.9	0.04

Table 6.3: Comparison of computational efficiency of polygonal and exponential activation discretization (objective function restricted to pure position approximation, 15 sampling points in case of polygonal parameterization)

The main results can be summarized as follows:

(1) The polygonal discretization does not yield a satisfactory approximation quality for small number of output sampling points. In the illustrated example, for 25 output sampling times, the polygonal approach converged to a local minimum in the vicinity of the initial guess (Tab. 6.3, 1st row, last column).

(2) Increasing the number of output sampling times improved the performance of the polygonal parameterization to an acceptable level of approximation (Tab. 6.3, 2nd row, last column).

(3) The exponential parameterization generally leads to acceptable approximation qualities. The presented example showed smaller final objective function values for larger number of output sampling times (Tab. 6.3, 4th row, last column), however increasing the number of output sampling times to values above 75 did not lead to further improvement (not displayed).

(4) Comparing the computational effort for similar target approximations (polygonal discretization with 75 output sampling points vs. exponential parameterization

with 25 output sampling points) shows an improvement of CPU time by the exponential approach by the factor of 16.8.

Summary of results

In conclusion, the following results are obtained:

- The simplified activation parameterizations on *activation* level reduces CPU-time consumption during the integration of the equations of motion by a factor of 2 in comparison to a the literature model including activation dynamics.
- The exponential approximation yields realistic regions of muscle activation in comparison to measurements reported in literature. Activation profiles predicted by the polygonal approach partially show deviations from literature reports.
- Accelerations obtained by application of the polygonal discretization can show an unnatural jerky behavior.
- The exponential approximation yields an improvement of CPU time by a factor of 16 for comparable result quality.

6.3.3 Model experiment for sensitivity analysis

Dynamic optimization of musculoskeletal motion typically suffers from sensitivity with respect to parameter perturbations. Such perturbations can be purely numerical (e.g. the choice of the initial guess for the optimization) or parametric (e.g. uncertainties in model parameters such as muscle origin/insertion location). In order to analyze the influence of these two perturbations, numerical experiments were carried out as follows.

The biomechanical model used for the investigation is similar to that described in Sec. 6.3.2. Perturbations were applied exclusively to muscle *biceps femoris caput brevis*:

(1) The initial activation parameters are variated. Starting from a reference initial guess $\{ A_1^*, A_2^*, C_1^*, C_2^*, T_1^*, T_2^* \}$ according to the exponential activation approximation, each parameter is decreased and increased by 10% of it's initial value. Variations were performed such that only one parameter is changed while all

other parameters remain at their reference values. Exemplarily, the first computations for a perturbed parameter set were performed for the initial activation parameters

$$\{\ 1.1 \cdot A_1^*, A_2^*, C_1^*, C_2^*, T_1^*, T_2^*\ \}\ . \tag{6.3.9}$$

After each perturbation, an identification process was accomplished using each of the objective functions (6.3.1)—(6.3.4).

(2) The ratio of tendon and muscle tissue reference length ℓ^{S} and ℓ^{M} in the actuator model is variated (Fig. 6.17(a)). With respect to the ratio reported in [Yamaguchi, 2001], the portion of muscle tissue is variated by ±6% in steps of 1% subsequently. The tendon length is modified correspondingly such that the total actuator reference length remains unchanged at its literature value. Exemplarily, the first computations for a perturbed parameter set were performed for muscle parameters

$$\ell^{\mathrm{M}} = 0.99 \cdot \ell^{\mathrm{M}}_{\mathrm{ref}}, \qquad \ell^{\mathrm{S}} = \ell^{\mathrm{S}}_{\mathrm{ref}} + 0.01 \cdot \ell^{\mathrm{M}}_{\mathrm{ref}}\ , \tag{6.3.10}$$

where $\ell^{\mathrm{M}}_{\mathrm{ref}}$ and $\ell^{\mathrm{S}}_{\mathrm{ref}}$ denote the literature reference parameters of muscle and tendon length, respectively. After each perturbation, an identification process was accomplished using each of the objective functions (6.3.1)—(6.3.4). For all considered optimization runs, equal initial activation parameters were applied.

(3) Muscle origin and insertion points are variated (Fig. 6.17(b)). They were initialized with the reference parameter set reported in [Yamaguchi, 2001] as

$${}^{\mathrm{T}}\mathbf{r}_{\mathrm{o}}^{\mathrm{right}} = \begin{bmatrix} o_x \\ o_y \\ o_z \end{bmatrix}\ , \qquad {}^{\mathrm{S}}\mathbf{r}_{\mathrm{i}}^{\mathrm{right}} = \begin{bmatrix} i_x \\ i_y \\ i_z \end{bmatrix} \tag{6.3.11}$$

and subsequently variated by the vectors

$$\left\{\ {}^{\mathrm{T}}\boldsymbol{\delta}_{\mathrm{o}},\ {}^{\mathrm{S}}\boldsymbol{\delta}_{\mathrm{i}}\ \right\} \in \left\{ \begin{bmatrix} \pm\Delta x \\ 0 \\ 0 \end{bmatrix}, \begin{bmatrix} 0 \\ \pm\Delta y \\ 0 \end{bmatrix}, \begin{bmatrix} 0 \\ 0 \\ \pm\Delta z \end{bmatrix} \right\} \tag{6.3.12}$$

with $\Delta x = \Delta y = \Delta z = 1\,\mathrm{mm}$ such that only one coordinate of either origin or insertion point was perturbed, while all other coordinates remained at the

literature values. Exemplarily, the first computations for a perturbed parameter set were performed for

$$ {}^{\mathrm{T}}_{p_1}\mathbf{r}_{\mathrm{o}}^{\mathrm{right}} = \begin{bmatrix} o_x + 1\mathrm{mm} \\ o_y \\ o_z \end{bmatrix}, \qquad {}^{\mathrm{S}}_{p_1}\mathbf{r}_{\mathrm{i}}^{\mathrm{right}} = {}^{\mathrm{S}}\mathbf{r}_{\mathrm{i}}^{\mathrm{right}} = \begin{bmatrix} i_x \\ i_y \\ i_z \end{bmatrix}. \tag{6.3.13} $$

After each perturbation, an identification process was accomplished using each of the objective functions (6.3.1)—(6.3.4). For all considered optimization runs, equal initial activation parameters were applied. To adapt the characteristic muscle parameters ℓ^{M} and ℓ^{S} (Appendix A) to the new configuration, the ratio

$$ r = \frac{\text{actuator length at literature coordinates for stretched knee}}{\text{actuator length at perturbed coordinates for stretched knee}} \tag{6.3.14} $$

was used to scale the literature values such that the amount of the contribution of the passive muscle part to the generated force was not unnaturally high due to pre-stressing or pre-relaxing the muscle in comparison to the reference situation ([Strobach et al., 2007]).

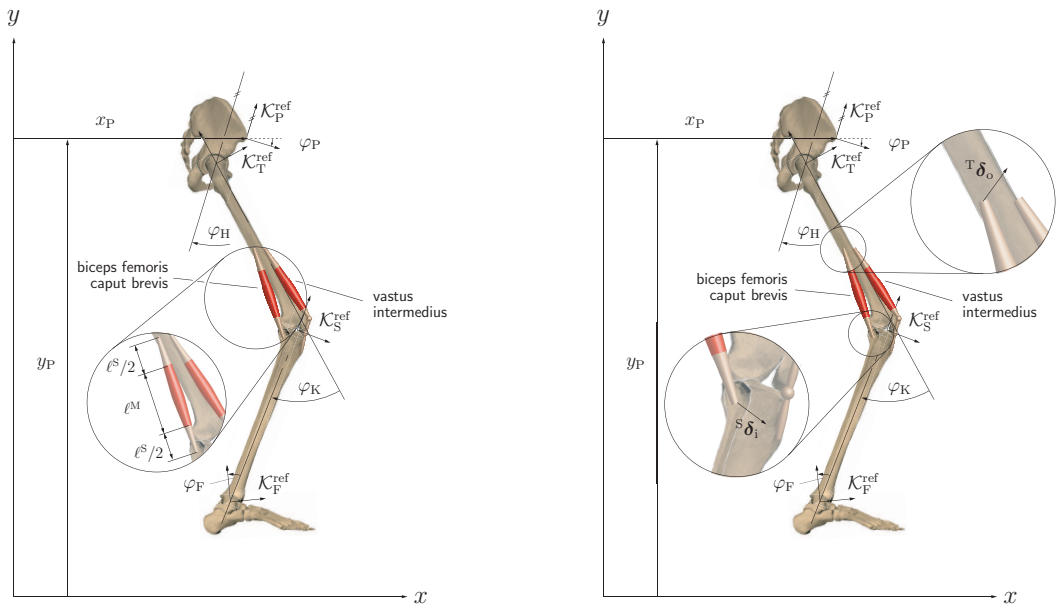

(a) Variation of tendon/muscle tissue length ratio

(b) Variation of origin/insertion points

Figure 6.17: Two-joint subsystem of right leg with guided pelvis and hip joint motion: parameter variation illustration (bone geometries taken from [Sobotta, 2005])

For all numerical simulations, the objective functions (6.3.1)—(6.3.4) were applied with weights chosen according to Tab. 6.3.1. For all optimization runs, $m = 100$ was used as number of output sampling points. Similar to the experiment discussed in Sec. 6.3.1, knee flexion-extension target velocity and acceleration time histories were determined by numerical differentiation of the measured knee flexion-extension time history. All other boundary conditions were set according to model experiment 2 discussed in Sec. 6.3.2.

Results of sensitivity investigation

Comparing the final computed knee flexion-extension angle time histories with the target curves shows that for all chosen objective functions the achieved target approximations are acceptable (Fig. 6.21–6.23). Due to the differential relationship between the considered quantities even the exclusive regard of the target position according to (6.3.1) leads to acceptable approximations also in angular velocity (see Fig. 6.21–6.23).

Additionally, these figures show that no significant reduction in standard deviation of velocity and acceleration approximation can be achieved by application of the objective functions (6.3.2)–(6.3.4). Hence, the results indicate that the application of the objective function (6.3.1) is sufficient to approximate the measured kinematic data. Furthermore, reducing the dimension of the objective function leads to a reduced computational time.

Considering the effect of initial guess variations in particular, a larger standard deviation in the optimization results than for other parameter variations can be observed (grey area in Fig. 6.21 in comparison to grey areas in Fig. 6.22 and Fig. 6.23), indicating a strong influence of the initial guess to the optimization result. This sensitivity can not be reduced by more detailed objective functions.

Considering the resulting activation curves qualitatively (Fig. 6.18–Fig. 6.20), it can be seen that they may vary in amplitude significantly in the second half of swing phase for all regarded objective functions. As *vastus intermedius* shows similar variations as *biceps femoris caput brevis*, only the latter is discussed.

In particular, the identified time histories of muscle activation for each variation of the initial guess (Fig. 6.18) and muscle origin/insertion point (Fig. 6.20) show differences of several orders of magnitude. Furthermore, also muscle coordination is severely affected, indicated by the noticeable time shift in the location of the maximum activation

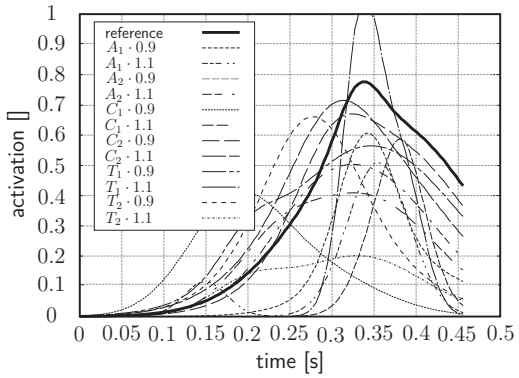

(a) Muscle activation for objective function (6.3.1)

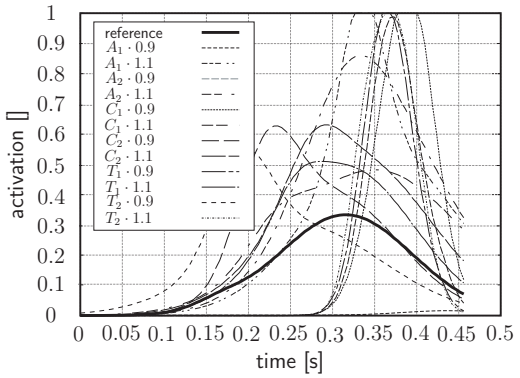

(b) Muscle activation for objective function (6.3.2)

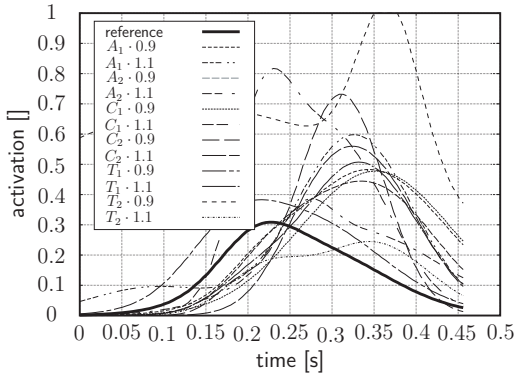

(c) Muscle activation for objective function (6.3.3)

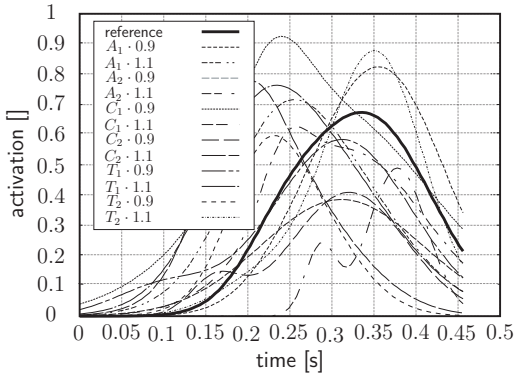

(d) Muscle activation for objective function (6.3.4)

Figure 6.18: Optimization results for objective functions (6.3.1)–(6.3.4): activation of muscle *biceps femoris caput brevis* after initial guess variation

amplitude. Additionally, it is remarkable that also in case of the unperturbed reference data set the results depend on the applied objective function, showing differences in amplitude of up to 300% (Fig. 6.20(a) and Fig. 6.20(d)). Again, no significant improvement by means of more detailed target prescriptions in terms of objective functions (6.3.2)–(6.3.4) is achieved. However, the consideration of additional data apart from pure angle time history seems to result in a stabilization of the solution in case of variations of muscle origin/insertion points. Here, the total variance in amplitudes is reduced especially in case of the objective functions (6.3.2) (Fig. 6.20(b)) and (6.3.4) (Fig.6.20(d)). In addition for regarding position and velocity target (6.3.2), apart from few exceptionally large amplitudes, the activation curves are located in a rather small environment of the "literature" curve according to the parameters reported by [Yamaguchi, 2001].

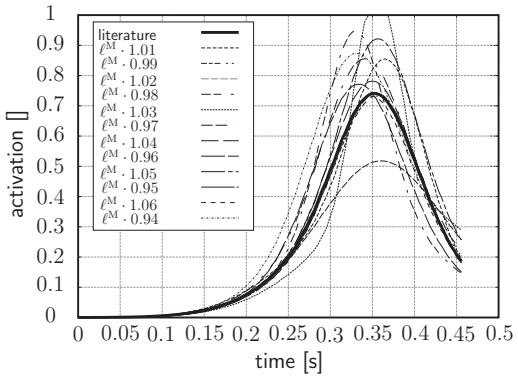

(a) Muscle activation for objective function (6.3.1)

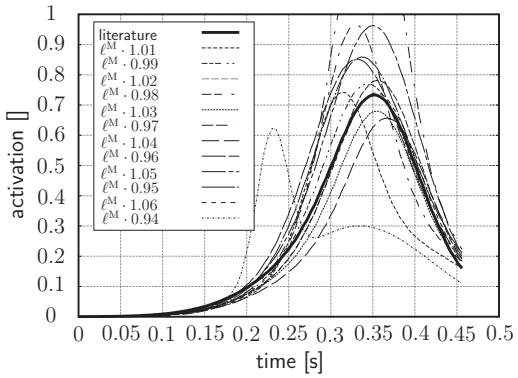

(b) Muscle activation for objective function (6.3.2)

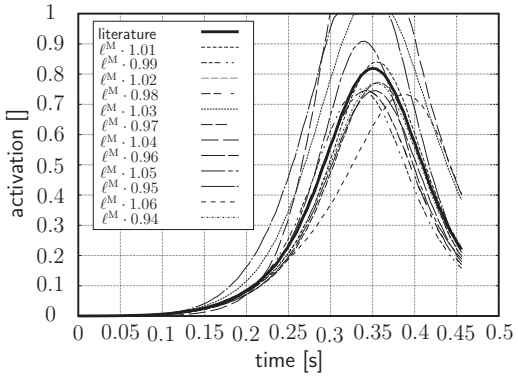

(c) Muscle activation for objective function (6.3.3)

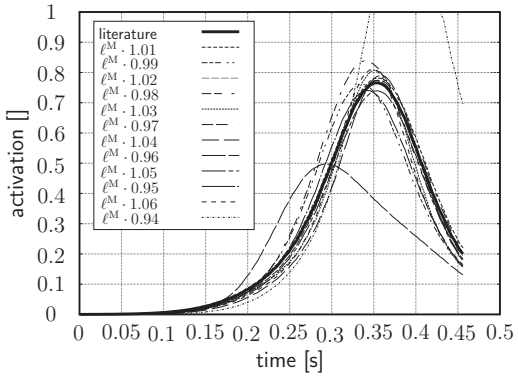

(d) Muscle activation for objective function (6.3.4)

Figure 6.19: Optimization results for objective functions (6.3.1)–(6.3.4): activation of muscle *biceps femoris caput brevis* after muscle/tendon ratio variation

Considering muscle/tendon tissue length ratio changes, the identified time histories of muscle activation appear comparatively robust with respect to the parameter variations (Fig. 6.19). For all applied objective functions, the same solution is computed for the reference parameter set. Moreover, the consideration of a detailed target prescription yields a generally smaller variation in the identified activation amplitudes (Fig. 6.19(d)).

In the following, for each perturbed initial parameter set $\underline{x}_0^{\text{pert}}$ and the corresponding final activation after optimization $a(\underline{x}_0^{\text{pert}})$,

$$\Delta a_{\max} = \max_{i=1,\ldots,100} \left| \, a_i(\underline{x}_0^{\text{ref}}) - a_i(\underline{x}_0^{\text{pert}}) \, \right| \tag{6.3.15}$$

represents the maximum deviation of $a(\underline{x}_0^{\text{pert}})$ from the activation $a(\underline{x}_0^{\text{ref}})$ achieved with the reference initial parameter set $\underline{x}_0^{\text{ref}}$ over all output sampling times. Moreover, σ

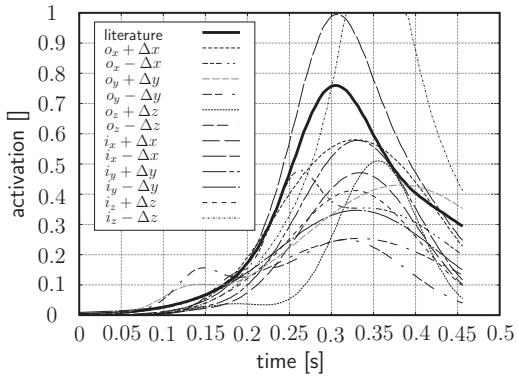

(a) Muscle activation for objective function (6.3.1)

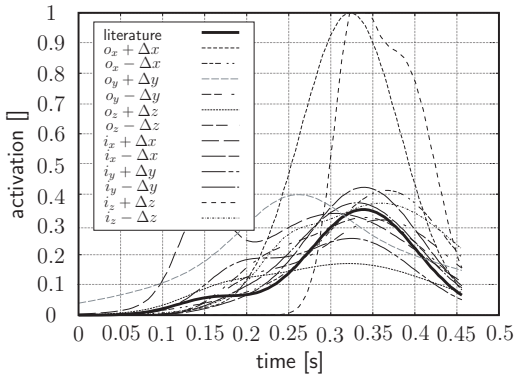

(b) Muscle activation for objective function (6.3.2)

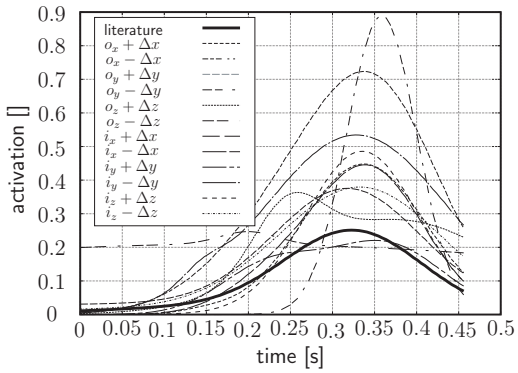

(c) Muscle activation for objective function (6.3.3)

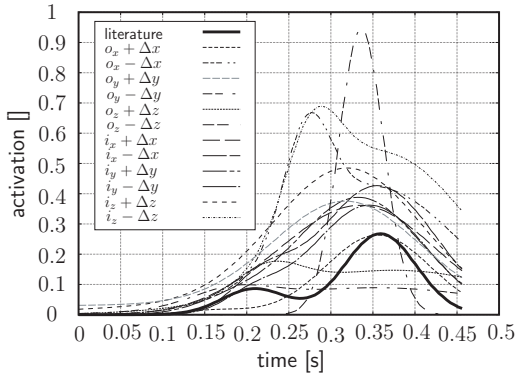

(d) Muscle activation for objective function (6.3.4)

Figure 6.20: Optimization results for objective functions (6.3.1)–(6.3.4): activation of muscle *biceps femoris caput brevis* after origin and insertion point variation

represents the standard deviation of the identified activation profiles for the perturbed data sets with respect to the unperturbed reference set. The results are summarized in Tab. 6.4–6.6. Here, one can observe that the standard deviations for all applied objective functions show similar values in the order of $10^{-3} \dots 10^{-2}$. This order is independent of the applied parameter variations. In particular, the observation of a comparatively robust behavior with respect to variations in muscle/tendon length ratio is confirmed by a generally small standard deviation (order of $10^{-4} \dots 10^{-3}$, Tab. 6.5).

Consideration of the results for initial guess variations confirm the above stated strong numerical sensitivity, indicated by the generally large normalized deviations $\Delta a_{\max}$. This result appears independent from the applied objective functions (Tab. 6.4). The deviations display 0.175 as smallest value (objective function (6.3.1), decrease of initial

C_2) but in most cases are larger than 0.5. The exceptional high value of 20.48 for objective function (6.3.2) and a decreased initial A_1 corresponds to the worst final motion approximation and is obviously caused by optimizer convergence problems. A particular sensitivity with respect to variations in specific parameters can not be derived from the data.

	cost function (6.3.1)		cost function (6.3.2)		cost function (6.3.3)		cost function (6.3.4)	
	$\frac{\Delta a_{\max}}{a_{\max}}$	σ	$\frac{\Delta a_{\max}}{a_{\max}}$	σ	$\frac{\Delta a_{\max}}{a_{\max}}$	σ	$\frac{\Delta a_{\max}}{a_{\max}}$	σ
$A_1 \cdot 1.1$	0.904	0.042	0.689	0.023	0.701	0.008	0.463	0.008
$A_1 \cdot 0.9$	0.62	0.032	20.48	0.006	0.711	0.021	0.25	0.008
$A_2 \cdot 1.1$	0.554	0.024	0.626	0.025	0.382	0.009	0.265	0.002
$A_2 \cdot 0.9$	1.032	0.039	0.741	0.003	0.656	0.013	0.798	0.005
$C_1 \cdot 1.1$	0.906	0.028	0.501	0.021	0.622	0.001	1.019	0.011
$C_1 \cdot 0.9$	1.621	0.043	0.811	0.005	0.731	0.022	0.611	0.004
$C_2 \cdot 1.1$	0.278	0.017	0.501	0.011	0.679	0.007	0.748	0.012
$C_2 \cdot 0.9$	0.175	0.007	0.703	0.002	0.719	0.001	0.743	0.009
$T_1 \cdot 1.1$	0.46	0.043	0.429	0.003	0.669	0.008	0.631	0.008
$T_1 \cdot 0.9$	0.379	0.01	0.733	0.006	0.354	0.001	0.287	0.005
$T_2 \cdot 1.1$	2.866	0.038	0.744	0.006	0.532	0.004	0.251	0.003
$T_2 \cdot 0.9$	0.684	0.038	0.778	0.003	0.891	0.035	0.924	0.13

Table 6.4: Normalized maximum deviation of activation patterns and standard deviation from reference curve for initial guess variation

In contrast, the normalized deviations in case of muscle/tendon length ratio variations generally appear smaller than 0.4 (Tab. 6.5). Again, this behavior is independent from the applied objective functions. Significant exceptions from this observation can be found for a reduction of muscle tissue length by the amount of 3% and 6% in case of objective function (6.3.2) (values of 0.446 and 0.739, respectively) and for a reduction of muscle tissue length by the amount of 4% and 6% in case of objective function (6.3.4) (values of 0.821 and 0.657, respectively). This indicates a slightly stronger sensitivity of the optimization with respect to muscle tissue length reduction. Nevertheless, variations in muscle/tendon length ratio seem to have comparatively little influence on the optimization result as long the total reference length remains at the literature value, i.e. both values are modified correspondingly.

	cost function (6.3.1)		cost function (6.3.2)		cost function (6.3.3)		cost function (6.3.4)	
	$\frac{\Delta a_{\max}}{a_{\max}}$	σ	$\frac{\Delta a_{\max}}{a_{\max}}$	σ	$\frac{\Delta a_{\max}}{a_{\max}}$	σ	$\frac{\Delta a_{\max}}{a_{\max}}$	σ
$\ell^{\mathrm{M}} \cdot 1.01$	0.191	0.001	0.412	0.0002	0.055	0.0007	0.043	0.002
$\ell^{\mathrm{M}} \cdot 0.99$	0.029	0.00007	0.101	0.002	0.217	0.006	0.176	0.004
$\ell^{\mathrm{M}} \cdot 1.02$	0.441	0.007	0.082	0.003	0.119	0.003	0.024	0.002
$\ell^{\mathrm{M}} \cdot 0.98$	0.313	0.004	0.328	0.02	0.155	0.005	0.184	0.001
$\ell^{\mathrm{M}} \cdot 1.03$	0.289	0.011	0.124	0.0005	0.245	0.016	0.098	0.004
$\ell^{\mathrm{M}} \cdot 0.97$	0.202	0.003	0.446	0.006	0.158	0.005	0.031	0.001
$\ell^{\mathrm{M}} \cdot 1.04$	0.064	0.001	0.259	0.004	0.441	0.018	0.107	0.002
$\ell^{\mathrm{M}} \cdot 0.96$	0.201	0.004	0.286	0.003	0.108	0.004	0.821	0.007
$\ell^{\mathrm{M}} \cdot 1.05$	0.205	0.007	0.239	0.005	0.143	0.003	0.038	0.002
$\ell^{\mathrm{M}} \cdot 0.95$	0.021	0.001	0.241	0.005	0.395	0.001	0.141	0.004
$\ell^{\mathrm{M}} \cdot 1.06$	0.048	0.001	0.042	0.002	0.338	0.183	0.116	0.004
$\ell^{\mathrm{M}} \cdot 0.94$	0.307	0.002	0.739	0.005	0.085	0.002	0.657	0.049

Table 6.5: Normalized maximum deviation of activation patterns and standard deviation from reference curve for muscle/tendon tissue length ratio variation

Regarding the normalized deviations in case of muscle origin/insertion point variations, there are directions of perturbation leading to significantly higher values than other directions. Regarding only knee angle position as target value reveals high normalized amplitude deviations for perturbations in negative y-direction for muscle origin (2.024) as well as for muscle insertion (1.23). These perturbations correspond to a medial relocation of the attachment points. Additionally, a deviation from the reference data set in negative z-direction of the origin (2.199) and positive z-direction of the insertion (0.929) leads to increased norms. These perturbations both comply with a shortening of the actuator, necessitating larger scaling factors being applied to the nominal optimal muscle fiber length ℓ^{M} and tendon slack length ℓ^{S}.

To compare the impact of numerical perturbations and parametric uncertainties with each other, as an overall measure for the effect of a type of perturbation the maximum difference factor between the activation amplitudes predicted for each of the perturbation types and the amplitude predicted for the corresponding reference parameter set is determined. The result can be interpreted as an influence number describing the

	cost function (6.3.1)		cost function (6.3.2)		cost function (6.3.3)		cost function (6.3.4)	
	$\frac{\Delta a_{\max}}{a_{\max}}$	σ	$\frac{\Delta a_{\max}}{a_{\max}}$	σ	$\frac{\Delta a_{\max}}{a_{\max}}$	σ	$\frac{\Delta a_{\max}}{a_{\max}}$	σ
$o_x + \Delta x$	0.356	0.004	0.665	0.001	0.453	0.006	0.263	0.005
$o_x - \Delta x$	0.856	0.001	0.379	0.012	0.661	0.019	0.910	0.022
$o_y + \Delta y$	0.805	0.017	0.685	0.008	0.337	0.005	0.758	0.010
$o_y - \Delta y$	2.024	0.005	0.361	0.003	0.744	0.001	1.800	0.004
$o_z + \Delta z$	0.497	0.013	1.062	0.001	0.515	0.016	0.687	0.010
$o_z - \Delta z$	2.199	0.014	0.292	0.009	0.764	0.011	0.754	0.002
$i_x + \Delta x$	0.680	0.008	0.844	0.005	0.417	0.013	0.673	0.013
$i_x - \Delta x$	0.542	0.006	0.174	0.003	0.452	0.003	0.492	0.013
$i_y + \Delta y$	0.408	0.007	0.458	0.002	0.218	0.001	0.643	0.008
$i_y - \Delta y$	1.230	0.003	0.182	0.002	0.535	0.019	0.501	0.008
$i_z + \Delta z$	0.929	0.008	0.661	0.009	0.492	0.003	0.783	0.013
$i_z - \Delta z$	0.384	0.023	0.423	0.015	0.036	0.010	0.893	0.032

Table 6.6: Normalized maximum deviation of activation patterns and standard deviation from reference curve for origin/insertion point variation

impact for the considered group of parameter variations. Denoting

$$a^p_{\max} = \max_{\text{all perturbations of kind } p} \max_{i=1,\ldots,100} a(t_i) \tag{6.3.16}$$

$$a^p_{\min} = \min_{\text{all perturbations of kind } p} \max_{i=1,\ldots,100} a(t_i) \tag{6.3.17}$$

as the maximum/minimum amplitude predicted for a group of perturbations of kind p (i.e. initial guess, muscle origin/insertion points or muscle/tendon tissue length ratio) and

$$a^p_{\max,\text{ref}} = \max_{i=1,\ldots,100} a_i({}^p\underline{x}_0^{\text{ref}}) \tag{6.3.18}$$

as the amplitude for the corresponding reference set, the influence number k_p for a group p of perturbations is defined as

$$k_p := \max\left\{ \frac{a^p_{\max}}{a^p_{\max,\text{ref}}}, \frac{a^p_{\max,\text{ref}}}{a^p_{\min}} \right\} . \tag{6.3.19}$$

Evaluation of (6.3.16)–(6.3.19) yields values of 16.83, 1.38 and 3.4 in case of perturbations in the initial guess, variations in muscle/tendon tissue length ratio and perturbed origin/insertion points of muscle, respectively.

Discussion

The model experiments performed for plausibility verification can be divided into two groups. While variations of the initial guess represent a purely numerical problem statement, variations of muscle/tendon tissue length ratio and muscle origin/insertion points simulate typical problems appearing due to e.g. scaling of generic models for patient-specific dynamic optimization problems.

Considering the impact on the results, numerical sensitivity dominates by large the parametric sensitivities. This is indicated by an influence factor of almost 17 for numerical sensitivity compared to an influence factor of 3.4 for parametric sensitivity. This result appears to be new in gait biomechanics literature.

In tendency the results presented in this thesis are confirmed by literature for parametric perturbations. [Redl et al., 2007] also neglected activation dynamics but they used static optimization as described in [Anderson and Pandy, 2001] to calculate time histories of muscle forces for a number of different muscles and assessed the results with a differently defined measure. Parameters perturbed were the physiological cross-sectional area (PCSA), optimal fiber length and tendon rest length. [Redl et al., 2007]. observed a sensitivity factor of 2.85 for muscle *soleus* (using the measure defined there). Other authors use probabilistic approaches with kinematically driven models. [Pal et al., 2007], [Richardson et al., 2007] and [Langenderfer et al., 2007] performed Monte Carlo simulations, assuming GAUSSian distributions for tendon slack length, optimal fiber length, pennation angle and maximum isometric muscle force. By this method, a significant sensitivity of muscle force prediction with respect to tendon slack length and muscle origin/insertion point location was identified. This again coincides in tendency with the results obtained here. [Scovil and Ronsky, 2006] focused on the investigation of model parameters defining the governing equations of a HILL-type model. They considered muscle force for the isolated muscle for variations in the inner parameters, the sensitivity of the governing equations with respect to the parameters in terms of partial derivatives and the impact of parameter variations for forward dynamics running and walking simulations (no optimization). The results uncovered a generally strong sensitivity of the isolated muscle with respect to a variety of parameters. Simulation results were identified to be less sensitive compared to isolated investigations of a single muscle.

The influence of perturbations on the optimization results appears to be independent of the chosen objective function. From Fig. 6.18—Fig. 6.20 one can see that the

variations resulting from parametric changes lie in the same area for all objective functions. However, one can see also that one obtains qualitatively different results for the different objective functions (e.g. Fig. 6.18, thick lines). This result makes it difficult to decide whether the "right" solution was found by the model.

The following conclusions can be drawn from the discussion:

- The critical sensitivity of optimization results with respect to numerical perturbations seem to indicate that the gait dynamics are not observable from kinematic measurements (motion capturing) only. Future research should investigate this issue also theoretically. To reduce this effect, objective functions including also force-related input should be applied.

- The influence of parametric perturbations indicate that muscle parameters have to be determined very exactly to achieve realistic results on a patient-specific level. In particular, current methods to obtain these parameters *in vivo* are limited. This may be the reason for the wide range of parameter values that can be found in literature. For example, for tendon slack length of the *vastus*-group, values of 0.1 m ([Hoy et al., 1989]) and 0.14 m ([Redl et al., 2007]) are reported. While this is influenced by the physical properties of the specific specimen at hand, until now models are obtained by scaling procedures and thus are very probable to yield erroneous results. Hence, methods for patient-specific *in vivo* determination of muscle parameters should become a major goal for future research.

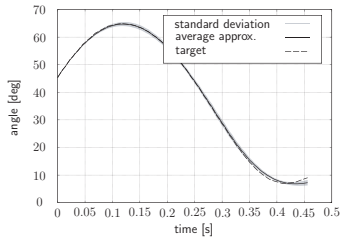

(a) Position approximation for objective function (6.3.1)

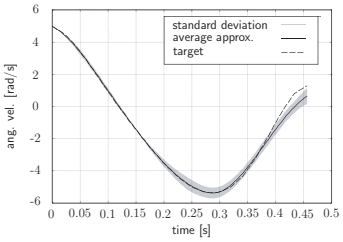

(b) Velocity approximation for objective function (6.3.1)

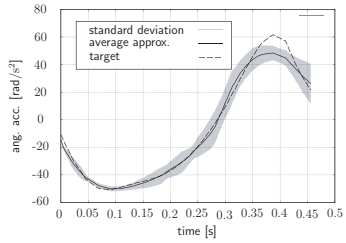

(c) Acceleration approximation for objective function (6.3.1)

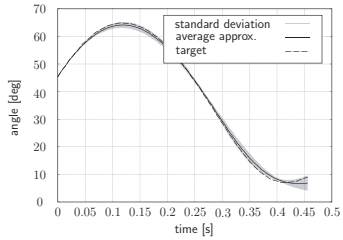

(d) Position approximation for objective function (6.3.2)

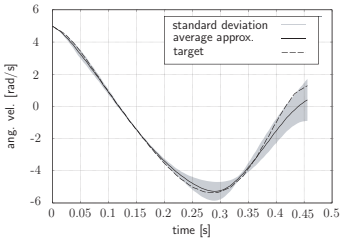

(e) Velocity approximation for objective function (6.3.2)

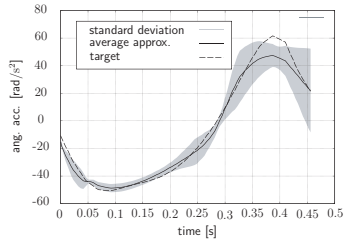

(f) Acceleration approximation for objective function (6.3.2)

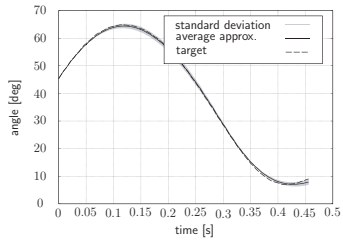

(g) Position approximation for objective function (6.3.3)

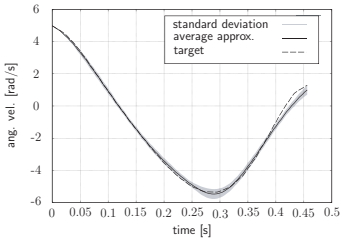

(h) Velocity approximation for objective function (6.3.3)

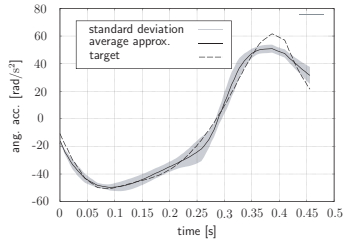

(i) Acceleration approximation for objective function (6.3.3)

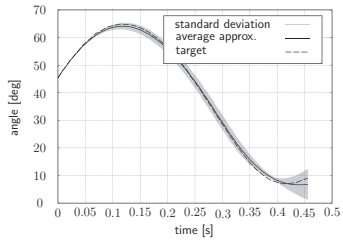

(j) Position approximation for objective function (6.3.4)

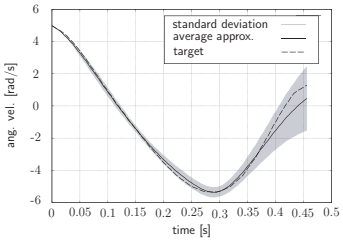

(k) Velocity approximation for objective function (6.3.4)

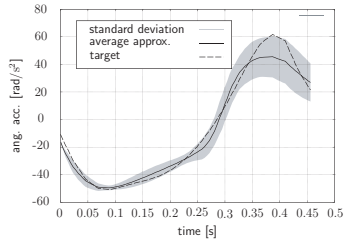

(l) Acceleration approximation for objective function (6.3.4)

Figure 6.21: Optimization results for objective functions (6.3.1)–(6.3.4): motion approximation for initial guess variation

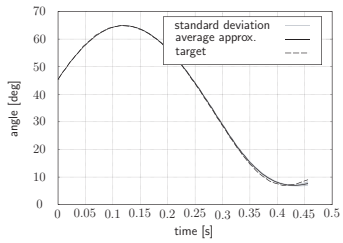

(a) Position approximation for objective function (6.3.1)

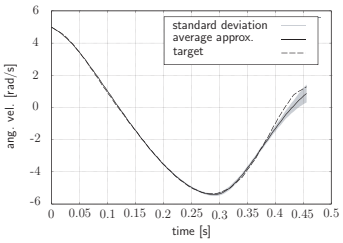

(b) Velocity approximation for objective function (6.3.1)

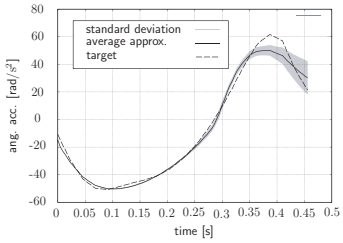

(c) Acceleration approximation for objective function (6.3.1)

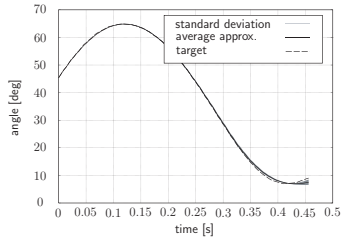

(d) Position approximation for objective function (6.3.2)

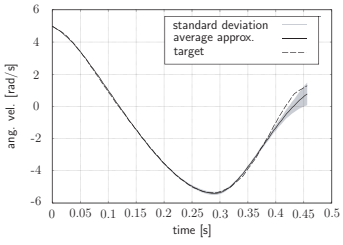

(e) Velocity approximation for objective function (6.3.2)

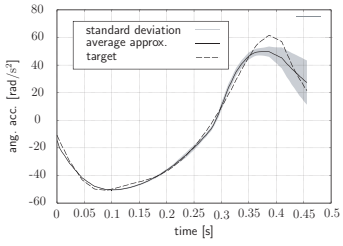

(f) Acceleration approximation for objective function (6.3.2)

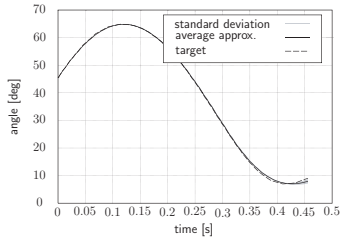

(g) Position approximation for objective function (6.3.3)

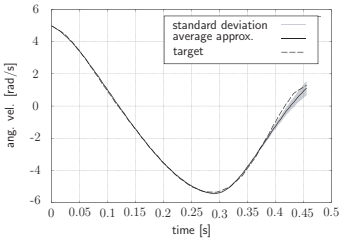

(h) Velocity approximation for objective function (6.3.3)

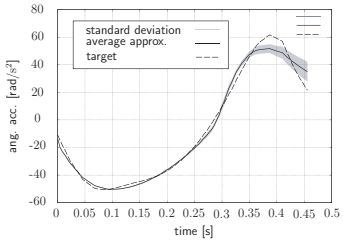

(i) Acceleration approximation for objective function (6.3.3)

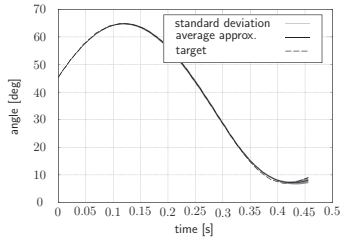

(j) Position approximation for objective function (6.3.4)

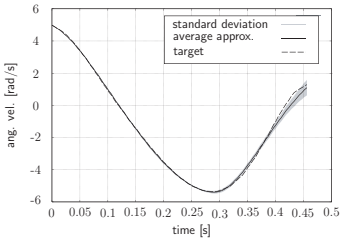

(k) Velocity approximation for objective function (6.3.4)

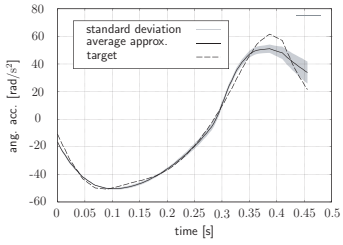

(l) Acceleration approximation for objective function (6.3.4)

Figure 6.22: Optimization results for objective functions (6.3.1)–(6.3.4): motion approximation for muscle/tendon ratio variation

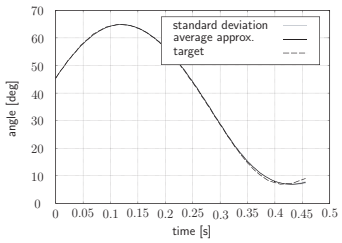

(a) Position approximation for objective function (6.3.1)

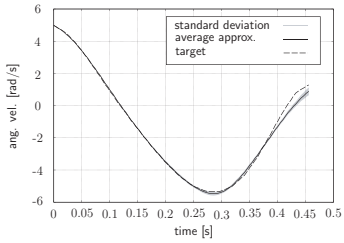

(b) Velocity approximation for objective function (6.3.1)

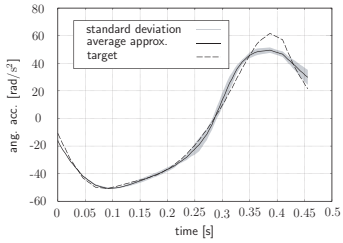

(c) Acceleration approximation for objective function (6.3.1)

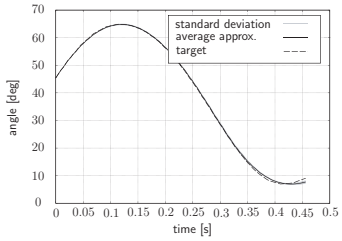

(d) Position approximation for objective function (6.3.2)

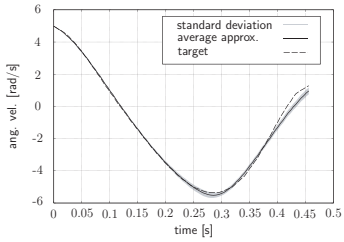

(e) Velocity approximation for objective function (6.3.2)

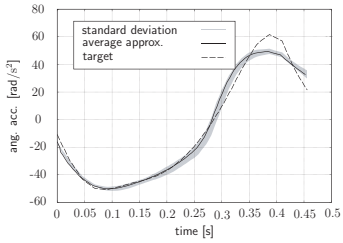

(f) Acceleration approximation for objective function (6.3.2)

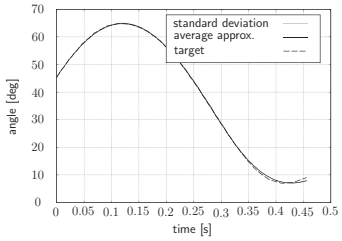

(g) Position approximation for objective function (6.3.3)

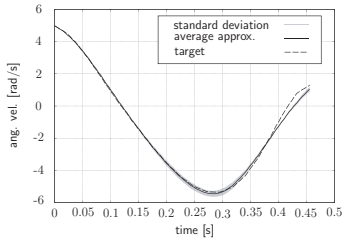

(h) Velocity approximation for objective function (6.3.3)

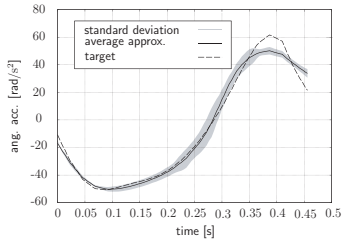

(i) Acceleration approximation for objective function (6.3.3)

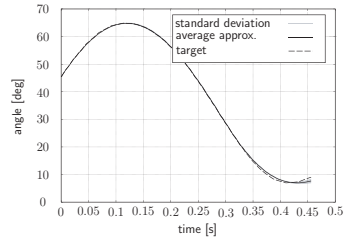

(j) Position approximation for objective function (6.3.4)

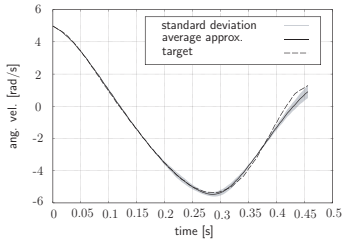

(k) Velocity approximation for objective function (6.3.4)

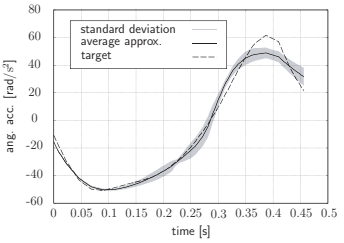

(l) Acceleration approximation for objective function (6.3.4)

Figure 6.23: Optimization results for objective functions (6.3.1)–(6.3.4): motion approximation for origin/insertion point variation

Chapter 7

Summary and outlook

Within the scope of this thesis, an open-architecture library to set up the model of the human lower extremity has been proposed. As a main characteristic, the library provides a construction kit for stetting up any leg model with easy exchange of modeling components starting from elementary descriptions (such as a revolute joint) to more involved representations (such as elastokinematical models).

The open-architecture benefits are: (1) model manageability, (2) an easily improved model depth, (3) the extension of model broadness and (4) the possibility of including efficient and tested code. In this respect, any functional unit can be replaced by a model of arbitrary complexity without the necessity to modify other model parts or code. This aspect becomes especially important with respect to future extensions of the library, for example when exchanging a thigh segment by a hip joint prosthesis or covering the characteristic properties after a femoral osteotomy. In comparison to existing packages (Sec. 1.3), the proposed library combines an open-architecture design with existing algorithms for gait simulation. This is illustrated by three example investigations related to gait analysis.

In a first example, the adaption of the lower extremity model to patient-specific physiognomy is discussed. To reduce systematic errors in the estimation of joint center locations from marker position, marker placement inaccuracy, skin artefacts and measurement noise in motion capturing, an automated tracking error reduction method was implemented. This method is based on a surrogate mechanism identifying the offsets between the assumed and anatomic joint center locations and the unknown segment vectors. The method lead to reductions in segment vector length variation between 19% and 32%.

As a second example, the proposed library was used to diagnose *talipes equinus* in the context of cerebral palsy. The tool allows to replace anesthesia and a physical test by a purely numerical procedure. The diagnosis given by the proposed method coincides with the medical one between 71% and 90% of all considered cases.

As a third example, a simulation for forward dynamics prediction of muscle activation time histories is described. The applied objective functions are based on kinematic measurements (motion capturing). To reduce model complexity, a simplified model of muscle activation based on a smooth exponential approach is proposed. The approach provides a more realistic activation prediction in comparison to measurements reported in literature, a better and more natural (smooth) approximation to the prescribed target motion and significantly less required computational time. In addition, the exponential activation model limits the number of design variables for each muscle and hence facilitates the optimization process due to a limited search space dimension. To analyze the effects of model perturbations to the predicted muscle activation profiles, a sensitivity investigation was performed. This investigation covered two types of perturbations. While numerical perturbations were assumed for the initial guess chosen for an optimization run, parametric uncertainties were considered in terms of small variations in inner muscle model parameters such as the ratio of muscle/tendon length and the location of muscle origin and insertion points. The results of this analysis uncovered a critical sensitivity of the optimization results with respect to numerical perturbations. The results of this thesis seem to indicate that the gait dynamics are not observable from kinematic measurements only. Future research could investigate the incorporation of muscle force activation, more detailed joint kinematics as well as more advanced numerical scoring techniques for predicting medical diagnosis.

Appendix A

Muscle parameters

Muscular parameters used in the model are mainly adapted from [Yamaguchi, 2001] and are based on the work of [Carhart, 2000] The following table comprises all characteristic quantities that are essential to the muscle model used in the presented work. In this context $\ell^{\mathrm{M}}, \alpha, \ell^{\mathrm{S}}$ and F^{M} denote the resting length of muscle fiber, the pennation angle, the slack length of tendon and the maximum isometric force of the muscle, respectively. The column "frame:coordinates" holds the coordinate frame with respect to which the coordinates of a given point are to be interpreted, the abbreviations P, T, S and F denote the reference frames in **p**elvis, **t**high, **s**hank and **f**oot. The location of these reference frames is described in chapter 4. The column "type" supplies information about the special characteristics of the given point. Here "O" denotes a muscle origin, "V" and "I" denote via points (if a muscle has to be "wrapped" around bones and/or ligaments) and muscle insertion points, respectively. Muscle data is reported in alphabetical order for a right leg, i.e. in case of consideration of a left leg, the y-coordinate changes its sign.

Musculoskeletal Images are from the University of Washington "Musculoskeletal Atlas: A Musculoskeletal Atlas of the Human Body" by Carol Teitz, M.D. and Dan Graney, Ph.D.

Copyright 2003-2004 University of Washington. All rights reserved including all photographs and images. No re-use, re-distribution or commercial use without prior written permission of the authors and the University of Washington

muscle name	location	$F^{\mathrm{M}}[N]$	α [°]	ℓ^{M} [m]	ℓ^{S} [m]	frame:coordinates [m,m,m]	type
adductor brevis		286.0	0.0	0.1330	0.0200	P:(-0.0580,-0.0904,0.0162) T:(0.0010,-0.1292,0.0318)	O I
adductor longus		418.0	6.0	0.1380	0.1100	P:(-0.0312,-0.0826,0.0167) T:(0.0054,-0.2281,0.0253)	O I
adductor magnus inferior		444.0	5.0	0.1310	0.2600	P:(-0.0762,-0.1167,0.0273) T:(0.0076,-0.4147,-0.0287)	O I
adductor magnus intermed.		312.0	3.0	0.1210	0.1300	P:(-0.0821,-0.1178,0.0304) T:(0.0058,-0.2469,0.0245)	O I
adductor magnus superior		346.0	5.0	0.0870	0.0600	P:(-0.0723,-0.1160,0.0252) T:(-0.0049,-0.1309,0.0366)	O I
biceps femoris caput longus		717.0	0.0	0.1090	0.3410	P:(-0.1229,-0.0989,0.0658) S:(-0.0083,-0.0751,0.0436)	O I
biceps femoris caput brevis		402.0	23.0	0.1730	0.1000	T:(0.0054,-0.2281,0.0253) S:(-0.0104,-0.0747,0.0419)	O I

muscle name	location	$F^{\mathrm{M}}[N]$	α [°]	ℓ^{M} [m]	ℓ^{S} [m]	frame:coordinates [m,m,m]	type
extensor digitorum longus		341.0	8.0	0.1020	0.3450	S:(0.0033,-0.1424,0.0284) S:(0.0298,-0.4130,0.0074) F:(0.0429,-0.0032,000077) F:(0.1116,-0.0360,0.0207)	O V V I
extensor hallucis longus		108.0	6.0	0.1110	0.3050	S:(0.0012,-0.1821,0.0235) S:(0.0336,-0.4108,-0.0088) F:(0.0477,-0.0031,-0.0131) F:(0.0796,-0.0110,-0.0176) F:(0.1232,-0.0277,-0.0199)	O V V V I
flexor digitorum longus		310.0	7.0	0.0340	0.4000	S:(-0.0086,-0.2109,-0.0019) S:(-0.0159,-0.4177,-0.0202) F:(-0.0051,-0.0104,-0.0199) F:(0.0218,-0.0240,-0.0182) F:(0.1157,-0.0495,0.0193)	O V V V I
flexor hallucis longus		322.0	10.0	0.0430	0.3800	S:(-0.0081,-0.2406,0.0252) S:(-0.0192,-0.4205,-0.0179) F:(-0.0113,-0.0141,-0.0160) F:(0.0544,-0.0348,-0.0175) F:(0.1224,-0.0468,-0.0188)	O V V V I
gastrocnemius lateralis		488.0	8.0	0.0640	0.3850	T:(-0.0167,-0.4264,000294) T:(-0.0303,-0.4447,0.0290) S:(-0.0249,-0.0496,0.0242) F:(-0.0439,-0.0108,0.0026)	O V V I
gastrocnemius medialis		1113.0	17.0	0.0450	0.4080	T:(-0.0137,-0.4246,-0.0254) T:(-0.0273,-0.4410,-0.0281) S:(-0.0224,-0.0502,-0.0304) F:(-0.0439,-0.0108,0.0026)	O V V I

muscle name	location	$F^{\mathrm{M}}[N]$	α [°]	ℓ^{M} [m]	ℓ^{S} [m]	frame:coordinates [m,m,m]	type
gemelli		109.0	0.0	0.0240	0.0390	P:(-0.0119,-0.0810,0.0705) T:(-0.0153,-0.0036,0.0479)	O I
gluteus maximus superior		382.0	5.0	0.1420	0.1250	P:(-0.1181, 0.0605,0.0692) P:(-0.1276,0.0012,0.0875) T:(-0.0949,-0.0268,0.0423) T:(-0.0299,-0.0611,0.0508)	O V V I
gluteus maximus intermedius		546.0	0.0	0.1470	0.1270	P:(-0.1333,0.0174,0.0556) P:(-0.1360,-0.0514,0.0903) T:(-0.0460,-0.0572,0.0316) T:(-0.0169,-0.1097,0.0453)	O V V I
gluteus maximus inferior		368.0	50.	0.1440	0.1450	P:(-0.1537,-0.0310,0.0057) P:(-0.1511,-0.1039,0.0398) T:(-0.0323,-0.1126,0.0146) T:(-0.0065,-0.1534,0.0444)	O V V I
gluteus medius anterior		546.0	8.0	0.0535	0.0780	P:(-0.0403,0.0300,0.1195) T:(-0.0235,-0.0126,0.0599)	O I
gluteus medius intermedius		382.0	0.0	0.0845	0.0530	P:(-0.0845,0.0440,0.0757) T:(-0.0279,-0.0063,0.0569)	O I
gluteus medius posterior		435.0	19.0	0.0646	0.0530	P:(-0.1208,0.0104,0.0640) T:(-0.0334,-0.0051,0.0560)	O I

muscle name	location	$F^{\mathrm{M}}[N]$	α [°]	ℓ^{M} [m]	ℓ^{S} [m]	frame:coordinates [m,m,m]	type
gluteus minimus anterior		180.0	10.0	0.0680	0.0160	P:(-0.0461,-0.0079,0.1043) T:(-0.0078,-0.0112,0.0605)	O I
gluteus minimus intermedius		190.0	0.0	0.0560	0.0260	P:(-0.0625,.0.0064,0.0979) T:(-0.0104,.0.0112,0.0605)	O I
gluteus minimus posterior		215.0	21.0	0.0380	0.0510	P:(-0.0824,-0.0062,0.0846) T:(-0.0146,-0.0090,0.0594)	O I
gracilis		108.0	30.	0.35200	0.1400	P:(-0.0556,-0.1026,0.0078) S:(-0.0159,-0.0490,-0.0369) S:(0.0062,-0.0862,-0.0235)	O V I
iliacus		429.0	7.0	0.1000	0.0900	P:(-0.0666,0.0361,0.0844) P:(-0.0215,-0.0543,0.0841) P:(-0.0291,-0.0800,0.0845) T:(0.0018,-0.0587,0.0062) T:(-0.0208,-0.0671,0.0139)	O V V V I
pectineus		177.0	0.0	0.1330	0.0010	P:(-0.0426,-0.0759,0.0446) T:(-0.0132,-0.0888,0.0273)	O I
peroneus brevis		348.0	5.0	0.0500	0.1610	S:(-0.0072,-0.2727,0.0335) S:(-0.0204,-0.4313,0.0292) S:(-0.0148,-0.4427,0.0298) F:(-0.0017,-0.0147,0.0309) F:(0.0187,-0.0198,0.0417)	O V V V I

muscle name	location	$F^{\mathrm{M}}[N]$	α [°]	ℓ^{M} [m]	ℓ^{S} [m]	frame:coordinates [m,m,m]	type
peroneus longus		754.0	10.0	0.0490	0.3450	S:(0.0005,-0.1616,0.0373)	O
						S:(-0.0213,-0.4334,0.0295)	V
						S:(-0.0167,-0.4452,000298)	V
						F:(-0.0049,-0.0187,0.0297)	V
						F:(0.0191,-0.0310,0.0359)	V
						F:(0.0360,-0.0346,0.0195)	V
						F:(0.0707,-0.0331,-0.0104)	I
peroneus tertius		90.0	13.0	0.0790	0.1000	S:(0.0010,-0.2890,0.0238)	O
						S:(0.0236,-0.4194,0.0164)	V
						F:(0.0365,-0.0190,0.0374)	I
piriformis		296.0	10.0	0.0260	0.1150	P:(-0.1379,0.0003,0.0232)	O
						P:(-0.1179,-0.0273,0.0649)	V
						T:(-0.0160,-0.0039,0.0472)	I
psoas		371.0	8.0	0.1040	0.1300	P:(-0.0639,0.0876,0.0286)	O
						P:(-0.0235,-0.0563,0.0750)	V
						P:(-0.0289,-0.0795,0.0838)	V
						T:(0.0017,-0.0548,0.0041)	V
						T:(-0.0203,-0.0645,0.0112)	I
quadratus femoris		254.0	0.0	0.0540	0.0240	P:(-0.1129,-0.1137,0.0514)	O
						T:(-0.0412,-0.0388,0.0395)	I
rectus femoris		779.0	5.0	0.0840	0.3460	P:(-0.0291,-0.0307,0.0956)	O
						T:(0.0392,-0.4340,0.0028)	V
						S:(0.0609,0.0224,0.0035)	V
						S:(0.0506,-0.0211,0.0026)	V
						S:(0.0403,-0.0847,0.0000)	I

muscle name	location	$F^{\mathrm{M}}[N]$	α [°]	ℓ^{M} [m]	ℓ^{S} [m]	frame:coordinates [m,m,m]	type
sartorius		104.0	0.0	0.5790	0.0400	P:(-0.0151,-0.0013,0.1227) T:(-0.0032,-0.3855,-0.0455) S:(-0.0058,-0.0432,-0.0411) S:(0.0062,-0.0607,-0.0395) S:(0.0250,-0.0866,-0.0260)	O V V V I
semimembra-nosus		1030.0	15.0	0.0800	0.3590	P:(-0.1178,-0.1003,0.0687) S:(-0.0250,-0.0553,-0.0200)	O I
semitendi-nosus		328.0	5.0	0.2010	0.2620	P:(-.01222,-0.1031,0.0596) S:(-0.0324,-0.0562,-0.0150) S:(-0.0116,-0.0769,-0.0253) S:(0.0028,-0.0985,-0.0199)	O V V I
soleus		2839.0	25.0	0.0300	0.2680	S:(-0.0025,-0.1580,0.0073) F:(-0.0439,-0.0108,0.0026)	O I
tensor fasciae latae		155.0	3.0	0.0950	0.4250	P:(-.01222,-0.1031,0.0596) T:(0.0318,-0.1075,0.0645) T:(0.0058,-0.4376,0.0386) S:(0.0062,-0.0502,0.0306)	O V V I
tibialis anterior		603.0	5.0	0.0980	0.2230	S:(0.0185,-0.1674,0.0119) S:(0.0339,-0.4073,-0.0182) F:(0.0671,-0.0239,-0.0224)	O V I

muscle name	location	$F^{\mathrm{M}}[N]$	α [°]	ℓ^{M} [m]	ℓ^{S} [m]	frame:coordinates [m,m,m]	type
tibialis posterior		1270.0	12.0	0.0310	0.3100	S:(-0.0097,-0.1390,0.0020)	O
						S:(-0.0148,-0.4177,-0.0236)	V
						F:(-0.0070,-0.0084,-0.0205)	V
						F:(0.0281,-0.0257,-0.0200)	I
vastus intermedius		1365.0	3.0	0.08700	0.1360	T:(0.313,-0.2079,0.0355)	O
						T:(0.0362,-0.2252,0.0308)	V
						T:(0.0382,-0.4339,0.0073)	V
						S:(0.0544,0.0268,0.0019)	V
						S:(0.0506,-0.0211,0.0026)	V
						S:(0.0403,-0.0847,0.0000)	I
vastus lateralis		1871.0	5.0	0.0840	0.15700	T:(0.0052,-0.2004,0.0377)	O
						T:(0.00291,-0.2800,0.0422)	V
						T:(0.0414,-0.4366,0.0238)	V
						S:(0.0591,0.0209,0.0170)	V
						S:(0.0506,-0.0211,0.0026)	V
						S:(0.0403,-0.0847,0.0000)	I
vastus medialis		1294.0	50.	0.0890	0.1260	T:(0.0151,-0.2268,0.0203)	O
						T:(0.0385,-0.2992,0.0010)	V
						T:(0.0441,-0.4382,-0.0129)	V
						S:(0.0549,0.0232,-0.0150)	V
						S:(0.0506,-0.0211,0.0026)	V
						S:(0.043,-0.0847,0.0000)	I

Nomenclature

$\delta \underline{q}$ vector of virtual displacements, page 46

$\dot{\mathbf{J}}_\phi$ time derivative of position transmission function Jacobian $\mathbf{J}_\phi$, page 46

ℓ^{MT} absolute length of musculotendon actuator, page 126

ℓ^{M} reference length of muscle part in musculotendon actuator, page 125

ℓ^{S} reference length of tendon part in musculotendon actuator, page 125

$\mathcal{K}_0$ inertial reference frame, page 46

$\mathcal{K}$ coordinate frame, page 13

$\mathcal{K}$ coordinate frame, page 46

$\mathcal{K}^{\mathrm{ref}}$ reference coordinate frame (body-fixed), page 60

$\mathbf{J}_\phi$ Jacobian of position transmission function $\underline{\phi}$, page 45

$\mathbf{J}_f(\underline{x})$ Jacobian matrix of a vector function $\underline{f}(\underline{x})$, page 15

$\mathbf{J}_G$ global Jacobian of multibody system, page 48

$[\mathbf{J}_G]_j$ j-th column of global Jacobian $\mathbf{J}_G$, page 49

$\mathbb{R}$ real numbers, page 13

$\mathbb{R}^n$ n-dimensional real numbers, page 13

$\ker A$ kernel of matrix A, page 13

$\nabla f(\underline{x})$ gradient of a scalar function $f(\underline{x}) \in \mathbb{R}$, page 14

$\underline{\phi}(\underline{q})$ position transmission function for set of generalized cc ordinates $\underline{q}$, page 45

$\underline{Q}$ generalized force vector, page 46

$\underline{q}$ n-tuple (not necessarily with a physical meaning), page 13

$\mathbf{F}, \mathbf{v}$ Example for physical vectors (boldfaced), page 13

$\mathbf{F}_{\mathrm{P}}$ physical vector belonging to item or point (here P), page 13

$\mathbf{R}$ general transformation matrix, page 13

$\mathbf{R}_x(\varphi)$ elementary rotation about x-axis of fixed frame with angle φ, page 14

$\mathbf{R}_y(\varphi)$ elementary rotation about y-axis of fixed frame with angle φ, page 14

$\mathbf{R}_z(\varphi)$ elementary rotation about z-axis of fixed frame with angle φ, page 14

τ dimensionless time, page 126

τ_c muscle specific time scaling factor, page 126

$\tilde{\ell}$ normalized musculotendon actuator length, page 125

$\tilde{\ell}^{\mathrm{MT}}$ normalized length of musculotendon actuator, page 126

$\tilde{F}^T$ normalized force applied to skeleton via tendon part of musculotendon actuator, page 126

$\tilde{k}^{\mathrm{T}}$ tendon stiffness, page 126

$\tilde{v}$ normalized muscle lengthening/shortening velocity, page 125

φ_S mapping describing the global kinematics of a multibody system, page 52

${}^{\mathrm{I}}\mathbf{v}$ representation of $\mathbf{v}$ in coordinate frame $\mathcal{K}_{\mathrm{I}}$, indicated by appropriate superscript left to the vector symbol, page 13

A matrix (upper case letter) if not explicitly denoted otherwise, page 13

$a(\tau)$ level of muscle activation as function of dimensionless time, page 126

$a(t)$ level of muscle activation as function of time, page 125

d_{M} marker diameter, page 59

F^{M} maximum isometric muscle force, page 125

$F_{\mathrm{H}}(\tilde{v})$ dimensionless function describing the force-velocity relation of muscle force, page 125

F_{H}^{-1} inverse force-velocity relation of muscle, page 129

$F_{\mathrm{L}}(\tilde{\ell})$ dimensionless function describing the force-length relation of muscle force, page 125

$F_{\mathrm{P}}(\tilde{\ell})$ dimensionless function describing the passive muscle part force contribution, page 125

$H_f(\underline{x})$ Hessian matrix of a scalar function $f(\underline{x}) \in \mathbb{R}$, page 14

$v_{\max}$ maximum shortening velocity of muscle, page 125

w_{A} patient-specific ankle width, page 59

w_{K} patient-specific knee width, page 59

AJC ankle joint center without side specification, page 57

ANK marker located at ankle without side specification, page 57

ASIS marker located at *spina iliaca anterior superior* without side specification, page 57

HEE marker located at heel without side specification, page 57

HJC hip joint center without side specification, page 57

KJC knee joint center without side specification, page 57

KNE marker located at knee without side specification, page 57

LAJC left ankle joint center, page 57

LANK marker located at left ankle, page 57

LASIS marker located at left *spina iliaca anterior superior*, page 57

LHEE marker located at left heel, page 57

LHJC left hip joint center, page 57

LKJC left knee joint center, page 57

LKNE marker located at left knee, page 57

LTHI marker located at left thigh, page 57

LTIB marker located at left shank, page 57

LTOE marker located at left toes, page 57

PSIS marker located at superior aspect at the L5-sacral interface, page 57

RAJC right ankle joint center, page 57

RANK marker located at right ankle, page 57

RASIS marker located at right *spina iliaca anterior superior*, page 57

RHEE marker located at right heel, page 57

RHJC right hip joint center, page 57

RKJC right knee joint center, page 57

RKNE marker located at right knee, page 57

RTHI marker located at right thigh, page 57

RTIB marker located at right shank, page 57

RTOE marker located at right toes, page 57

THI marker located at thigh without side specification, page 57

TIB marker located at shank without side specification, page 57

TOE marker located at toes without side specification, page 57

Bibliography

[Alonso et al., 2007] Alonso, F. J., Del Castillo, J. M., and Pintado, P. (2007). Motion data processing and wobbling mass modelling in the inverse dynamics of skeletal motion. *Mechanism and Machine Theory*, 42:1153–1169.

[An et al., 1990] An, K.-N., Berglund, L., Cooney, W. P., Chao, E. Y. S., and Kovacevic, N. (1990). Direct in vivo tendon force measurment system. *Journal of Bioemchanics*, 23:1269–1271.

[Anderson and Pandy, 1999a] Anderson, F. C. and Pandy, M. G. (1999a). A dynamic optimization solution for vertical jumping in three dimension. *Computer Methods in Biomechanics and Biomedical Engineering*, 2:201–231.

[Anderson and Pandy, 1999b] Anderson, F. C. and Pandy, M. G. (1999b). Static and dynamic optimization solutions for gait are practically equivalent. *Journal of Biomechanics*, 34:153–161.

[Anderson and Pandy, 2001] Anderson, F. C. and Pandy, M. G. (2001). Dynamic optimization of human walking. *Journal of Biomechanical Engineering*, 123:381–390.

[Arnold et al., 2000] Arnold, A. S., Asakawa, D. J., and Delp, S. L. (2000). Do the hamstrings and adductors contribute to excessived internal rotation of the hip in persons with cerebral palsy? *Gait and Posture*, 11:181–190.

[Asakawa et al., 2002] Asakawa, D. S., Blemker, S. S., Gold, G. E., and Delp, S. L. (2002). In vivo motion of the rectus femoris muscle after tendon tranfer surgery. *Journal of Biomechanics*, 35:1029–1037.

[Asakawa et al., 2004] Asakawa, D. S., Blemker, S. S., Rab, G. T., Bagley, A., and Delp, S. L. (2004). Three-dimensional muscle-tendon geometry after rectus femoris tendon transfer. *Journal of Bone and Joint Surgery*, 86A(2):348–354.

[Automotive, 2003] Automotive, T. (2003). Madymo v6.1 theory manual.

[Basmajian, 1974] Basmajian, J. (1974). *Muscles alive: their functions revealed by electromyography*. Williams and Wilkins, Baltimore.

[Bechtol, 1975] Bechtol, C. O. (1975). Normal human gait. In *J.H. Bowker and C. B. Hall: Atlas of orthoticis*, pages 133–143, American Academy of Orthopaedic Surgeon.

[Benninghoff, 1985] Benninghoff, A. (1985). *Makroskopische und mikroskopische Anatomie des Menschen, Band 1: Cytologie, Histologie, allgemeine Anatomie und Anatomie des Bewegungsapparates*. Urban & Schwarzenberg, München.

[Bhargava et al., 2004] Bhargava, L. J., Pandy, M. G., and Anderson, F. C. (2004). A phenomenological model for estimating metabolic energy consumption in muscle contraction. *Journal of Biomechanics*, 37:81–88.

[Bjørnstrup, 1995] Bjørnstrup, J. (1995). Estimation of Human Body Segment Parameters: Historical Background. Technical report, Aalborg University, Aalborg.

[Bjørnstrup, 1996] Bjørnstrup, J. (1996). Estimation of Human Body Segment Parameters: Statistical Analysis of Results from Prior Investigations. Technical report, Aalborg University, Aalborg.

[Blankevoort et al., 1991] Blankevoort, L., Kuiper, J., Huiskens, R., and Grootenboer, H. (1991). Articular contact in a three-dimensional model of the knee. *Journal of Biomechanics*, 24(11):1019–1031.

[Borelli, 1680] Borelli, G. (1680). *De Motu Animalium*. Ex typographia A. Bernabo, Rome.

[Braune and Fischer, 1889] Braune, W. and Fischer, O. (1889). *Ueber den Schwerpunkt des menschlichen Koerpers mit Ruecksicht auf die Ausruestung des deutschen Infanteristen*. ABH Math. Mhy. Cl K Sachs Ges Wissensch.

[Camilleri and Hull, 2005] Camilleri, M. J. and Hull, M. L. (2005). Are the maximum shortening velocity and the shape parameter in a hill-type model of a whole muscle related ot activation? *Journal of Biomechanics*, 38:2172–2180.

[Carhart, 2000] Carhart, M. (2000). *Biomechanical analysis fo compensatory stepping: implications for paraplegics standing via FNS (Ph.D. Dissertation)*. Department of Bioengineering, Arizona State University, Tempe, Arizona, USA, Tempe.

[Carlet, 1872] Carlet, M. (1872). Sur la locomoiton humaine. *Annales des Sciences Naturelles*, 5.

[Cheng et al., 2000] Cheng, C.-K., Chen, H.-H., Chen, C.-S., Lee, C.-L., and Chen, C.-Y. (2000). Segment inertial properties of chinese adults determined from magnetic resonance imaging. *Clinical Biomechanics*, 15:559–566.

[Crowninshield and Brand, 1981] Crowninshield, R. D. and Brand, R. A. (1981). A physiologically based criterion of muscle force prediction in locomotion. *Journal of Biomechanics*, 14(11):793–801.

[Cunningham and Brown, 1952] Cunningham, D. and Brown, G. (1952). Two devices for measuring the forces acting on the humnan body during walking. In *Proceedings of the Society for Experimental Stress Analysis*.

[Davis et al., 1991] Davis, R., Õunpuu, S., Tyburski, D., and Gage, J. (1991). A gait analysis data collection and reduction technique. *Human Movement Science*, 10:575–587.

[Davy and Audu, 1987] Davy, D. T. and Audu, M. L. (1987). A dynamic optimization technique for predicting muscle forces in the swing phase of gait. *Journal of Biomechanics*, 20:187–201.

[de Silva and Ambrósio, 2004] de Silva, M. P. T. and Ambrósio, J. A. C. (2004). Human motion analysis using multibody dynamics and optimization tools. Technical report, Instituto Superior Técnico, Lissabon.

[Delp et al., 1999a] Delp, S., Hess, W., Hungerford, D., and Jones, L. (1999a). Variation of rotation moment arms with hip flexion. *Journal of Biomechanics*, 32:493–501.

[Delp and Loan, 1995] Delp, S. and Loan, J. (1995). A graphics-based software system to develop and analyze models of musculoskeletal systems. *Comput. Biol. Med.*, 25(1):21–34.

[Delp and Loan, 2000] Delp, S. and Loan, J. (2000). A computational framework for simulating and analyzing human and animal movement. *Computing in Science and Engineering*, pages 46–55.

[Delp et al., 1994] Delp, S., Ringwelksi, D., and Carroll, N. (1994). Transfer of the rectus femoris: effects of transfer site on moment arms about the knee and the hip. *Journal of Biomechanics*, 27(10):1201–1211.

[Delp, 2000] Delp, S. L. (2000). *Surgery simulation: a computer graphics system to analyze and design musculoskeletal reconstructions of the lower limb (Ph.D. Dissertation)*. Department of Mechanical Engineering, Stanford University, Kalifornien, USA, Stanford.

[Delp et al., 1999b] Delp, S. L., Hess, W. E., Hungerford, D. S., and Jones, L. C. (1999b). Variation of rotation moment arms with hip flexion. *Journal of Biomechanics*, 32:493–501.

[Dempster, 1955] Dempster, W. T. (1955). Space Requirements of the Seated Operator: Geometrical, Kinematic and Mechanical Aspects of the Body With Special Reference to the Limbs. Technical report, WADAC Technical Report 55-159, Wright Air Development Center, Michigan.

[Dettwyler et al., 2004] Dettwyler, M., Stacoff, A., de Quervain, I. K., and Stüssi, E. (2004). Modelling of the ankle joint complex. reflections with regards to ankle prostheses. *Foot and Anlke Surgery*, 10:109–119.

[Drillis and Contini, 1966] Drillis, R. and Contini, R. (1966). Body Segment Parameters. Technical report, Office of Vocational Rehabilitytion, Department of Health, Education and Welfare, New York.

[Erdemir et al., 2007] Erdemir, A., McLean, S., Herzog, W., and van den Bogert, A. (2007). Model-based estimation of muscle forces exerted during movements. *Clinical Biomechanics*, 22:131–154.

[Fischer, 1904] Fischer, O. (1904). *Der Gang des Menschen*. Abh. Kgl. Sachs. Ges. d. Wiss.

[Fletcher, 2003] Fletcher, R. (2003). *Practical Methods of Optimization*. Wiley.

[Forwood et al., 1985] Forwood, M., Neal, R., and Wilson, B. (1985). Scaling segmental moments of inertia for individual subjects. *Journal of Biomechanics*, 18:755–761.

[Furnée, 1967] Furnée, E. (1967). Hybrid instrumentation in prosthetic research. In *Dig. 7th Int. Conf. Medical and Biological Engineering*, Stockholm.

[Gill et al., 2004] Gill, P. E., Murray, W., and Wright, M. H. (2004). *Practical Optimization*. Elsevier Academic Press.

[Hall et al., 1999] Hall, G. W., Crandall, J. R., Carmines, D. V., and Hale, J. E. (1999). Rate-independent characteristics of an arthoscopically implantable force probe in the human achilles tendon. *Journal of Bioemchanics*, 32:203–207.

[Hartley and Zisserman, 2004] Hartley, R. and Zisserman, A. (2004). *Multiple View Geometry in computer vision*. Cambridge University Press.

[Hatze, 1977] Hatze, H. (1977). A complete set of control equations for the human musculo-skeletal system. *Journal of Biomechanics*, 10:799–805.

[Hatze, 1980] Hatze, H. (1980). A mathematical model for the computational determination of parameter values of anthropometric semgents. *Journal of Biomechanics*, 13:833–843.

[Herzog et al., 1996] Herzog, W., Hasler, E. M., and Leonard, T. R. (1996). In-situ calibration of the implantable force transducer. *Journal of Bioemchanics*, 29:1649–1652.

[Hill, 1938] Hill, A. (1938). The heat of shortening and the dynamic constants of muscle. *Proc. R. Soc. Lond.*, 126:136–195.

[Hill, 1953] Hill, A. (1953). The mechanics of active muscle. *Proc. R. Soc. Lond.*, 141:104–117.

[Hinrichs, 1985] Hinrichs, R. (1985). Regression equations to predict segmental moments of inertia from anthropometric measurments: an extension of the data of chandler et al. (1975). *Journal of Biomechanics*, 18:621–624.

[Hoy et al., 1989] Hoy, M., Zajac, F., and Gordon, M. (1989). A musculoskeletal model of the human lower extremity: The effect of muscle, tendon ans moment arm on the knee and ankle. *Journal of Biomechanics*, 23:157–169.

[http://www.about-cerebral palsy.org, 2009] http://www.about-cerebral palsy.org (2009).

[http://www.adams.com, 2008] http://www.adams.com (MSC Software Corporation, Michigan, USA, 2008).

[http://www.automotive.tno.nl, 2006] http://www.automotive.tno.nl (TNO Automotive, Eindhoven, Niederlande, 2006).

[http://www.c motion.com, 2006] http://www.c motion.com (2006).

[http://www.onmeda.de, 2008] http://www.onmeda.de (2008).

[http://www.simpack.de, 2008] http://www.simpack.de (Intec GmbH, 2008).

[http://www.sonderpaed-online.de, 2008] http://www.sonderpaed-online.de (2008).

[http://www.vicon.com, 2008] http://www.vicon.com (2008).

[http://www.zebris.de, 2006] http://www.zebris.de (2006).

[Huxley, 1957] Huxley, A. (1957). Muscle structure and theories of contraction. *Progress in Biophysics and Biophysical Chemistry*, 7:257–318.

[Huxley, 1974] Huxley, A. (1974). Musclular contraction. *Journal of Physiology*, 243:1–43.

[Huxley, 1969] Huxley, H. (1969). The mechanism of muscular contraction. *Science*, 164:1356–1365.

[Inman et al., 1981] Inman, V., Ralston, H., and Todd, F. (1981). *Human walking*. Williams and Wilkins, Baltimore.

[Jarret et al., 1976] Jarret, M., Andrews, B., and Paul, J. (1976). A television computer system for the analysis of human motion. In *IERE Conf. Proc.*

[Jonkers and Spaepen, 2003] Jonkers, C. S. and Spaepen, A. (2003). The study of muscle activation during single support and swing phase of gait: clinical relevance of forward simulation techniques. *Gait and Posture*, 17:97–105.

[Kapandji, 1999] Kapandji, I. (1999). *Funktionelle Anatomie der Gelenke*. Hippokrates Verlag GmbH, Stuttgart.

[Kecskeméthy, 1993] Kecskeméthy, A. (1993). *Objektorientierte Modellierung der Dynamik von Mehrkörpersystemen mit Hilfe von Übertragungselementen*. Fortschrittberichte VDI, Reihe 20 Nr. 88. VDI-Verlag, Düsseldorf.

[Kecskeméthy, 2003] Kecskeméthy, A. (2003). M□BILE 1.3 *User's Guide*. Lehrstuhl für Mechanik, Universität Duisburg-Essen.

[Kecskeméthy and Hiller, 1994] Kecskeméthy, A. and Hiller, M. (1994). An object-oriented approach for an effective formulation of multibody dynamics. *Computer Methods in Applied Mechanics and Engineering*, 115:287–314.

[Kecskeméthy et al., 2003] Kecskeméthy, A., Stolz, M., Strobach, D., Saraph, V., Steinwender, G., and Zwick, B. (2003). Improvements in measure-based simulation of the human lower extremity. In *Proceedings of the IASTED Conference on Biomechanics*, pages 155–160, Rhodes, Greece.

[Koh and Herzog, 1998] Koh, T. J. and Herzog, W. (1998). Increasing the moment arm of the tibialis anterior induces structural and functional adaption: implications for tendon transfer. *Journal of Biomechanics*, 31:593–599.

[Kuzelicki et al., 2005] Kuzelicki, J., Zefran, M., Burger, H., and Bajd, T. (2005). Synthesis of standing-up trajectories using dynamic optimization. *Journal for Gait and Posture*, 21:1–11.

[Langenderfer et al., 2007] Langenderfer, J., Laz, J., Petrella, A., and Rullkoetter, P. (2007). Incorporating uncertainty in body segment parameters and anatomical landmarks in inverse dynamics calculation of joint loads. In *53rd Annual Meeting of the Orthopaedic Research Society*, page Poster No. 1816, San Diego.

[Leardini et al., 1999a] Leardini, A., O'Connor, J., Catani, F., and Giannini, S. (1999a). A geometric model of the human ankle joint. *Journal of Biomechanics*, 32:585–591.

[Leardini et al., 1999b] Leardini, A., O'Connor, J., Catani, F., and Giannini, S. (1999b). Kinematics of the human ankle complex in passive flexion; a single degree of freedom system. *Journal of Biomechanics*, 32:111–118.

[Lloyd and Besier, 2003] Lloyd, D. G. and Besier, T. F. (2003). An emg-driven musculosceletal model to estimate muscle forces and knee joint moments in vivo. *Journal of Biomechanics*, 36:765–776.

[Lund, 2005] Lund, M. (2005). *Biomechanical study of cross-country skiing (Master Thesis)*. Mid Sweden University, Department of Engineering, Physics and Mathematics, Östersund, Mid Sweden University, Department of Engineering, Physics and Mathematics, Östersund.

[Meyer et al., 1990] Meyer, D. C., Jacob, H. A. C., Nyffeler, R. W., and Gerber, C. (1990). In vivo tendon force measurement of 2-week duration in sheep. *Journal of Bioemchanics*, 37:135–140.

[Murray et al., 1964] Murray, M., Drought, A., and Korey, R. (1964). Walking patterns of normal men. *Journal of Bone and Joint Surgery*, 46A:335–360.

[Murray et al., 1970] Murray, M., Korey, R., and Sepic, S. (1970). Walking patterns of normal women. *Arch. Phys. Med. Rehabil.*, 51:636–650.

[Numerical Algorithms Group, 2004] Numerical Algorithms Group (2004). *NAG C Library Manual NP3491/6*. Numerical Algorithms Group.

[Oxford Metrics, 2004] Oxford Metrics, L. (2004). *Vicon Clinical Manager User's Manual*. Oxford, England.

[Pal et al., 2007] Pal, S., Stowe, J., Rullkoetter, P., Laz, P., Petrella, A., and Lengenderfer, J. (2007). Effects of origin, insertion and kinematic uncertainties on muscle moment arms. In *53rd Annual Meeting of the Orthopaedic Research Society*, page Poster No. 0755, San Diego.

[Paul, 1998] Paul, J. (1998). History and fundamentals of gait analysis. *Bio-Medical Materials and Engineering*, 8:123–135.

[Perry, 1992] Perry, J. (1992). *Gait Analysis: Normal and Pathological Function*. SLACK Incorporated, Thorofare, NJ.

[Platt et al., 1994] Platt, D., Wilson, A. M., Timbs, A., Wright, I. M., and Goodship, A. E. (1994). Novel force transducer for the measurement of tendon force in vivo. *Journal of Bioemchanics*, 27:1489–1493.

[Ralston, 1976] Ralston, H. J. (1976). Energetics of human walking. In et. al., R. M. H., editor, *Neural Control of Locomotion*, pages 77–98. Plenum Press.

[Rasmussen et al., 2000] Rasmussen, J., Damsgaard, M., Christensen, S. T., and Surma, E. (2000). Design optimization with respect to ergonomic properties. In *Mechanics and materials in design 3, Book of Abstracts*, University of Toronto.

[Rasmussen et al., 2003] Rasmussen, J., Damsgaard, M., Surma, E., Christensen, S. T., de Zee, M., and Vondrak, V. (2003). Anybody — a software system for ergonomic optimization. In *Proceedings of the 5th World Congress on Structural and Multidisziplinary Optimization*, Venedig.

[Rasmussen et al., 1999] Rasmussen, J., Damsgaard, M., and Voigt, M. (1999). Ergonomic optimization of a bycicle. In *Proceedings of the 3rd World Congress of Structural and Multidisciplinary Optimization*, Amherst, New York, USA.

[Ravary et al., 2004] Ravary, B., Pourcelot, P., Bortolussi, C., Konieczka, S., and Crevier-Denoix, N. (2004). Strain and force transducers used in human and veterinary tendon and ligament biomechanical studies. *Clinical Biomechanics*, 19:433–447.

[Redl et al., 2007] Redl, C., Gfoehler, M., and Pandy, M. G. (2007). Sensitivity of muscle force estimates to variations in muscle-tendon properties. *Human Movement Science*, 26:306–319.

[Richardson et al., 2007] Richardson, T., Baldwin, M., Langenderfer, J., Laz, J., Petrella, A., and Rullkoetter, P. (2007). Probabilistic muscle force prediction during gait. In *53rd Annual Meeting of the Orthopaedic Research Society*, page Poster No. 1218, San Diego.

[Ryschon et al., 1997] Ryschon, T., Fowler, M., Wysong, R., Anthony, A.-R., and Balaban, R. (1997). Efficiency of human skeletal muscle in vivo: comparison of isometric, concentric and eccentric muscle action. *Journal of Applied Physiology*, 83:867–874.

[Saraph et al., 2006] Saraph, V., Zwick, E., Steinwender, G., Auner, C., Schneider, F., and Linhart, W. (2006). Leg lengthening as part of gait improvement surgery in cerebral palsy: an evaluation using gait analysis. *Gait and Posture*, 23:83–90.

[Schiebler et al., 1997] Schiebler, T., Schmitt, W., and Zilles, K. (1997). *Anotomie — Zytologie, Histologie, Entwicklungsgeschichte, makroskopische und mikroskopische Anatomie des Menschen*. Springer, Berlin.

[Schmidt et al., 1999] Schmidt, D. J., Arnold, A. S., Carroll, N. C., and Delp, S. L. (1999). Length changes of the hamstrings and adductors resulting from derotational osteotomies of the femur. *Journal of Orthopaedic Research*, 17:279–285.

[Schweiger, 1983] Schweiger, E. (1983). *Digitale Butterworthfilter: Auslegungsrezepte und Anwendungen*. Oldenbourg Verlag München Wien, München.

[Scovil and Ronsky, 2006] Scovil, C. Y. and Ronsky, J. L. (2006). Sensitivity of a hill-based muscle model to perturbations in model parameters. *Journal of Biomechanics*, 39:2055–2063.

[Shelburne and Pandy, 1997] Shelburne, K. and Pandy, M. (1997). A musculoskeletal model of the knee for evaluating ligament forces during isometric contractions. *Journal of Biomechanics*, 30(2):163–176.

[Sobotta, 2005] Sobotta, J. (2005). Sobotta interaktiv: Bewegungsapparat Version 1.5. CD-ROM.

[Spaegele, 1998] Spaegele, T. (1998). *Modellierung, Simulation und Optimierung menschlicher Bewegungen*. Institut A fuer Mechanik der Universitaet Stuttgart, Stuttgart.

[Stolz, 2002] Stolz, M. (2002). Modellbildung, Simulation und Analyse der menschlichen Beinbewegung zur Vorbereitung chirurgischer Eingriffe. Technical report, Technische Universität Graz, Graz.

[Strobach and Kecskeméthy, 2005] Strobach, D. and Kecskeméthy, A. (2005). Rapid identification of muscle activation profiles via optimization and smooth profiles patches. In *Proceedings of the 76th Annual Scientific Conference of GAMM*, pages 521 – 522, Luxembourg, Luxembourg.

[Strobach and Kecskeméthy, 2006] Strobach, D. and Kecskeméthy, A. (2006). An analysis of simplified muscle activation parameterization. In *Proceedings of the 77th Annual Scientific Conference of GAMM*, Berlin, Germany. Accepted for Publication.

[Strobach et al., 2007] Strobach, D., Kecskeméthy, A., Auer, E., Luther, W., Steinwender, G., and Zwick, B. (2007). A sensitivity analysis of origin and insertion points of Hill muscle models with respect to gait dynamics. In *CD Proceedings of the International ECCOMAS Thematic Conference on Advances in Computational Multibody Dynamics*, Milano, Italy. ECCOMAS.

[Strobach et al., 2005] Strobach, D., Kecskeméthy, A., Steinwender, G., and Zwick, B. (2005). A simplified approach for rough identification of muscle activation profiles via optimization and smooth profile patches. In *CD Proceedings of the International ECCOMAS Thematic Conference on Advances in Computational Multibody Dynamics*, Madrid, Spain. ECCOMAS.

[Stroustrup, 2000] Stroustrup, B. (2000). *Die C++ Programmiersprache*. Addison-Wesley, München.

[Sutherland, 2001] Sutherland, D. (2001). The evolution of clinical gait analysis part 1: Kinesiological EMG. *Gait and Posture*, 14:61–70.

[Sutherland, 2002] Sutherland, D. (2002). The evolution of clinical gait analysis part II Kinematics. *Gait and Posture*, 16:159–179.

[Sutherland, 2005] Sutherland, D. (2005). The evolution of clinical gait analysis part III – Kinetics and energy assessment. *Gait and Posture*, 21:447–461.

[Technology, 2003] Technology, A. (2003). *AnyGait Manual*. AnyBody Technology.

[Thelen, 2003] Thelen, D. (2003). Adjustment of muscle mechanics model parameters to simulate dynamic contractions in older adults. *Journal of Biomechanical Engineering*, 125:70–77.

[Weber and Weber, 1836] Weber, W. and Weber, E. (1836). *Mechanik der menschlichen Gehwerkzeuge*. Fisher-Verlag, Göttingen.

[Whittle, 1996] Whittle, M. (1996). *Gait Analysis: an introduction (2nd Edition)*. Butterworth-Heinemann, Oxford.

[Winter, 1990] Winter, D. A. (1990). *Biomechanics and motor control of human movement*. Wiley-Interscience, New York.

[Wismans et al., 1980] Wismans, J., Veldpaus, F., and Jansen, J. (1980). A three-dimensional mathematical model of the knee joint. *Journal of Biomechanics*, 13:677–685.

[Wittenburg, 2007] Wittenburg, J. (2007). *Dynamics Multibody Systems: Dynamics of Systems of Rigid Bodies*. Springer, Heidelberg.

[Yamaguchi, 2001] Yamaguchi, G. (2001). *Dynamic modeling of musculoskeletal motion*. Kluwer Academic Publishers, Boston.

[Yamaguchi and Zajac, 1989] Yamaguchi, G. and Zajac, F. (1989). A planar model of the knee joint to characterize the knee extensor mechanism. *Journal of Biomechanics*, 22(1):1–10.

[Zajac, 1989] Zajac, F. E. (1989). Muscle and tendon: properties, models, scaling and application to biomechanics and motor control. *Critical Reviews in Biomedical Engineering*, 17:359–411.

[Zajac, 2002] Zajac, F. E. (2002). Understanding muscle coordination of the human leg with dynamical simulations. *Journal of Biomechanics*, 35:1011–1018.

[Zajac et al., 2002] Zajac, F. E., Neptune, R. R., and Kautz, S. A. (2002). Biomechanics and muscle coordination of human walking Part I: Introduction to concepts, power transfer, dynamics and simulations. *Journal of Gait and Posture*, 16:215–232.

[Zajac et al., 2003] Zajac, F. E., Neptune, R. R., and Kautz, S. A. (2003). Biomechanics and muscle coordination of human walking Part II: Lessons form dynamial simulations and clinical implications. *Journal of Gait and Posture*, 17:1–17.

[Zwick et al., 2002] Zwick, E., Saraph, V., Zwick, G., Steinwender, C., Linhart, W., and Steinwender, G. (2002). Medial hamstring lengthening in the presence of hip flexor tightness in spastic diplegia. *Journal of Gait and Posture*, 16:288–296.